Quantum Electronic Transport in Atomically Layered Topological Insulators

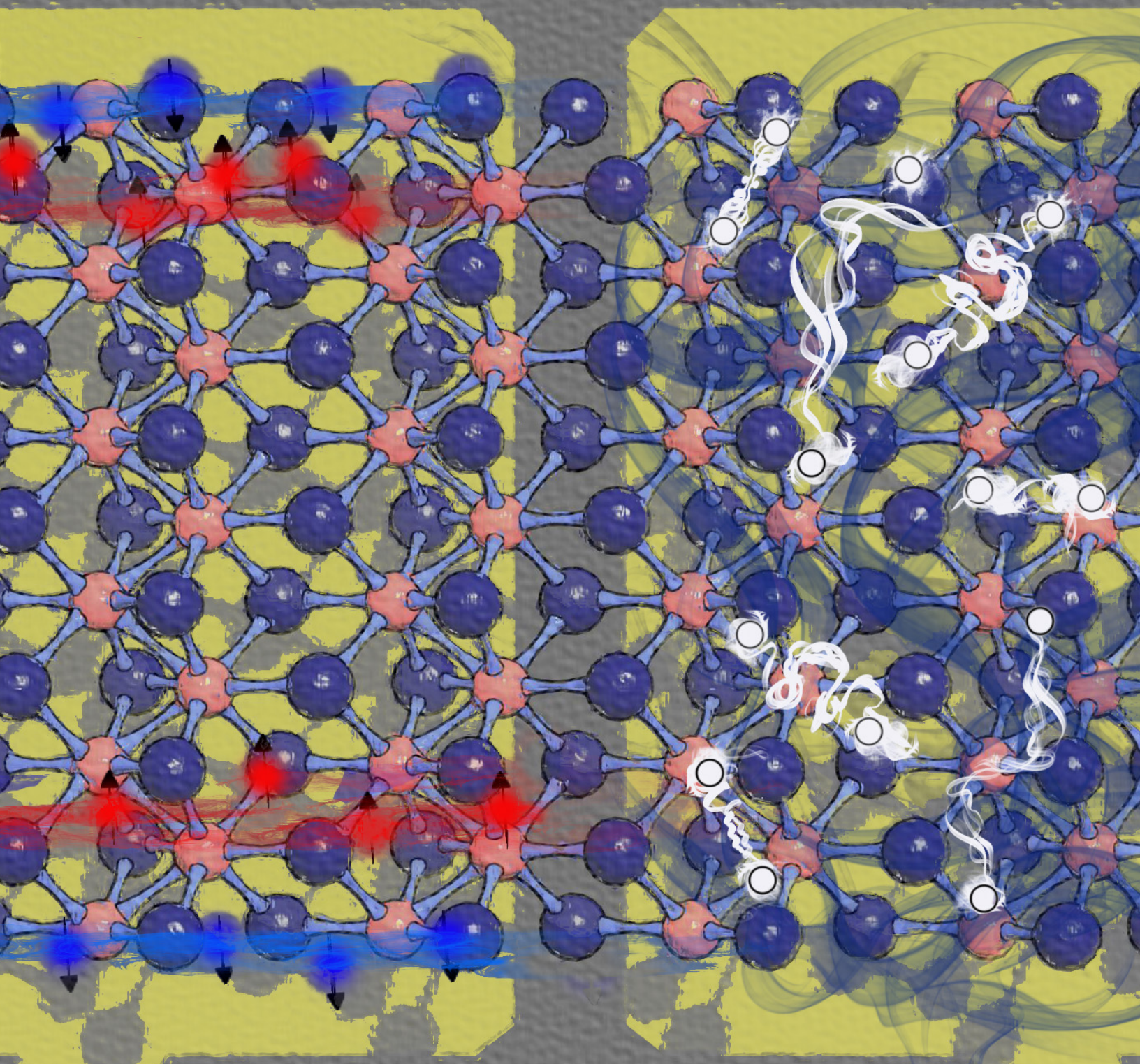

Valla Fatemi

Quantum Electronic Transport in Atomically Layered Topological Insulators

by

Valla Fatemi

Submitted to the Department of Physics
in partial fulfillment of the requirements for the degree of

Doctor of Philosophy
in Physics
at the Massachusetts Institute of Technology

Signature of Author: _____

Valla Fatemi
Department of Physics
January XX, 2017

Certified by: _____

Pablo Jarillo-Herrero
Professor of Physics
Thesis Supervisor

Accepted by: _____

Scott Hughes
Professor of Physics
Associate Department Head

Quantum Electronic Transport in Atomically Layered Topological Insulators

by Valla Fatemi

Submitted to the Department of Physics on January 8, 2018, in partial fulfillment of the requirements for the degree of Doctor of Philosophy.

Abstract

The merger of topology and symmetry established a new foundation for understanding the physics of condensed matter, beginning with the notion of topological insulators (TIs) for electronic systems. For the time-reversal invariant TIs, a key aspect is the "helical" mode at the boundary of the system – that is, the 1D edge of a 2D topological insulator or the 2D surface of a 3D topological insulator. These helical modes represent the extreme limit of spin-orbit coupling in that the spin-degenercy has been completely lifted while preserving time-reversal symmetry. This property is crucial for proposals realizing exotic excitations like the Majorana bound state.

In this thesis, I present a series of experiments investigating electronic transport through the boundary modes of 3D and 2D topological insulators, specifically $Bi_{1.5}Sb_{0.5}Te_{1.7}Se_{1.3}$ and monolayer WTe_2, respectively. For the case of ultra-thin WTe_2, I also present experiments detailing investigations of the 2D bulk states, finding a semimetallic state for the trilayer and a superconducting phase for the monolayer, both of which are strongly tunable by the electric field effect. The discovery of 2D topological insulator and 2D superconductor phases within the same material, accessible by standard solid state elecrostatic gates, places WTe_2 in a unique situation among both TIs and superconductors, potentially enabling gate-configurable topological devices within a homogenous material platform.

Thesis Supervisor: Pablo Jarillo-Herrero
Title: Professor of Physics

Contents

Abstract 1

Acknowledgments 7

1. Introduction and Background 23
1.1. van der Waals Materials . . . 23
1.2. Topological Insulators . . . 26
1.2.1. Non-expert Introduction . . . 26
1.2.2. Deeper Dive . . . 28
1.3. This Thesis . . . 31

I. Electrostatics of Disordered 3D Topological Insulators 33

2. Electrostatic Coupling between Surface States of a 3D Topological Insulator 35
2.1. Introduction and Overview . . . 35
2.2. Electrostatic Coupling between Two Surfaces of a Topological Insulator Nanodevice . . . 36
2.2.1. Abstract . . . 36
2.2.2. Main Text . . . 37
2.2.3. Acknowledgements . . . 43
2.3. On Achieving a True Dielectric in a 3D Topological Insulator . . . 44
2.3.1. Prologue: On Charge Puddles in Topological Insulators . . . 44
2.3.2. Prior Results . . . 45
2.3.3. Two Perfectly Screening Surfaces (Thin Film) . . . 47
2.3.4. Topological Insulator Slab . . . 48
2.4. Epilogue . . . 51

II. The Many Phases of WTe_2 53

3. Introduction to WTe_2 55
3.1. As-Grown 3D Crystal . . . 55
3.2. Two Dimensions . . . 57
3.2.1. Crystal Structure . . . 57
3.2.2. Band Structure and Topology . . . 58
3.2.3. Setting the Stage . . . 60

4. Semimetal **63**
4.1. What is a Semimetal? . . . 63
4.2. Magnetoresistance in Metals . . . 64
4.2.1. Classical magnetoresistance of a diffusive (semi)metal . . . 64
4.2.2. Experimental Discrepancies for WTe_2 . . . 68
4.3. Magnetoresistance and Quantum Oscillations of an Electrostatically-Tuned Semimetal-to-Metal Transition in Ultra-Thin WTe_2 . . . 72
4.3.1. Abstract . . . 72
4.3.2. Main Text . . . 72
4.4. Concluding Note on the Electron Valley Splitting . . . 80

5. Topological Insulator **81**
5.1. Overview . . . 81
5.2. Observation of the Quantum Spin Hall Effect up to 100 Kelvin in a Monolayer Crystal . . . 81
5.2.1. Abstract . . . 82
5.2.2. Main Text . . . 82
5.2.3. Acknowledgments . . . 88
5.3. On the Imperfection of 2D TI Edge Modes . . . 89

6. Superconductor **91**
6.1. Discovery . . . 92
6.2. Observation of Zero Resistance . . . 93
6.2.1. Device Geometry and Basic Characteristics . . . 93
6.2.2. Aspects of 2D Superconductivity . . . 94
6.3. Gate Dependence of Important Quantities . . . 96
6.3.1. Critical Temperature and Critical Current . . . 96
6.3.2. Magnetic Field Effects . . . 98
6.3.3. Preliminary Phase Diagram . . . 101
6.4. Extra Commentary . . . 101
6.4.1. Clean or Dirty Superconductivity . . . 101
6.4.2. On the Pairing Mechanism . . . 103
6.5. Concluding Remarks . . . 103

III. Appendices **105**

A. The Magic of "Topological Protection" **107**
A.1. 2D Helical Surface . . . 107
A.1.1. Small-Angle Scattering . . . 108
A.1.2. Point-Like Scatterers . . . 108
A.2. Graphene vs TI surface State . . . 108

B. Additional Details for Experiment on Electrostatic Coupling between Surface States of a 3D Topological Insulator **111**
B.1. ARPES Measurement Methods and Analysis . . . 111
B.2. Third Device . . . 112
B.3. Temperature Dependence . . . 113
B.4. Hall Effect . . . 113
B.5. Evidence for top-gate to lower-surface coupling . . . 115
B.6. Model Details . . . 115
B.6.1. Charging Model Equations . . . 115
B.6.2. Fitting Procedure . . . 117
B.6.3. Surface-State Model . . . 118
B.7. Temperature-Dependence of Charging Behavior . . . 119

C. Additional Details for Charge Puddle Model **121**
C.1. Reminder On Dielectric Image Charges . . . 121
C.2. Image Charge Approximation for Imperfect 2DEG . . . 122
C.3. Slab Geometry Results . . . 124
C.3.1. Potential at a test charge . . . 124
C.3.2. Potential with Perfectly Screening Surfaces . . . 124

D. Additional Details for Experiment on Semimetallic Phase in Trilayer WTe_2 **127**
D.1. Semiclassical Model . . . 127
D.1.1. Two-Carrier Model . . . 127
D.2. Characterization of Few-Layer Graphene Contacts . . . 130
D.3. Quantum Oscillation Analysis . . . 131
D.3.1. Additional Plots of the SdH Data . . . 131
D.3.2. Temperature Dependence . . . 132
D.4. Additional Data . . . 133

E. Additional Details for Topological Insulator Study **137**
E.1. Materials and Methods . . . 137
E.1.1. General Fabrication Scheme . . . 137
E.1.2. Individual Device Details . . . 139
E.1.3. Raman Analysis . . . 139
E.1.4. Measurement Details . . . 140
E.2. Additional Data . . . 141
E.2.1. Extracting the Plateau Values . . . 141
E.2.2. Bulk State Magnetic Field Dependence . . . 145
E.2.3. Saturation Conductance in High Magnetic Field . . . 145
E.2.4. In-Plane Magnetic Field . . . 146
E.2.5. Temperature Dependence of the Edge Resistance in High Magnetic Field 147

F. Additional Details for Experiment on Superconductivity in Monolayer WTe_2 **149**
F.1. Transition to Insulating State in Device 1 . . . 149
F.2. Extrapolation of T_C . . . 149

F.3. Model Device to Infer Resistivity 150

Bibliography **153**

Acknowledgments

The road to this moment would not have been possible without a great many individuals. I especially thank my graduate research adviser, Pablo Jarillo-Herrero, for providing the opportunity to work on the exciting new systems that will be described in this thesis, for his continued high expectations and attention to detail, for his excellent training in effective communication and well-written papers, for his flexibility in changing research directions when it was prudent, and for the many physics debates from which I have learned much. I thank Liang Fu for his guidance through the years while always being available for discussions on all aspects of topology and condensed matter systems. I thank Vladan Vuletic for his helpful comments regarding my thesis and his positive contributions as a member of my committee. Ray Ashoori, my academic adviser, has been a consistent positive influence and a collaborator, and I believe his initiative to establish the MIT CMX Journal Club was, for me, one of the most important developments in the department during my time here. I also thank my undergraduate research adviser, Latha Venkataraman, for sparking in me the thirst for discovery and patiently mentoring me during my undergraduate years.

I have had the good fortune to work with with several post-doctoral scholars that have been excellent partners on projects through my time in the lab. The first four years of my PhD were alongside Hadar Steinberg, from whom I learned sample fabrication, cryogenic systems, device measurements, how to install a vector magnet fridge, when to trust or distrust data, etc. In particular, our many vigorous debates, from the finest details to the broadest perspectives, have been extremely important for me. (I apologize to my hall-mates, especially Monica, for the occasionally excessive volume.) Ben Hunt was instrumental in obtaining and working on the material that resulted in my first first-authored work in the group, and he has been a continued source of support and positivity. Efren Navarro-Moratalla succeeded Hadar as my office-mate, and we became partners in setting up the glove box system, which is now a core component of the lab's capabilities. In my final year, Sanfeng Wu arrived. He and I have enjoyed an excellent partnership on the WTe_2 project, and I have learned from him a particular brand of optimism and focus on simplicity[1]. And of course, I am grateful for my overlap with Landry Bretheau with whom I enjoyed a great many discussions spanning all possible topics.

I thank Charles Marcus for the opportunity to be a visiting summer student in his lab. Hugh Churchill, Kasper Grove-Rasmussen, and I formed an effective and efficient partnership there. Working hard that summer under very constrained time circumstances, we managed to fabricate devices and measure data that resulted in a nice paper [1]. I learned particularly about efficient work, goal-setting, and decision making with limited information. When

[1] More precisely, as the famous adage attributed to Einstein goes, a focus on keeping things "as simple as possible, but no simpler."

Hugh joined Pablo's group, he was a constant source of discussion, encouragement, and useful information. I also had the pleasure of working with him to complete the Helium Recovery System, which continues to dutifully serve the group.

Every member of the Jarillo-Herrero group has been important to me. When I first joined the group, Javier Sanchez-Yamagishi was the glue that held the group together and helped me and other new members always feel at home. Since then, he and I have grown into fast friends, strengthened through the difficulties of research and the joy of discovery. The same can be said of most of the group members, and especially the "old-guard" who were present in my first year. These include Joel I-Jan Wang, Leonardo Campos, Thiti Taychatanapat, Nathan Gabor, and particularly Qiong Ma, who joined the group at the same time as me and with whom I enjoyed being among the last graduate students at MIT to take the full gauntlet of three qualifying exams. Since those early days, I have had the pleasure of sharing the lab with many newer members of the group. Among those, I particularly thank Yuan Cao, Jason Luo, Dahlia Klein, Yafang Yang, and David MacNeill for having allowed me to distract myself by helping, advising, or otherwise contributing in some way to their research projects. I also enjoyed the opportunity to work with several excellent UROPs, particularly Stephen Eltinge and Lucas Orona who were involved in some of the work here. Monica Wolf, possibly the most important individual in the group, made all non-scientific matters a breeze and our chats were always a bright spot in my day.

Outside the group, I have enjoyed the camaraderie of the MIT (and Harvard) physics community. In particular I mention Ray Ashoori, Fahad Mahmood, Justin Song, Alex Frenzel, Spencer Tomarken, Di Wei, Marco Furchi (visiting student from Vienna), Andrea Young, Joe Checkelsky, Brian Skinner, and Jonathan Ruhman. Fahad was instrumental in obtaining data to complete the research in Chapter 2 and Brian was particularly helpful for the theoretical work in the same Chapter. I also thank (in no particular order) Daniel Rodan-Legrain, Jason, Javier, Efren, Andrea, Francisco Machado, Fahad, Dan Pilon, Ray, and Pablo for numerous excellent games on the squash court, and the MIT Rugby team for many good times outside the lab.

Finally, I am indebted to my partner Tina for her unending patience and love throughout these trying years in Cambridge. I thank all of my family for their love and support, including my grandparents, aunts, uncles, and cousins (aghabi!). I thank my parents and my brother for their love and support from the beginning to the end, and particularly for the space to explore my own path in life.

The most exciting phrase to hear in science, the one that heralds new discoveries, is not "eureka!", but "that's funny..."

– Isaac Asimov

...there is really no place in this enterprise for a rogue physicist.

– Wallace Breen

Look at me still talking when there's science to do.
When I look out there, it makes me glad I'm not you.
I've experiments to run.
There is research to be done
On the [samples] that are still alive.

– GLaDoS

List of Figures

1.1. **A,** A WTe_2 crystal. Scale bar is about 1 mm. **B,** Zoom-in to area where the crystal is naturally peeling apart, indicative of the weak interlayer bonding. Scale bar is about 0.2 mm. **C,** Cross-sectional schematic of the WTe_2 crystal structure at the region being peeled apart at the van der Waals cleavage plane indicated by the dashed line. This is indicative of the exfoliation process used to isolate monolayer and few-layer crystals. See Section 3 for details on the crystal structure. 24

1.2. **A,** vdW heterostructure with an exposed monolayer of WTe_2 on top of hexagonal boron nitride (hBN). Volatile molcules in the air react with and deteriorate the exposed WTe_2. **B,** vdW heterostructure of the materials discovery type. Encapsulating the WTe_2 with hBN on both sides protects it from the reactive molecules in the air. **C,** vdW heterostructure of the hybrid material type utilizing a monolayer of WTe_2 and a monolayer of CrI_3, a ferromagnet, protected on both sides by hBN. This heterostructure has not been investigated at the time of this writing. 25

1.3. **A,** Genus-0 surfaces: spheres and footballs (both inflated and deflated). **B,** Genus-1 surfaces: a torus and a coffee mug. **C,** Genus-3 surfaces: the double-torus and the hybrid donut-mug, which has a hole for the handle as well as in the center of the mug. **D,** Artistic representation of electrons bound within closed geometries on the left and right sides (torus and sphere, respectively), representing topologically distinct materials. At the interface (purple broken shapes) it is impossible to have a closed manifold equivalent to either the torus or sphere, so the the electrons are freed and can flow. 27

1.4. **A,** Schematic of a quantum Hall state with $\nu_{tot} = 1$. Solid and dashed lines indicate occupied and unocupied states, respectively. **B,** Schematic of a quantum spin Hall state with $\mathbb{Z}_2 = 1$. **C,** Schematic of the 3D time-reversal invariant topological insulator. 30

2.1. **A,** Colorized AFM image of device A, including schematic circuit elements describing the transport measurement. Red is BSTS, blue is h-BN, and gold is Ti/Au (contacts and gate electrode). The scale bar is 2 microns. **B,** TrARPES measurement of a BSTS crystal. The white line indicates the chemical potential. 38

2.2. Gate-dependence of the resistivity of devices A and B. **A,** Bottom gate dependence of resistivity at $V_T = 0$ at low temperature (blue, green) and 270K (dashed) from cooldown 2. **C,** Top gate dependence of resistivity at $V_B = 0$ at low temperature (blue, green) and 270K (dashed) from cooldown 2. **B & D,** 2D map of resistivity while modulating both gate electrodes for devices B and A, respectively, from cooldown 1. The black dots track the location of the upper surface R_{peak} at each V_B. 39

2.3. **A,** Schematic of the charging model used in this study with important parameters labeled. For comparison to the experiment, the upper surface state is kept at charge neutrality while charge is distributed between the lower surface state and the gate electrodes. Three voltage loops indicated by the blue dashed lines are used in deriving the charging model. **B,** The position of the upper surface R_{peak} as a function of both gate voltages $V_{peak}(V_B)$ (left, black dots), and the resistivity at those gate voltages R_{peak} (right, blue), extracted from Fig. (2.2)d. **C,** The fit of the energy-density relationship as derived from ARPES (red line) and from $V_{peak}(V_B)$ (black dots). 41

2.4. Effect of high magnetic fields on the transport data. **A,** $V_{peak}(V_B)$ at 0T and 8T from cooldown 2. For comparison, the dashed pink line would be the gate-gate dependence if the lower surface has no electronic states, given by a ratio of geometric capacitances: C ratio $= -\frac{1}{C_T}\frac{C_B C_{TI}}{(C_B+C_{TI})}$. The transport data approaches this slope at 8T. **B,** The extracted energy-density relationship of the lower surface state at 8T for the case of fixed inter-surface capacitance $C_{TI} = C^0_{TI}$ (blue) and when using C_{TI} as a fit parameter (green) to the zero-field density of states (ARPES model, red curve). Arrows indicate increase in the total chemical potential change assuming fixed C_{TI}. **C,** The difference in the total change of the chemical potential of the lower surface with magnetic field (blue, left axis, error bars are the standard deviation of possible values) and the best fit C_{TI} as a function of magnetic field (green, right axis, error bars are 90% confidence intervals). **D,** The temperature dependence of the resistivity at different magnetic fields and when both surfaces are at charge neutrality. 43

2.5. Schematic of the energy of the conduction and valence bands as a function of a real-space coordinate. Labeled energy scales are the intrinsic spectral band gap of the material E_g, the average energies of the conduction and valence bands E_c and E_v, the chemical potential μ, the lowest energy to access a metallic percolating paths E_e and E_h, and the new transport band gap between the chemical potential and the percolating paths Δ. The average size of a puddle is indicated by R. This figure used with permission from [2]. 45

2.6. Location of image charges for a single charge between two metallic plates with $d = 1$. Color indicates the sign of the charge. 47

2.7. Γ^2 and Γ as a function of z for the case of perfectly screening surfaces. For this model calculation, we have artificially set $\kappa_1 = N_D = 1$. 48

2.8. Orange: Γ^2 and $|\Gamma|$ as a function of position for $r_s = \frac{d}{8}$. In this case we have again artificially set $\kappa_1 = \kappa_2 = N_D = 1$. Blue curves are the same as in Figure (2.7). A finite r_s approximately results in a rigid upward shift of the squared potential fluctuations. 49

2.9. $\Gamma(z)$ for different $\kappa_2 = \{1, 4, 8, 20, 40\}$, from top to bottom. The constants are the impurity density $N_D = 10^{19} cm^{-3}$, the interior permittivity $\kappa_1 = 40$, and the thickness of the film $d = 60nm$. The left panel is for $r_s = 4nm$ and the right panel is for $r_s = 20nm$. 50

2.10. Phase diagram of puddles bulk puddles for $\kappa_{TI} = 36$. Data-points indicate the point at which potential fluctuations are of order the size of the band gap. Upper right: schematic of the topological insulator thin film geometry. . . . 51

3.1. An optical microscopy image of a 3D WTe_2 crystal. **A,** Scale bar ~ 1 mm. **B,** Zoom-in of the red square region in **A**, where the layered structure is readily apparent and the ease of exfoliation is anticipated by the visible "natural peeling apart" of the crystal. 55

3.2. Bulk atomic positions for the **A,** 1T' and **B,** Td structures. Orange dots represent centers of the M-Te rhombi, which represent true inversion centers for the 1T' case. 56

3.3. Schematic Fermi surface presented by Feng, et al [3]. Green and blue are the bulk bands at $k_z = 0$, and red is the surface state which may be a surface arc due to the presence of Weyl nodes [3, 4, 5, 6, 7]. 57

3.4. Monolayer atomic positions, as extracted from bulk crystallography data, for the (**A**,**C**) 1T' and (**B**,**D**) Td structures. 58

3.5. **A,** Band structure of monolayer WTe_2 from a DFT-derived tight-binding model. The conduction and valence bands were shifted have roughly the band gap seen in spectroscopy measurements [8]. Center: zoom-in to the bottom of one of the conduction band valleys to show the intrinsic spin-orbit splitting. **B,** Same calculation with a large displacement field added, showing that the spin-orbit splitting can be enhanced. 60

4.1. Schematic band structures of some different types of semimetals: **A,** traditional. **B,** Dirac. **C,** Weyl (type I). **D,** Weyl (type II). Red or Blue coloring indicates Berry curvature around nodes with positive or negative chirality. Note that **A** and **B** may occur in any extended dimensionality (particularly 1D, 2D, or 3D), but **C** and **D** are in 3D only. 64

4.2. Cartoons depicting simple metals and semimetals in two classic geometries: linear transport channel (equivalent to a Hall bar) and Corbino. Only the simple metal in a standard bar geometry has a Hall electric field, and therefore it is the only scenario that does not have a magnetoresistance. 65

4.3. Black sheep model for magnetoresistance, which can give subtle inflections amid generally quadratic magnetoresistance (plot scale and range is modeled after [9]). Blue is the actual model, while the red dashed line represents a simple quadratic. 71

4.4. **A,** Optical image of a completed device. The edges of the original FLG flakes are indicated by dashed white line, and the original boundary of the WTe_2 flake is outlined in purple. The dark regions are where the stack was fully etched to the SiO_2 substrate. Solid white scale bar is 2 microns long. **B,** Cross-sectional schematic of the device structure, with all components labeled. **C,** Temperature dependence of device A at two representative gate voltages. The average RRR for all gate voltages is 13. Inset: Temperature dependence of a similar-thickness WTe_2 device fabricated in air and without encapsulation. **D,** Gate dependence of R_{xx} at $B = 0T$ and $T = 4K$. The vertical dashed line at $V_{BG} = 87$ indicating the resistance maximum. 73

4.5. **A,** MR as a function of magnetic field for a range of V_{BG} at $T = 30mK$. Inset: a zoom-in of the data at $V_{BG} = 120V$. **B,** R_{xy} as a function of magnetic field for a range of V_{BG} at $T = 300mK$, displaying a transition from non-linear to linear Hall effect. Inset: Extracted saturation parameter (equation (4.40)) as a function of gate voltage (black) at $B = 10T$. The blue dotted line is unity. **C,** Individual carrier densities and the total carrier density, including charge sign, from the semiclassical model fit. Black dashed line is an extrapolation of the hole density from the slope at lower gate voltages. **D,** Mobilities from the model fit. Error bars in **C-D** represent 95\% confidence intervals of the fit. **E,** Same data as **A** in log-log format with each curve offset vertically for clarity. The blue dotted line is a quadratic power law, whereas the cyan line is a power law fit to the data at $V_{BG} = 10V$. **F,** The fitted exponent of the MR power law for $B \in [0.4, 1.5]\,T$ as a function of gate voltage. The limits were chosen to avoid the high relative noise at low fields ($B < 0.2T$) and onset of saturation at high field. Dot color corresponds to gate voltage in accordance with **A** and **E**. Dot size is larger than the 95\% confidence interval of the fit. The black dashed line indicates the mean exponent for $V_{BG} < 95V$. 75

4.6. **A,** SdH oscillations in $\Delta R_{xx}(1/B)$ at different temperatures and **B,** their fast Fourier transforms (FFTs) at $V_{BG} = 120V$. **C,** Gate- and field-dependence of ΔR_{xx} at $T = 30mK$. White dotted lines guide the eye to the δ pocket oscillation. **D,** FFT peak frequencies (dots) at each gate voltage, and extrapolation of the δ frequency to zero (dotted line). **E,** Temperature dependence of ΔR_{xx} maxima associated with the α pocket at $V_{BG} = 120V$. **F,** Effective mass of each pocket, from fits such as in **E** (see Appendix D for more details). 78

5.1. To-scale, cross-sectional schematic of the tenting effect of hBN as it comes down off of a 20nm tall electrode. The typical contact angle at the substrate is ~ 16 degrees, resulting in roughly a 70nm "tent zone". Nitrogen (black) and oxygen (red) molecules (drawn at ~ 4 times their actual size for visibility) are placed on a grid of 4 nm spacing, which is roughly the intermolecular spacing of molecules in air. It is clear that many molecules easily fit into the gap. . 82

5.2. Device structure and resistance near $h/2e^2$. **A,** Schematic of the device structure. **B,** Four probe conductance measurement at 4 K of Device 1 as a function of V_{tg} across all the local gates, which are floating. Inset: the optical image of Device 1 (left) and the corresponding monolayer WTe_2 flake before fabrication (right). **C,** Color map of the flake resistance tuned by V_{tg} and the 100nm-wide local gate V_c at 4K. Two regions are separated by a step in the resistance distinguishing the doped and undoped local channel, as depicted by the inset schematics. **D,** ΔR versus V_c for the 100 nm wide gate on Device 1 at $V_{tg} = 3.5$V, and the 60 and 70 nm wide gates on Device 2 at $V_{tg} = 4.1$V (taken at 5 K). For clarity, the two curves from Device 2 are offset by +3 V along the x axis. Inset: the average step height $\langle \Delta R \rangle$, extracted from **C**, as a function of V_{tg}, showing a clear saturation towards $h/2e^2$ for large V_{tg}. 84

5.3. Length dependence of the undoped channel resistance. Data taken at 4 K from 5 different devices (Table E.1), each denoted by a different color and symbol. The device numbers and associated colors are: 1, Black; 2, green; 3, purple; 4, red; 5, blue. The ΔRs values reach a minimum of $h/2e^2$ in the short-channel limit on one sample, and approach this value in other samples, confirming a conductance of $2e^2/h$ for the undoped channel, i.e. a conductance of e^2/h per each edge of the device, in agreement with QSHE. Detailed analysis of raw data can be found in Fig. E.4-E.7. 85

5.4. Time reversal symmetry breaking by a magnetic field and Zeeman-like gap at the Dirac point. **A,** The evolution of the edges conductance G_s versus gate under the application of a perpendicular magnetic field, B (from 0T, thick blue curve, to 8T, thick red curve) at 1.8K, for Device 1, 100 nm channel. **B,** Traces of G_s vs. B for a few selected local gate voltages V_c showing two types of behavior: saturation and non-saturation, associated with whether or not the Fermi energy is in the Zeeman gap, as depicted in the band schematics a. (linear bands at zero B, E_F at Dirac point), b. (gapped bands at finite B, E_F at Dirac point), and c. (gapped bands at finite B, E_F away from Dirac point). **C,** Inset: temperature dependence of G_s vs. B for the non-saturating curves (V_c = -6.44V). Main: All the curves in the inset collapse to a single trend in the normalized plot of $-\log(G_s/G_0)$ vs $\mu_B B/k_B T$. The black line is a linear fit. Additional inspection of the temperature- and magnetic-field dependence is shown in Fig. E.9-E.11. 86

5.5. **A,** Temperature dependence of the edges conductance at a few representative gate voltages for 100 nm channel in Device 1. The conductance is dominated by the QSHE up to about 100K. The schematics depict the increase of the conductance due to onset of conduction from bulk states. Inset: gate dependence of ΔR at various temperatures. **B,** Temperature dependence of the resistance of the whole flake (full length), when the Fermi energy in the local channel is in the doped (V_c = -1V, red) and undoped (V_c = -5.7V, blue) regimes, at $V_{tg} = 3.5$V. The difference between the curves yields the temperature dependent channel resistance ΔRs (yellow). The vertical dashed line highlights the kink in the undoped regime at 100K, indicating the transition to the QSHE edge-dominated regime. 88

6.1. **A**, The resistance drop as a function of temperature at $V_{tg} = 4$V. **B,** dV/dI as a function of direct current bias at different magnetic fields, with critical current labeled as I_c. This data taken at $V_{tg} = 4V$. Upper: line traces as a function of I_{dc}. Lower: Same data in color map format. 92

6.2. **A**, Schematic of the structure of device 2. See also Ref. (2) for more details. **B-D**, Four probe V-I curves for different sets of contacts. **B & D**, The case of half-encapsulated WTe_2, in which superconductivity is not detected down to 300 mK. **C**, The channel that includes fully encapsulated WTe_2 shows a transition toward superconducting behavior at low temperature. 93

6.3. **A,** Cartoon illustration of the device structure and the crystal structure of monolayer WTe_2. **B,** Optical microscopy image of device 2, with the monolayer WTe_2 (red) and graphite top gate (orange) highlighted. Circuit elements show the measurement configuration. **C,** Temperature dependence of the resistance for $V_{bg} = 4$ V and $V_{tg} = 5$ V. Inset shows the resistance as a function of both gate voltages, at base temperature. **D,** V-I characteristics from base temperature (black) up to 940 mK (red). **E,** Magnetic field dependence of the nonlinear V-I behavior, measured at base temperature, captured by the differential resistance curves, at base temperature. 94

6.4. **A,** Power law exponent of the V-I curve near the critical current. Inset: log-log plot of the V-I curves, with a cubic relationship plotted in the dashed blue line. **B,** Plot of the logarithm of resistance as a function of a reduced temperature to find T_{BKT}. For this device we had to account for the "shoulder" seen in Figure 6.3C, so $R' = R - 250\Omega$. 96

6.5. **A,** $R(T)$ characteristic for different gate voltages, showing the transition from a superconducting state to an insulating state. Dashed line is a guide to the gate voltage, V_c^{MIT}, that separates the two regimes. Inset: color plot of the same data, normalized to the normal state resistance R_n, with T_c marked in black. **B,** Upper panel: gate dependent critical temperature T_c, summarized from **A**. The zero-resistance region is shaded dark blue. Lower panel: gate dependent critical current, I_c and I_c', summarized from **D**. For $V_{bg} < 1V$, I_c is found to bifurcate into two peaks, the values of which are determined by extrema of the second derivative of $\frac{dV}{dI}(I_{DC})$ data. The corresponding electron density (n_{2D}), estimated from the capacitance model, is shown on the top axis. **C,** Differential resistance $\frac{dV}{dI}$ v.s. current bias I_{DC} for $V_{tg} = V_{bg} = 5V$. Inset: zoom-in to the zero-resistance region. **D,** Differential resistance $\frac{dV}{dI}$ vs. current bias I_{DC} and gate voltage V_{bg}. Close to $V_{bg} \sim 1V$, the observed I_c trace bifurcates, as more clearly indicated in **B**. Dashed line indicates the gate voltage at which the peaks in differential resistance merge at zero bias, indicating destruction of superconductivity. 97

6.6. **A,** Gate-dependent $R(B)$ traces, normalized to the normal state resistance R_n. **B,** Color map of the same data, as a function of V_{bg} and B. Circles denote B_c, referring to the magnetic field at which 50% of the normal state resistance is recovered. **C,** Temperature dependence of B_c for selected gate voltages, including fits to the GL formula for T close to T_c (see main text). **D,** Coherence length extracted from fits such as in **C**. Color of all data points and lines represents the gate voltage of that data point. 98

6.7. **A,** LEFT: The same perpendicular field data as in Fig. 6.6, plotted here for comparison. RIGHT: a schematic indicating the color coding for perpendicular and parallel magnetic field (note for clarification: the orientation of the parallel field with the crystal lattice is not known). **B,** Normalized device resistance as a function of parallel magnetic field (black) and perpendicular magnetic field (blue). 100

6.8. Schematic phase diagram for temperature and carrier density. 101

B.1. **A,** Static ARPES and **B,** TrARPES data (t = 1500 fs after pumping the system). The chemical potential is indicated by a white dashed line, and the energy of the valence band maximum is indicated by a dark dashed line. In **B**, the cubic fit to the surface state dispersion is superimposed on the data by a blue line. The magenta quadratic curve is the estimation for the conduction band energy and effective mass. 111

B.2. Data from a second thin device, 42nm thick, showing similar behavior to the thin device in the main text. **A,** Color plot of resistivity as a function of both gate voltages, with the upper surface resistance peak marked by black circles. **B,** Fit of the transport data (black dots) to ARPES data (red line). 113

B.3. Temperature dependence without any applied gate voltages for **A,** device A and **B,** device B, which display qualitatively different behavior. 114

B.4. Hall effect data in device A. **A,** $R_{xy}(B)$ at three different back gate voltages. **B,** R_H, obtained from the slope of $R_{xy}(B)$, as a function of V_B. **C,** R_{xy} at 8T as a function of back-gate voltage at different temperatures. 114

B.5. Derivative of resistance as a function of either gate voltage. **A-B,** Device A, $\frac{dR}{dV_B}$ and $\frac{dR}{dV_T}$ as a function of both gate voltages, respectively. **C-D,** Device B, $\frac{dR}{dV_B}$ and $\frac{dR}{dV_T}$ as a function of both gate voltages, respectively. The black dots are the position of the resistance peak for upper surface (panels **A** and **C**) and lower surface (**B** and **D**). 116

B.6. Schematic of the charging model from the main text. The equation labels refer to the equation associated with the surrounding voltage loop. 117

B.7. Evolution of quantum well states of the conduction band when the upper surface is at the Dirac point while the lower surface is charged by a gate. **A,** Schematic of the band structure at three different doping configurations. (i) is when both surface states are at the Dirac point; (ii) is when μ_L state is at the nominal ARPES value for the conduction band minimum; (iii) is the condition when a bulk sub-band actually begins to be filled. **B,** Energy levels of states in the system as a function of μ_L while keeping μ_U at the Dirac point. The red line is μ_L itself, and the solid black line is the nominal energy of the conduction band minimum given by ARPES. The three blue lines are the first three sub-bands if a half-triangular confining potential is assumed. In reality the confinement is stronger due to the finite thickness of the sample, as shown schematically in **A**. Finally, the configurations i, ii, and iii are labeled at the top of **B**, including vertical dashed lines for ii and iii to emphasize the energy difference. 119

B.8. Temperature dependence of the device A's charging behavior. **A,** $V_{peak}(V_B)$ at $T = 100$ K and at different magnetic fields. The behavior is qualitatively similar to the low-temperature data. Curves have been offset to align at $V_B = -70$ V to increase clarity of the field dependence. **B,** Temperature dependence of the inter-surface capacitance for different magnetic fields normalized to the low-temperature value: $C_{TI}(T)/C_{TI}^{T=4\mathrm{K}}$. The dashed line is a guide to the eye. Error bars represent 90% confidence intervals from the fit. **C,** The total chemical potential change as a function of magnetic field assuming C_{TI} only depends on temperature and not magnetic field. For all three temperatures, the total chemical potential change remains approximately the same magnitude. Error bars represent a standard-deviation of possible values. 120

C.1. Potential at the position of the test charge as a result of its images. From black to red are lines indicating progressively more terms being included in the sum the convergence eventually is very slow and alternates about the ultimate mean curve. The blue line is Eq. (C.26), which is clearly the converged case, and the green line represents the analytical value at the position exactly between the surfaces ($z = 0.5$). 125

C.2. Electrostatic potential due to a test charge at different positions in a slab geometry. Black line is the bare test charge potential, while the red line includes the image charges. 126

D.1. Unconstrained Fit. (a) $R_{xx}(B)$ and (b) $R_{xy}(B)$ for a representative set of gate voltages. Solid lines are the raw data, and dashed lines are the fits. (c) The electron, hole, and total charge densities (including charge sign) as a function of gate voltage. (d) Mobility of the electrons and holes as a function of gate voltage. 95% confidence intervals are included in (c-d) but may be smaller than the marker size. 128

D.2. Constrained Fit. (a) $R_{xx}(B)$ and (b) $R_{xy}(B)$ for a representative set of gate voltages. Solid lines are the raw data and dashed lines are the constrained fits described in the text. (c) The electron, hole, and total charge densities (including charge sign) as a function of gate voltage. (d) Mobility of the electrons and holes as a function of gate voltage. 95% confidence intervals are included in (c-d) but may be smaller than the marker size. 129
D.3. Fitting without magnetoresistance. (a) $R_{xx}(B)$ and (b) $R_{xy}(B)$ at a representative set of gate voltages. Solid lines are the raw data and dashed lines are the fits described in the main text. (c) The electron, hole, and total charge densities (including charge sign) as a function of gate voltage. (d) Mobility of the electrons and holes as a function of gate voltage. 95% confidence intervals are included in (c-d) but may be smaller than the marker size. 129
D.4. First row: source and drain electrodes. Second row: side contacts. (a,d) Raw two-probe resistance as a function of gate voltage and magnetic field. (b,e) Two-probe resistance after subtracting a smooth polynomial as a function of magnetic field for each gate voltage, ΔR_{2p}. (c,f) The amplitude of the Fourier transform of $\Delta R_{2p}(\frac{1}{B})$ (from b and e, respectively) at each gate voltage. 130
D.5. Data same as in Figure (4.6) in the main text, which is from cooldown 2 at 30 mK. (a) Color map of the longitudinal resistance as a function of magnetic field and gate voltage. (b) Colormap of the longitudinal resistance with a smooth magnetoresistance background subtracted at each gate voltage. The colorscale is normalized at each gate voltage to highlight the gate voltage dependence independent of oscillation amplitude. (c) FFT of the quantum oscillations at each gate voltage. The FFT is normalized in separate sections above and below $90T$ to highlight the different FFT peak positions. 131
D.6. Data from cooldown 1 at 300mK. Colormaps of the (a) longitudinal resistance and (b) transverse resistance with a smooth background subtracted at each gate voltage. Here the colorscale is NOT normalized at each gate voltage. (c,d) FFT of the quantum oscillations in R_{xx} and R_{xy} at each gate voltage, again with no normalization. In (d) we highlight the gate-dependence of the α pocket with an arrow. 132
D.7. Temperature dependence of different SdH oscillation maxima at a fixed gate voltage for each of the three pockets . (a) The α pocket at $V_{BG} = 120V$. (b) The β pocket at $V_{BG} = 120V$. (c) The δ pocket at $V_{BG} = 0V$. 133
D.8. Optical microscopy images of devices B (left) and C (right), with different aspects labeled. Scale bar is $3\mu m$. 134
D.9. (a-b) Magnetoresistance of device B before applying a gate voltage. In (b) the black and red lines are quadratic field dependence and power law fit (fit between 0.3 and 11.5 T), giving an exponent of 1.6. (c) Data (connected dots) at several different gate voltages (color indexed by color in (d)) between -80V and +80V, with solid lines showing B^2 (black) and $B^{1.6}$ (blue) behaviors for comparison. Note that this is after a change of the device mobility, resulting in a lower total MR but the same power law. (d) Fitted exponent (for the field range between 1 and 11.5 T) as a function of gate voltage. 134

D.10. Measurements for device C. For this device, only the source, drain, and a pair of Hall probes were functioning. The Hall measurements were found to have a large mixing of the longitudinal signal. The data presented as R_{xx} and R_{xy} is the symmetric and antisymmetric portion of this signal, respectively. (a-b) Magnetoresistance ratio and Hall effect at different gate voltages. Weak quantum oscillations can also be seen in (b). (c) Data (connected dots) at several different gate voltages between -60V and +60V indexed by color consistent with (d). Solid lines show B^2 (black) and $B^{1.6}$ (blue) behaviors for comparison. (d) Fitted exponent (for the field range between 3 and 11.5 T) as a function of gate voltage. 135

E.1. Images of fabrication steps. Optical microscopy (OM) images (upper row) and atomic force microscopy (AFM) images (middle row) taken at each key stage of the fabrication process. The images in the lower row are cross-sectional schematics to illustrate the structure. 139

E.2. Raman spectrum of an exfoliated monolayer of WTe_2 taken at room temperature with a 532nm excitation laser, consistent with the 1T' phase of monolayer WTe_2. 140

E.3. dV/dI as a function of DC bias for $V_{tg} = 3.5$V on device 1 measured in four-terminal configuration at 4K. Blue and orange correspond to the bulk regime ($V_c = 3$V) and edge regime ($V_c = -6$V), respectively. The difference is in yellow. The flat dV/dI indicates linear ohmic contacts. 140

E.4. Analysis to extract the edge resistance – Device 1, 100nm gate, 4 K. (a) Total resistance as a function of top gate and local gate voltage (V_{tg} and V_c, respectively), for device 1 with the 100nm-wide local gate. (b) The same data as (a) with the resistance at $V_c = 3$V subtracted away, which we designate ΔR. The space between the red dotted lines indicates the range of ΔR on the step that is averaged to extract the step height. (c) Specific traces of total resistance vs V_c showing how the traces change progressively with increasing top-gate voltage. (see the Appendix text and Fig. E.7 for explanation on signatures of second step). (d) A plot of the step resistance as a function of V_{tg}, showing the saturation at large V_{tg}. The error bars indicate a full standard deviation from the mean ΔR in the range given by the red dots in (b). . . . 142

E.5. Analysis to extract the edge resistance – Device 4, 400nm gate, 4 K. Same as Fig.E.4, but for the 400nm-wide gate in Device 4. The resistance of this long channel saturates to a resistance well above what is measured in the short-channel limit. In general, we have observed increased resistance with increasing length in long channel devices (Fig. 5.3). This increase of resistance can be understood by considering dephasing scatterers at the edges. The helical edge mode is equilibrated at the dephasing sites, which effectively break the long edge mode into multiple in series, resulting in a trend of increasing total resistance. Device-to-device variation for the same channel length can thus be attributed to differing disorder realizations for the different devices. . 143

E.6. Analysis to extract the edge resistance – Device 2, 100 nm gate, 4 K. Same as Fig. E.4, but for the 100nm-wide gate in Device 2, which shows a similar converged resistance step value as in Device 1. 144

E.7. Channel resistance with a second step. (a) ΔR as a function of both gate voltages and (b) a representative line-cut of ΔR vs. V_c at $V_{tg} = 2.6$ V for the 500nm-wide local gate in Device 1 at 4 K. The second step exhibited here appears especially for a few of our longer channels. It could be related to the creation of an n-edge-p-edge-n junction as indicated by the schematics in panel (b). See supplementary text for details. The height of the first step is extracted as the channel resistance of the edge mode with length defined by the local gate. 144

E.8. Magnetic field dependence of the resistance in the bulk-doped regime ($V_{tg} = +3.5$ V) at different temperatures. The weak magnetoresistance here shows that the strong magnetoresistance observed in the edge regime is unrelated to bulk states. 145

E.9. Saturation conductance of the edge modes at high magnetic fields. (a) Magnetic field dependence of the edge conductance from $B = 5$T to 8T, with three specific traces highlighted and all others in gray. The dotted lines indicate values (0.5, 0.66, 0.83, 1) expected from scenarios based on charge puddles (see supplemental text for details). (b) A few specific traces of the edge conductance as a function of magnetic field. In red is the exponential behavior near the Dirac point, and the other three traces show typical saturation behavior. Dotted lines are the same as in (a). (c) A histogram of all local conductance extrema along gate voltage traces ($G_{high\ field}$) from 5T to 8T, with dotted lines again highlighting the same values (see supplementary text for details). 146

E.10. In-plane magnetoresistance. (a) Edge conductance as a function of local gate voltage V_c for different in-plane, roughly perpendicular-to-edge, magnetic field strengths at 4 K for the 100nm-wide gate of Device 2. (b) Line traces of resistance as a function of magnetic field for selected V_c. The conductance is clearly suppressed under in-plane magnetic fields. This device does not have a distinct Dirac point, but instead sees a uniform decrease in conductance, possibly due to a different edge configuration or non-uniform disorder strength at the edges compared to Device 1. 147

E.11. Magnetic field effect at different temperatures. Raw data for the temperature dependent magnetoresistance measurements for Device 1, 100 nm local channel. Resistance vs. local gate voltage V_c subjected to different magnetic fields for a representative set of temperatures: (a) 4 K, (b) 8.3 K, (c) 18K, and (d) 34 K. 148

F.1. Gate voltage dependence of of the $R(T)$ curves for device 1. 149

F.2. T_c as a function of ρ_n, which exhibits a less non-linear relationship than T_c as a function of V_{bg}. The red and blue curves are cubic and linear fits with extrapolation to $T_c = 0$. 150

F.3. Image of the simulated device in COMSOL, with colored lines representing constant voltage lines. 151

1. Introduction and Background

1.1. van der Waals Materials

van der Waals (vdW) materials are often first introduced through the common material graphite. Graphite is composed of sheets of pure carbon stacked upon each other. Like a stack of paper, the individual sheets are relatively easy to pull away from the stack. The easy separation of layers is part of the basis for being used as the writing element in pencils, and macroscopic crystals can often be seen to be peeling open like the pages of a book, as can be seen for WTe_2, another vdW material, in Figure 1.1A-C. In the lab, we use various forms of adhesive tape to peel away layers of vdW materials from the parent crystal. The name "van der Waals" honors the scientist Johannes Diderik van der Waals who discovered the weak force that binds the sheets together, originally in the context of gases and molecules, for which he won the Nobel Prize in Physics in 1910 [10].

A single atom-thick sheet of carbon extracted from graphite is called graphene [11], which was first reported in 2005 [12, 13], preceded by the measurement of few-layer thick samples [14]. These discoveries kicked off the field of ultrathin vdW materials[1]. Since then, the library of accessible two-dimensional (2D) crystals has expanded to encompass a virtual zoo spanning the full extremes of material behaviors – insulators, metals, semiconductors, magnets, superconductors, and more have now all been isolated as individual crystalline layers.

[1] There were a few prior reports on ultra-thin vdW materials [15, 16, 17, 18], but none with results as striking as the first reports related to graphene.

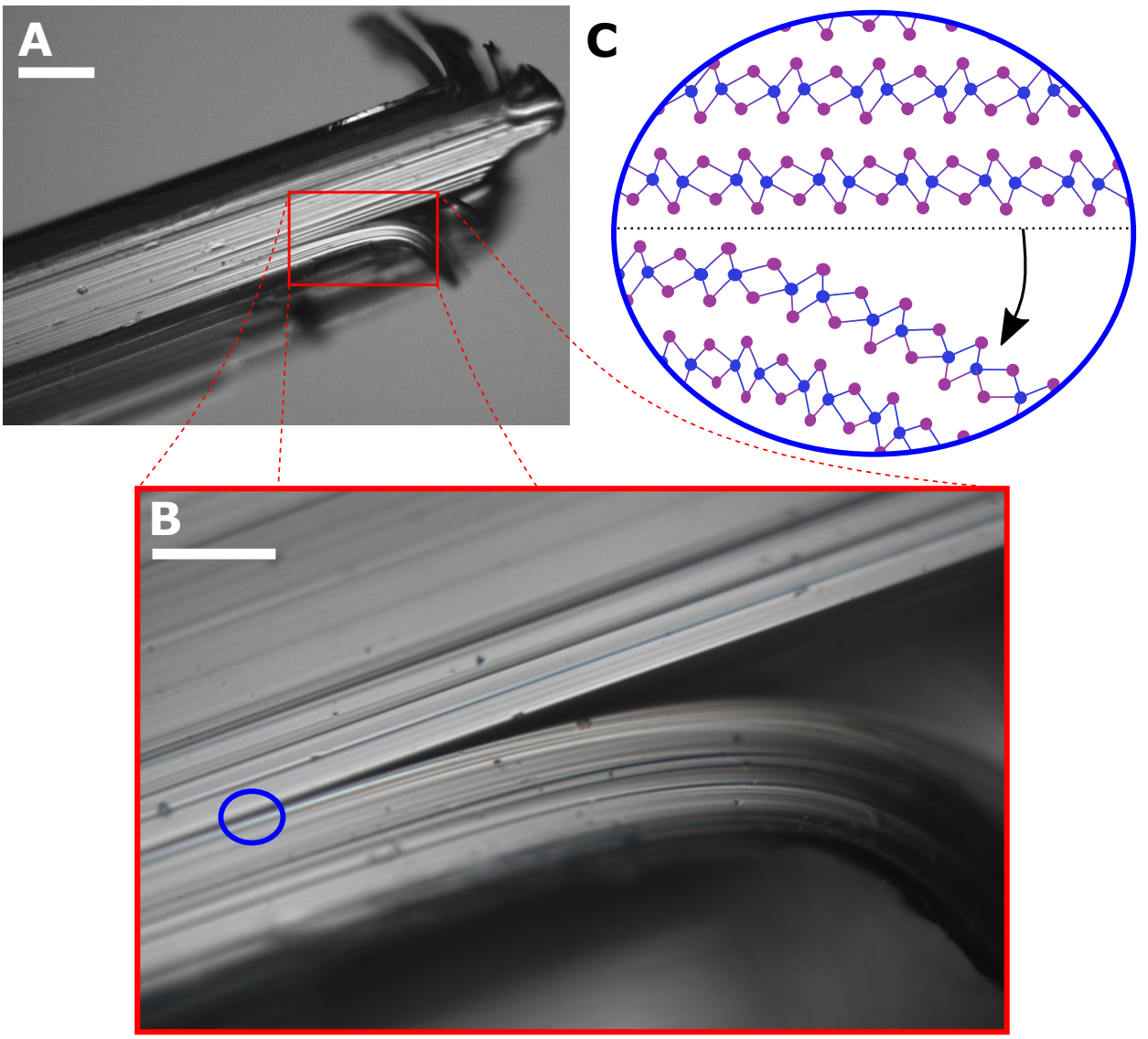

Figure 1.1.: **A,** A WTe_2 crystal. Scale bar is about 1 mm. **B,** Zoom-in to area where the crystal is naturally peeling apart, indicative of the weak interlayer bonding. Scale bar is about 0.2 mm. **C,** Cross-sectional schematic of the WTe_2 crystal structure at the region being peeled apart at the van der Waals cleavage plane indicated by the dashed line. This is indicative of the exfoliation process used to isolate monolayer and few-layer crystals. See Section 3 for details on the crystal structure.

Just as easily as individual sheets can be extracted, they may be placed back onto each other. The isotropic nature of the van der Waals force means that any combination of these atomically-thin crystals can be easily placed on each other without regard to differences in crystal structure (see Figure 1.2(A-C)). Such artificially formed stacks are called van der Waals heterostructures [19]. In reality, these atomic sheets are less like paper and more like cellophane wrap – sticky, flexible, and prone to wrinkling and sticking back onto themselves. As a result, the process for re-stacking the layers onto each other in a controlled manner is time consuming and imperfect. A great deal of our effort in the lab goes towards improving

this process in order to get cleaner, more uniform heterostructures [20].

A simple framework for what we hope to achieve with vdW systems has two broad categories. First is materials discovery, e.g. expansion of the library of known 2D materials, which is the initial and (usually) most straightforward step for a new material. This involves isolation and identification of a single layer (or few-layer) sample from its three-dimensional parent compound and measurement of its properties. Sometimes the measured properties are straightforwardly related to the parent material. This is often the case for materials whose electrons are in the extreme limits of possible states. At these extremes the materials are less susceptible to change as a result of the thinning process. Examples include the insulator hBN, the superconductor $NbSe_2$, the magnet CrI_3, and the semimetal WTe_2 when thicker than 2 layers (see Chapter 4). More interesting is the case when the thin crystals display strongly modified or even completely new phenomena. Graphene falls into this category. Also included are the monolayer semiconductors such as MoS_2, the density-wave compound 2H-TaS_2, and monolayer WTe_2 (see Chapters 5 and 6).

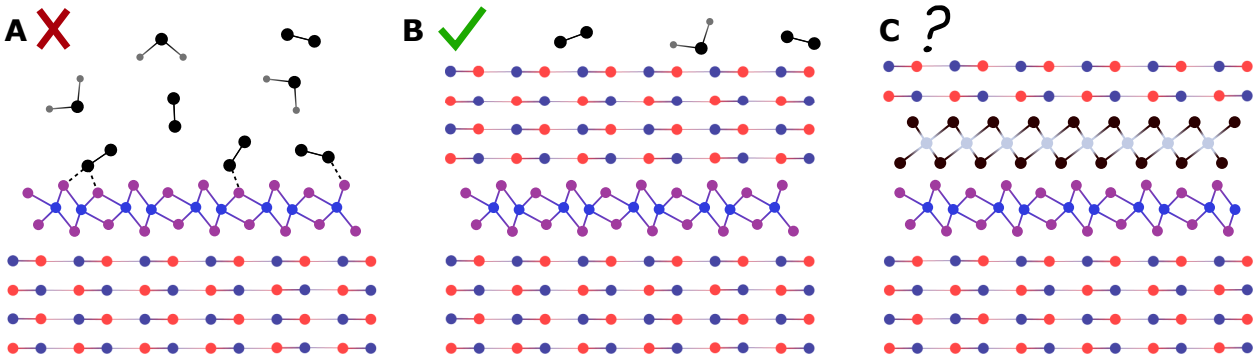

Figure 1.2.: **A,** vdW heterostructure with an exposed monolayer of WTe_2 on top of hexagonal boron nitride (hBN). Volatile molcules in the air react with and deteriorate the exposed WTe_2. **B,** vdW heterostructure of the materials discovery type. Encapsulating the WTe_2 with hBN on both sides protects it from the reactive molecules in the air. **C,** vdW heterostructure of the hybrid material type utilizing a monolayer of WTe_2 and a monolayer of CrI_3, a ferromagnet, protected on both sides by hBN. This heterostructure has not been investigated at the time of this writing.

As we build our understanding of the behavior of the individual layers, we can begin to investigate the novel behaviors of combinations of such layers, e.g. in vdW heterostructures. Sometimes the heterostructures are useful for relatively mundane reasons, such as using inert materials (such as boron nitride and graphite) to sandwich a more sensitive one (such as WTe_2 or CrI_3) in order to protect the latter from degrading (see Figure 1.2(A vs B)). This type of structure frequently enables the materials discovery previously noted. An extremely exciting and powerful research area involves combining two vdW materials in a fashion that they "talk" to one another and exhibit different phenomena than the individual materials would separately display, which may be called a hybrid material (see Figure 1.2C for a hypothetical example). The scientific community is still just beginning to scratch the surface of this direction – so far, for electronic transport only graphene and boron nitride have featured prominently. As one example, our group and others have shown that special

types of graphene-hBN and graphene-graphene vdW heterostructures can transform the normally metallic monolayers into a hybrid system that is an insulator (keep in mind that no chemical reaction has occurred) [21, 22, 23, 24]. Incorporation of other vdW materials into such heterostructures promises an exciting future of new and interesting phenomena. Hybrid materials and devices are not the focus of this thesis but will be touched upon in the final outlook section.

1.2. Topological Insulators

1.2.1. Non-expert Introduction

Every day in the world, we encounter electrical conductors and insulators. Conductors are useful for generating and transmitting electrical power and signals, the importance of which to modern society cannot be understated. Insulators serve to protect us from these same electrical systems. Typically, a material will be classified as one or the other[2]. It is important to know that the distinction between conductor and insulator boils down to the way in which electrons behave inside the material – if the electrons are free to flow then the system is a conductor, if the electrons are held firmly in place then the system is an insulator.

Historically it was known that some insulators (say pure silicon [25]) may have naturally conducting surfaces. These nominally conducting surfaces are extremely fragile, and even small imperfections can cause them not to conduct[3]. As a result, these surfaces are generally too difficult to work with towards any useful purpose.

It was only recently discovered that certain types of nominal insulators, such as bismuth selenide (Bi_2Se_3), exhibit a naturally conducting boundary that is extremely robust and guaranteed to resist even substantial mechanical and chemical damage [26, 27, 28]. That is to say that a block of this material would not conduct electricity through its interior, but the surface will conduct electricity; in contrast, a metal conducts electricity throughout its interior, and a normal insulator does not conduct electricity at all. The conducting surfaces of these materials have a number of unusual properties which have the potential for interesting new physics and unique applications. These new materials were dubbed *topological insulators* [29].

[2] An intermediate case is the semiconductor. Coarsely speaking, semiconductors are insulators which may conduct electricity at room temperature. Lower the temperature enough and the distinction between semiconductor and insulator is lost.

[3] More robust surface conductors have been engineered in the form of the field-effect transistor (FET), which uses electric fields to accumulate electrons at the surface of a material. These electrons are able to conduct electricity. It also works in reverse – the electric fields can remove the electrons and return the surface to its insulating form. This technologically crucial type of surface conductor does not concern us here, as it is not the result of a "natural" surface, per se.

Figure 1.3.: **A,** Genus-0 surfaces: spheres and footballs (both inflated and deflated). **B,** Genus-1 surfaces: a torus and a coffee mug. **C,** Genus-3 surfaces: the double-torus and the hybrid donut-mug, which has a hole for the handle as well as in the center of the mug. **D,** Artistic representation of electrons bound within closed geometries on the left and right sides (torus and sphere, respectively), representing topologically distinct materials. At the interface (purple broken shapes) it is impossible to have a closed manifold equivalent to either the torus or sphere, so the the electrons are freed and can flow.

What does this name mean? To understand this, we turn briefly to the topology of geometric shapes, from which we will build an analogy. A topology of an object is an aspect of the shape that does not change even under substantial deformation. A common example is the "number of holes" in an object. As shown in Figure 1.3A-C, we can draw relationships between different types of shapes that retain the same number of holes, regardless of how different they may otherwise seem:

1. Sphere: a sphere is the same as a football, which is the same as a deflated football.[4]
2. Torus: A donut can be bent into a coffee mug shape. The hole in the center of the donut is preserved as the hole of the handle of the cup.
3. Double-Torus: The double-torus is equivalent to the hybrid donut-mug, which both

[4]Clearly, topologists were not helpful during the "deflate gate" scandal that rocked the National Football League throughout the years 2015 and 2016.

have **two** holes. This particular mug has a hole in the handle and a hole in the center of the mug.[5]

By these analogies, we recognize that the number of holes can be a defining quantity, and this number is defined as a *topologically invariant number*. In the real world, it is usually "easy" to add new holes (with a power drill perhaps), but mathematically this can be considered a drastic action that fundamentally changes the object.

Equivalent kinds of topologically invariant numbers can be defined for electrical insulators, albeit more abstractly. In this case, the numbers are related to the fundamentally different ways in which the electrons in the material are being held in place and prevented from conducting electricity (see next section for more details). This number is zero for most materials, which represents the standard situation we are familiar with, such as in wood, most plastics and rubbers, typical gemstones, and air. Perhaps somewhat unfairly, we call these *trivial insulators*. Some materials have a non-zero number, and we call these materials *topological insulators*. Crucially, the different ways these materials prevent electrons from conducting electricity are incompatible with each other. This fundamental incompatibility means that at the boundary between a trivial and a topological insulator the electrons cannot be held in place. As a result, the electrons are free to move and a conducting state is guaranteed to exist there.[6] An artistic representation of this is shown in Figure 1.3D. Such conducting states have been the subject of a great deal of research both for their intrinsic properties and for unusual phenomena that may occur when interacting with other systems. The study of two vdW materials which are also topological insulators is the main subject of this thesis.

1.2.2. Deeper Dive

In order to develop a more quantitative understanding of topological insulators, we again take a quick look into the topology of closed orientable 2D manifolds. On such a manifold M, a local Gaussian curvature K_M can be defined. For a perfect sphere of radius r, the curvature is a constant $K_M = r^{-2}$. For these kinds of manifolds, the Gauss-Bonnet theorm states:

$$\chi_M = \frac{1}{2\pi}\int_M K_M dA, \tag{1.1}$$

that is, the integral of the curvature K over the area of the manifold M provides the Euler characteristic χ_M of the manifold. For the case of the sphere, the integral is easy and gives $\chi_M = 2$. Finally we can define the genus of the manifold g_M which is straightforwardly related to the Euler characteristic

$$\chi_M = 2 - 2g_M. \tag{1.2}$$

[5] It is now difficult to know what to make of the old joke, "a topologist is someone who can't tell a donut from a coffee mug".

[6] It is important to note that because vacuum (the absence of material) is a trivial insulator, the natural surface of a topological insulator represents a such a boundary.

The genus equivalently counts the number of "holes" in the manifold, as discussed in the previous section. One can again clearly see that the sphere has $g_{sphere} = 0$.

How does this relate to electronic systems? We can go through an almost exactly analogous procedure as above for electronic band structures. For the moment we focus on 2D crystals. Recall that for a crystal, the electronic spectrum in momentum space is described within the Brillouin zone, which periodically tiles the plane. The periodic boundary conditions of the Brillouin zone mean that the electronic wave function ψ can be described as on a closed surface in momentum space. We can define a local quantity of the wave-function and integrate over all momenta within the Brillouin zone. One such quantity is the Berry curvature $\Omega_i = \vec{\nabla}\psi_i \times \vec{\nabla}\psi_i$[7], where ψ_i is the wavefunction in band i. Integrating this quantity over an entire band results in the Chern number ν_i of that band, an integer:

$$\nu_i = \frac{1}{2\pi}\int_{BZ} \Omega_i d^2\vec{k} \tag{1.3}$$

Note the similarity with equation (1.1). The extra twist here is that one must do this integration for all occupied bands and add all the individual band Chern numbers to obtain the final, total Chern number of system $\sum_i \nu_i = \nu_{tot}$. From the analogy with 2D manifolds, we can understand that the Chern number represents a classical topology of a geometry of the quantum mechanical electronic wave-function [30, 27, 28].

The Chern number, for electronic systems, was first identified in the early 1980s by Thouless and collaborators [31] as a fundamentally important aspect of the recently discovered quantum Hall effect [32]. The total Chern number cannot change without closing of the band gap (or shifting the chemical potential out of the gap). Importantly, the Chern number enters into an observable, the integer quantized Hall effect:

$$\sigma_{xy} = \frac{e^2}{h}\nu_{tot}. \tag{1.4}$$

Fundamentally related to all these deep properties of the 2D bands is the question of what happens at the boundary. As described earlier in qualitative terms, at the interface of two materials with different topological invariants, a conducting state must exist. One way to picture this is by recalling that the Chern number cannot change without closing the band gap. If the outside region (say vacuum) has a Chern number of $\nu_{out} = 0$, and the interior has a Chern number of $\nu_{in} = 1$, then one knows that the gap must close at the boundary between the two regions. This and many other formulations of the *bulk-boundary correspondence* have been made [33, 34, 35, 36, 37, 38, 39], which is a generic concept for these types of topological systems. For the case of quantum Hall systems, the finite Chern number ν_{tot} requires that exactly ν_{tot} edge modes will exist at the boundary of the material, and these modes will be "chiral", or one-way directional[8], as shown in Figure 1.4A. It is important to know that the Chern number is zero if time-reversal symmetry is preserved.

[7] The Berry curvature is a pseudovector in 3D, but in 2D its only component is along the $\hat{z}$ direction so it can be treated as a pseudoscalar.

[8] A more precise statement is that the difference in the total number of left and right movers must equal ν_{tot}.

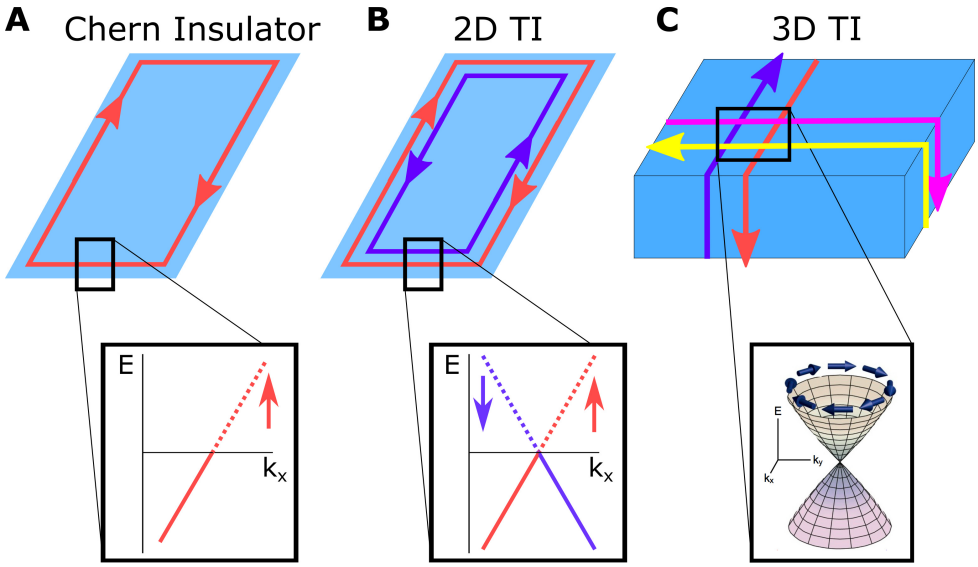

Figure 1.4.: **A,** Schematic of a quantum Hall state with $\nu_{tot} = 1$. Solid and dashed lines indicate occupied and unocupied states, respectively. **B,** Schematic of a quantum spin Hall state with $\mathbb{Z}_2 = 1$. **C,** Schematic of the 3D time-reversal invariant topological insulator.

Finally, we come to the crucial development of the mid-2000s: new topological classes can be defined based on an enforced symmetry, thereby generating *symmetry-protected* topological states [26]. The first such case to be identified was for time-reversal symmetry in two dimensions, which has a binary ($\mathbb{Z}_2$) topological invariant n. In this case, the bulk-boundary correspondence dictates that the parity of counterpropagating edge modes is preserved to be odd. In the simplest case, a single pair of counterpropagating boundary modes will exist, as shown in Figure 1.4B. The forward and backward moving carriers also carry opposite spin. Because only a single pair of such modes exists on the boundary, the spin degeneracy has been lifted. These types of modes have been dubbed *helical*, in contrast to the chiral modes of the quantum Hall systems.

In a special case where S_z (z-component of electronic spin) is preserved, one can find that each spin branch has a finite, opposite Chern number, for example $\nu_\uparrow = +1$ and $\nu_\downarrow = -1$. Here it is easy to see that the total Chern number is zero as required by time-reversal symmetry. The *difference* defines the topological invariant

$$n = \left[\frac{\nu_\uparrow - \nu_\downarrow}{2}\right] \mod 2 \tag{1.5}$$

which is also associated with an observable: a quantized spin Hall conductivity.

S_z is not generally conserved in a real material, so a quantized spin Hall conductivity may not be strictly realized in a given material. Moreover, experimentally the spin Hall conductivity is difficult to measure, whereas electronic charge transport measurements are much simpler to conduct. Fortunately, n retains its identity as a topological invariant regardless of S_z conservation, and 2D TIs still have unique signatures in charge transport. These signatures have been used to identify candidate systems as topologically nontrivial (see e.g. [40]) which be disccussed in detail in Chapter 5.

Soon after the prediction of 2D TIs, its topological state was generalized to 3 dimensions (3D TIs) [41, 29, 42]. For this class, a 3D insulator hosts a 2D electron gas (2DEG) with spin-momentum locking around its Fermi surface, e.g. a helical 2DEG, as shown schematically in Figure 1.4C. Materials that are 3D TIs are far more common than 2D TIs, and because their boundary modes reside on exposed 2D surfaces such materials are easier to probe by a greater number of experimental techniques. As a result, a large proportion of the early research efforts on topological insulators focused on 3D TIs.

Soon again after that[9], symmetry protected topological electronic phases were expanded to all dimensions and 10 generic symmetry classes, forming a so-called periodic table of topological insulators and superconductors[10] [43]. Topological superconductors host exotic quasiparticles at their boundaries known as Majorana fermions. In a special case, certain zero-dimensional modes are known as Majorana zero modes or Majorana bound states (MBSs), which are not fermions but instead display non-abelian statistics [44, 45, 46, 47, 48, 49]. MBSs come as correlated pairs that can be well separated, allowing for non-local storage of quantum information. Computational operations can also be done non-locally via "braiding", e.g. a spatial interchange of the location of MBSs, which changes the state of the global wavefunction. While MBSs are not able to execute a universal set of quantum operations [44], these properties suggest potential immunity to local noise sources, which make MBSs an attractive basis for a quantum computation platform. Natural topological superconductors are extremely rare, but hybrid materials composed of topological insulators and conventional superconductors can simulate topological superconductors, providing a route to creation of MBSs. This has been one of the driving motivations for continued work on topological insulator systems.

1.3. This Thesis

Experimentally, vdW materials and wavefunction topology have their foremost intersections at two points: the quantum Hall effect and 3D TIs. The latter has overlapped with vdW materials from the discovery of Bi_2Se_3-type crystals, which have interlayer bonding just weak enough reliably exfoliate crystals as thin as 10 nm. The vdW cleavage plane is so favorable that surface sensitive probes have been a dominant source of information about these unusual electornic states. Spectroscopic tools like angle-resolved photoemission spectroscopy (ARPES) and scanning tunneling microscopy (STM) have generated fantastic results for inspection of this helical 2DEG and for identification of topologically nontrivial materials. In contrast, electronic transport has been somewhat trickier, as these materials are typically doped, highly disordered, or both. Indications of surface state transport have been widespread, but transport through surface states without the presence of bulk states has been much rarer. This background information and context will be discussed in greater detail in Chapter 2. In the same Chapter, our results on independently accessible surface

[9] Theoretically, this field developed extremely quickly.

[10] Like insulators, superconductors host a gap to single-particle excitations. Because of this "band gap", superconductors also have topological classifications.

states and observation of true dielectric behavior of the topological insulator interior will be presented and discussed.

The quantum Hall effect in vdW materials has been extensively studied in graphene-based systems [50, 51] and more recently in transition metal dichalcogenides [52, 53, 54] and helical surface states [55, 56]. Graphene's unique band structure and high quality has even been used to generate a state that exhibits a quantum spin Hall effect [57, 58, 59] at the cost of requiring large magnetic fields which are deleterious to superconductors; as such, these systems are not ideal for use towards the creation of MBSs. Until very recently, a quantum spin Hall insulator that respects time reversal symmetry has not been experimentally isolated and investigated among vdW materials. Part II of this thesis will detail our efforts to this end on WTe_2. In Chapter 4 I will describe phenomena observed in trilayer samples which are semimetallic, and which served as our "canary in the coal mine" for testing new fabrication techniques to investigate novel physics in air sensitive materials. In Chapter 5 I detail our results on monolayer WTe_2, in which we observed edge state conductance approaching the quantum value of e^2/h per edge and an apparent band-gap opening in the edge upon breaking of time-reversal symmetry. Finally, in Chapter 6 I introduce our most recent experiments in which we have discovered that electrostatically doped monolayer WTe_2 is a 2D superconductor. Electrostatic accessibility of a 2D TI phase and a 2D superconductor phase in the same compound allows us to envision, for the first time, devices that push for discovery and manipulation of MBSs in a homogenous material platform, which will hopefully be the focus of much work following the submission of this thesis.

Part I.

Electrostatics of Disordered 3D Topological Insulators

2. Electrostatic Coupling between Surface States of a 3D Topological Insulator

2.1. Introduction and Overview

Shortly after the theoretical conception of 3D TIs [41, 29, 42], spectroscopic techniques (ARPES and STM) obtained spectacular results on the surfaces of 3D TIs that were cleaved in vacuum [60, 61, 62, 63, 64]. However, electronic transport in the same crystals was fraught with difficulty and frustration. In the early days, doped 3D crystals managed to show high mobilities [65], and crystal growers were able to achieve low-density crystals of the "classic" binary compounds like Bi_2Se_3 [65, 66, 67, 68].

Unfortunately, devices fabricated from exfoliated Bi_2Se_3 were not reliably of the same low doping as the macroscopic parent crystals [69, 70], and the mobility of the surfaces was typically poor (with exceptions [71]) likely due to surface oxidation [72]. For a discussion on the notion of how "topological protection" relates to transport scattering times, see Appendix A.1. Ironically, these topological insulators were not truly insulators at all. Nonetheless, transport groups attempted to access the surface states in these doped materials [73, 69, 70, 74, 75, 76, 67]. I highlight in particular the efforts of our group. The first observation of ambipolar field effect behavior on the surface of a 3D TI was made by Steinberg, et al, in 2010 using arsenic-doped Bi_2Se_3 [69]. Later, using Bi_2Se_3 thin films grown in collaboration with the Moodera group, we saw even stronger ambipolar behaviors, again with a single gate. Moreover, in that study we found evidence that depleting the surface resulted in a curious evolution of phase coherent phenomena. We deduced that the creation of a depletion zone at the gated surface resulted in a tunnel barrier between those states and the surface state, resulting in decoupled phase coherent phenomena in the two electron baths [76] (similar phenomena were observed by other groups at roughly the same time [70, 75]). Amid much other work [71, 77, 78, 79, 80, 81, 82], a missing piece in the literature was observation of dielectric-like behavior of the bulk with separable observation of the surface states on the top and bottom cleaved surfaces.

In the meantime, crystal growers were developing methods to counteract the natural doping tendencies in the binary compounds. Mixed compounds were presumed to be a route toward truly insulating 3D TIs by balancing these natural tendencies. In particular, the materials Bi_2Te_2Se [83, 84, 85, 86] and $Bi_{2-x}Sb_xTe_{3-y}Se_y$ [87, 88, 89, 90, 91] achieved reliably low doping density in 3D crystals and large bulk resistivities (up to 6 Ωcm) at low temperature. The

surfaces could even be the dominant contribution to conductivity in samples of order a few microns thick [88], and ambipolar tuning of resistance of bulk crystals was observed by ionic liquid gating, suggestive of substantial surface transport [92].

However, not everything was perfect. Despite the large band gaps $\Delta \sim 300meV$ expected from theory and spectroscopic studies [93, 94], transport behavior indicated much smaller thermal activation barrier, even by as much as a factor of 5 [87, 88, 89, 90, 91]. The charged impurity density of these systems was estimated to be in the range 10^{18} to $10^{20}cm^{-3}$, which would induce a 3D landscape[1] of charge puddles in the interior. This notion was theoretically explored in several works by Skinner, et al, and found to explain the anomalously small activation gaps [95, 96, 2]. An important aspect of such a charge puddle landscape is that while it may have a high resistivity, it results in a finite density of states at all chemical potentials. This means that these states can screen electric fields. Despite being highly resistive, the bulk would not behave like a dielectric. Should the inability to screen DC electric fields be a requirement for calling a material an "insulator"?

Nonetheless, the charge-neutral and highly insulating crystals of the $Bi_{2-x}Sb_xTe_{3-y}Se_y$ type opened an opportunity to investigate gate-tunable electronic transport in a surface state-dominated 3D TI. In the following experimental section, we indeed found that thin samples were surface dominated and that the Dirac point of the top and bottom surfaces could be accessed independently for the first time. Curiously, electric fields only penetrated the interior of the thinner samples, not the thick one. To explain this discrepancy, in the subsequent section, I extend existing models for impurity-induced charge puddles to the thin-film case and show that bulk charge puddles can be completely evaporated due to screening by the surface states for sufficiently thin crystals. The transition from the thick (puddle) limit to the thin (dielectric) limit occurs in the range of a few 10s of nanometers of thickness for typical impurity densities, consistent with our measurements. Finally I conclude this Part of the thesis with an epilogue detailing subsequent work on thin and electrostatically tuned devices based on these same materials.

2.2. Electrostatic Coupling between Two Surfaces of a Topological Insulator Nanodevice

This section is a reproduction of a published work [94], with a few modifications to the text to adapt for the structure of this thesis.

2.2.1. Abstract

We report on electronic transport measurements of dual-gated nanodevices of the low-carrier density topological insulator $Bi_{1.5}Sb_{0.5}Te_{1.7}Se_{1.3}$. In all devices the upper and lower surface states are independently tunable to the Dirac point by the top and bottom gate electrodes. In thin devices, electric fields are found to penetrate through the bulk, indicating finite

[1] Perhaps a better term here would be space-scape or volume-scape.

capacitive coupling between the surface states. A charging model allows us to use the penetrating electric field as a measurement of the inter-surface capacitance C_{TI} and the surface state energy-density relationship $\mu(n)$, which is found to be consistent with independent ARPES measurements. At high magnetic fields, increased field penetration through the surface states is observed, strongly suggestive of the opening of a surface state band gap due to broken time-reversal symmetry.

2.2.2. Main Text

Three dimensional topological insulators (3D TIs) have been undergoing intense theoretical and experimental research on the properties of their unique surface states [27, 28]. The presence of bulk carriers has hampered experimental progress, so a variety of crystal growth[66, 83, 87, 89, 84, 97] and in-situ charge displacement techniques [69, 70, 98, 77, 92] have been applied to suppress bulk conductivity. For example, quaternary TI materials of the form $Bi_{2-x}Sb_xTe_{3-y}Se_y$ have a significantly suppressed bulk contribution to transport, reaching large bulk resistivities and insulating-like temperature dependence [89, 90, 88]. Furthermore, exfoliation or growth of thin crystals has been used to achieve surface-dominated transport [80, 84, 77, 81, 97]. However, amid the extensive experimental effort on TI device transport, there is no study reporting independent control over the density of both the upper and lower surface states in a single TI device. A full understanding of transport phenomena in TIs, such as the quantum Hall [99, 100] and Josephon effects [101, 102, 103], will require independent tuning of the density of each surface state. Additionally, proposals for topological exciton condensates explicitly require fine tuning the density of both surfaces [104], and finite displacement fields from two gates can affect the quantum anomalous Hall effect in TI-based systems [105, 106].

In this Letter, we report electronic transport measurements of exfoliated $Bi_{1.5}Sb_{0.5}Te_{1.7}Se_{1.3}$ (BSTS) nanodevices with top and bottom gate electrodes. We show for the first time that the chemical potential of the upper and lower surface states can be controlled independently, resulting in different resistance peaks when either surface chemical potential crosses the Dirac point. For thin devices, we find signatures of finite capacitive coupling between the surface states, consistent with fully depleted bulk states. We explain the data through a charging model which incorporates the finite density of states of the surface bands. Using angle-resolved photoemission spectroscopy (ARPES) as a control measurement of the surface state, this model allows us to measure the chemical potential μ and charge density n of a topological surface state as well as the inter-surface capacitance C_{TI}. At high magnetic fields, increased field penetration through the surface states is observed, strongly suggestive of the opening of a surface state band gap.

BSTS was prepared by melting high purity samples of the constituent elements in a sealed quartz ampoule under inert atmosphere. Sample structure was confirmed by x-ray powder diffraction, and large single crystals showed similar bulk transport behavior to previous reports [89]. Static ARPES shows that the chemical potential is inside the bulk band gap and that the Dirac point energy is above the bulk valence band edge (see SM). Pump-probe time-resolved ARPES (TrARPES) allows access to unoccupied states as shown in Fig. 2.1b

[107, 108] The Fermi velocity near the Dirac point is $v_F \approx 3.2 \times 10^5$m/s, and the band gap at room temperature is $E_g \approx 240$ meV. Note that the surface state dispersion is strongly electron-hole asymmetric. These data are consistent with previous experiments [90, 109].

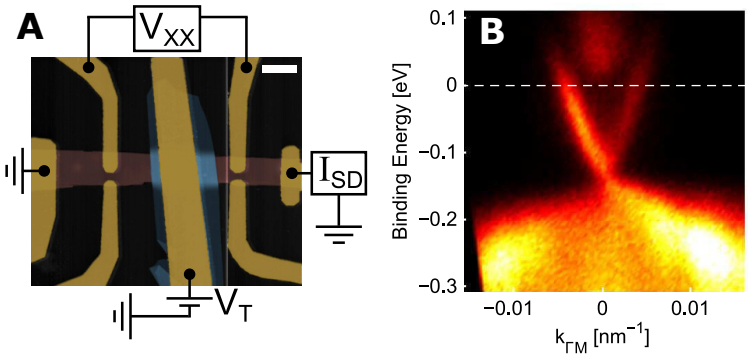

Figure 2.1.: A, Colorized AFM image of device A, including schematic circuit elements describing the transport measurement. Red is BSTS, blue is h-BN, and gold is Ti/Au (contacts and gate electrode). The scale bar is 2 microns. **B,** TrARPES measurement of a BSTS crystal. The white line indicates the chemical potential.

Thin flakes for transport studies were obtained by mechanical exfoliation onto a doped silicon wafer with a 285nm thick thermal SiO_2 surface layer that serves as the bottom gate electrode and dielectric, respectively. A thin layer of hexagonal boron nitride (h-BN) was mechanically transferred on top to serve as the top gate dielectric [110]. Thermally evaporated Ti/Au layers were used to make ohmic contacts and top gate electrodes. Atomic Force Microscopy was used to determine the thickness of the BSTS and h-BN layers. For all data presented here, a four-probe voltage measurement was used determine the 2D resistivity. Here we report results measured on BSTS devices of different thicknesses: device A is 42 nm, and device B is 82 nm. The behavior of device A was reproduced in a third device (see Appendix B). All three devices were fabricated from flakes from the same exfoliation, and therefore from the same region of the bulk crystal. Fig. 2.1a, shows an AFM image of device A.

On devices A and B, both the top and bottom gates easily tune the device through a resistance peak (R_{peak}) by adjusting the applied voltages V_T and V_B, respectively, as shown in Fig. 2.2a-b. R_{peak} is associated with a minimum in carrier density (i.e. the surface Dirac point), as confirmed via the Hall effect (see Appendix B). Interestingly, the top-gate R_{peak} is observable up to room temperature; in contrast, for the bottom gate $R(V_B)$ changes into a broad S-shape, consistent with gating studies of other TIs using SiO_2 gate dielectrics [70, 81, 84]. The disappearance of a distinct resistance peak in the limit of strong disorder was predicted by recent theories for TI surface states with electron-hole asymmetry [111], suggesting that the difference in the field-effect behavior may be related to the disorder profile at the interface. Strong differences in the disorder profile at SiO_2 and h-BN interfaces have been observed in graphene [112].

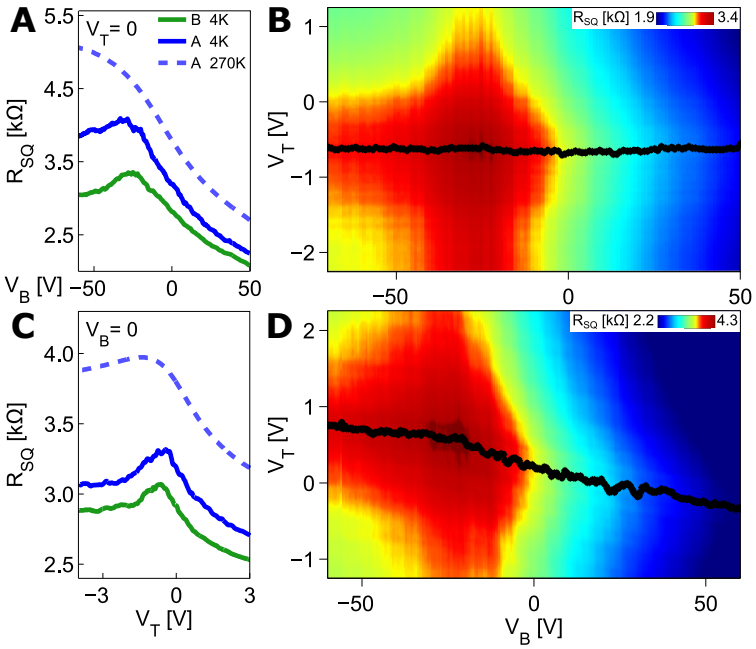

Figure 2.2.: Gate-dependence of the resistivity of devices A and B. **A,** Bottom gate dependence of resistivity at $V_T = 0$ at low temperature (blue, green) and 270K (dashed) from cooldown 2. **C,** Top gate dependence of resistivity at $V_B = 0$ at low temperature (blue, green) and 270K (dashed) from cooldown 2. **B & D,** 2D map of resistivity while modulating both gate electrodes for devices B and A, respectively, from cooldown 1. The black dots track the location of the upper surface R_{peak} at each V_B.

Two-dimensional maps of the resistivity with respect to both top and bottom gate voltage reveal a distinct difference in the behavior of devices A and B, shown in Fig. 2.2d and 2.2c, respectively. The black dots identify V_T, the top gate voltage at which R_{peak} is found, at each V_B. We associate V_{peak} with charge neutrality of the upper surface state: $n_U = 0$. For device B, V_{peak} is independent of V_B, demonstrating no capacitive coupling between the upper surface and the bottom gate electrode. The fact that thicker devices do not have this capacitive coupling suggests that mobile bulk electronic states exist in the interior. By contrast, V_{peak} in device A is dependent on V_B. The observed relationship $V_{peak}(V_B)$ means that there exists a finite and *non-constant* capacitive coupling between the upper surface and the bottom gate. This capacitive coupling requires field penetration through the lower surface state and the interior of the thinner crystal, which fail to completely screen electric fields. The contrasting gating behavior of the devices is corroborated by the temperature dependence of their resistivities (see Appendix B). We also note that while dual-gated TI devices have been previously reported [77, 113], the devices reported here are unique in that the two surface states are tuned independently and separately observed.

Here we focus on the capacitive coupling between the bottom gate and the upper surface in the thin crystal, and data regarding coupling of the top gate and lower surface are presented in Appendix B. The slope of $V_{peak}(V_B)$ is a measure of the ratio of the capacitive coupling of the bottom and top gates to the upper surface, which includes partial screening of electric fields by the lower surface state. At $V_B \sim -20$ V the slope of $V_{peak}(V_B)$ and the resistance of

the lower surface are simultaneously at a maximum, i.e. near the Dirac point (see Fig. 2.3b). This is consistent with a minimum in the screening effectiveness of the lower surface state at the Dirac point. Understanding this behavior quantitatively requires a detailed charging model, which we discuss below.

By considering the BSTS surface states as a grounded pair of 2D electronic states, the general gating behavior can be understood via a charging model construction originally developed for parallel graphene layers [114]. This model is schematically represented in Fig. 2.3a, where the important quantities are the applied gate voltages (V_T, V_B), the geometric capacitances per unit area of the gates (C_B, C_T), the inter-surface capacitance per unit area (C_{TI}, the charge densities of the gate electrodes (n_T, n_B), and the charge density and chemical potentials of the lower (n_L, μ_L) and upper (n_U, μ_U) surface states. Four coupled equations completely describe the charging of the system: one from charge neutrality, and three from Faraday's law, which restricts the sum of voltage drops around a loop to equal zero, which includes the change in chemical potential of the surface states $\Delta\mu_j = \mu_j - \mu_j^0$, where μ_j^0 is the initial Fermi energy relative to the Dirac point for surface state $j = U, L$. A detailed derivation is provided in Appendix B. For this study, we are interested in the condition that the chemical potential at the upper surface is at the Dirac point. By setting $n_U = 0$ and $\mu_U = 0$, a useful pair of equations can be derived:

$$\mu_L = -\frac{C_T}{C_{TI}} e V_T' \tag{2.1}$$

$$\frac{1}{C_B} e n_L = V_B' + \left(\frac{1}{C_B} + \frac{1}{C_{TI}}\right) C_T V_T' \tag{2.2}$$

where $V_{T,B}' = V_{T,B} - V_{T,B}^0$, and $V_{T,B}^0$ are constants that depend on the initial densities and chemical potentials of the two surfaces (see Appendix B). Equations (2.1) and (2.2) serve as a linear transformation from a trajectory in gate voltage space (Fig. 2.3b) to a relationship between chemical potential and density for the lower surface state (Fig. 2.3c).

Experimentally, three unknowns remain: the inter-surface capacitance C_{TI} and the initial offset carrier densities of the upper and lower surfaces $n_{L,U}^0$. To constrain these parameters, an independent measurement of $\mu(n)$ is required. ARPES measurements of the surface state band structure can be easily converted to a model for $E(n)$, including an explicit treatment of the bulk states (Appendix B). A three-parameter least-squares fit between the transformation of the transport data and the ARPES model is performed and shown in Fig. 2.3c (see Appendix B). The inter-layer capacitance from this fit is $C_{TI} = 740 \pm 20$ nF/cm^2, corresponding to an effective bulk permittivity of $\kappa_{TI} \approx 32$, comparable to values for similar compounds [115, 116, 117]. The initial electron densities of the upper and lower surface states are found to be $n_U^0 \approx -0.1 \times 10^{12} cm^{-2}$ and $n_L^0 \approx 1.2 \times 10^{12} cm^{-2}$, which agrees well with values simply calculated from the magnitude of V_T and V_B necessary to reach the resistance peaks.

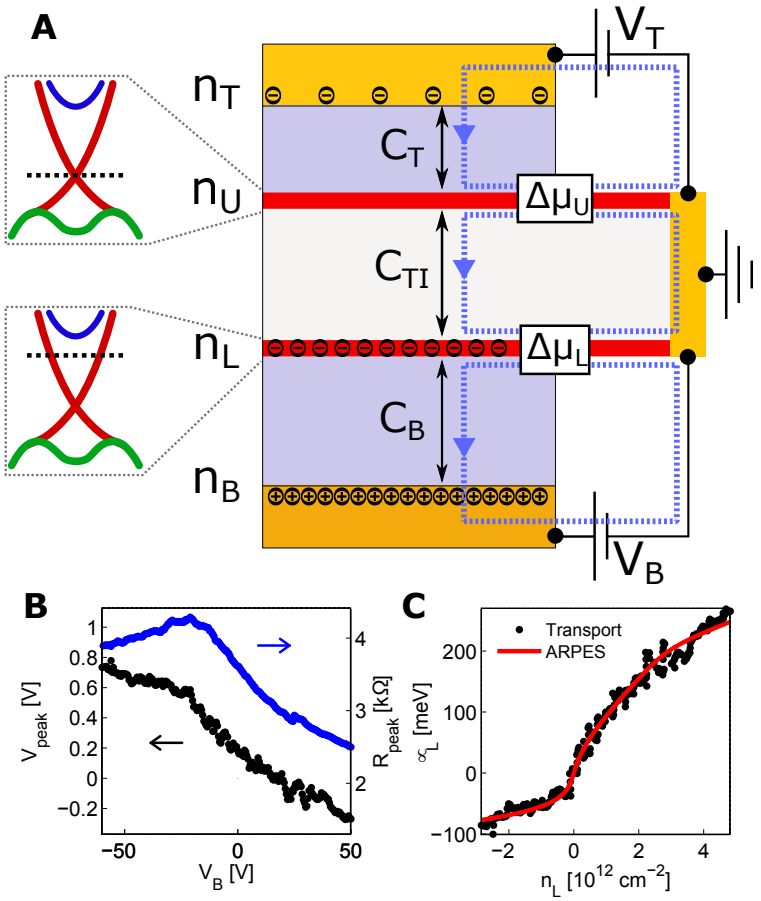

Figure 2.3.: **A,** Schematic of the charging model used in this study with important parameters labeled. For comparison to the experiment, the upper surface state is kept at charge neutrality while charge is distributed between the lower surface state and the gate electrodes. Three voltage loops indicated by the blue dashed lines are used in deriving the charging model. **B,** The position of the upper surface R_{peak} as a function of both gate voltages $V_{peak}(V_B)$ (left, black dots), and the resistivity at those gate voltages R_{peak} (right, blue), extracted from Fig. (2.2)d. **C,** The fit of the energy-density relationship as derived from ARPES (red line) and from $V_{peak}(V_B)$ (black dots).

It is important to note that C_{TI} can be affected in a few ways. For example, localized electronic states could polarize, increasing C_{TI}. As another possibility, low-density, poorly conducting bulk states could weakly screen electric fields, reducing C_{TI}. However, in the thin limit the surface states should efficiently screen charged bulk impurities, resulting in an absence of charged puddles of bulk states at charge neutrality for crystals of thickness $\lesssim 70$ nm [2]. This length scale is consistent with the observation that device B (82 nm thick) appears to have conducting states screening the two surfaces from each other.

We now turn to the behavior of the thin device in high magnetic fields. The Hall mobility of this sample is low, of order 200 $cm^2/(\mathrm{Vs})$; as a result, no evidence of Landau levels is found, and a clear R_{peak} remains. Nevertheless, the charging behavior of the device changes significantly at finite field. Fig. 2.4a shows $V_{T,peak}(V_B)$ of the upper surface R_{peak} at $B = 0$ T and 8 T. V_{peak} is affected by V_B much more strongly at 8T. Assuming C_{TI} does not change,

equations (2.1) and (2.2) can be applied without changing parameters, as shown in Fig. 2.4b (blue dots). For the same total change in charge density, the total chemical potential change of the lower surface is about 60% larger. More precisely, the chemical potential appears to change more rapidly at low carrier densities, indicating a distinctly smaller thermodynamic density of states. Fig. 2.4c (left axis) shows the difference in total chemical potential change as a function of magnetic field. The energy difference increases roughly quadratically with magnetic field. A possible interpretation is that the surface states develop a band gap that forms as a result of breaking time-reversal symmetry. While a non-linear magnetic field dependence would naively rule out a Zeeman-induced band gap, disorder will mask this effect at low fields when the gap is small [2], causing a non-linear increase in the apparent gap in the density of states. Detailed Shubnikov-de-Haas analysis of similar TI materials estimate a surface g-factor in the range 40 to 80 [118], which would be too small to explain this effect, although the g-factor has not yet been measured for this particular compound.

We further observe that the temperature dependence of resistivity also changes significantly at high magnetic fields. In Figure 2.4d, the temperature dependence of resistivity when both surfaces are at charge neutrality changes from metallic-like at zero magnetic field to non-metallic at high magnetic field, suggestive of a possible metal-insulator transition. This is consistent with the formation of a gap in the surface states with a high level of disorder. Similar non-metallic resistivity vs temperature curves were observed in bilayer graphene studies with similar band gaps in the high-disorder limit [119].

However, we cannot rule out the possibility of an inter-surface magneto-capacitance. Restricting the model such that the total chemical potential change is the same as at zero magnetic field (i.e. a field-independent *average* density of states, see green curve in Fig. 2.4b), we find that C_{TI} must increase in magnetic field to compensate (Fig. 2.4c, right axis). C_{TI} increases in a similar way as the chemical potential difference because $\Delta\mu_L \cdot C_{TI} \propto \Delta V_T$, as in equation (2.1). The raw bulk permittivity cannot explain this change, because the optical phonon spectra of related TI compounds show little change at similar magnetic fields [120, 121]. Electronic contributions to C_{TI} such as those mentioned earlier (polarizable localized states or weakly screening bulk states) could be modified by a magnetic field. In Appendix B we show evidence that the effects of temperature and magnetic field separately affect C_{TI} and $\mu_L(n)$, respectively}, further suggesting that the magnetic field is modifying the density of states and not causing a magneto-capacitive effect.

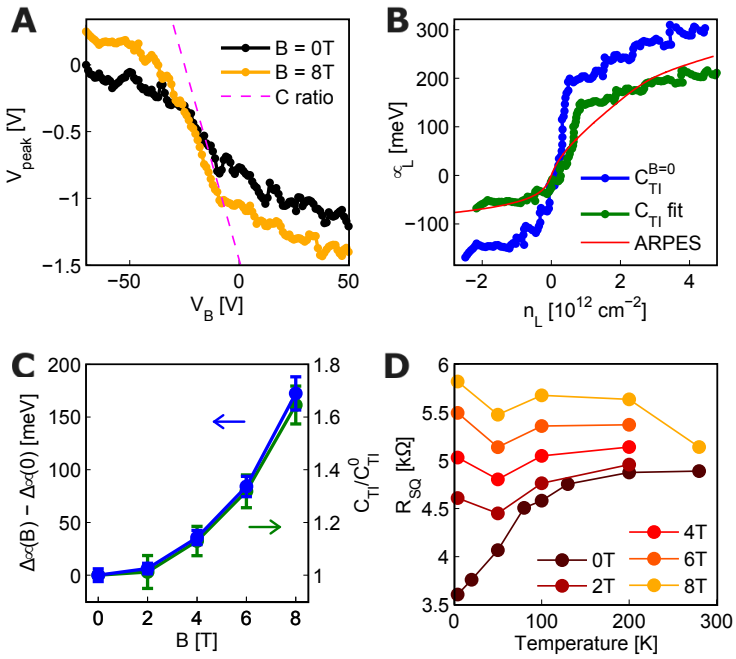

Figure 2.4.: Effect of high magnetic fields on the transport data. **A,** $V_{peak}(V_B)$ at 0T and 8T from cooldown 2. For comparison, the dashed pink line would be the gate-gate dependence if the lower surface has no electronic states, given by a ratio of geometric capacitances: C ratio $= -\frac{1}{C_T}\frac{C_B C_{TI}}{(C_B+C_{TI})}$. The transport data approaches this slope at 8T. **B,** The extracted energy-density relationship of the lower surface state at 8T for the case of fixed inter-surface capacitance $C_{TI} = C_{TI}^0$ (blue) and when using C_{TI} as a fit parameter (green) to the zero-field density of states (ARPES model, red curve). Arrows indicate increase in the total chemical potential change assuming fixed C_{TI}. **C,** The difference in the total change of the chemical potential of the lower surface with magnetic field (blue, left axis, error bars are the standard deviation of possible values) and the best fit C_{TI} as a function of magnetic field (green, right axis, error bars are 90% confidence intervals). **D,** The temperature dependence of the resistivity at different magnetic fields and when both surfaces are at charge neutrality.

In summary, exfoliated nanoflakes of BSTS are of sufficiently low total carrier density for both the upper and lower surface state densities to be independently modulated by electrostatic gates and for electric fields to penetrate through the bulk. Utilizing a model that captures the charging of the system, we measure the inter-surface capacitance C_{TI} as well as the energy-density relationship $\mu(n)$ of the surface states, which agrees well with independent ARPES measurements. At high magnetic fields, increased field penetration is observed, strongly suggestive of band gap opening in the lower surface state.

2.2.3. Acknowledgements

This work was partly supported by the DOE, Basic Energy Sciences Office, Division of Materials Sciences and Engineering, under award DE-SC0006418 (VF, SE, HS, and PJH), by the Gordon and Betty Moore Foundation grant GBMF2931 and the STC Center for Integrated Quantum Materials, NSF grant DMR-1231319 (BH and RCA), and by an MIT

MRSEC Initiative under NSF award DMR-0819762 (FM and NG). This work made use of the Materials Research Science and Engineering Center Shared Experimental Facilities supported by NSF under award DMR-0819762. Sample fabrication was performed partly at the Harvard Center for Nanoscale Science supported by the NSF under grant no. ECS-0335765. Sample synthesis and initial characterization were performed under LDRD (Tracking Code 12-ERD-013) at Lawrence Livermore National Laboratory (LLNL). LLNL is operated by Lawrence Livermore National Security, LLC, for the US Department of Energy, National Nuclear Security Administration, under Contract No. DE-AC52-07NA27344. We thank A. Stern, Y. Baum, K. Burch, D. Drew, B. Skinner, A. Frenzel, and J.D. Sanchez-Yamagishi for discussions and J. R. Jeffries for performing x-ray diffraction measurements.

2.3. On Achieving a True Dielectric in a 3D Topological Insulator

2.3.1. Prologue: On Charge Puddles in Topological Insulators

The previous section focuses on the case of a thin (40 nm) crystal in which electric field penetration is finite and measurable. However, it is curious that no electric field penetration is measureable at only double that thickness. If the bulk were truly a dielectric, one would expect the effective capacitance between the surface states to drop only by half. In this section, we develop a model to explain this discrepancy[2].

The story begins with puddles of carriers resulting from the potential of charged impurities. The surface states of topoogical insulators are well-known to have disorder-induced potential fluctuations, as has been strikingly visualized by scanning tunneling microscopy measurements [122, 123, 109, 124]. Potential fluctuations at the surface are small (20 meV at most) due to generally efficient screening by the surface states themselves. Presuming the same density of charged impurities exist deep in the bulk[3], one can expect the potential fluctuations to be much larger in the interior due to the absense of free carriers. This was anticipated by theory as a result of attempts to understand the small bulk resistance of 3D TIs [95, 2, 96], and since then more direct experimental evidence for the bulk puddles has come to light [125, 126, 127, 128].

As noted, the bulk puddles exist to screen the potential of the impurities and therefore can screen external electric fields. From this perspective, the fact that we were able to observe any electric field penetration in the experiment may come as a surprise. Nonetheless, by extending the existing theoretical framework to the thin-film limit one can explain all the phenomena, particularly including the thickness discrepancy. I begin by briefly (re)introducing the existing theory of charge puddles in 3D TIs from [2], including its successful predictions, and then develop the extension to thin films.

I am indebted to Brian Skinner for his guidance and related prior work on this topic [95, 2, 96].

[2] Small sample size notwithstanding.

[3] This may not be the case, as surfaces are known to become doped shortly after becoming exposed. See e.g. [72, 88].

2.3.2. Prior Results

2.3.2.1. Puddles in the Bulk

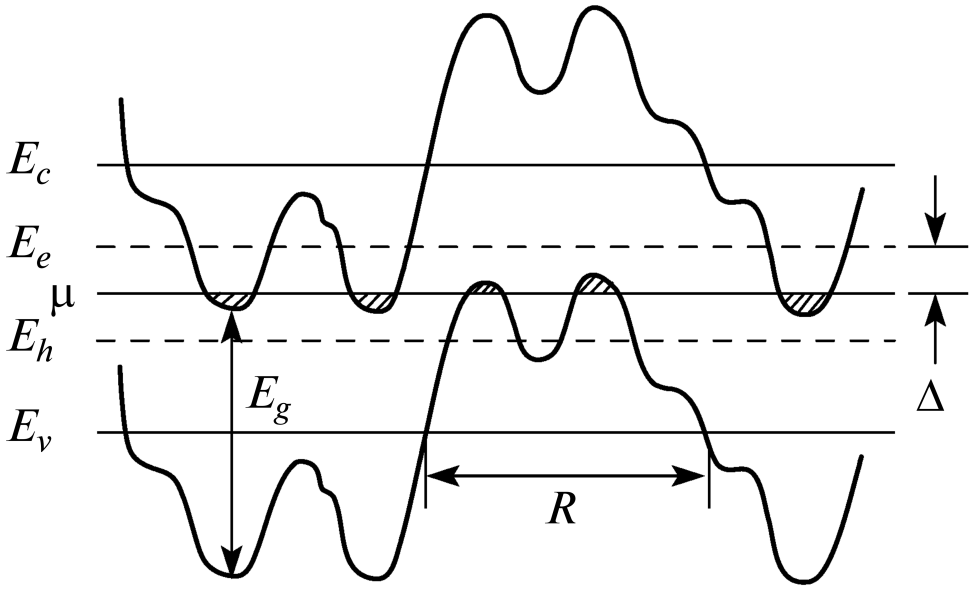

Figure 2.5.: Schematic of the energy of the conduction and valence bands as a function of a real-space coordinate. Labeled energy scales are the intrinsic spectral band gap of the material E_g, the average energies of the conduction and valence bands E_c and E_v, the chemical potential μ, the lowest energy to access a metallic percolating paths E_e and E_h, and the new transport band gap between the chemical potential and the percolating paths Δ. The average size of a puddle is indicated by R. This figure used with permission from [2].

The main concept for the consequences of charged impurities in a narrow-gap semiconductor is shown in Figure 2.5, where many of the relevant energy scales are defined. Throughout the material there is an average density $N_D \sim 10^{19} cm^{-3}$ of charged impurities of random sign. Locally this results in a fluctuating electric potential that bends the conduction and valence bands with it, sometimes dipping low enough to cross the chemical potential and accumulate charge to screen the local potential. The length-scale associated with these puddles is

$$R = \frac{E_g^2 \kappa^2}{8\pi N_D e^4} \tag{2.3}$$

where κ is the relative permittivity of the material. A key consequence of this potential landscape is that the classical percolation levels for the conduction and valence bands are at much lower energy than the average position of the band edge. This means that the thermal activation barrier for high temperature conduction is lower by roughly a third compared to the clean case:

$$\Delta \approx 0.3 \frac{E_g}{2}. \tag{2.4}$$

At lower temperature, the puddles themselves are the dominant source of conduction via variable range hopping. Altogether, these results seem to explain the relatively low resistivity of the bulk states of 3D TIs and appear to be consistent with experimental data [87, 88, 89, 90, 91].

2.3.2.2. Puddles at a Single Surface

From this point we use $\Gamma(z)$ to indicate amplitude of the disorder potential (units of energy) as a function of distance away from the surface at $z = 0$. In the bulk Γ is a constant because the bulk states screen strongly once they start becoming occupied, e.g. $\Gamma(z \gg R) \sim E_g/2$. The amplitude of the disorder potential is the root mean square of the total potential ϕ:

$$\Gamma = e\sqrt{\langle\phi^2\rangle}. \tag{2.5}$$

The total potential at a particular spot, say the origin, is

$$\phi = \sum_i q_i \phi_i(r, z) \tag{2.6}$$

where i labels an individual impurity, r and z are the radial and vertical coordinates of the impurity, and q is the impurity charge. Assuming that impurity positions are uncorrelated and randomly distributed throughout the material, we can then write down:

$$\Gamma^2(z) = 2N_D \int d^2r'dz' \left[\phi_1(r', z'; z)\right]^2 \tag{2.7}$$

where $\phi_1(r', z'; z)$ is the screened potential at point $(r = 0,\ z)$ of an individual charge located at $(r',\ z')$. All systems are taken to be cylindrically symmetric and infinite in the planar dimension. We first reproduce some results for the case of semi-infinite slabs.

Perfect Screener This is just the image charge problem, which serves as a good starting point. We set the metallic sheet at $z = 0$ and place the charge at $(r',\ z')$ and its image at $(r',\ -z')$. Then we can write down

$$\phi_1\left(r,' z'; z\right) = \frac{e}{\kappa_1}\left(\frac{1}{\sqrt{r'^2 + (z' - z)^2}} - \frac{1}{\sqrt{r'^2 + (z' + z)^2}}\right) \tag{2.8}$$

where κ_1 is the permittivity of the TI bulk. We can solve for $\Gamma^2(z)$, which gives

$$\Gamma^2(z) = 8\pi N_D \frac{e^4}{\kappa_1^2} z \tag{2.9}$$

The square amplitude of the potential fluctuations increases linearly with the distance from the surface.

Single Imperfectly Screening Surface Now introduce a finite screening length r_s to the metallic sheet. A good approximation is to treat the image charge problem as if a perfectly metallic sheet rests at $-r_s/2$ from its true location [2]. As a result, the potential is modified as follows for $z > r_s$ (see Appendix C.2 for details):

$$\phi_1\left(r,' z';z\right) \approx \frac{e}{\kappa_1}\left(\frac{1}{\sqrt{r'^2+(z'-z)^2}} - \frac{1}{\sqrt{r'^2+(z'+z)^2}} + \frac{2\kappa_1 r_s}{\kappa_1+\kappa_2}\frac{(z'+z)+\frac{1}{2}r_s}{\left(r'^2+(z'+z)^2\right)^{3/2}}\right) \tag{2.10}$$

where κ_2 is the permittivity of the outside dielectric. The first two terms are just as before. The new term is a dipole-like correction proportional to r_s. We can then do the same procedure to obtain the approximate result

$$\Gamma^2(z) \approx 8\pi N_D \frac{e^4}{\kappa_1^2}\left(z + \frac{\kappa_1}{\kappa_1+\kappa_2} r_s\right) \tag{2.11}$$

Note that in Section 6 of [2] a constant permittivity was considered, resulting in a $\frac{1}{2}r_s$ offset instead of $\frac{\kappa_1}{\kappa_1+\kappa_2}r_s$. Here that result is reproduced for $\kappa_1 = \kappa_2$, whereas for $\kappa_1 \gg \kappa_2$ the offset is approximately doubled.

2.3.3. Two Perfectly Screening Surfaces (Thin Film)

2.3.3.1. The Image Charge Series

If a charge is located at position x between two metallic plates located at positions 0 and d, there will be an infinite set of image charges on both sides. These can be grouped into two sets, the set which was initiated by reflection via the plane at 0, and the set that was initiated by the reflection at d. The reflection operators are:

$$R_0 x' = -x' \tag{2.12}$$
$$R_d x' = -(x'-d)+d \tag{2.13}$$
$$= -x'+2d \tag{2.14}$$

We can apply these operators one after another to generate all the images as per Figure 2.6. Red is the original charge and images with the same sign of charge and blue are images with the opposite sign of charge.

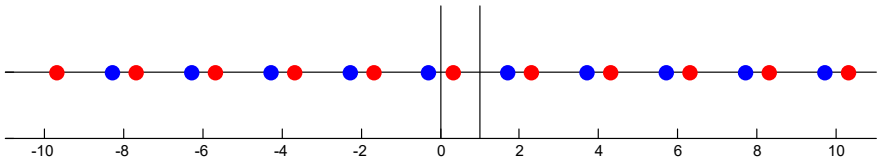

Figure 2.6.: Location of image charges for a single charge between two metallic plates with $d = 1$. Color indicates the sign of the charge.

2.3.3.2. Potential and Fluctuations

With the series of images noted above, we can write down the equation for the potential inside the slab due to a single charge.

$$\begin{aligned}\tfrac{\kappa_1}{e}\phi_1\left(r,' z';z\right) = & \frac{1}{\sqrt{r'^2+(z'-z)^2}} - \frac{1}{\sqrt{r'^2+(-z'-z)^2}} \\ & + \tfrac{1}{2d}\textstyle\sum_{n=1}^{\infty}\left[\frac{1}{\sqrt{\left(\frac{r'}{2d}\right)^2+\left(n-\frac{z-z'}{2d}\right)^2}} + \frac{1}{\sqrt{\left(\frac{r'}{2d}\right)^2+\left(-n-\frac{z'-z}{2d}\right)^2}}\right] \\ & - \tfrac{1}{2d}\textstyle\sum_{n=1}^{\infty}\left[\frac{1}{\sqrt{\left(\frac{r'}{2d}\right)^2+\left(n-\frac{z'+z}{2d}\right)^2}} + \frac{1}{\sqrt{\left(\frac{r'}{2d}\right)^2+\left(-n-\frac{z'+z}{2d}\right)^2}}\right]\end{aligned} \tag{2.15}$$

See Appendix C.3.2 for a simplification of this potential for $r = 0$. We can use this potential to calculate Γ^2 for this scenario, as shown in Figure 2.7. We see that close to the surfaces $\Gamma^2 \sim z$ as we expect. A maximum naturally forms in the center.

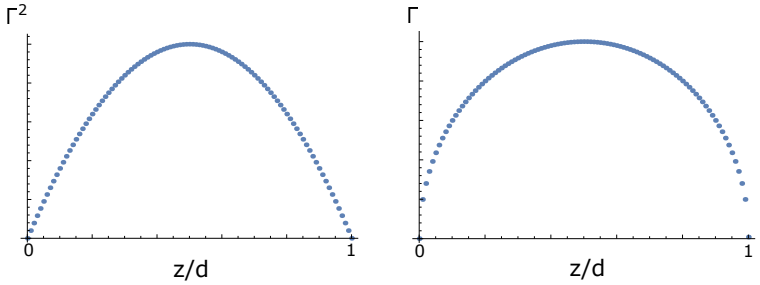

Figure 2.7.: Γ^2 and Γ as a function of z for the case of perfectly screening surfaces. For this model calculation, we have artificially set $\kappa_1 = N_D = 1$.

2.3.4. Topological Insulator Slab

2.3.4.1. Two Imperfectly Screening Surfaces

The results of the previous section can be expanded to account for imperfect screening. The math is tedious, so I simply write down the result here:

$$\begin{aligned}\tfrac{\kappa_1}{e}\phi_1\left(r',z';z,r_s,\xi,\beta_1\right) = & \frac{1}{\sqrt{r'^2+(z'-z)^2}} \\ & + \textstyle\sum_{n=1}^{\infty}\sum_{j=0}^{n}\frac{\binom{n}{j}\beta_1^j\xi^{n-j}}{\sqrt{r'^2+((-1)^n z-jr_s-nd-z')^2}} \\ & + \textstyle\sum_{n=1}^{\infty}\sum_{j=0}^{n}\frac{\binom{n}{j}\beta_1^j\xi^{n-j}}{\sqrt{r'^2+((-1)^n z+jr_s+nd-z')^2}}\end{aligned} \tag{2.16}$$

where $\beta_1 = \frac{2\kappa_1}{\kappa_1+\kappa_2}$ and $\xi = \frac{\kappa_1-\kappa_2}{\kappa_1+\kappa_2}$, which are related to the magnitude of the dielectric image charges that form due to the dielectric interfaces (a refresher is in Appendix C.1). Note the combinatorically larger number of images due to multiple reflections of both metallic and

dielectric image charges. It can be checked that for either $r_s = 0$ or $\kappa_2 \gg \kappa_1$ (e.g. $\beta_1 = 0$ and $\xi = -1$) the potential reduces to that of equation (2.15). I note that for Equation (2.16) I have chosen the interfaces to exist at $z = \pm\frac{d}{2}$, in order to obtain a more elegant formula.

We can solve for the potential fluctuations numerically by using the above formula. Normalizing everything by setting $d = 1$ and choosing $r_s = \frac{1}{8}d$, we get the following plots, which sensibly show that the potential fluctuations at the surfaces are now finite (recall that at the surface itself we expect (analytically) $\Gamma^2 \sim N_D r_s$). The square amplitude again rises approximately linearly from the boundaries as expected.

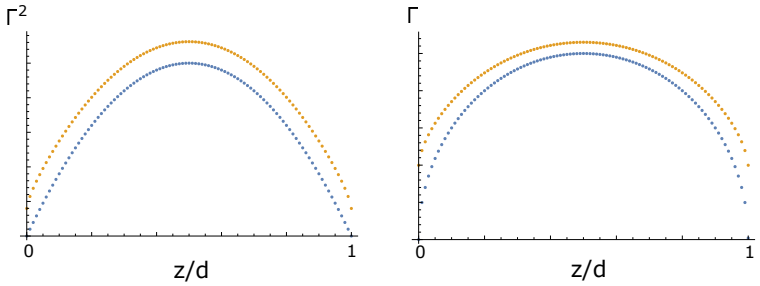

Figure 2.8.: Orange: Γ^2 and $|\Gamma|$ as a function of position for $r_s = \frac{d}{8}$. In this case we have again artificially set $\kappa_1 = \kappa_2 = N_D = 1$. Blue curves are the same as in Figure (2.7). A finite r_s approximately results in a rigid upward shift of the squared potential fluctuations.

2.3.4.2. Effect of Dielectric Mismatch

With the machinery above now developed, we can do a full calculation of the potential fluctuations as a function of different parameters. In Figure 2.9 we show $\Gamma(z)$ for a range of values of the outside permittivity: $\kappa_2 = \{1, 4, 8, 20, 40\}$. The constants are the impurity density $N_D = 10^{19} cm^{-3}$, the interior permittivity $\kappa_1 = 40$, and the thickness of the film $d = 60nm$. The left panel is for $r_s = 4nm$ and the right panel is for $r_s = 20nm$. Two things are immediately clear:

1. For fixed κ_1, the disorder potential is larger if κ_2 is smaller due to anti-screening.

2. The effect noted in #1 is stronger when the surfaces are poorly screening (large r_s).

These are intuitive notions, but they are important observations because typical TIs do have much larger dielectric constants than standard gate dielectrics.

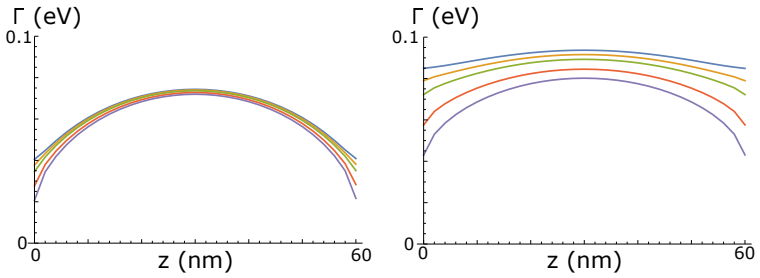

Figure 2.9.: $\Gamma(z)$ for different $\kappa_2 = \{1, 4, 8, 20, 40\}$, from top to bottom. The constants are the impurity density $N_D = 10^{19} cm^{-3}$, the interior permittivity $\kappa_1 = 40$, and the thickness of the film $d = 60nm$. The left panel is for $r_s = 4nm$ and the right panel is for $r_s = 20nm$.

2.3.4.3. Phase Diagram

Now, we can construct a phase diagram as a function of impurity density and film thickness that describes when the TI bulk behaves like a true dielectric as opposed to when it will have puddles that can screen electric fields. The procedure is as follows: for a given film thickness, increase the impurity density N_{imp} until the potential fluctuations at the center of the slab are of the same scale as the band gap, or $\Gamma \sim E_G/2$. This marks the boundary between dielectric behavior and screening behavior. For modeling impact of the surface states, we will test extreme values of the screening length $r_s = \{2, 20\}\, nm$. The first case would be indicative of a high chemical potential at the surface, e.g. where it screens well. The second case is more typical of the screening length near the Dirac point (see [96] for discussion about this). As a result, these two extremes capture a good range of values for comparison to devices in which the surface may be either highly doped or near the Dirac point.

The results are summarized in Figure 2.10. We see that, for a given impurity density, thinner devices are less susceptible to forming bulk puddles due to the screening by the surface states. When the surfaces are screening well, the dielectric mismatch has little impact (comparison not shown): the screening of the surfaces is strong enough that very little electric field leaks to polarize the outside dielectric. When the surfaces are screening poorly (large r_s, green lines), the dielectric mismatch has a significant impact, substantially reducing the N_{imp} necessary to induce puddles in the bulk. The gray shaded region is the curious regime in which there is neither a total absence or permanent presence of puddles. The existence of puddles will depend on the chemical potential of the surface states, e.g. near the Dirac point vs. heavily doped. This presents a curious scenario in which the bulk puddles can disappear and appear as the surface states are doped and undoped *in-situ*.

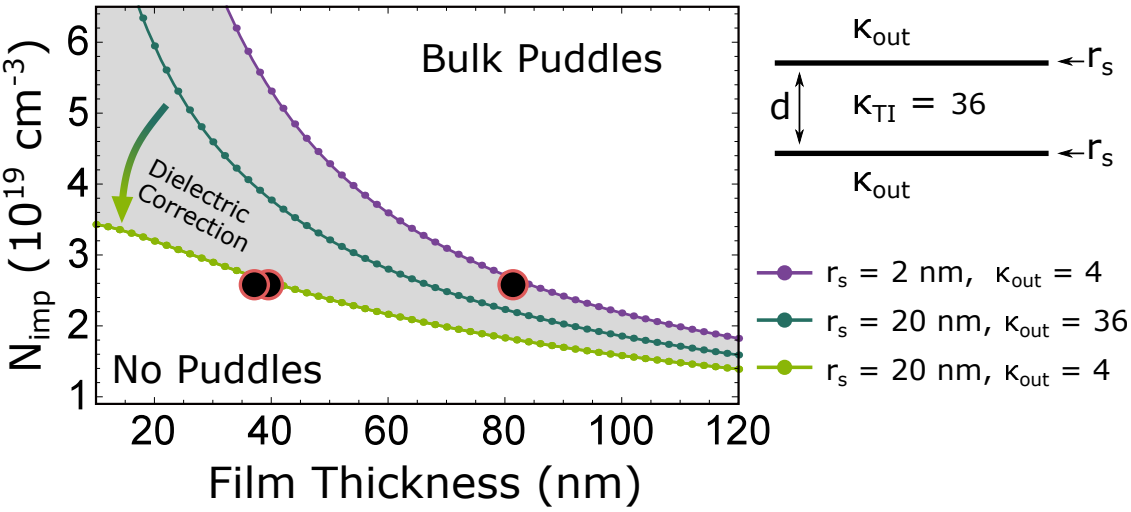

Figure 2.10.: Phase diagram of puddles bulk puddles for $\kappa_{TI} = 36$. Data-points indicate the point at which potential fluctuations are of order the size of the band gap. Upper right: schematic of the topological insulator thin film geometry.

The three devices measured in our experiment have thicknesses of 38, 40, and 80 nm. The thickest device shows no electric field penetration, while the thinner ones do. With this in mind, we can mark their positions on the phase diagram and estimate that the bulk impurity density is of order $2.5 \times 10^{19} cm^{-3}$, which is similar to that estimated in the initial studies of this material [89] but smaller than in others [125]. Nonetheless, this is encouraging, given the simplicity of the theoretical approach.

Finally, we recall for a moment the unusual magnetic field dependence in the experiment (see Figure (2.4)). It may be that a finite density of bulk puddles does exist at the 40nm thickness, but only enough to partially screen electric fields. The application of a magnetic field can alter the properties of the puddles, for example by shrinking their size [129, 130], resulting in an approach to the natural dielectric constant of the insulating crystal. To understand this fully would require a study compiling the statistics of field penetration for many devices of different thickness to establish a complete trend.

2.4. Epilogue

In this short section we briefly review some experimental accomplishments on BSTS crystals that were published following our work. Experimental studies on BSTS-type TIs continued in the community on both exfoliated crystals and thin films. On exfoliated crystals, the first observation of the quantum Hall effect of 3D TI surface states was made on the quaternary compound $BiSbTeSe_2$ [55]. Following this, dual-gated studies showed precisely what would be expected for the surface-state origin of this quantum Hall effect, and also showed electric field penetration even for samples at least as thick as 100nm [56]. We can understand this through the model developed here: all phenomena critically depend on the defect density N_D, and for that particular stoichiometry of BSTS the defect density has been estimated to

be an order of magnitude lower than in other stoichiometries ($\sim 10^{18} cm^{-3}$ vs. $\sim 10^{19} cm^{-3}$) [89]. As a result, we can expect from our phase diagram that puddles are screened away for a very large range of device thicknesses. The lower defect density may also contribute to a higher mobility, allowing for access to the quantum Hall regime in experimentally accessible magnetic fields.

Low-density thin films grown by molecular beam epitaxy have been magnetically doped in order to achieve the quantum anomalous Hall effect (QAHE), which is the achievement of quantized Hall resistance at zero external magnetic field [106, 131, 132, 133, 134]. Most studies of the QAHE utilize $SrTiO_3$ substrates[4], which have exceptionally large dielectric constants at low temperature. These thin films are highly disordered, but the high dielectric constant environment may be useful for screening disorder (as per our investigation above) in order to obtain a strongly insulating phase in the thin film.

[4] InP substrates have also been used [131].

Part II.

The Many Phases of WTe_2

3. Introduction to WTe_2

3.1. As-Grown 3D Crystal

Three-dimensional WTe_2 is a beautiful crystal (see Figure 3.1) in an orthorhombic structural phase ("Td" structure) [135, 136, 137, 9]. The samples used in our experiments are grown by the flux method [138]. It is not only a layered vdW material, but additionally within each layer the tungsten atoms dimerize into chains. As a result, the material is fully anisotropic (all three cardinal directions are inequivalent). In the monolayer limit, it represents one of the first measured two-dimensional crystals with a non-triangular lattice.

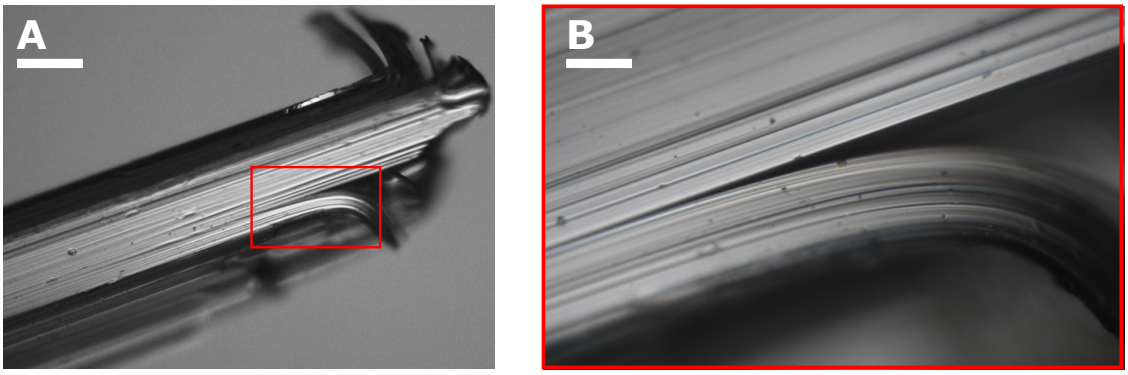

Figure 3.1.: An optical microscopy image of a 3D WTe_2 crystal. **A,** Scale bar ~ 1 mm. **B,** Zoom-in of the red square region in **A**, where the layered structure is readily apparent and the ease of exfoliation is anticipated by the visible "natural peeling apart" of the crystal.

The crystal structure of Td-WTe_2 is shown in Figure 3.2, alongside the case for 1T'-$MoTe_2$ for comparison. There are two qualitative differences in the atomic coordinates:

1. Within each plane, the metal-tellurium rhombus is distorted in the Td structure but inversion symmetric in the 1T' structure.
2. The stacking of the layers is different, resulting in a tilted unit cell in the 1T' structure and an non-tilted unit cell in the Td structure.

The two crystal structures differ in the set of symmetries they respect. The 1T' structure maintains inversion symmetry as well as a mirror symmetry and an in-plane two-fold rotational axis. The Td structure breaks inversion symmetry, but has two mirror planes (one is non-symmorphic) and an out-of-plane two-fold screw axis. A comparison of crystal symmetries is shown in Table 3.1.

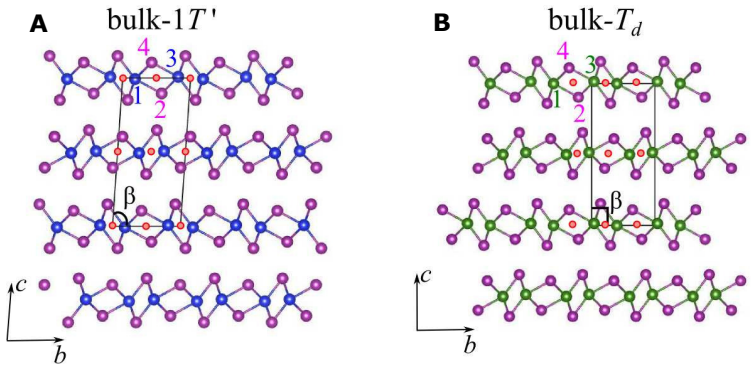

Figure 3.2.: Bulk atomic positions for the **A,** 1T' and **B,** Td structures. Orange dots represent centers of the M-Te rhombi, which represent true inversion centers for the 1T' case.

	bulk 1T'	bulk Td
Structural Phase	primitive monoclinic	primitive orthorhombic
Lattice Constants	$a \neq b \neq c$	$a \neq b \neq c$
Unit Cell Angles	$\alpha = \gamma = 90^o$, $\beta \neq 90^o$	$\alpha = \beta = \gamma = 90^o$
Space Group	$P2/m(\#11)$	$Pmn2_1(\#31)$
Point Group	C_{2h}	C_{2v}
Symmetry Operations	I, C_{2a}, M_a	M_a, M_b, C_{2c}

Table 3.1.: Properties of the 3D versions of the distorted 1T structure, known as 1T' and Td. I is inversion symmetry, C_{2X} is a two-fold rotation about the X axis, and M_X is a mirror plane normal to the X axis. Note that in the Td structure M_b is actually a glide plane and C_{2c} is actually a screw rotation.

A schematic band structure of 3D WTe_2 is shown in Figure 3.3 for $k_z = 0$. Electron and hole valleys are located along the $\Gamma - X$ direction. Each valley has a nested pair of pockets with substantial spin texture [3] due to a spin-orbit splitting resulting from broken inversion symmetry. Magnetoresistance measurements, in conjunction with quantum oscillations and spectroscopy studies, have given evidence that the occupation of these pockets is nearly compensated, with equal numbers of electrons and holes [9, 139, 138, 140, 141, 142, 143]. In Section 4 I introduce semimetals more thoroughly and develop intuition for these claims. In WTe_2 the magnetoresistance ratio has been found to be in excess of 10^5 at large magnetic fields, suggesting large mobilities and high crystalline quality [138]. The initial discovery of the extreme magnetoresistance [9] has since spurred the discovery of many new semimetallic systems with similarly large magnetoresistance effects [144, 145, 146, 147, 148, 149, 150, 151, 152].

In addition to the above, WTe_2 has been the subject of much discussion regarding possible topological aspects of the electronic structure. There are two independent cases: one for the 3D crystal and one for the 2D crystal. The 3D compound has been predicted to be a Weyl semimetal, with Type-II Weyl nodes [153]. Because inversion symmetry is only weakly broken, the Weyl nodes are close to each other in momentum space. As a result, there has

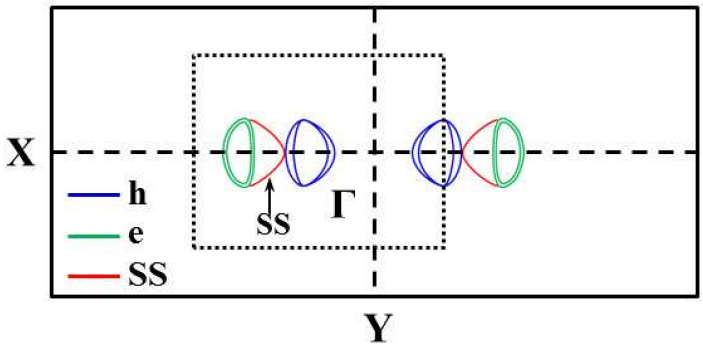

Figure 3.3.: Schematic Fermi surface presented by Feng, et al [3]. Green and blue are the bulk bands at $k_z = 0$, and red is the surface state which may be a surface arc due to the presence of Weyl nodes [3, 4, 5, 6, 7].

been some evidence for this topological phase, but not yet a smoking-gun proof [3, 4, 5, 6, 7]. The 2D topological phase will be discussed in the next section.

3.2. Two Dimensions

3.2.1. Crystal Structure

The simplest assumption for the crystal structure of an exfoliated monolayer is that it is the same as if one were to extract a single layer from the parent compound's 3D crystal structure, which is usually well-documented. For monolayer WTe_2, this would mean the Td structure. However, the distinction between 1T' and Td is not always made in the literature.

As noted previously, the difference between the two structures structures amounts to a small distortion of the W-Te rhombus in the Td case and a different stacking of the layers, both of which resulting in weakly broken inversion symmetry in the Td structure. The distortion of the W-Te rhombus would mean the Td monolayer would be expected to have an intrinsic spin-orbit splitting, in contrast to the inversion symmetric 1T' phase. The spin-orbit splitting for the bulk (which is most strongly influenced by the layer stacking) is documented in 3D bulk crystals from quantum oscillation data [143, 140] as well as ARPES spectra [139, 3] interpreted alongside band structure calculations. Our quantum oscillation data on trilayer samples also finds two electron pockets, suggestive of a spin-orbit splitting ([154] and Section 4). Raman spectra taken on ultra-thin samples has been found to be consistent with theoretical calculations of the vibrational modes of Td-WTe_2 [155, 156]. STM studies on MBE-grown films has found a structure consistent with the 1T' phase [8, 157] but did not specify or were unable to make the distinction between the 1T' and Td structures.

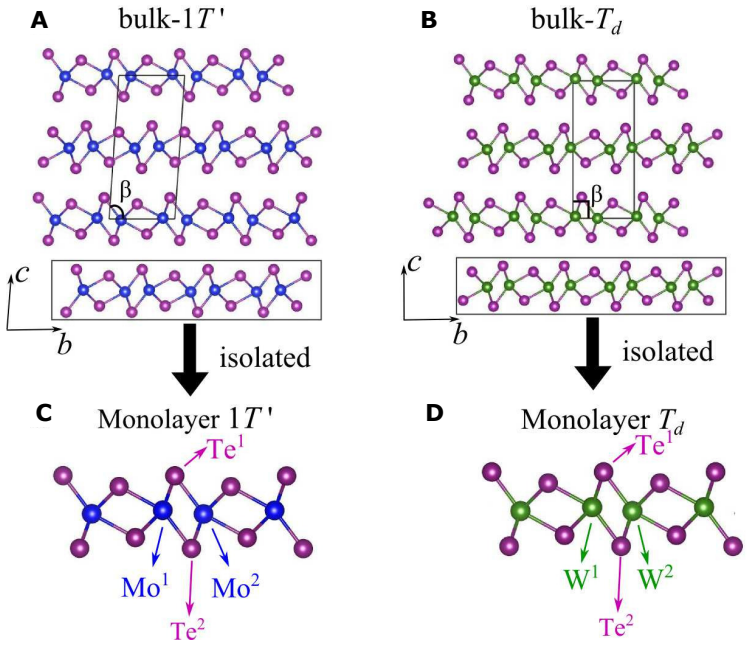

Figure 3.4.: Monolayer atomic positions, as extracted from bulk crystallography data, for the (**A,C**) 1T' and (**B,D**) Td structures.

	monolayer 1T'	monolayer Td
Structural Phase	primitive monoclinic	primitive monoclinic
Lattice Constants	$a \neq b$	$a \neq b$
Unit Cell Angles	$\alpha = 90^o$	$\alpha = 90^o$
Space Group	$P2/m(\#11)$	$P1m1(\#6)$
Point Group	C_{2h}	C_s
Symmetry Operations	I, C_{2a}, M_a	M_a

Table 3.2.: Properties of the 3D versions of the distorted 1T structure, known as 1T' and Td. I is inversion symmetry, C_{2X} is a two-fold rotation about the X axis, and M_X is a mirror plane normal to the X axis.

3.2.2. Band Structure and Topology

Independent of the proposed topological semimetal phase in 3D is the 2D topological insulator state in the monolayer, which is what concerns us in this thesis. This was first conceived by Qian, et al, who proposed that monolayer transition metal dichalcogenides in the 1T' structure are 2D time-reversal invariant topological insulators [158]. The intuition is as follows:

1. We begin with the undistorted 1T structure. This phase is structurally unstable, but it has been calculated to be metallic [159, 160]. The important orbitals are the Te p-orbitals and the W d-orbitals.

2. With distortion to the 1T' structure, the Brillouin zone changes from hexagonal to rectangular, but the bands near the chemical potential still arise from the same orbitals. The new structure splits a p-orbital degeneracy and a d-orbital degeneracy. For the sulfur and selenium based compounds, one finds a simple inversion of a Te p-orbital and a W d-orbital, as shown in Figure 2A of [158]. For the tellurium based compounds, the p-orbitals are a priori well-mixed with a W d-orbital (d_{z^2}) that does not participate in the lighter chalcogen compounds. In this case, the inversion is a mixture of p-d and d-d type inversion [160]. Nonetheless, the topologically non-trivial state remains. The band inversion at Γ from these orbitals of differing parity is where the topologically non-trivial character arises [161, 158, 160]. Because the band inversion is generated by strong crystal fields, this energy scale is large, of order $0.5eV$. This intuition is discussed in greater detail by Qian, et al [158] and Choe, et al [160].

3. Spin-orbit coupling then generates the band gaps at finite momenta along the $\Gamma - X$ direction. The energy scale of this spin-orbit driven hybridization gap is smaller, predicted to range from 10s of meV up to 150 meV [158, 162], although the transport gap may be smaller or even negative (e.g. a semimetallic state) depending on the calculation.

4. Finally, the true crystal structure may be of the Td type, not 1T'. This small inversion-breaking distortion leads to a small spin-orbit splitting (of order 5 meV) in the conduction and valence bands, but does not close the band gap. As a result, we deduce that the Td monolayers retain a non-trivial topological invariant, despite not being strictly in the 1T' structure.

Among the typical transition metal dichalcogenides, WTe_2 and $MoTe_2$ were the only compounds known to have a 1T' phase. $MoTe_2$ can be grown in both 1T', Td, and 2H forms depending on growth conditions [163, 164, 165, 166, 167, 168, 169, 170], while WTe_2 is almost universally stable in the Td structure [135, 136, 137, 9]. Fortunately, as per the above discussion, the 1T' and Td structures are very close to each other, and we know that both should be topologically non-trivial. The conclusion is that WTe_2, due to its structural stability and high crystalline quality, is an ideal candidate material in which to search for a 2D topological insulator phase in a vdW material.

A calculation of the monolayer WTe_2 band structure, from a tight-binding model derived from DFT calculations, is shown in Figure 3.5[1].

[1] I thank Shiang Fang for his generosity in sharing his tight-binding code for use in my thesis.

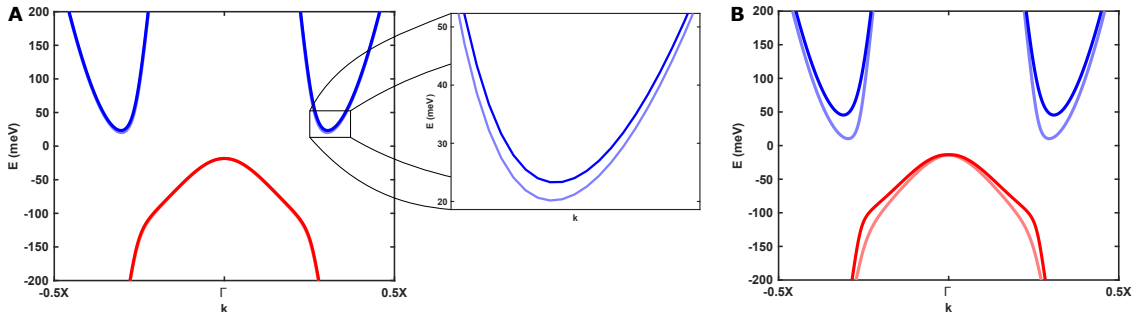

Figure 3.5.: **A,** Band structure of monolayer WTe_2 from a DFT-derived tight-binding model. The conduction and valence bands were shifted have roughly the band gap seen in spectroscopy measurements [8]. Center: zoom-in to the bottom of one of the conduction band valleys to show the intrinsic spin-orbit splitting. **B,** Same calculation with a large displacement field added, showing that the spin-orbit splitting can be enhanced.

3.2.3. Setting the Stage

Having chosen monolayer WTe_2, it is a good idea to be aware of other outstanding questions prior to jumping in. The initial theoretical prediction found a negative band gap, meaning that the system remains a semimetal [158]. A follow-up work agreed [171] while another disagreed [162], predicting a transport gap as large as 150 meV.

Experimentally, it had already been shown that ultra-thin WTe_2 degrades with exposure to air, likely due to oxidation [172, 173, 174]. Our internal tests (not shown here) were similar to those found in [172], in which thin samples (single-digit layers thick) would display insulating-like behavior, while thicker ones would exhibit high mobility semimetallic behavior as expected for 3D samples. As a result, the challenge was to develop techniques that would enable the fabrication of transport devices in which thin WTe_2 flakes would survive without oxidation or other chemical degradation. With similar objectives in mind for a wide variety of air-sensitive vdW materials, we embarked upon the creation of a glove box with equipment specialized for exfoliation and inspection of these vdW materials as well as the creation of novel vdW heterostructures. The glove box itself was purchased from MBraun, Inc., and is filled with a slight over pressure of pure argon gas supplied from pressurized dewars of liquid argon. The internal oxygen and water levels are continuously monitored and remain below 0.1 parts-per-million under normal use. I designed and constructed a custom mechanical transfer setup for creating vdW heterostructures, similar to those described elsewhere [20], but with the added functionality of remote operation for the x-y-z motion of the sample stage and transfer arm as well as the focus knob. For details regarding this setup, please contact me.

Scientifically, we began with trilayer samples as our "canary in the coal mine" to test that our new fabrication schemes are indeed working. All theoretical calculations agreed that WTe_2 retains a band overlap down to three layers thick, and so it should exhibit the physics of a semimetal: a metallic temperature dependence and semimetallic magnetoresistance. The chemical reactivity of layered materials also increases as thickness is reduced. Thus, the

trilayer gives us an excellent opportunity as a control sample: a reactive crystal with clear predictions for what to expect. This effort is detailed in Chapter 4.

Following this, we pursued the monolayer samples. By this time, several groups had determined that monolayer WTe_2 does indeed have a full band gap [175, 8, 157], and one group explicitly showed edge conduction in transport devices [175]. These exciting results motivated more careful studies of the edge conductance in hopes of ascertaining that the system is indeed a 2D topological insulator. Our efforts confirming this state are detailed in Chapter 5.

Finally, during our investigation of the edge modes, we happened upon a surprising discovery: when doped into the conduction band, monolayer WTe_2 undergoes a superconducting transition. With only an electrostatic gate electrode, this monolayer crystal can be tuned in situ from the topological insulating state into the superconducting state. The results on this state are presented in Chapter 6.

4. Semimetal

4.1. What is a Semimetal?

Semimetals have a deep history in condensed matter physics, particularly with the compounds bismuth and graphite. The former in particular has led to a number of important first discoveries and records:

- Discovery of diamagnetism (still holds the record for the largest average magnetic susceptibility in a non-magnetic solid) [176]
- Discovery of the Seebeck effect [177]
- Discovery of the Nernst effect [178]
- Discovery of the Shubnikov-de Haas effect (and separately the de Haas-van Alphen effect) [179]
- Discovery of 3D topological insulators (Bi with light Sb doping) [60]
- Superconductivity at the lowest recorded 3D carrier densities [180]

In addition to these discoveries, both graphite and bismuth have long been known to display a positive, sometimes very large magnetoresistance (MR) [181, 182, 183, 184, 185]. This will be discussed in detail in the next section. Due to the long history, the definition of semimetal had been established to involve two key components: a low carrier density (as compared with a metal) and band overlap of both the conduction and valence bands at the Fermi energy, resulting in coexistence of electrons and holes.

In the new millennium, the definition of semimetal has broadened. This began with graphene, which has been alternately called a semimetal and a zero-band gap semiconductor. As a semimetal, the stricter definition would be as a zero band-overlap semimetal. So is it a semimetal with zero band overlap, or a semiconductor with zero band gap? Either might be acceptable, but the tie may be reasonably broken by the fact that graphene will remain metallic at zero temperature even despite a strictly zero density of states at charge neutrality. Hence, the definition of graphene as a semimetal.

Since the discovery of graphene, similar sorts of zero-gap/zero-overlap systems have been predicted and discovered, in both 2D and 3D. These include, but may not be limited to, Dirac semimetals [186, 187, 188], Weyl semimetals [189, 190, 191], nodal-line semimetals [192], and 2D Dirac semimetals protected by non-symmorphic symmetries [193]. While extremely interesting in their own right, we need only the traditional definition of semimetal for our purposes here.

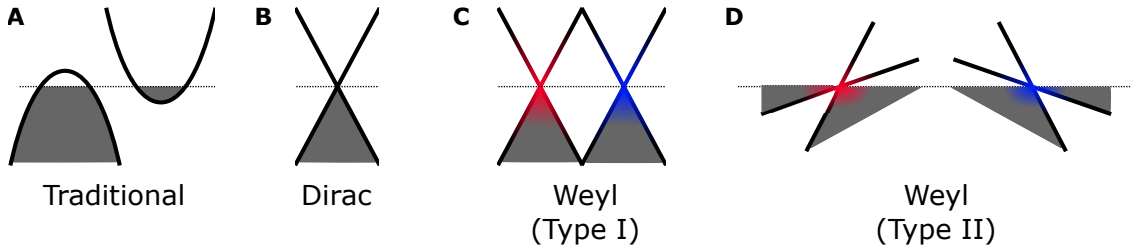

Figure 4.1.: Schematic band structures of some different types of semimetals: **A,** traditional. **B,** Dirac. **C,** Weyl (type I). **D,** Weyl (type II). Red or Blue coloring indicates Berry curvature around nodes with positive or negative chirality. Note that **A** and **B** may occur in any extended dimensionality (particularly 1D, 2D, or 3D), but **C** and **D** are in 3D only.

4.2. Magnetoresistance in Metals

It is known that the MR of a semimetal, at low magnetic fields, is related to the co-existence of electrons and holes at the chemical potential. Historically, in the case of graphite and bismuth, the MR may saturate [194] or deviate strongly from quadratic behavior [195], which is usually attributed to reaching the "quantum limit" in which the lowest Landau level is occupied. More recently, semimetals like WTe_2 have been discovered with magnetoresistance that does not saturate at even the highest applied magnetic fields [9, 145, 146, 147, 148, 149, 150, 151, 152, 144]. Here we give an introduction that addresses the basis of magnetoresistance in non-magnetic metals and semimetals.

4.2.1. Classical magnetoresistance of a diffusive (semi)metal

The physics of semiclassical, quadratic magnetoresistance in diffusive charge transport of simple metals and semimetals is intimately tied to the absence or reduction of Hall electric fields. Two typical ways to excise the Hall field in realistic transport devices are

1. Device geometry: using a Corbino geometry to avoid edges that would allow charge to build up means no transverse electric fields.
2. Band structure of the sample: compensating positive and negative charges of a semimetal can avoid transverse electric fields regardless of device geometry.

These concepts are summarized in Figure 4.2, and will be investigated in detail in the following subsections.

We note that schemes based on more complicated device geometries (not shown or discussed here) have also been used to generate large magnetoresistances [196, 197, 198]. Another magnetoresistance effect, which has a convenient qualitative analogy with the two-component model, is that which results from an energy-dependent scattering time [199]. Other types of magnetoresistance not discussed here include the different longitudinal magnetoresistances predicted to occur for generic 3D metals [199] and Weyl semimetals [200, 201, 202, 203, 204, 205], various types of magnetoresistance effects that occur in devices utilizing magnetic

materials [206, 207], and the magnetoresistance that is expected to occur in systems with strong Berry curvature due to the density of states correction [208].

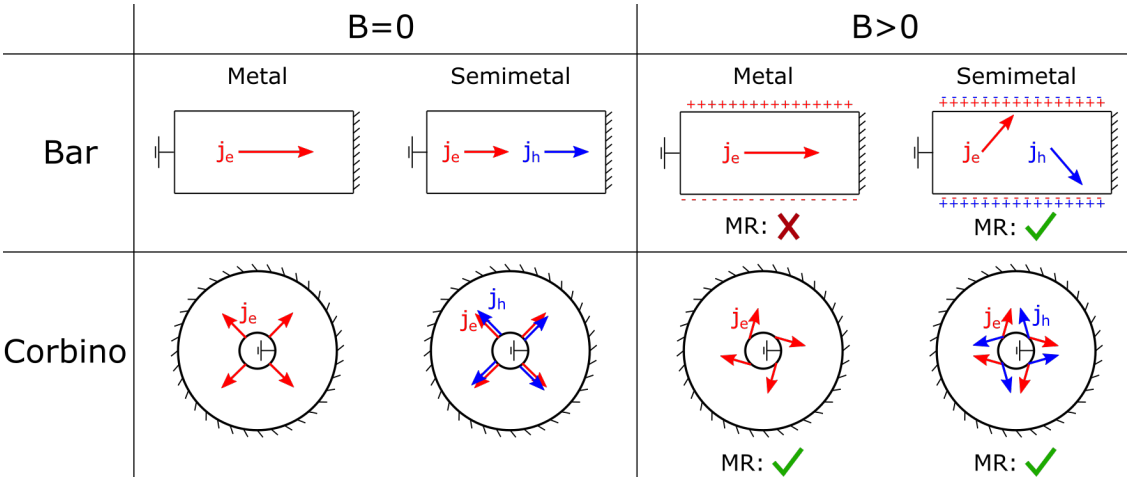

Figure 4.2.: Cartoons depicting simple metals and semimetals in two classic geometries: linear transport channel (equivalent to a Hall bar) and Corbino. Only the simple metal in a standard bar geometry has a Hall electric field, and therefore it is the only scenario that does not have a magnetoresistance.

4.2.1.1. Single-Component Metal

We begin with the conductivity tensor of a simple metal with a single carrier type, as derived from the Drude model:

$$\sigma = \frac{\sigma_0}{1+\mu^2 B^2}\begin{pmatrix} 1 & \mu B \\ -\mu B & 1 \end{pmatrix} \tag{4.1}$$

where B is magnetic field, μ is mobility (which has units of $\frac{cm^2}{V \cdot s}$ or $T^{-1} = 10^4 \frac{cm^2}{V \cdot s}$), and $\sigma_0 = ne\mu$, where n is the carrier density and e is the electron charge. Inverting to the resistivity tensor we find

$$\rho = \rho_0 \begin{pmatrix} 1 & \mu B \\ -\mu B & 1 \end{pmatrix} \tag{4.2}$$

where $\rho_0 = \sigma_0^{-1}$.

So $\sigma_{xx} \sim B^{-2}$ while $\rho_{xx} = \rho_0$. How do we reconcile these two results? One must consider when it is appropriate to use σ or ρ. This depends on the geometry of the device, which determines the boundary conditions for charge in the system. Without a boundary, σ is the natural tensor, whereas with fixed boundary conditions one uses ρ. This is because

$$\vec{j} = \overleftrightarrow{\sigma}\vec{E} \tag{4.3}$$

$$\vec{E} = \overleftrightarrow{\rho}\vec{j} \tag{4.4}$$

e.g. σ naturally describes the resultant current density when the local electric field vector can be considered as fixed, whereas ρ naturally obtains the local electric field when the local current density vector can be fixed. From this consideration we come to understand that in a Corbino geometry (lower row of Figure 4.2) we may use σ, which tells us that any diffusive conductor would exhibit a quadratic magnetoresistance in this geometry.

However, in the more standard Hall bar geometry, no magnetoresistance occurs for a simple metal. Consider that the drift velocity can be written in the following way:

$$\vec{v}_d = \frac{1}{1+\mu^2 B^2}\left(\mu\vec{E} - \mu\vec{E}\times\mu\vec{B}\right). \tag{4.5}$$

For large magnetic fields in a Hall bar, it must be considered that $\vec{E} = E_{app}\,(\hat{x} + \mu B\hat{y})$, where E_{app} is the magnitude of the applied electric field, and the term proportional to $\hat{y}$ describes the Hall field that develops in response to an applied magnetic field. In the limit of very large magnetic fields $\mu B \gg 1$, the electric field is dominated by the Hall component, and the physics becomes that of the motion of guiding centers rather than simple electrons. In this case:

$$\vec{v}_d = \mu E_{app}\frac{1+\mu^2B^2}{1+\mu^2B^2}\hat{x} + \mu E_{app}\frac{\mu B - \mu B}{1+\mu^2B^2}\hat{y} \tag{4.6}$$

$$= \mu E_{app}\hat{x} \tag{4.7}$$

and hence no magnetoresistance occurs due to the Hall electric field which induces the classic $\vec{E}\times\vec{B}$ drift of the guiding centers.

4.2.1.2. Perfectly Compensated Semimetal

Compensation refers to the condition that the densities of electrons and holes are equal. Momentarily, let us also consider the situation that the mobilities are equal. In this case, the off-diagonal components of the total conductivity tensor are strictly zero.

$$\sigma = \sigma_e + \sigma_h \tag{4.8}$$

$$= \frac{\sigma_0}{1+\mu^2B^2}\begin{pmatrix} 1 & \mu B \\ -\mu B & 1\end{pmatrix} + \frac{\sigma_0}{1+\mu^2B^2}\begin{pmatrix} 1 & -\mu B \\ \mu B & 1\end{pmatrix} \tag{4.9}$$

$$= \frac{2\sigma_0}{1+\mu^2B^2}\begin{pmatrix} 1 & 0 \\ 0 & 1\end{pmatrix} \tag{4.10}$$

$$\rho = \frac{1+\mu^2B^2}{2\sigma_0}\begin{pmatrix} 1 & 0 \\ 0 & 1\end{pmatrix} \tag{4.11}$$

Here we see that strictly quadratic, and unsaturating, magnetoresistance appears because the Hall field is negated via compensating Hall effects from the two types of carriers.

If the mobilities are different, as will generically be the case, the unsaturating quadratic

magnetoresistance still occurs:

$$\frac{1}{en}\sigma = \frac{\mu_1}{1+\mu_1^2B^2}\begin{pmatrix} 1 & \mu_1 B \\ -\mu_1 B & 1 \end{pmatrix} + \frac{\mu_2}{1+\mu_2^2B^2}\begin{pmatrix} 1 & -\mu_2 B \\ \mu_2 B & 1 \end{pmatrix} \tag{4.12}$$

$$ne\rho_{xx} = \frac{1}{\mu_1+\mu_2}\left(1+\mu_1\mu_2B^2\right) \tag{4.13}$$

$$ne\rho_{xy} = \frac{\mu_1-\mu_2}{\mu_1+\mu_2}B \tag{4.14}$$

Here, we also have a finite, but small, Hall effect given by the mobility difference of the two carriers. A Hall field associated with negatively charged carriers will cause a reduction in the drift velocity of positively charged carriers. As a result, we recover the positive magnetoresistance.

4.2.1.3. Uncompensated Semimetal

The general formula for a two-carrier system is reproduced below.

$$\rho_{xx} = \frac{1}{e}\frac{n\mu_n + p\mu_p + (n\mu_p + p\mu_n)\,\mu_n\mu_p B^2}{(n\mu_n + p\mu_p)^2 + (p-n)^2\,\mu_n^2\mu_p^2B^2} \tag{4.15}$$

$$\rho_{xy} = \frac{1}{e}\frac{\left(p\mu_p^2 - n\mu_n^2\right)B + (p-n)\,\mu_n^2\mu_p^2B^3}{(n\mu_n + p\mu_p)^2 + (p-n)^2\,\mu_n^2\mu_p^2B^2} \tag{4.16}$$

The quadratic magnetoresistance at low magnetic field is obvious here. The high field limit, when ρ_{xx} has saturated, is

$$\rho_{xx} \sim \frac{1}{e}\frac{1}{|p-n|}\frac{n\mu_p + p\mu_n}{|p-n|\,\mu_n\mu_p} \tag{4.17}$$

$$\rho_{xy} \sim \frac{1}{e}\frac{1}{p-n}B. \tag{4.18}$$

These limits highlight the importance of a difference in density to achieve saturation. For additional intuition on the behavior at high fields, let us assume that the mobility is the same for both carriers. This then gives us:

$$\rho_{xx} \sim \frac{1}{e}\frac{1}{|p-n|}\frac{1}{\mu}\frac{n+p}{|p-n|} \tag{4.19}$$

$$\rho_{xy} \sim \frac{1}{e}\frac{1}{p-n}B \tag{4.20}$$

When saturation has occurred, the system behaves like a simple metal with new "effective" charge densities and mobilities:

$$\rho_{xx} = \frac{1}{en_{eff}\mu_{eff}} \tag{4.21}$$

$$\rho_{xy} = \frac{1}{en_{eff}}B \tag{4.22}$$

$$n_{eff} = p - n \tag{4.23}$$

$$\mu_{eff} = \mu\frac{|p-n|}{n+p} \tag{4.24}$$

How can we understand this? At high magnetic fields, the Hall effect is given by an exact subtraction of densities, which is sensible. The effective mobility is then related to the magnitude of the $\vec{E} \times \vec{B}$ drift velocity for this reduced Hall field.

4.2.2. Experimental Discrepancies for WTe_2

After the discovery of the unsaturating magnetoresistance in WTe_2 and other compounds, a variety of studies cast some doubt that simple charge compensation is the origin of the magnetoresistance. The main points are that quantum oscillation studies (which measure the Fermi surface area, and therefore the electron density) did not find exact compensation, with at best a 5% difference between the total electron and hole densities [143, 142, 140, 141]. It was even found that the oscillation frequencies are magnetic field dependent [140], suggesting substantial band structure modification as a function of magnetic field. Proposed alternative magnetoresistance mechanisms centered around the Zeeman effect, particularly that it may induce a magnetic field dependence to either scattering rates or the band structure itself.

In this subsection, I first argue that these alternative mechanisms are unlikely to contribute significantly to magnetoresistance effects that are both (a) unsaturating and (b) with changes of resistance that are several orders of magnitude or more. I conclude with a suggestion that appears to be consistent with existing data on magnetoresistance in this material.

4.2.2.1. Comment on Helicity-Based Magnetoresistance

The main argument for helicity-based magnetoresistance as follows. Spin-orbit coupling imbues a helicity to the Fermi surface that, at zero magnetic field, can result in a reduced transport scattering rate. With an applied magnetic field, the helicity is no longer perfect, and the backscattering matrix element becomes non-zero. We note in particular that this mechanism does not require any notion of electron-hole compensation. As will be shown in Section 4.3, when thin WTe_2 is doped to a chemical potential at which only carriers of a single charge sign are present, the magnetoresistance is completely suppressed. There is no reason *a priori* that any existing Fermi surface helicity would be removed by doping, further suggesting that a helicity-lifting mechanism is unlikely to be the cause of, or even involved in, the magnetoresistance observed in WTe_2 or other systems.

Nonetheless, we can still attempt model calculations to this end. An extreme case of spin-orbit induced helicity is that of the surface state of a 3D topological insulator, which can be shown to provide an maximal improvement in the transport scattering rate of a factor of 4 compared to the non-helical case (see Appendix A.1). We see from that example that the maximal effect is limited in its total magnitude, absent disorder strong enough to localize the non-helical state.

We can attempt a similar calculation for a 3D Fermi surface. Here, our "extreme" example will be a Weyl fermion system, with well-separated spherical Fermi surfaces. These Fermi surfaces individually have have spin texture preventing back-scattering, just as in the boundary modes of time-reversal invariant topological insulators. The transport scattering rate can be written as [209]

$$\frac{1}{\tau_{tr}} = \frac{2\pi n_i}{\hbar} \int \frac{d^3k}{8\pi^3} \left\langle (V(k,k'))^2 \right\rangle M(k,k') \left(1 - \cos\theta_{kk'}\right) \delta\left(\epsilon_k - \epsilon_{k'}\right) \tag{4.25}$$

$$M(k,k') = \begin{cases} 1 & \text{normal} \\ \frac{1}{2}\left(1 + \cos\theta_{kk'}\right) & \text{helical} \end{cases} \tag{4.26}$$

Note that this formula is the same as in the 2D case of Section (1.2.2), but with a 3D integral instead of a 2D integral. We again take the extreme case of point-like disorder $\langle (V(k,k'))^2 \rangle = v_0^2$ that is constant in momentum space[1] as the extremal case in which the benefit of helicity should be maximal.

$$\frac{1}{\tau_{tr}} = \frac{n_i v_0^2 k_F^2}{2\pi\hbar^2 v_F} \int_0^\pi M(\theta) \sin\theta \left(1 - \cos\theta\right) d\theta \tag{4.27}$$

The extra $\sin\theta$ term is the key difference between the 2D and 3D calculations. We now compare the ratio of the helical and non-helical cases:

$$\frac{\tau_{tr}^h}{\tau_{tr}^n} = 3 \tag{4.28}$$

which is not as strong as the 2D case. In 3D the number of states available for "right-angle" scattering is comparatively large compared to back-scattering events, which reduces the beneficial effects of helicity-based protection.

For a system without a strongly lifted spin degeneracy, as in WTe_2, the situation is even worse. For point-like scatterers, the Fermi surfaces are fully "mixed" and the system should behave more like a non-helical system. This is because for each matrix element that is "turned on" by the Zeeman effect, there will be another matrix element that is concomitantly suppressed. In the opposite limit, extremely small angle scattering, helicity has almost no impact in the first place. Perhaps something interesting could occur in an intermediate regime, where an interplay between different momentum scales could play a roll (e.g. the relationship between k_F and the momentum separation between different valleys). How-

[1] We assume this quantity to be constant for $q \leq 2k_F$ and that the disorder potential is zero at the scale of the momentum difference of the Weyl nodes.

ever, the limiting scenarios mentioned here do not present obvious answers for explaining magnetoresistance effects with $\frac{\Delta\rho}{\rho_0}$ in excess of 10^5 at high fields with no apparent onset of saturation.

4.2.2.2. Comment on Band Structure Modification

A second proposed scenario is that the Zeeman effect strongly modifies the band structure in the vicinity of E_F. Evidence for this in quantum oscillation data has been observed, e.g. in [140]. However, regardless of the band structure modifications that may occur, the charge neutrality condition (accounting for any unintended doping) must be satisfied. With N total electron and hole pockets, this can be described by the following relationship:

$$\sum_i^N n_i(B) = \sum_i^N n_i(0), \tag{4.29}$$

where n_i is the *charge* density of the ith pocket (which includes the sign of the charge carrier). Even if some pockets are completely depleted, the sum of the total density must remain constant.

As a result, we can write the saturation resistance at high-field if a finite density difference exists in the system, regardless of any band structure modifications due to the Zeeman effect along the way:

$$\rho_{xx}^{saturation} = \frac{\sum_{i=1}^N \frac{|n_i|}{e\mu_i}}{\left(\sum_{i=1}^N n_i\right)^2} \tag{4.30}$$

where "high field" is defined by $\min(\mu_i) \cdot B \gg 1$[2]. It is easy to see that if the denominator is zero (e.g. exact compensation) then there is no saturation within this model.

Black Sheep Model One possibility that is the notion of a "black sheep" pocket which has substantially lower mobility *and* density than the others. These carriers would not contribute to SdH oscillations at experimentally accessible magnetic fields. In the case of WTe_2, such a pocket could make up the few percent deviation from compensation observed in quantum oscillations. ARPES measurements find a small occupied hole pocket at the Γ point [141, 210, 211], which could be a candidate pocket [3]. For simplicity, let us assume a system with N pockets of equal mobility and similar carrier density (some electrons and some holes), plus a black sheep pocket b with low mobility and low density. Charge neutrality dictates

$$n_b + Nn_i = 0 \tag{4.31}$$

[2] We assume that none of these bands are in the quantum limit, e.g. occupying a single Landau level, in the high field limit

[3] Note that due to possible band bending at the surface, ARPES data is not always indicative of the chemical potential deep inside the bulk.

The conductivity elements add in parallel:

$$\sigma_{xx} = \frac{|n_b|\, e\mu_b}{1+\mu_b^2 B^2} + \sum_{i=1}^{N} \frac{|n_i|\, e\mu_i}{1+\mu_i^2 B^2} \tag{4.32}$$

$$= \frac{|n_b|\, e\mu_b}{1+\mu_b^2 B^2} + \frac{N\,|n_i|\, e\mu_i}{1+\mu_i^2 B^2} \tag{4.33}$$

$$\sigma_{xy} = \frac{n_b e\mu_b^2 B}{1+\mu_b^2 B^2} + \sum_{i=1}^{N} \frac{n_i e\mu_i^2 B}{1+\mu_i^2 B^2} \tag{4.34}$$

$$= n_b eB \left(\frac{\mu_b^2}{1+\mu_b^2 B^2} - \frac{\mu_i^2}{1+\mu_i^2 B^2} \right) \tag{4.35}$$

We then obtain the magnetoresistance from the usual relationship $\rho_{xx} = \frac{\sigma_{xx}}{\sigma_{xx}^2+\sigma_{xy}^2}$. So far we have an exact expression. We can simplify ρ_{xx} into two magnetic field regimes

$$\rho_{low}/\rho_0 \approx 1+\mu_i^2 B^2 \tag{4.36}$$

$$\rho_{high}/\rho_0 \approx \frac{1}{1+\frac{|n_b|\mu_i}{N|n_i|\mu_b}} \mu_i^2 B^2 \tag{4.37}$$

Since $\mu_i \gg \mu_b$ and $Nn_i \gg n_b$, the prefactor in the high-field case is roughly of order 1. The exact expression is plotted in Figure 4.3 for $n_b = 0.01$ (2% difference in the high mobility electron and hole densities [140, 143]), $\mu_b = 0.05T^{-1}$, and $\mu_i = 5T$ (the latter is roughly what is measured in [9]). As can be seen, the transition region can be subtle and could be masked by other effects like quantum oscillations or changes in scattering rates (which are multiplicative since they enter in the mobility term). A fully accurate model must account for the observed linear Nernst effect [143], which deviates from what typically occurs in semimetallic systems [212]. It will be interesting to extend the black sheep model to thermoelectric phenomena.

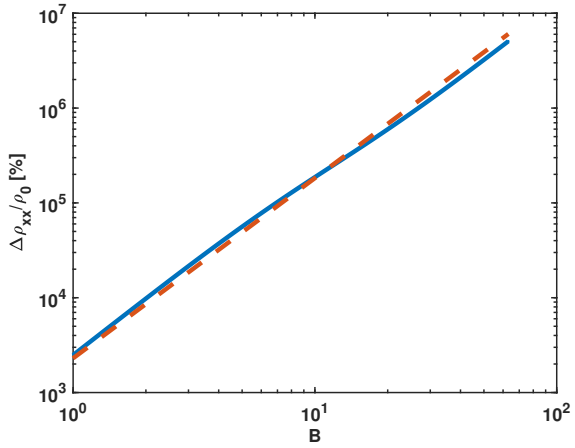

Figure 4.3.: Black sheep model for magnetoresistance, which can give subtle inflections amid generally quadratic magnetoresistance (plot scale and range is modeled after [9]). Blue is the actual model, while the red dashed line represents a simple quadratic.

4.3. Magnetoresistance and Quantum Oscillations of an Electrostatically-Tuned Semimetal-to-Metal Transition in Ultra-Thin WTe_2

This section is a reproduction of a published work [154], with a few modifications to the text to adapt for the structure of this thesis.

4.3.1. Abstract

We report on electronic transport measurements of electrostatically gated nanodevices of the semimetal WTe_2. High mobility metallic behavior is achieved in the 2D limit by encapsulating thin flakes in an inert atmosphere. At low temperatures, we find that a large magnetoresistance can be turned on and off by electrostatically doping the system between a semimetallic state and an electron-only metallic state, respectively. We confirm the nature of the two regimes by analyzing the magnetoresistance and Hall effect with a two-carrier model, as well as by analysis of Shubnikov-de Haas oscillations, both of which indicate depletion of hole carriers via the electrostatic gate. This confirms that semiclassical transport of two oppositely charged carriers accurately describes the exceptional magnetoresistance observed in this material. Finally, we also find that the magnetoresistance power law is sub-quadratic and density-independent, suggesting new physics specifically in the semimetallic regime.

4.3.2. Main Text

The compound WTe_2 bridges both of these phenomena: experimentally it showcases exceptionally large, quadratic magnetoresistance in magnetic fields up to 60T [9, 138], and theoretically it is predicted to be a Weyl semimetal in 3D [153] and near a quantum spin Hall state in 2D [158]. The observed magnetoresistance in bulk samples has been proposed to be the result of near-compensated electron and hole carriers, described by a semiclassical two carrier model [9, 213, 214]. However, a number of questions have been raised regarding the mechanisms at play. First, quantum oscillations revealed multiple Fermi pockets as well as imperfect compensation [143, 139, 211], suggesting other effects may play a role. Moreover, the small Fermi energy and orbital helicity of the Fermi surface suggest that the band structure and scattering mechanisms, respectively, are liable to change under application of a magnetic field [141, 140, 215]. To elucidate the origins of the magnetoresistance, a natural experiment would be to study the effect of changing the carrier density of a thin sample in-situ, which recent transport studies have attempted with varying results [216, 172, 217]. A major difficulty at the ultrathin limit is that sample quality degrades significantly as the thickness is reduced: oxidation induces insulating behavior below 6 layers thick, rendering phenomena related to the high quality bulk crystals inaccessible in the 2D limit [172, 218, 174].

In this Letter, we investigate exfoliated WTe_2 devices that are fabricated in a glove box under inert atmosphere in order to minimize degradation [175]. Doing so enables creation of high quality nanodevices that display the intrinsic physics of the material [219]. At low

temperatures, we use an electrostatic gate to dope the system from a semimetallic regime to a single-carrier regime. During this crossover we observe an evolution of the magnetoresistance and Hall effect that is qualitatively well captured by a semiclassical two-carrier model. We additionally observe that the exponent of the magnetoresistance power law is subquadratic and gate-independent within the semimetallic regime. Finally, the semimetal-to-metal transition is further confirmed by analysis of SdH oscillations, which give insight to the low-energy band structure.

To fabricate the devices, WTe_2 is exfoliated in an argon atmosphere (< 1 ppm oxygen) and then encapsulated between layers of hexagonal Boron Nitride (h-BN) with a polymer pick-up and transfer technique [110]. For the device discussed in the main text, we also include few-layer graphene (FLG) between the WTe_2 and the bottom h-BN layer as an electronic contact. This FLG layer has a natural lateral gap between two independent sheets, which the WTe_2 spans. Finally, we contact the FLG with evaporated Cr-Au via the edge-contact technique [220], and then etch the device into a Hall bar geometry with a reactive ion etch. The FLG serves as an intermediary conductor between the evaporated electrodes and the WTe_2 while also maintaining a good van der Waals seal with the encapsulating h-BN [221]. The device sits on a doped silicon wafer with $285nm$ of thermal SiO_2, which serve as the back-gate electrode and dielectric, respectively. All electronic transport measurements are conducted in a four-probe configuration. An optical micrograph and a schematic cross-section of the device are shown in Fig. 4.4A-B. Here we report on the behavior of a 3-layer thick device (sample A, thickness confirmed by AFM and Raman spectroscopy [172]), and in Appendix D we show data on additional devices.

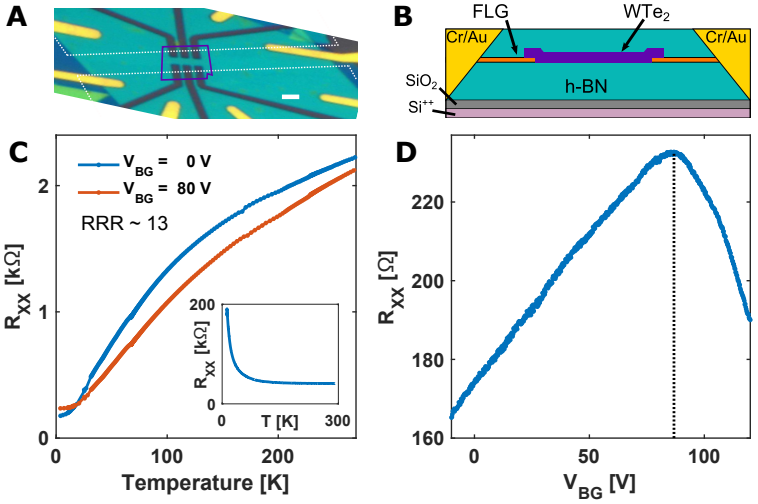

Figure 4.4.: A, Optical image of a completed device. The edges of the original FLG flakes are indicated by dashed white line, and the original boundary of the WTe_2 flake is outlined in purple. The dark regions are where the stack was fully etched to the SiO_2 substrate. Solid white scale bar is 2 microns long. **B,** Cross-sectional schematic of the device structure, with all components labeled. **C,** Temperature dependence of device A at two representative gate voltages. The average RRR for all gate voltages is 13. Inset: Temperature dependence of a similar-thickness WTe_2 device fabricated in air and without encapsulation. **D,** Gate dependence of R_{xx} at $B = 0T$ and $T = 4K$. The vertical dashed line at $V_{BG} = 87$ indicating the resistance maximum.

The first indication that inert atmosphere fabrication maintains crystal integrity is the temperature dependence of the resistance, shown in Fig. 4.4C. We observe metallic behavior with a residual resistivity ratio (RRR) of 13. In contrast, non-encapsulated devices fabricated in air display insulating behavior (inset of Fig. 4.4C). In fact, in the literature a RRR of 13 is only achieved for samples greater than 33nm thick [172]. Applying a bias V_{BG} to the electrostatic gate, we capacitively modulate the carrier density in the sample, finding that the low-temperature resistivity increases linearly with V_{BG} until ~ 87V, beyond which the resistivity drops sharply (see Fig. 4.4D)[4]. The noted metallic temperature dependence with RRR of order 10 is observed for all gate voltages, with two representative gate voltages shown in Fig. 4.4C.

[4]Data in Figure (4.4) are from initial measurements in a 4K probe. Data and analysis in Figure (4.5)B–D are from a second cooldown at 300 mK. All other data and analysis in the main text are from a third cooldown with base temperature of 30 mK.

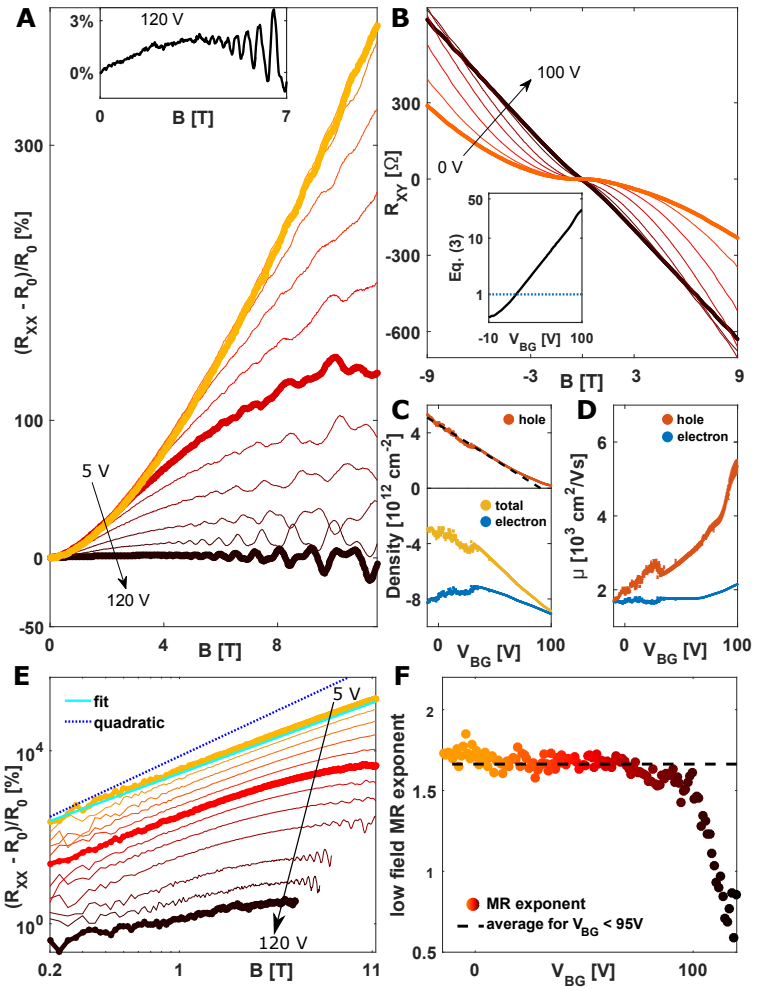

Figure 4.5.: A, MR as a function of magnetic field for a range of V_{BG} at $T = 30mK$. Inset: a zoom-in of the data at $V_{BG} = 120V$. **B,** R_{xy} as a function of magnetic field for a range of V_{BG} at $T = 300mK$, displaying a transition from non-linear to linear Hall effect. Inset: Extracted saturation parameter (equation (4.40)) as a function of gate voltage (black) at $B = 10T$. The blue dotted line is unity. **C,** Individual carrier densities and the total carrier density, including charge sign, from the semiclassical model fit. Black dashed line is an extrapolation of the hole density from the slope at lower gate voltages. **D,** Mobilities from the model fit. Error bars in **C-D** represent 95\% confidence intervals of the fit. **E,** Same data as **A** in log-log format with each curve offset vertically for clarity. The blue dotted line is a quadratic power law, whereas the cyan line is a power law fit to the data at $V_{BG} = 10V$. **F,** The fitted exponent of the MR power law for $B \in [0.4, 1.5]\,T$ as a function of gate voltage. The limits were chosen to avoid the high relative noise at low fields ($B < 0.2T$) and onset of saturation at high field. Dot color corresponds to gate voltage in accordance with **A** and **E**. Dot size is larger than the 95\% confidence interval of the fit. The black dashed line indicates the mean exponent for $V_{BG} < 95V$.

We then measure both the longitudinal (R_{xx}) and transverse (R_{xy}) resistances as a function of magnetic field and gate voltage in order to investigate the magnetoresistance behavior at different total carrier densities. Both measurements are shown in Fig. 4.5A-B for a range of gate voltages, where in Fig 4.5A we plot the magnetoresistance ratio (MR), defined

as $(R_{xx}(B) - R_{xx}(0))/R_{xx}(0)$. The MR shows a clear transition from strong, superlinear behavior near zero gate voltage ($\sim 400\%$ increase at 11.5T) to suppressed MR ($< 3\%$) at the highest gate voltage (inset of Fig. 4.5A). During the crossover at intermediate gate voltages, we find that R_{xx} saturates at large B, as expected for a non-compensated semimetal [222, 181]. Importantly, we observe that this crossover coincides with the Hall effect transitioning from nonlinear to linear magnetic field dependence, indicating a transition from two carrier types to a single carrier type.

To investigate this behavior in more detail, we employ the semiclassical two-carrier model, which gives the following equations for the longitudinal and transverse resistivity of a semimetal:

$$\rho_{xx} = \frac{1}{e}\frac{n\mu_n + p\mu_p + (n\mu_p + p\mu_n)\,\mu_n\mu_p B^2}{(n\mu_n + p\mu_p)^2 + (p-n)^2\,\mu_n^2\mu_p^2 B^2} \tag{4.38}$$

$$\rho_{xy} = \frac{1}{e}\frac{\left(p\mu_p^2 - n\mu_n^2\right)B + (p-n)\,\mu_n^2\mu_p^2 B^3}{(n\mu_n + p\mu_p)^2 + (p-n)^2\,\mu_n^2\mu_p^2 B^2} \tag{4.39}$$

which include the electron charge e and four free parameters: the density (n, p) and mobility ($\mu_{n,p}$) of each carrier type, where n and p refer to electron-like and hole-like carriers, respectively. We fit $R_{xx}(B)$ and $R_{xy}(B)$ simultaneously to extract all four quantities at each gate voltage. (Here we constrain the electron density based on the SdH analysis presented below, but the important qualitative behavior doesn't require this. See Appendix D for details.) The fit parameters are plotted as a function of V_{BG} in Fig. 4.5C-D. Most notably, we find that the hole density decreases monotonically to nearly zero at $V_{BG} \sim 100V$, consistent with our earlier, qualitative interpretation of the data.

We highlight now a particular aspect of the semiclassical model regarding the onset of saturation (or absence thereof). The condition for onset of significant saturation in the MR is given by the ratio of the two terms in the denominator of equation (4.38):

$$\frac{(p-n)^2\mu_n^2\mu_p^2 B^2}{(n\mu_n + p\mu_p)^2} \sim 1, \tag{4.40}$$

which is plotted in the inset to Fig. 4.5B for $B = 10T$. This condition is satisfied for $V_{BG} > 22V$, around which gate voltage we see the onset of saturation in the MR. The ratio is greater than 10 for $V_{BG} > 70V$ for which gate voltages we observe near complete saturation at high magnetic field. When seemingly unsaturating MR is observed in a semimetal, equation (4.40) can set a bound for the degree of non-compensation. For example, Ali, et al, [9] measure effectively no saturation in bulk WTe_2 in fields up to 60T. From this and the mobility (which sets the magnitude of the MR), one may estimate an upper bound for the relative carrier density difference $\left|\frac{n-p}{n+p}\right| \lesssim 0.3\%$, which is an order of magnitude smaller than that estimated from SdH measurements of the bulk Fermi surface [143, 140]. This suggests that other factors may be involved in avoiding saturation at the highest fields for 3D samples [216]. A possible avenue would be to investigate the role of mobility anisotropies, known to be important in bismuth [183]. Nonetheless, for the range of magnetic fields studied here, our

analysis confirms that the large MR observed in WTe_2 is rooted in the near-compensation of electron and hole densities.

Upon closer examination of our data, we find that the MR is actually sub-quadratic[5]. We can see this clearly by looking at the data in log-log format, as shown in Figure 4.5E. An explicit fit of the power law gives an exponent near 1.6, which is consistent for sample A in two different cooldowns as well as for additional devices presented in Appendix D. The exponent is stable for nearly all gate voltages for all devices, except above $V_{BG} \sim 100V$ for sample A, beyond which the exponent drops rapidly (Fig. 4.5F). This drop-off coincides with the indications of depletion of the holes, reinforcing that the MR can be understood as that of a standard semimetal with a correction to the exponent.

The origin of the correction to the exponent is as yet unclear. Many studies on bulk WTe_2 have noted a large, quadratic MR [9, 211, 140, 143, 172, 217, 223], but some that explicitly fit the power law also find sub-quadratic exponents [142, 216]. While we observe a similar deviation, our sample is in the 2D limit, whereas the Fermi surface of bulk WTe_2 is 3D in character [143, 140], suggesting that dimensionality is not a driving factor. Additionally, we find that the power law is density-independent in the semimetallic regime, and almost no MR is observed in the electron-only regime. This suggests that the coexistence of electrons and holes is crucial. One might look to semimetallic Boltzmann transport models which predict that boundary effects can generate linear MR when the valley recombination length is comparable to the transport channel widths [213, 214], but this requires classically strong magnetic fields not present here ($\mu_{n,p}B \lesssim 3$ for this work). Inter-species drag effects may also play a role in magnetoresistance [224], but finite inter-valley scattering should suppress such physics. The question of the unusual magnetoresistance poses an experimental and theoretical challenge for future investigation.

[5] While the non-parabolicity of the low-field MR may introduce a systematic error to the fits by the semi-classical MR equations, it does not change the qualitative behavior of the fit parameters nor our general conclusions – similar behavior is observed when fitting the Hall data with a constraint given only by the zero-field longitudinal resistance (see Appendix D for details). Lacking a physical model for the modified power law, we choose not to artificially alter the two-carrier model for the fits.

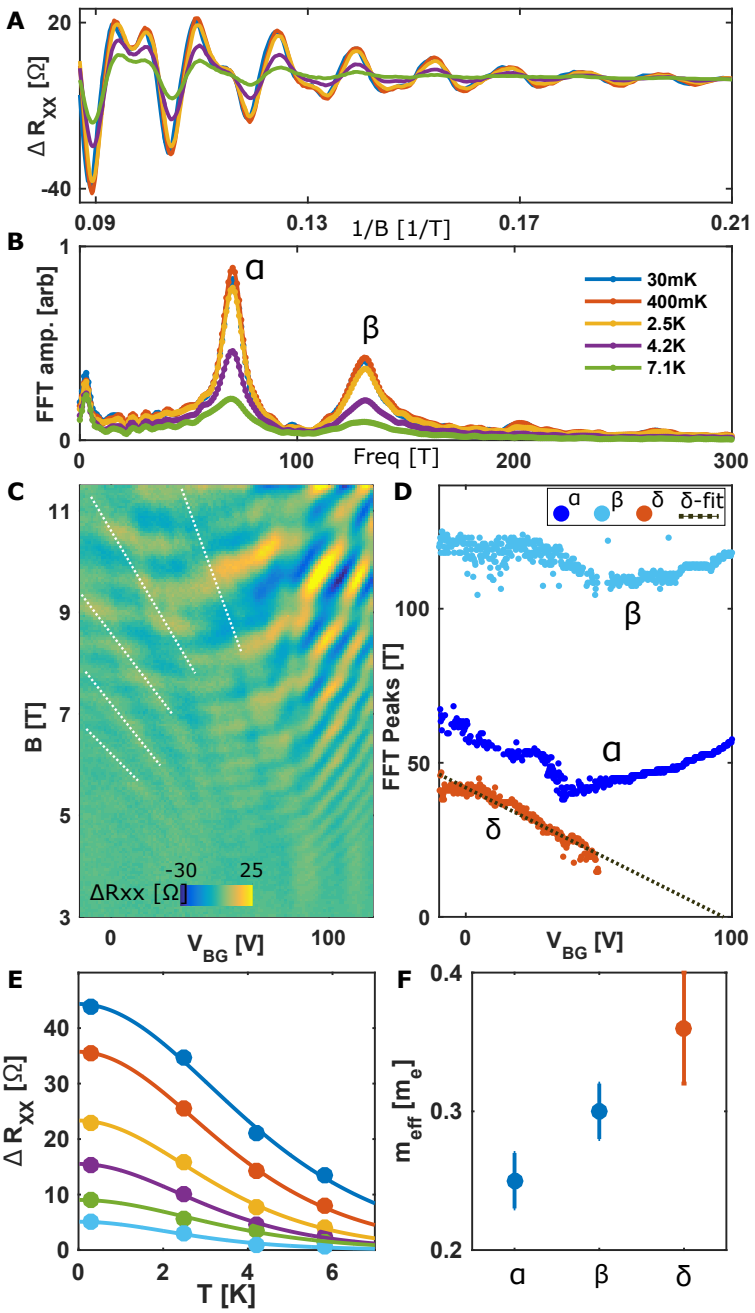

Figure 4.6.: A, SdH oscillations in $\Delta R_{xx}(1/B)$ at different temperatures and **B,** their fast Fourier transforms (FFTs) at $V_{BG} = 120V$. **C,** Gate- and field-dependence of ΔR_{xx} at $T = 30mK$. White dotted lines guide the eye to the δ pocket oscillation. **D,** FFT peak frequencies (dots) at each gate voltage, and extrapolation of the δ frequency to zero (dotted line). **E,** Temperature dependence of ΔR_{xx} maxima associated with the α pocket at $V_{BG} = 120V$. **F,** Effective mass of each pocket, from fits such as in **E** (see Appendix D for more details).

We now turn to analysis of the quantum oscillations. In Fig. 4.6A we show representative measurements of $\Delta R_{xx}(1/B)$, the resistivity after subtracting a smooth quadratic background above 2 T, in the electron-only regime ($V_{BG} = 120V$). At this gate voltage, two

oscillations are clearly visible, confirmed by the two peaks visible in the Fourier transform of the data in Fig. 4.6B, which we label α and β. In Fig. 4.6C we show a map of ΔR_{xx} with respect to both B and V_{BG}. A third, hole-like dispersing oscillation is additionally visible for lower gate voltages (highlighted by dotted white lines), which we label δ. This is made clearer by fast Fourier transform (FFT) analysis, as shown in Figure 4.6D where the three observed peak frequencies are tracked as a function of gate voltage. The α and β frequencies disperse weakly with gate voltage in a very similar manner as the electron carrier density from the semiclassical analysis. The non-monotonic gate dependence of the electron bands is likely the result of strong electric field effects, which can be explored in future devices employing a dual-gate geometry [158, 225]. The third oscillation frequency, δ, decreases monotonically with increasing gate voltage, which we can extrapolate to zero frequency (full depletion) at roughly $V_{BG} = 90V$. This depletion voltage agrees with what is found for the positive charge carriers in the semiclassical analysis, so we ascribe the δ pocket to a valence band. Curiously, this depletion also coincides with a peak in the amplitude of the SdH oscillations of the α and β pockets (see Fig. 4.6C), suggesting that scattering between the electron and hole valleys is important.

We also conduct temperature dependence of the SdH oscillations. Fitting the Lifshitz-Kosevich formula to the temperature dependence of resistance oscillation maxima allows for extraction of the effective mass. In multi-band systems care must be taken to extract the oscillation amplitude of an individual frequency, which can be done by an appropriate FFT analysis (see Appendix D for more details). An example fit for the α pocket oscillation is shown in Fig. 4.6E, giving $m_\alpha/m_e = 0.25 \pm 0.02$, where m_e is the bare electron mass. Similar analysis for the other bands give $m_\beta/m_e = 0.30 \pm 0.02$ and $m_\delta/m_e = 0.36 \pm 0.04$ (see Fig. 4.6F and Appendix D)[6]. These values are somewhat smaller than those reported for bulk crystals, which range from 0.3 to 1 m_e [223, 143]. The electron effective masses are in good agreement with theory for the monolayer, while the hole mass is again smaller than that prediction by about a factor of two[171] . We note that explicit predictions for few-layer WTe_2 have not yet been made.

In summary, we investigated electronic transport in encapsulated, ultra-thin WTe_2. We find that a strong, intrinsic MR can be turned off by electrostatically doping the sample from a semimetallic state to an electron-only regime. We confirm the basis of the two regimes by simultaneously analyzing the MR and the Hall effect with a two-carrier model as well as by analysis of Shubnikov-de Haas oscillations, both of which indicate depletion of hole-like carriers in the suppressed-MR regime. These observations confirm that the MR in WTe_2 is qualitatively explained by semiclassical transport of a semimetal, with potentially new physics in a modified exponent to the MR power law.

4.3.2.1. Acknowledgments

This work was partly supported by the DOE, Basic Energy Sciences Office, Division of Materials Sciences and Engineering, under award DE-SC0006418 (sample fabrication and

[6]Fits to the temperature dependence of multiple resistance maxima at several (nearby) gate voltages are averaged to obtain the mean effective mass. At least 20 different fits are made for each Fermi pocket.

measurements), and partly through AFOSR grant FA9550-16-1-0382 (data analysis), as well as the Gordon and Betty Moore Foundation's EPiQS Initiative through Grant GBMF4541 to PJH. Crystal growth at Princeton University was supported by the NSF MRSEC program grant DMR-1005438. This work made use of the Materials Research Science and Engineering Center Shared Experimental Facilities supported by NSF under award DMR-0819762. Sample fabrication was performed partly at the Harvard Center for Nanoscale Science supported by the NSF under grant no. ECS-0335765. We thank E. Navarro-Moratalla, J. D. Sanchez-Yamagishi, and L. Bretheau for discussions and Sanfeng Wu for help with crystal exfoliation.

4.4. Concluding Note on the Electron Valley Splitting

I include here a final note on the two apparent electron-like pockets observed in the SdH oscillations. Given the experimental measurement of both the effective masses and Fermi surface areas (see Figure 4.6), we can estimate the valley splitting of the WTe_2 trilayer, which could serve as a point of comparison for future studies on ultrathin WTe_2. We use the effective mass approximation for each pocket:

$$E_F^{(i)} = \frac{\hbar^2 k_F^{(i)}}{2m_{eff}^{(i)}} \tag{4.41}$$

$$= \frac{\hbar^2 A_F^{(i)}}{2\pi m_{eff}^{(i)}} \tag{4.42}$$

where $(i) = (\alpha),\ (\beta)$ refers to the case of the α and β pockets, respectively, and A_F refers to the Fermi surface area. We can convert SdH oscillation frequency to Fermi surface area by the following relationship:

$$A_F^{(i)} = \frac{2\pi e}{\hbar} f^{(i)} \tag{4.43}$$

thus giving

$$E_F^{(i)} = \hbar e \frac{f_F^{(i)}}{m_{eff}^{(i)}}. \tag{4.44}$$

Plugging in the measured numbers in Figure 4.6, we estimate $E_F^{(\alpha)} \sim 28$ meV and $E_F^{(\beta)} \sim 46$ meV. This suggests a splitting of around 20 meV, which is possibly a spin-orbit splitting [140].

5. Topological Insulator

5.1. Overview

After the study of the 2D semimetallic state in trilayer WTe_2, but prior to the work detailed in this chapter, a few important experimental studies were published. Key among these was the study from the University of Washington, which found a true transport gap in the interior of exfoliated monolayer flakes [226]. (This study also confirms a metallic phase for the trilayer, although does not report on magnetoresistance.) Additionally, spectroscopy studies of MBE grown thin films explicitly measured band gaps in the 40-50 meV range [8, 157]. These important papers established that monolayer WTe_2 indeed exhibits a fully developed band gap, which makes possible the detection of the predicted helical edge modes.

Moreover, Fei, et al, found that exfoliated monolayers do exhibit finite edge conduction, coming to within a half of the value expected for a ballistic edge mode [226]. Their study also revealed some challenges to overcome in the effort to observe edge conductance near the quantized value. First, in quasi-two-terminal geometries the differential resistance is highly nonlinear. This leads to some confusion regarding the true value of the edge conductance – is it the zero bias value (as suggested by Figure 4d of that paper) or the finite bias value (as suggested by Figure 1f)? Ideally, ohmic contacts would be achieved to avoid this ambiguity. Second, immediately adjacent to each contact there exists a "tented" region which is susceptible to degradation, as the WTe_2 has an open face there. For a 20 nm tall metal electrode, the tented length can be of order 100 nm. Figure 5.1 shows, to scale, roughly the size of this gap as compared with typical air molecule density, showing that air molecules have plenty of access to the exposed region. Uncontrolled degradation in the tented region could lead to backscattering in the edge. Ideally one would measure a length of the edge that is in a uniform, fully encapsulated environment. These considerations motivated the device geometry and fabrication scheme described in detail in Section 5.2 and Appendix E.

5.2. Observation of the Quantum Spin Hall Effect up to 100 Kelvin in a Monolayer Crystal

This section is a reproduction of a soon-to-be-published work [227], with a few modifications to the text to adapt for the structure of this thesis.

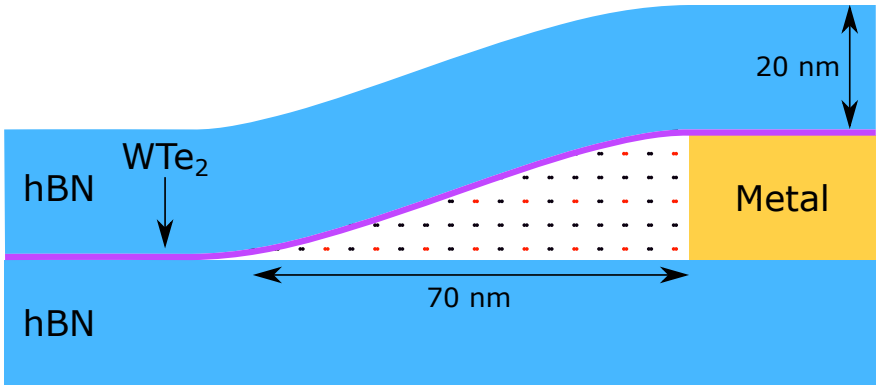

Figure 5.1.: To-scale, cross-sectional schematic of the tenting effect of hBN as it comes down off of a 20nm tall electrode. The typical contact angle at the substrate is ~ 16 degrees, resulting in roughly a 70nm "tent zone". Nitrogen (black) and oxygen (red) molecules (drawn at ~ 4 times their actual size for visibility) are placed on a grid of 4 nm spacing, which is roughly the intermolecular spacing of molecules in air. It is clear that many molecules easily fit into the gap.

5.2.1. Abstract

The field of topological insulators (TI) was sparked by the prediction of the quantum spin Hall effect (QSHE) in time reversal invariant systems, such as spin-orbit coupled monolayer graphene. Ever since, a variety of monolayer crystals have been proposed as two-dimensional (2D) TIs exhibiting the QSHE, possibly even at high temperatures. However, conclusive evidence for a monolayer QSHE is still lacking, and systems based on semiconductor heterostructures operate at temperatures close to liquid helium. Here we report the observation of the QSHE in monolayer WTe_2 at temperatures up to 100 Kelvin. The monolayer exhibits the hallmark quantized transport conductance, e^2/h per edge, in the short edge limit. Moreover, a magnetic field suppresses the conductance, and the observed Zeeman-type gap indicates the existence of a Kramers degenerate point, demonstrating the importance of time reversal symmetry for protection from elastic backscattering. Our results establish the high-temperature QSHE and open a new realm for the discovery of topological phases based on 2D crystals.

5.2.2. Main Text

A time-reversal (TR) invariant topological insulator (TI) in two dimensions (2D), also known as a quantum spin Hall (QSH) insulator, can be identified by its unique helical edge modes [228, 229, 27, 28]. So far, evidence for the helical edge mode in 2D TIs, particularly quantized transport, has been limited to very low temperatures (i.e. near liquid helium temperature) in HgTe and InAs/GaSb quantum wells [40, 230]. In the search for high temperature TIs, substantial efforts have focused on a variety of atomically thin materials [231, 232, 158, 233, 234, 175, 8, 157, 128], which have the additional promise of advancing the field of topological physics using the tools developed for 2D crystals. However, experimental observation of the quantum spin Hall effect (QSHE) in monolayer systems is challenging, often due to structural or chemical instabilities [158, 235, 172, 174]. Indications of a high temperature

QSH phase in bulk-attached bismuth bilayers have been reported [231, 236, 237], but a conclusive demonstration is still lacking.

Among the proposals for atomically thin TIs are monolayer transition metal dichalcogenides (TMDs), materials that are either 2D semiconductors or semimetals depending on their structural phase [158]. Calculations suggest that an inverted band gap can develop in 1T' TMD monolayers, resulting in a nontrivial Z2 topological phase [158, 162]. Recent experiments have shown promising results [175, 8, 157], including that 1T' monolayer WTe_2 exhibits a ground state with an insulating interior and conducting edges associated with a zero-bias anomaly [175], distinct from its multilayer counterparts [175, 154]. However, the QSHE, the hallmark of a 2D TI, has yet to be observed, and hence its topological nature is far from conclusive. Here we observe the QSHE in WTe_2 monolayers and identify this 2D material as an atomically layered TI with conductance $\sim e^2/h$ per edge at high-temperatures.

QSH transport through a 2D TR-invariant TI should exhibit the following characteristics: (a) helical edge modes, characterized by an edge conductance that is approximately the quantum value of e^2/h per edge [40]; (b) saturation to the conductance quantum in the short edge limit [238]; and (c) suppression of conductance quantization upon application of a magnetic field, due to the loss of protection by TR symmetry [40, 239, 240]. Signatures of a Zeeman gap should be seen if the Kramers degeneracy (Dirac point) is located inside the bulk band gap. To date, simultaneous observation of the above criteria in existing 2D TI systems is still lacking [40, 230, 238, 239, 241], prompting the search for new QSH materials.

To check the above criteria in monolayer WTe_2, we fabricated devices with the structure depicted in Fig. 5.2A (see also Fig. E.1, E.2, and Materials & Methods). The goal of the design has three objectives: (1) ensure an atomically flat, chemically protected channel (no flake bending or exposure) by fully encapsulating the flake with hexagonal boron nitride [235, 154]; (2) minimize the effect of contact resistance; and (3) enable a length-dependence study on a single device. Our devices generally consist of eight contact electrodes, a top graphite gate, and a series of in-channel local bottom gates with width L_c varying from 50 nm to 900 nm. The monolayer flakes are carefully selected to have a long strip shape, typically a few μm wide and about ten μm long (Table E.1). Fig. 5.2B shows a typical measurement of the four-probe conductance (in Device 1) across all the local gates (~ 8 μm long) as a function of top gate voltage, V_{tg}. A finite conductance plateau develops around V_{tg} = 0 V. This characteristic feature for monolayer WTe_2 is due to conduction along the edges [175]. The measured value is highly sensitive to (typically poor) contact properties [175], which prevents observation of the intrinsic edge conductance. We overcome this obstacle in our devices through selective doping of the flake using a combination of global top and local bottom gates. A short transport channel with length L_c can be selectively defined by a local gate voltage V_c, while the rest of the flake is highly doped by V_{tg} to secure good contact to the electrodes (see Fig. E.3 for dI/dV characteristics). Figure 5.2C maps out the resistance R in the same device as a function of V_{tg} and V_c (for a local gate with L_c =100 nm). The step structure indicates a transition from a bulk-metallic state (doped) to a bulk-insulating state (undoped) within the locally gated region. We define the offset resistance, $\Delta R = R(V_c) - R(V_c = -1V)$, as the resistance change from the value in the highly doped limit (V_c = -1V in this case). Figure 5.2D shows a ΔR trace (red curve) extracted from Fig 5.2C (dashed white line in Fig. 5.2C), where V_{tg} is fixed at 3.5 V. The average value of

ΔR at the plateau, which measures the step height, saturates when V_{tg} is high enough (Fig. 5.2D inset and Fig. E.4-E.7).

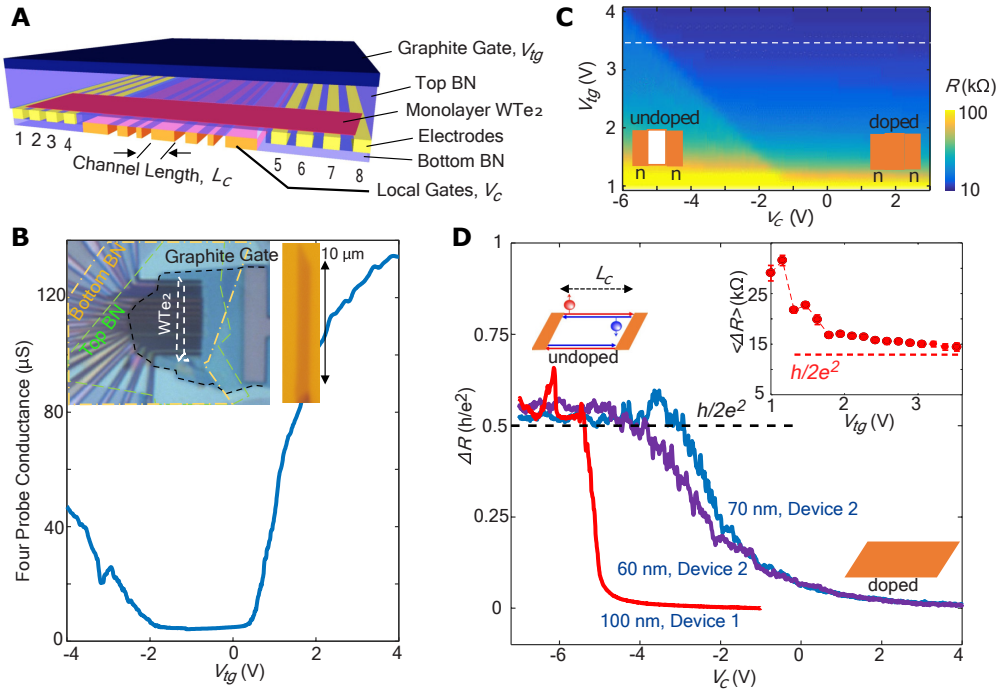

Figure 5.2.: Device structure and resistance near $h/2e^2$. **A,** Schematic of the device structure. **B,** Four probe conductance measurement at 4 K of Device 1 as a function of V_{tg} across all the local gates, which are floating. Inset: the optical image of Device 1 (left) and the corresponding monolayer WTe_2 flake before fabrication (right). **C,** Color map of the flake resistance tuned by V_{tg} and the 100nm-wide local gate V_c at 4K. Two regions are separated by a step in the resistance distinguishing the doped and undoped local channel, as depicted by the inset schematics. **D,** ΔR versus V_c for the 100 nm wide gate on Device 1 at $V_{tg} = 3.5$V, and the 60 and 70 nm wide gates on Device 2 at $V_{tg} = 4.1$V (taken at 5 K). For clarity, the two curves from Device 2 are offset by +3 V along the x axis. Inset: the average step height $\langle \Delta R \rangle$, extracted from **C**, as a function of V_{tg}, showing a clear saturation towards $h/2e^2$ for large V_{tg}.

This saturated value, ΔR_s, thus measures the resistance of the undoped channel, which can only originate from the edges, because the bulk is insulating. Notably, ΔR_s is approximately equal to $h/2e^2$ for both this 100 nm channel and the 60 nm and 70 nm channels on Device 2 (Fig. 5.2D). Fluctuations in the range of few kΩ, which may originate from residual disorder or correlation effects [242, 243, 175, 244], are visible but decrease substantially above 4K. Given that the sample has two edges, the observed conductance per edge is therefore $\sim e^2/h$, pointing to helical edge modes as the source of the conductance [40, 230]. In order to confirm this scenario, one must rule out the possibility of trivial diffusive edge modes that happen to exhibit the quantized conductance value for some particular length [238]. We thus performed a length dependence study utilizing a series of local gates with different L_c. Detailed analysis of measurements from representative devices and gates at $\sim$ 4 K can be found in Figs. E.4-E.6. In Fig. 5.3 we summarize the data by plotting the undoped channel resistance, ΔR_s, as a function of L_c. For long edges the resistance generally decreases with

decreasing length, which is arguably captured by a linear trend. The behavior, however, clearly deviates from the trend when L_c is reduced to 100 nm or less, where the resistance saturates to a value close to $h/2e^2$. Such behavior is present in all three devices that enter this short-length regime, independent of the width of the monolayer flake (varying from 1 to 4 µm). These observations reveal the intrinsic conductance as e^2/h per edge as per the above-mentioned criteria (a) and (b) for the QSHE.

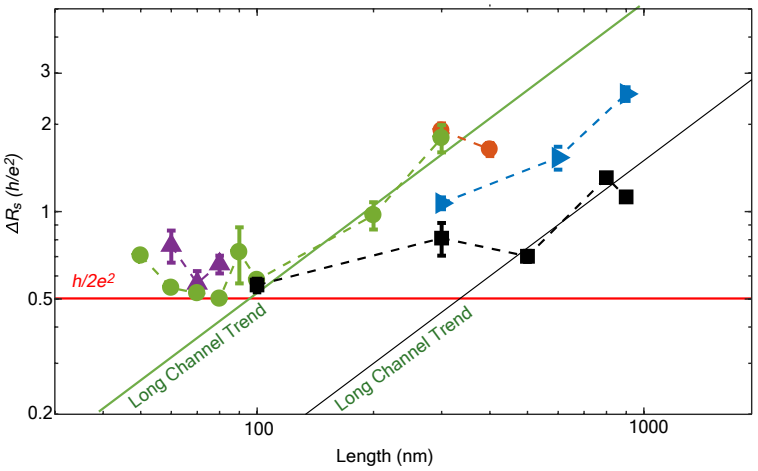

Figure 5.3.: Length dependence of the undoped channel resistance. Data taken at 4 K from 5 different devices (Table E.1), each denoted by a different color and symbol. The device numbers and associated colors are: 1, Black; 2, green; 3, purple; 4, red; 5, blue. The ΔRs values reach a minimum of $h/2e^2$ in the short-channel limit on one sample, and approach this value in other samples, confirming a conductance of $2e^2/h$ for the undoped channel, i.e. a conductance of e^2/h per each edge of the device, in agreement with QSHE. Detailed analysis of raw data can be found in Fig. E.4-E.7.

To check criterion (c), regarding TR symmetry protection from elastic scattering, we performed magneto-conductance measurements. The data taken from the 100 nm long channel in Device 1 in the QSHE regime (i.e. gate range on plateau) is shown in Fig. 5.4. We define G_s as $1/\Delta R_s$„ which measures the conductance of the edges in the short channel limit. G_s is plotted as a function of V_c in Fig. 5.4A for a series of magnetic fields B applied perpendicular to the monolayer at 1.6 K. G_s decreases significantly once B is turned on, in contrast to the bulk state which is hardly affected (Fig. E.8). For all V_c, G_s decreases rapidly for low magnetic fields ($B < 2$T). After this initial stage, two types of behavior are observed, depending on V_c, as shown in Fig. 5.4B. When V_c is near -6.44V, G_s decreases exponentially, without saturation up to 8 T. For other values of V_c, G_s saturates at high B. These behaviors are significantly different from the previous observations for resistive channels [238].

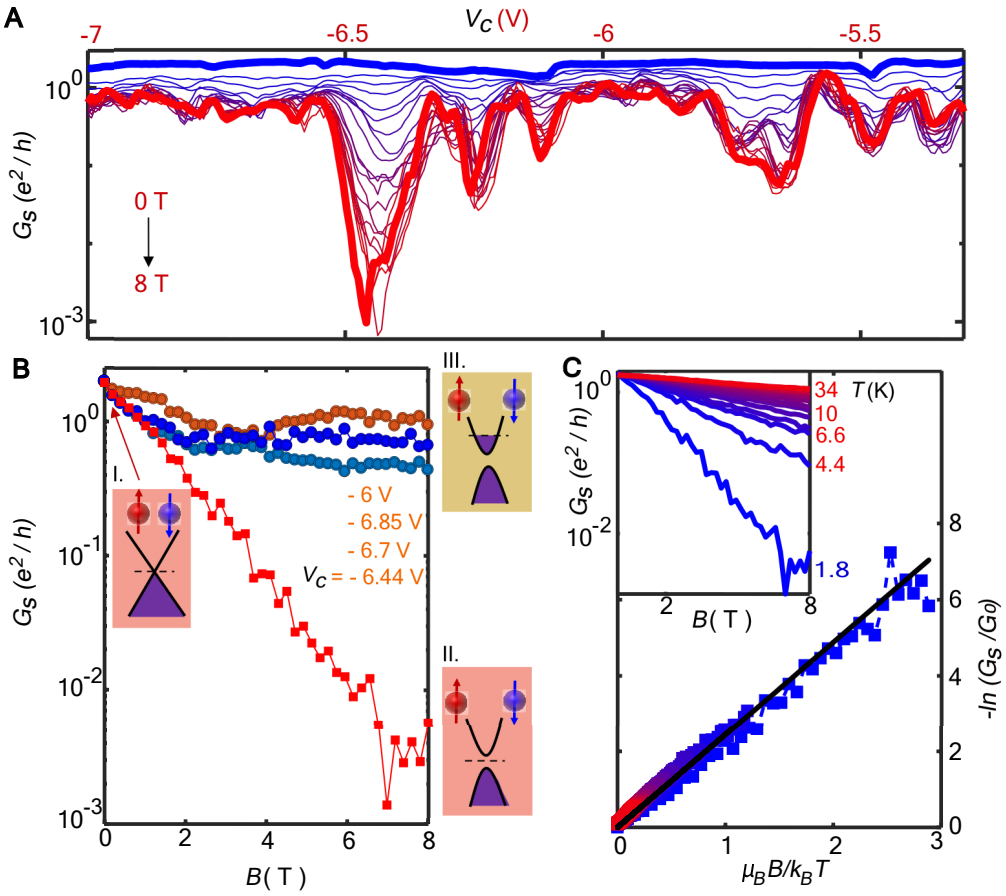

Figure 5.4.: Time reversal symmetry breaking by a magnetic field and Zeeman-like gap at the Dirac point. **A,** The evolution of the edges conductance G_s versus gate under the application of a perpendicular magnetic field, B (from 0T, thick blue curve, to 8T, thick red curve) at 1.8K, for Device 1, 100 nm channel. **B,** Traces of G_s vs. B for a few selected local gate voltages V_c showing two types of behavior: saturation and non-saturation, associated with whether or not the Fermi energy is in the Zeeman gap, as depicted in the band schematics a. (linear bands at zero B, E_F at Dirac point), b. (gapped bands at finite B, E_F at Dirac point), and c. (gapped bands at finite B, E_F away from Dirac point). **C,** Inset: temperature dependence of G_s vs. B for the non-saturating curves (V_c = -6.44V). Main: All the curves in the inset collapse to a single trend in the normalized plot of $-\log(G_s/G_0)$ vs $\mu_B B/k_B T$. The black line is a linear fit. Additional inspection of the temperature- and magnetic-field dependence is shown in Fig. E.9-E.11.

Both types of behavior can be understood in the context of the QSHE. The 1D edge state of the QSH phase consists of two species: left and right movers associated with opposite spin polarization. The two linearly dispersing bands cross at the Kramers degeneracy point (Fig 5.4B, panel a). Magnetic fields applied nonparallel to the spin polarization are expected to open an energy gap at the Kramers point due to the Zeeman effect [245]. For a homogeneous chemical potential close to the degeneracy point (Fig 5.4B, panel b), one would expect an exponential decay of the conductance without saturation. To reveal the existence of the gap, we performed temperature dependence measurements of the magneto-conductance at

V_c = -6.44 V. The exponential decay of G_s persists up to high temperatures (measured up to 34 K, inset of Fig. 5.4C). Moreover, all the curves collapse onto a single universal trend when renormalized by plotting the dimensionless values $-\log(G_s/G_0)$ vs $\mu_B B/k_B T$ (Fig. 5.4C), where G_0 is the zero-field conductance, μ_B is the Bohr magneton, k_B is the Boltzmann constant, and T is the temperature. The slope of the trend yields an effective g-factor $\sim$ 4.8 for the out-of-plane field in this device (i.e. the device conductance obeys $G_s = G_0 \exp(-g\mu_B B/2k_B T)$. This observation confirms a Zeeman-type gap opening in the edge bands.

If the Fermi energy at the edge is gated away from the Kramers point (Fig 5.4B, panel c), the Zeeman gap will not be directly observed, and the magneto-conductance should be determined by the scattering mechanisms at the edge allowed by the TR symmetry breaking. For example, in our devices the presence of local charge puddles can be natural. According to theoretical calculations, the edge conductance will be reduced to $\alpha e^2/h$, where α is determined by the microscopic details of the edge [240, 246]. Calculations show that at high magnetic fields an individual puddle can reduce transmission along an edge by 50% [240, 247], leading to a saturated α determined by the distribution of the puddles along the edges. We find the conductance saturation is consistent with this picture (Fig. E.9). In addition to vertical magnetic fields, we have also found significantly reduced edge conductance when in-plane magnetic field is applied (Fig. E.10). In general, we expect that both in- and out-of-plane magnetic fields suppress the conductance because that the time reversal symmetry is broken such that the edge conduction is no longer protected and that the edge spin polarization is not necessarily normal nor parallel to the layer due to the lack of out-of-plane mirror symmetry in the monolayer. The exact spin polarization vector is determined by multiple factors, such as the direction of the crystallographic cut, the chemical termination (e.g. W or Te termination), and the existence of displacement electric fields. The irregular edge of the exfoliated monolayer further complicates the situation. Overall, the magneto-conductance behavior reveals the expected necessity of TR symmetry for the QSHE to take place, and thus confirms criterion (c). Therefore, the QSHE is indeed observed in monolayer WTe_2.

Remarkably, the distinctive conductance value survives up to high temperatures. Figure 5.5A plots the temperature dependence of G_s at different V_c in the QSHE regime; G_s stays approximately constant and close to $2e^2/h$ up to 100 K, indicating that the conductance is dominated by the QSHE up to those temperatures. In terms of ΔR, the resistance plateau starts to drop at around 100 K (Fig. 5.5A inset). The fact that the edge conductance persists up to such high temperatures may indicate that inelastic processes are not important backscattering mechanisms for the edge mode. Above this temperature, the channel conductance increases rapidly with temperature, indicating the activation of bulk conduction channels. To reveal the transition more clearly, in Fig. 5.5B we plot the temperature dependence of the resistance R of the whole flake (i.e. entire length, which consists of locally gated region in series with the rest of the flake) when the Fermi energy in the local channel is placed in the metallic regime (V_c = -1V) and the QSH regime ($V_c <$ -5.3V). A clear kink at 100 K can be seen in the QSH regime. The difference between the two curves yields the channel resistance which drops above the transition temperature.

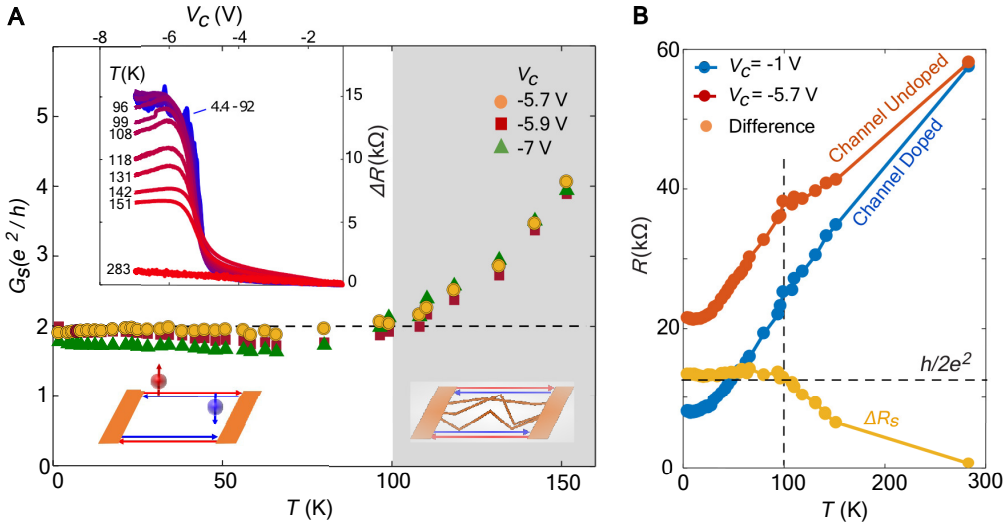

Figure 5.5.: A, Temperature dependence of the edges conductance at a few representative gate voltages for 100 nm channel in Device 1. The conductance is dominated by the QSHE up to about 100K. The schematics depict the increase of the conductance due to onset of conduction from bulk states. Inset: gate dependence of ΔR at various temperatures. **B,** Temperature dependence of the resistance of the whole flake (full length), when the Fermi energy in the local channel is in the doped (V_c = -1V, red) and undoped (V_c = -5.7V, blue) regimes, at V_{tg} = 3.5V. The difference between the curves yields the temperature dependent channel resistance ΔRs (yellow). The vertical dashed line highlights the kink in the undoped regime at 100K, indicating the transition to the QSHE edge-dominated regime.

This high temperature QSHE is consistent with the prediction of a large inverted band gap (~100 meV) in monolayer WTe_2 [162] as well as recent experiments that observe a ~ 45 meV bulk band gap in spectroscopy [8, 157] and a similar onset temperature for bulk conduction [175]. We suspect the 100 K transition temperature may not be an intrinsic limit. Improvements in device quality may enable observation of the QSHE at even higher temperatures and for longer edges.

Our observations have confirmed the nontrivial TR invariant topological phase in monolayer WTe_2 and have demonstrated the QSHE at high temperatures for the first time in an isolated 2D monolayer device. The exploration of 2D topological physics and device performance above liquid nitrogen temperatures has therefore become possible. Distinct from quantum well systems, the exposed nature of isolated monolayers may allow to engineer topological phases in unprecedented ways. In particular, WTe_2 can be readily combined with other 2D materials to form novel van der Waals heterostructures, a promising platform for studying the proximity effect between a QSH system and superconductors or magnets [27, 28] at the atomic scale.

5.2.3. Acknowledgments

We thank Liang Fu for helpful discussions. This work was partly supported through AFOSR Grant No. FA9550-16-1-0382 as well as the Gordon and Betty Moore Foundation's EPiQS

Initiative through Grant No. GBMF4541 to P. J-H. Device nanofabrication was partly supported by the Center for Excitonics, an Energy Frontier Research Center funded by the DOE, Basic Energy Sciences Office, under Award No. DE-SC0001088. This work made use of the Materials Research Science and Engineering Center's Shared Experimental Facilities supported by NSF under Award No. DMR-0819762. Sample fabrication was performed partly at the Harvard Center for Nanoscale Science supported by the NSF under Grant No. ECS-0335765. S.W. acknowledges the support of the MIT Pappalardo Fellowship in Physics. The WTe_2 crystal growth performed at Princeton University was supported by an NSF MRSEC grant, DMR-1420541. Growth of hexagonal boron nitride crystals was supported by the Elemental Strategy Initiative conducted by the MEXT, Japan and JSPS KAKENHI Grant Numbers JP15K21722 and JP25106006.

5.3. On the Imperfection of 2D TI Edge Modes

Section 5.2 details a number of important comparisons between monolayer WTe_2 and the preexisting 2D TI platforms. Important among these is the larger band gap, which we show allows for transport near the quantum of conductance well above liquid helium temperatures, unlike the case for other 2D TIs [40, 230]. A particularly interesting question regards mean free path of electrons in helical edge modes.

The first point of comparison is with quantum Hall systems. Quantized conductance (either in Hall conductance or two-terminal longitudinal conductance) due to quantum Hall edge modes has been established at the millimeter length scale from the first discoveries [32, 248]. Recently centimeter scale quantum Hall effect was achieved in graphene-based devices as well [249]. This occurs because only states with a single group velocity are available local to the edge[1]. A backscattering event would require transporting the electron from one edge of the sample, across the entire bulk, to the other edge, in order to access states with opposite group velocity.

In contrast, 2D topological insulators host counter-propagating modes at the same location in space. Protection from backscattering comes from the fact that the wavefunctions of the counter-propagating states have exactly zero inner product, e.g. the matrix element for elastic scattering processes is exactly zero. Inelastic scattering is allowed but is also expected to be absent at zero temperature[2] [242] . Unfortunately, in experimental systems, helical edge modes are ballistic at length scales three orders of magnitude shorter than in typical quantum Hall systems. To my knowledge, the longest measured helical edge to date is 16 microns, accomplished in a helical state engineered out of the quantum Hall states of a twisted bilayer graphene heterostructure [59][3]. In existing time-reversal invariant 2D TIs, the maximal ballistic length scale is a few microns for both HgTe- and InAs/GaSb-based systems [250, 251, 247, 40, 252, 253, 241]. This length scale happens to be comparable

[1] Actually, edge reconstruction effects can break such intuition, but this is subtlety unimportant for our discussion.

[2] An exception is for the impact of the Kondo effect on a strongly interacting 1D state [243].

[3] The is however just a lower bound. It would be quite interesting to extend study to much longer edges and see if it ever breaks down.

to the elastic mean free path of the bulk (2D) electrons [254, 40, 230]. For WTe_2, the situation can different. Although the ballistic length scale for the edge modes is shorter than the semiconductor 2D TIs, of order 100nm, the elastic mean free path for the bulk 2D electrons can be shorter, as low as 10nm (see Section 6.4.1). Given that the atomically disordered edges of the monolayer essentially guarantee a stronger disorder potential at the edge compared to the interior, it is a good guess that the edge modes must have *some* added robustness to disorder to have such a long mean free path compared to the bulk electrons. Nonetheless, all 2D TIs have an associated length scale beyond which the edges are no longer ballistic. Developing a better understanding of this experimental fact continues to be a point of interest in the community.

6. Superconductor

This chapter is structured somewhat differently from prior chapters, as a result of the relative recency of the results and the absence of published work (a manuscript is under review at the time of this writing). I acknowledge here fruitful discussions with Liang Fu, Senthil Todadri, and Jonathan Ruhman, and I thank Yuan Cao, Landry Bretheau, and Joel I-Jan Wang for their important contributions and technical help towards completing this work. As before, WTe_2 crystals were synthesized by Quinn D. Gibson and Robert J. Cava at Princeton University [138].

Superconductivity, a zero-resistance state with macroscopic phase coherence, has been a cornerstone of solid state physics for over a century since its discovery in 1911 [255]. Its realization in thin films, effectively creating a superconducting state in the two dimensional limit, adds a number of twists to the phenomenon that are continuing to be explored today [256, 257, 258]. As semiconductor technology developed, it became apparent that a superconducting field-effect transistor would be an attractive technological device, with much experimental effort expended to this end [259, 260, 261, 262, 263, 264, 265, 266, 267, 268]. A key difficulty of this effort is the large electron density typically required for superconductivity to exhibit a zero-resistance state at experimentally accessible temperatures. Low-density superconductivity is additionally of high interest as the phonon-mediated attraction for Cooper pairing in standard superconductors [269, 270] may be insufficient to explain superconductivity in such cases, so new physics is often anticipated [271, 272, 273, 274, 275, 180, 276]. Moreover, low-density superconductivity in a 2D material would allow for the realization of a field effect device that would enable investigation of the superconductor-to-insulator transition as a continuous function of density and possibly useful technological applications. A density-tuned transition has been observed in some systems, but at average densities at best on the edge of accessibility by standard low-permittivity gate dielectrics [268, 277, 278, 279, 280, 281]. Moreover, the interface of superconductivity with 1D helical modes (such as those present in topological insulator systems) is currently undergoing intense experimental effort in order to realize Majorana bound states, with the hope that such quasiparticles may be used towards eventual construction of a "topological" quantum computer or robust quantum memory [44, 45, 46, 47, 48, 49]. To date, all experimental efforts seeking the combination of 1D helical modes and superconductivity have required a materials heterointerface between a standard superconductor and the helical mode [282, 1, 283, 284, 285, 286, 287, 288, 289]. Achievement of a high quality, low-transparency heterointerface in a device is possible [283], but requires a fine-tuned interface that adds to the complexity of such systems.

Here, I present our experimental results on the discovery of intrinsic superconductivity at record low induced electron densities accessible by standard field-effect transistor device

scheme in monolayer WTe_2, which is also a 2D topological insulator hosting 1D helical edge modes (see Chapter 5).

6.1. Discovery

The initial discovery of superconductivity in monolayer WTe_2 occurred as we were pursuing the investigation of the quantum spin Hall phase (as detailed in Chapter 5). We were studying the first device to show resistance plateaus that approached the hoped-for quantum value (h/e^2 per edge), which is labeled device 1 in Chapter 5. We observed that this same device, when homogeneously doped into the conduction band, appeared to undergo a superconducting transition below about 1 Kelvin. See Figure F.1 for the gate-voltage dependence of this curve, in which a transition to an insulating phase is observed as carriers are depleted. In Figure 6.1A, we show the resistance as a function of temperature when the top gate is biased to 4 Volts, where it is apparent that the resistance drops by about a factor of 7 as temperature is reduce from 5 Kelvin down to 0.3 Kelvin. This discovery occurred on January 26, 2017. We also observed non-linear V-I characteristics and magnetic field dependence indicative of a superconducting state (Figure 6.1B).

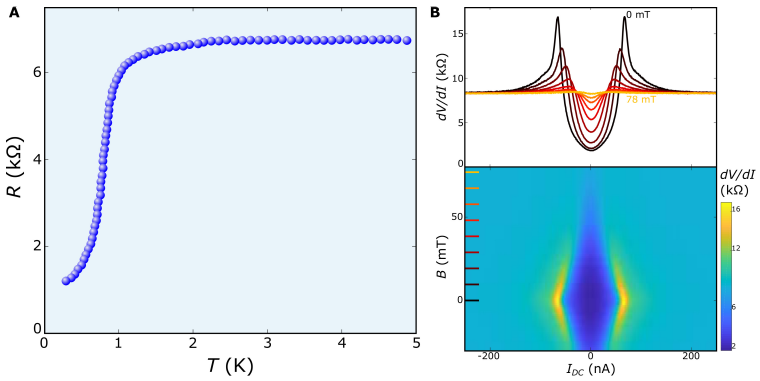

Figure 6.1.: A, The resistance drop as a function of temperature at $V_{tg} = 4$V. **B,** dV/dI as a function of direct current bias at different magnetic fields, with critical current labeled as I_c. This data taken at $V_{tg} = 4V$. Upper: line traces as a function of I_{dc}. Lower: Same data in color map format.

In this device, the resistance did not drop to zero. This may have been partly due to insufficiently low temperatures, but another clue was important. In Figure 6.2 we show the V-I characteristics for two different types of channels on the device: channels in which the WTe_2 is only protected by hBN on one side and is exposed on the other (half-encapsulation), and the channel in which the monolayer is encapsulated on both sides by hBN (full-encapsulation) for most of the distance between the contacts. Only the latter case showed signatures of superconductivity. The fact that the resistance did not drop all the way to zero was likely due to the quasi-two-terminal nature of the device, which results in half-encapsulated regions in series with the fully encapsulated area. Because the half-encapsulated region can be separately identified as non-superconducting (likely due to degradation from exposure), it

was clear that in order to observe zero resistance we needed to engineer a device structure that would ensure measurement only of fully encapsulated WTe_2 in a true four-probe geometry.

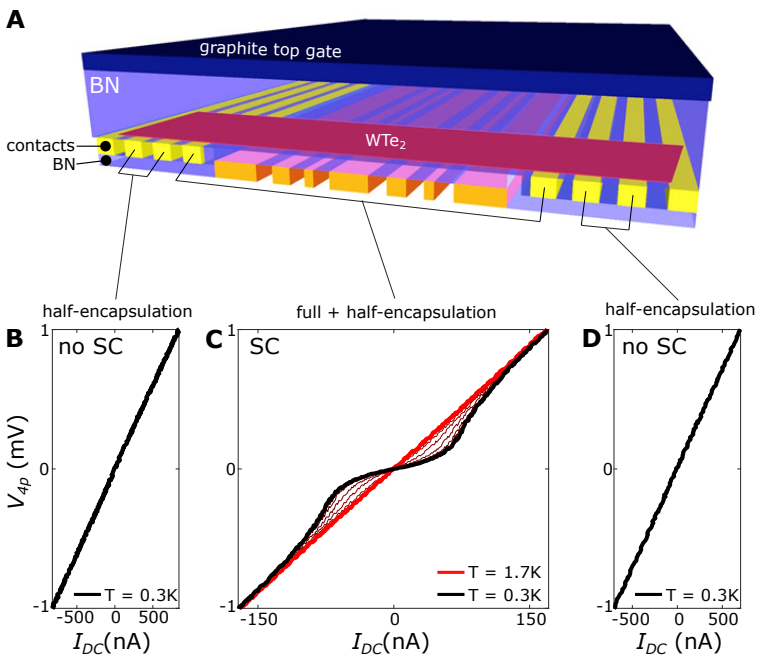

Figure 6.2.: **A**, Schematic of the structure of device 2. See also Ref. (2) for more details. **B-D**, Four probe V-I curves for different sets of contacts. **B & D**, The case of half-encapsulated WTe_2, in which superconductivity is not detected down to 300 mK. **C**, The channel that includes fully encapsulated WTe_2 shows a transition toward superconducting behavior at low temperature.

6.2. Observation of Zero Resistance

6.2.1. Device Geometry and Basic Characteristics

After we concluded the QSH study, we turned our attention to reproducing the superconducting state in a four-terminal geometry in order to see that the system does indeed achieve zero resistance. Figure 6.3A shows a schematic of such a device structure, and panel B gives an actual optical microscopy image of the main device investigated in this study, which we dub here device 2[1]. In Figure 6.3B we also include schematic circuit elements of the measurement configuration employed for all measurements presented here, unless otherwise specified.

In this device, at high doping ($V_{tg} \sim V_{bg} \sim 5V$) we see that the resistance begins to drop starting from around 1 Kelvin and reaching zero resistance at just above 300 mK, as shown in Figure 6.3C. This zero resistance phase is observed for a wide range of gate voltage parameters (inset of Figure 6.3C). In the normal state near 1 Kelvin the V-I characteristic is ohmic, and becomes highly nonlinear at low temperatures (Figure 6.3D). For this case,

[1]Note that this labeling is different from the manuscript under review that will hopefully be published soon.

the primary critical current is readily identified by the sharp jump in voltage at $I_c \sim 160$ nA. The same non-linearity can be observed in even more striking fashion by measuring the differential resistance dV/dI as a function of direct current bias I_{dc}, as shown in Figure 6.3E. The jump in voltage at the critical current manifests as an extremely sharp peak in the differential resistance. In the same panel, we show that perpendicular magnetic field suppresses the superconducting state as expected, in this case by observing that the device returns to an ohmic state at high magnetic field.

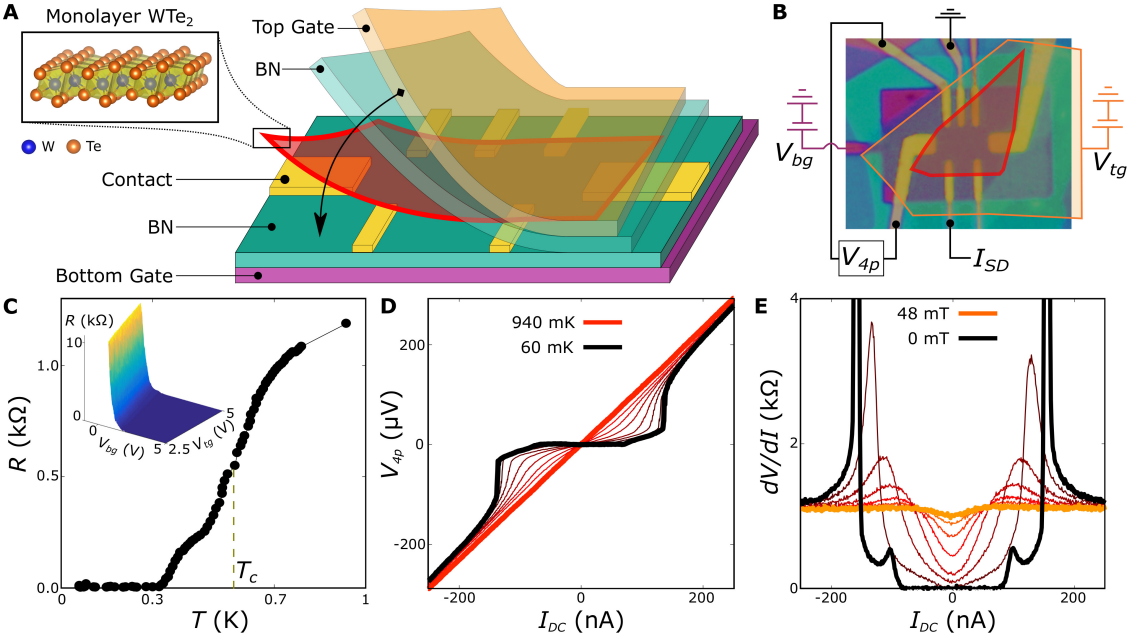

Figure 6.3.: A, Cartoon illustration of the device structure and the crystal structure of monolayer WTe_2. **B,** Optical microscopy image of device 2, with the monolayer WTe_2 (red) and graphite top gate (orange) highlighted. Circuit elements show the measurement configuration. **C,** Temperature dependence of the resistance for $V_{bg} = 4$ V and $V_{tg} = 5$ V. Inset shows the resistance as a function of both gate voltages, at base temperature. **D,** V-I characteristics from base temperature (black) up to 940 mK (red). **E,** Magnetic field dependence of the nonlinear V-I behavior, measured at base temperature, captured by the differential resistance curves, at base temperature.

6.2.2. Aspects of 2D Superconductivity

When a 2D material is also a superconductor, one can expect two special events to occur as temperature is lowered from from well above the critical temperature(s). We begin in the normal state with resistance R_n, which displays Ohmic (linear) V-I behaviors.

1. First, as temperature is lowered, fluctuating Cooper pairs provide an enhancement to the conductivity. High resistivity superconducting systems often exhibit two additive contributions, the Aslamazov-Larkin (AL) [290] and Maki-Thompson (MT) [291, 292] corrections, although others also exist [293]. Qualitatively, these effects serve to "smear out" the superconducting transition as a function of temperature. Quantitatively, the

AL and MT contributions are

$$\Delta\sigma_{AL} = \frac{e^2}{16\hbar}\frac{1}{t} \tag{6.1}$$

$$\Delta\sigma_{MT} = \frac{e^2}{8\hbar}\frac{1}{t-\delta}\ln\frac{t}{\delta} \tag{6.2}$$

$$t = \frac{T}{T_{c0}} - 1, \tag{6.3}$$

where δ is a phenomenological, material-dependent, dimensionless number called the "pair breaking parameter". The "mean-field" temperature T_{c0} marks the temperature at which Cooper pairs have formed. T_{c0} is a fit parameter to the above fluctuation conductivity formulae, and so they are frequently used to determine this value. Usage of these formulae requires accurate determination of the sheet conductivity, which requires a well-understood geometry and contact resistances and a large enough sample so that disorder effects are fully averaged out. Without this, it is difficult to accurately determine T_{c0} and as such the analysis is not shown here, although I mention that values of order $T_{c0} \sim 550mK$ were typically extracted.

2. The Berezinskii-Kosterlitz-Thouless transition occurs below the mean-field temperature at T_{BKT} [294, 295, 296]. In between, thermally excited vortices (the topological defect of a 2D superconductor) are independently mobile and generate dissipation. However, vortex-antivortex pairs are energetically stable and eventually all vortices become bound to anti-vortex partners. This pair is a "neutral" defect and cannot cause dissipation. The temperature scale for this process is denoted T_{BKT}. Two complementary methods for determining T_{BKT} are frequently used in the literature:

   a) The first involves an inspection of the V-I curves. At very low temperatures $T \ll T_{BKT}$, the V-I curve is highly non-linear, with a sharp jump in voltage at a specific critical current. As temperature rises and approaches T_{BKT}, the V-I curve smooths out and is expected to exhibit a cubic relationship at $T = T_{BKT}$. As temperature rises further, a linear V-I curve should result at high temperature. Our analysis of this behavior in monolayer WTe_2 is shown in Figure 6.4A, which gives $T_{BKT} \sim 470mK$ for $V_{bg} = 4V$ and $V_{tg} = 5V$.

   b) The second method involves investigation of the temperature-scaling of the zero-bias resistance. In the vicinity of T_{BKT} the resistance is expected to scale as

$$R \approx 10.8 R_n b \exp\left(-2b^2 \frac{\sqrt{\frac{T_{c0}}{T_{BKT}} - 1}}{\sqrt{\frac{T}{T_{BKT}} - 1}}\right), \tag{6.4}$$

   where b is a constant of order unity [297, 298]. As such, a second way to determine T_{BKT} is to find the value for T_{BKT} which results in a linear relationship between $\ln\frac{R}{R_0}$ and $\left(\frac{T}{T_{BKT}} - 1\right)^{-1/2}$. Using T_{BKT} from the previous analysis, we find the expected behavior (Figure 6.4B). It is worth noting that this formula is a particular limit of a theory that considers AL-type terms, and does not reproduce

the MT term noted earlier.

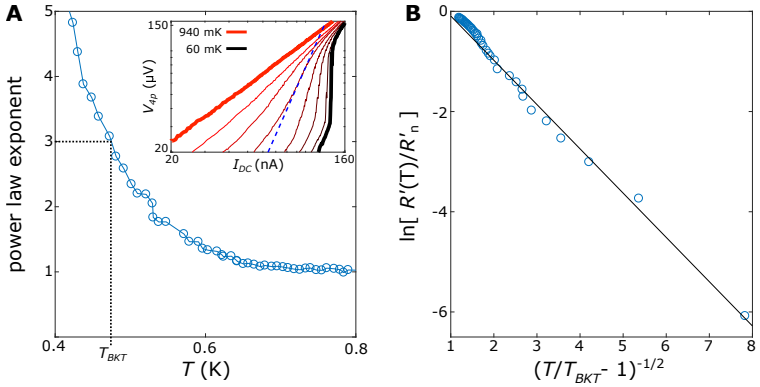

Figure 6.4.: A, Power law exponent of the V-I curve near the critical current. Inset: log-log plot of the V-I curves, with a cubic relationship plotted in the dashed blue line. **B,** Plot of the logarithm of resistance as a function of a reduced temperature to find T_{BKT}. For this device we had to account for the "shoulder" seen in Figure 6.3C, so $R' = R - 250\Omega$.

6.3. Gate Dependence of Important Quantities

6.3.1. Critical Temperature and Critical Current

With the superconducting state established, we now study its behavior as electrons are depleted from the system. We begin with the temperature dependence $R(T)$, as shown in Figure 6.5A, where the top gate is fixed at $V_{tg} = 5V$ and the back gate voltage is varied (hereafter simply referred to as the gate voltage). At high gate voltage, the resistance drops to zero as shown above. As the gate voltage is lowered, the zero resistance state is progressively weakened and eventually disappears for experimentally accessible temperatures, as also shown in Figure 6.5B (upper panel). At still lower gate voltages, a metallic temperature dependence remains, until a critical gate voltage $V_c^{MIT} \sim -0.75V$, below which the temperature dependence is distinctly insulating, e.g. $\frac{dR}{dT} < 0$. From this dataset, we can extract the temperature at which a resistance at 50% of the normal state value is recovered, which we will define as T_c for the remainder of this chapter. $T_c(V_{bg})$ is plotted in the upper panel of Figure 6.5B, with an extrapolation that provides an estimate for a critical gate voltage $V_c^1 \sim -0.65V$ (see Appendix F).

We can additionally inspect the critical current behavior. Figure 6.5C shows a typical dV/dI trace as a function of I_{dc}, similar to that of Figure 6.3E, with both critical currents identified. The lower critical current I_c' is consistent with the shoulder seen in the $R(T)$ curve just before achieving zero resistance. Figure 6.5D plots the dV/dI traces as a function of V_{bg} in color plot form, in which both critical currents can be seen to evolve monotonically with V_{bg}. This data is also summarized in the lower panel of Figure 6.5B. The primary critical current bifurcates weakly around $V_{bg} \sim 1V$, and evolves to zero by $V_c^2 \sim -0.8V$. For $V_{bg} < V_c^2$, dV/dI is peaked at zero bias and decreases with increasing I_{dc}, indicative of a gapped state.

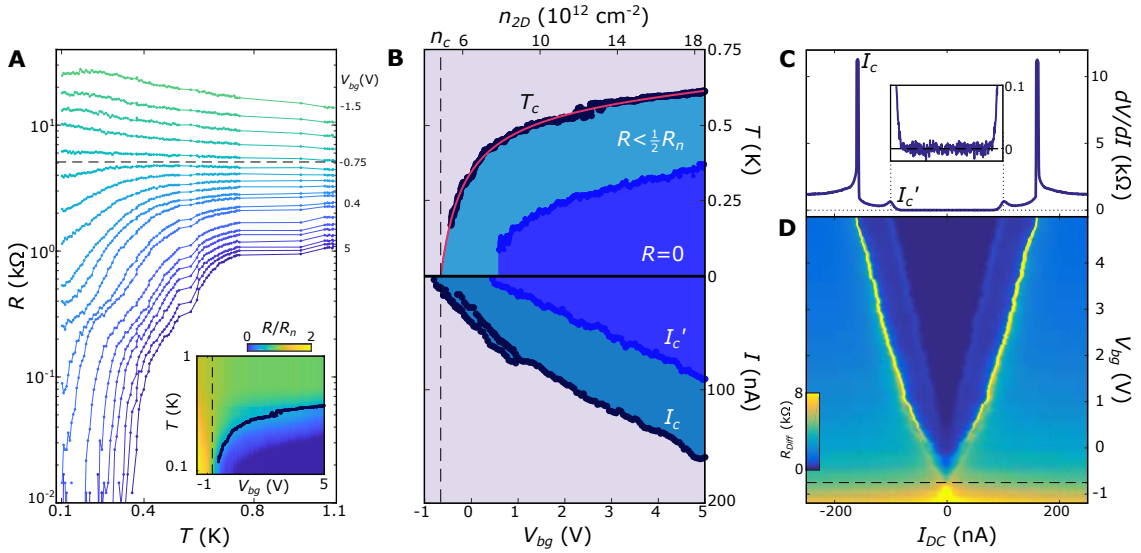

Figure 6.5.: **A,** $R(T)$ characteristic for different gate voltages, showing the transition from a superconducting state to an insulating state. Dashed line is a guide to the gate voltage, V_c^{MIT}, that separates the two regimes. Inset: color plot of the same data, normalized to the normal state resistance R_n, with T_c marked in black. **B,** Upper panel: gate dependent critical temperature T_c, summarized from **A**. The zero-resistance region is shaded dark blue. Lower panel: gate dependent critical current, I_c and I_c', summarized from **D**. For $V_{bg} < 1V$, I_c is found to bifurcate into two peaks, the values of which are determined by extrema of the second derivative of $\frac{dV}{dI}(I_{DC})$ data. The corresponding electron density (n_{2D}), estimated from the capacitance model, is shown on the top axis. **C,** Differential resistance $\frac{dV}{dI}$ v.s. current bias I_{DC} for $V_{tg} = V_{bg} = 5V$. Inset: zoom-in to the zero-resistance region. **D,** Differential resistance $\frac{dV}{dI}$ vs. current bias I_{DC} and gate voltage V_{bg}. Close to $V_{bg} \sim 1V$, the observed I_c trace bifurcates, as more clearly indicated in **B**. Dashed line indicates the gate voltage at which the peaks in differential resistance merge at zero bias, indicating destruction of superconductivity.

Altogether, the three methods of identifying a critical gate voltage agree with each other to identify a value $V_c \sim -0.75V$.[2] Utilizing a standard capacitance model, we can estimate the critical density as $n_c \sim 5 \times 10^{12} cm^{-2}$, which, if confirmed by other measurements of the normal state carrier density, would make monolayer WTe_2 the lowest density homogeneous 2D superconductor[3] [258]. It is also worth noting that the values of T_c measured at our highest densities are relatively high compared to other 2D superconductors [268, 258].

The critical density may not be intrinsic. Indeed, in device 1 we estimate a lower critical density of about $3 \times 10^{12} cm^{-2}$ (see Section F.1). It may be that these devices are disorder limited – the superconductivity is in the dirty limit (Section 6.4.1), and both devices seem

[2] While a scaling analysis is often attempted in these situations with a critical parameter (see e.g. [299, 300, 301]), the "shoulder" in the $R(T)$ curve at low temperature makes such analysis difficult to interpret and as such is not presented here. This shoulder could be indicative of the presence of a "quantum metal state" that is an active area of work in the current literature [302, 303, 304, 305, 306, 307, 308, 309, 310, 311, 312, 313, 314], although there are still issues to be resolved [315].

[3] A very interesting hybrid, non-intrinsic superconductor consisting of atomically disordered graphene with superconducting tin nanoparticles exhibits a critical density of $\sim 10^{12} cm^{-2}$ [316].

to also have a critical resistivity of around $\sim 10k\Omega$ which is higher (but not my much) than the pair quantum resistance $R_Q = \frac{h}{4e^2} \sim 6.5k\Omega$. Higher mobility samples could become superconducting at yet lower densities due to a reduction of disorder [317, 318, 319]. A closer inspection of the transition to determine whether density or resistance are the crucial quantity will deserve future work.

6.3.2. Magnetic Field Effects

6.3.2.1. Perpendicular Magnetic Field

In Figure 6.3E we showed how the dV/dI curve evolves with increasing magnetic field, indicative of a return to the normal state. Figure 6.6 shows the resistance as a function of magnetic field $R(B)$ for different V_{bg} (again fixing $V_{tg} = 5V$). We see that at the highest densities the transition to the normal state due to magnetic field is relatively sharp. As the system is depleted the transition becomes broader and extends to higher magnetic fields. Characterizing B_c as the magnetic field at which 50% of the normal state resistance is recovered, we find that B_c increases as the system is depleted, which is strictly opposite the trend seen in T_c or I_c. This is summarized in Figure 6.6B, where B_c is marked on a colormap plot of R as a function of V_{bg} and B. How can we understand this?

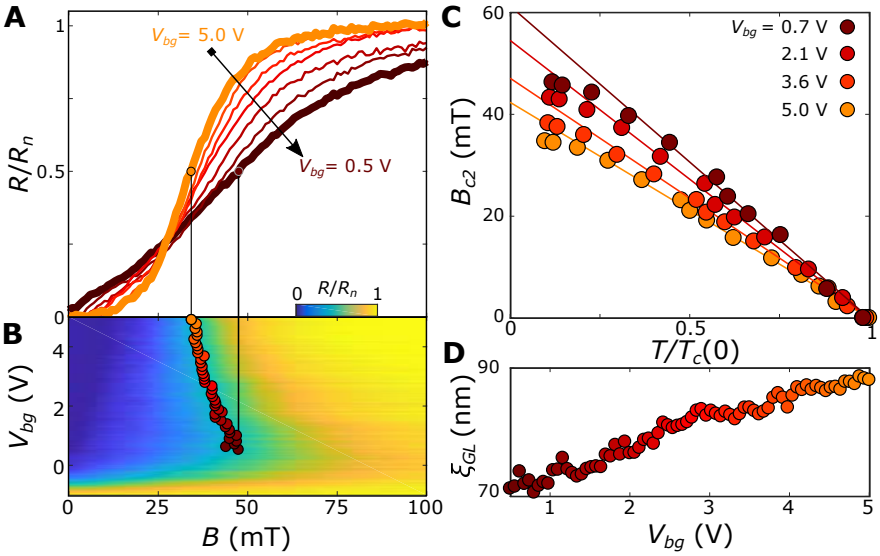

Figure 6.6.: **A,** Gate-dependent $R(B)$ traces, normalized to the normal state resistance R_n. **B,** Color map of the same data, as a function of V_{bg} and B. Circles denote B_c, referring to the magnetic field at which 50% of the normal state resistance is recovered. **C,** Temperature dependence of B_c for selected gate voltages, including fits to the GL formula for T close to T_c (see main text). **D,** Coherence length extracted from fits such as in **C**. Color of all data points and lines represents the gate voltage of that data point.

To begin the inspection, we first note that for 2D superconductors, the upper critical field for perpendicular magnetic fields has a linear temperature dependence near the critical tem-

perature [320]:

$$B_c = \frac{\Phi_0}{2\pi\xi^2}\left(1 - \frac{T}{T_c}\right) \tag{6.5}$$

where $\Phi_0 = \frac{h}{2e}$ is the superconducting flux quantum and ξ is the Ginzburg-Landau coherence length. By taking a temperature dependence of B_c as a function for each gate voltage, we can fit the data to the above formula, with T_c and ξ as fitting parameters, as shown in Figure 6.6C. We can then plot ξ_{GL} as a function of V_{bg} (Figure 6.6D) to see that it increases monotonically with increasing V_{bg}, despite a simultaneously increasing T_c. By inspecting the formula for the coherence length in both the clean and dirty limits, the answer becomes apparent:

$$\xi_c = 0.163 v_F \frac{\hbar}{k_B T_c} \tag{6.6}$$

$$\xi_d = 0.441 v_F \sqrt{\frac{\hbar\tau}{k_B T_c}} \tag{6.7}$$

Here we have used the relationships $\Delta_{BCS} = 1.76 k_B T_c$ and $l_{mfp} = v_F \tau$ (assuming isotropic bands for simplicity). In both the clean and dirty cases, the coherence length depends linearly on the Fermi velocity, which is expected to increase with increasing electron density. In Section 6.4.1, we take this analysis further in order to deduce that our samples are "dirty" superconductors.

6.3.2.2. Parallel Magnetic Field

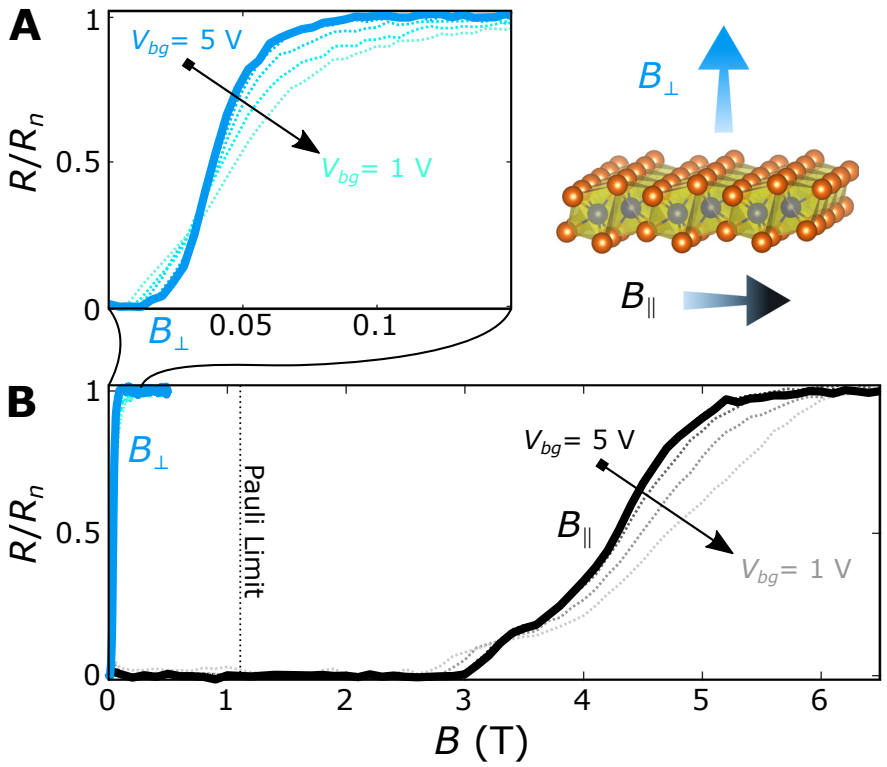

Figure 6.7.: A, LEFT: The same perpendicular field data as in Fig. 6.6, plotted here for comparison. RIGHT: a schematic indicating the color coding for perpendicular and parallel magnetic field (note for clarification: the orientation of the parallel field with the crystal lattice is not known). **B,** Normalized device resistance as a function of parallel magnetic field (black) and perpendicular magnetic field (blue).

Figure 6.7B, we show the normalized resistance as a function of parallel magnetic field for a sequence of gate voltages. The main aspect to note is that about 3 Tesla is required to exit the zero resistance state, and upwards of 5 Tesla are necessary to fully recover the normal state. According to our estimates for the critical temperature $T_c \lesssim 0.65K$, we estimate that the usual Pauli limit for the in-plane critical field is $B_P[T] = 1.86T_c \lesssim 1.2T$. That the parallel critical field is clearly much higher than this is an indication of strong spin-orbit effects, such as what has been recently found in Ising-type superconductivity in the 2H-structure TMDs [321, 322, 323, 324]. However, WTe_2, being in a distorted 1T phase, does not break inversion symmetry as strongly as the 2H compounds and may not at all. Any weak inversion breaking will also not be of the same form. In the 2H compounds, the polarity of the inversion breaking is entirely in-plane, resulting in an out-of-plane spin-orbit field, which gives the Fermi surfaces (and the superconducting state) the Ising-like character. In WTe_2, any inversion breaking will have a mixture of orientations and include some helicity around the Fermi surface as well as some Ising-like character. Studying the exact nature of the impact of spin-orbital coupling will be an interesting direction for future research.

We also found that the parallel critical field increased with decreasing density similar to

the perpendicular field case. This is not currently understood and is a topic of ongoing investigation.

6.3.3. Preliminary Phase Diagram

In conjunction with the results of Chapter 5, we can draw a preliminary schematic phase diagram in temperature and density, shown in Figure 6.8, which highlights the accessible density scales of both the 2D TI phase and the superconducting phase. At the critical density n_c I leave a gap between the two phases, as we currently have insufficient data to determine whether there is a true quantum phase transition there or if an intermediate phase intervenes [302, 303, 304, 305, 306, 307, 308, 309, 310, 311, 312, 313, 314]. Extending this phase diagram along additional axes (such as magnetic field and displacement field) will be an interesting direction for future analysis and experiments.

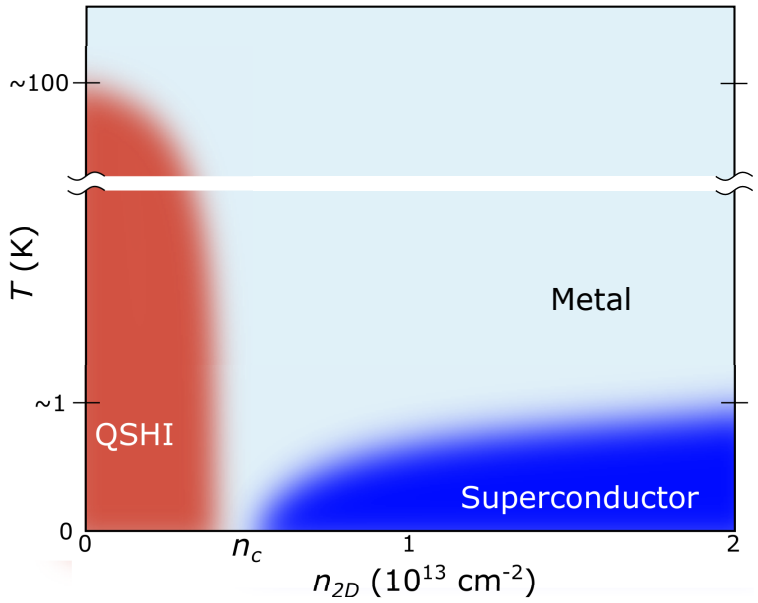

Figure 6.8.: Schematic phase diagram for temperature and carrier density.

6.4. Extra Commentary

6.4.1. Clean or Dirty Superconductivity

The notion of clean and dirty superconductivity comes down to the interplay between mean free path $l_{mfp} = v_F\tau$ and the intrinsic coherence length ξ_{BCS}:

$$\text{Dirty:} \quad \xi_{BCS} \gg l_{mfp} \tag{6.8}$$

$$\text{Clean:} \quad \xi_{BCS} \ll l_{mfp} \tag{6.9}$$

Recall that

$$\xi_{BCS} = \frac{\hbar v_F}{\pi \Delta} \tag{6.10}$$

and the coherence length measured in our experiment is more directly related to the Ginzburg-Landau (GL) coherence length, which in 2D is [293]

$$\xi_c = 0.91 \xi_{BCS} \tag{6.11}$$

$$\xi_d = 1.04 \sqrt{\xi_{BCS} l_{mfp}} \tag{6.12}$$

for the clean and dirty cases, respectively. With our definitions above for the BCS coherence length and mean free path, and knowing the relationship between the superconducting gap and critical temperature for BCS theory $\Delta = 1.77 k_B T_c$, we can rewrite the GL coherence length as:

$$\xi_c = 0.163 v_F \frac{\hbar}{k_B T_c} \tag{6.13}$$

$$\xi_d = 0.441 v_F \sqrt{\frac{\hbar \tau}{k_B T_c}} \tag{6.14}$$

Finally, we can replace the transport scattering time by our measurement of the normal state conductivity via the standard relationship

$$\sigma = \frac{1}{2} e^2 \tau v_F^2 D(\varepsilon_F) \tag{6.15}$$

where $D(\varepsilon_F)$ is the density of states at the Fermi energy and in which we have assumed an isotropic Fermi surface for simplicity. Plugging this into the formula for the coherence length of a dirty superconductor, we obtain specific predictions for the clean and dirty cases:

$$\begin{array}{lll} \text{clean:} & v_F & = 0.98 h \xi_c k_B T_c \\ \text{dirty:} & D(\varepsilon_F) & = 0.062 \frac{h}{k_B e^2} \frac{\sigma}{T_c \xi_d^2} \end{array} \tag{6.16}$$

With all the measured values in hand, we can use the above formulae to estimate band parameters and compare to theoretical calculations. The clean limit calculation yields $v_F \sim 4 \times 10^4 \frac{m}{s}$, which is about an order of magnitude smaller than we would expect for monolayer WTe_2 at these densities. The dirty limit calculation yields $D(\varepsilon_F) \sim 0.15 eV^{-1} nm^{-2}$ per species, corresponding to an effective mass of $m_{eff} \sim 0.17 m_e$, which is about 70% of the value predicted by *ab initio* calculations. The latter suggests reasonably good agreement with expectation, given the simplicity of the approach.

We can do a few other checks to this end. For the clean limit, $l_{mfp} \gg \xi_{BCS} \sim 100nm$. A mean free path of even 100nm, with the estimated Fermi velocity, gives $\tau \sim 2ps$. This would imply a normal state conductivity about an order of magnitude higher than is measured, which is another inconsistency. In contrast, the dirty limit calculation allows us to estimate $\tau \sim 10fs$ after inferring $v_F \sim 5 \times 10^5 \frac{m}{s}$ at the experimental densities, using the parabolic

band approximation. This gives a mean-free path of $l_{mfp} \sim 5nm$ and a BCS coherence length $\xi_{BCS} \sim 1\mu m$, which is internally self-consistent.

6.4.2. On the Pairing Mechanism

An important question is whether superconductivity in monolayer WTe_2 can result from a phonon-based pairing mechanism at carrier densities $n_{2D} \leq 2\times10^{13}cm^{-2}$. Three-dimensional WTe_2, in its natural form, has a per-layer electron density comparable with the densities we have induced into the 2D monolayer. However, it does not exhibit superconductivity until pressure induces a Fermi surface about an order of magnitude larger than the intrinsic case [325, 326], and it has been calculated that phonon-based mechanisms are sufficiently strong at that point [327]. For 2D WTe_2, a very recent calculation has predicted measurable critical temperatures at densities $n_{2D} > 5 \times 10^{13}cm^{-2}$, which results from a softening phonon mode [328]. This density is too high to be accessible by standard solid-state electrostatic gates, and would suggest that simple phonon-based mechanisms are unlikely to be the cause. It is possible that the proximity to a charge ordered state predicted by [328] could occur at lower density; an STM study finds a natural charge-ordered phase in MBE grown films of WTe_2 [157]. Curiously, our results on trilayer WTe_2 showed no hint of superconductivity down to 300 mK in either the semimetallic or metallic phases despite the higher cleanliness (e.g. higher mobility) exhibited there (see Chapter 4 or [154]), so the number of layers also appears to be important. Clearly, much work remains to be done.

6.5. Concluding Remarks

At this time the observed phenomena are not fully understood, but the amount of experimental and theoretical phase space available for exploration remains high. We have only just taken a peek at the tip of the iceberg in the distance. Important features to characterize include the impact of the material's strong anisotropy [142] and tunable noncentrosymmetry [158, 329]. Here, it is possible that all the relevant energy scales (Fermi energy, spin orbit splitting, and Zeeman energy) can be appreciably tuned in the same sample. The superconducting gap can be characterized by tunneling spectroscopy measurements [330, 331, 332], and scanning SQUID-based techniques may be used to infer the superfluid density in real space [279]. Reducing disorder may stabilize superconductivity at yet lower densities [333, 334, 317, 319] and allow access to superconductivity in the clean limit, where more non-trivial behaviors may come to light [333, 334, 329].

Beyond understanding the superconductivity itself, an exciting research direction is to study the interplay between the superconducting state, the helical edge modes, and other vdW materials. The first natural experiment is to create junctions similar to those studied in Chapter 5 and search for a Josephson effect, which is expected to exhibit SQUID-like Fraunhofer patterns when the supercurrent is carried only be edge modes [285] and unusual phenomena in the microwave regime [287, 286, 335, 288]. Beyond WTe_2-only devices, the recently discovered 2D layered ferromagnets [336, 337] would be a natural choice to interface with WTe_2. If

one of those magnetic materials can be found to induce magnetism in WTe_2, it could be used to generate a local magnetic gap in the helical edge modes. Adjacent to this region, electrostatic gates may dope monolayer WTe_2 into the superconducting phase. At the interface, the correct conditions for realization of Majorana bound states would have been engineered [338, 339, 340]. Electrostatically accessible superconductivity in a vdW material presents a wide array of future experiments on its own, and its presence in a topologically non-trivial material multiplies the number further. One hopes these prospects will serve to inspire a rich array of scientific efforts in the coming years.

Part III.

Appendices

A. The Magic of "Topological Protection"

The notion of "topological protection" has been somewhat misunderstood or misused by the scientific community, at least in the early days. What is topologically protected is the *existence* of a metallic state at the boundary of a topologically non-trivial insulator. Additionally, a very specific class of scattering mechanisms are suppressed: first-order elastic backscattering that preserves the symmetry of the topological state. In the case of time-reversal invariant TIs, the last point means that momentum scattering must simultaneously include a spin-flip process in order to induce a 180 degree change in the momentum state. For the 1D boundary of a 2D TI, this seemed (in theory) like an excellent form of protection, although experiments have shown that backscattering will always occur at some length scale. See Section 5.3 for a discussion of this case. For the 2D surface state of a 3D TI, this does not even theoretically guarantee long mean free-paths, as we will show below.

A.1. 2D Helical Surface

In the relaxation time approximation, we can write down the transport scattering rate formula for a single Dirac cone on the surface of a 3D TI:

$$\frac{1}{\tau_{tr}} = \frac{n_i}{h} \int d^2k' \left\langle (V(q))^2 \right\rangle M(k,k') \left(1 - \cos\theta_{kk'}\right) \delta\left(\epsilon_k - \epsilon_{k'}\right) \tag{A.1}$$

$$M(k,k') = \begin{cases} 1 & \text{normal} \\ \frac{1}{2}\left(1 + \cos\theta_{kk'}\right) & \text{helical} \end{cases} \tag{A.2}$$

where n_i is the concentration of impurity centers, M represents the overlap of the initial and final states, and $V(q)$ represents the scattering matrix element [341]. Considering a circular Fermi surface, we can convert the integral to one over the Fermi surface

$$\frac{1}{\tau_{tr}} = \frac{2n_i k_F}{h} \int_0^{\pi} d\theta \left\langle (V(q))^2 \right\rangle M_\theta \left(1 - \cos\theta\right) \tag{A.3}$$

$$q = 2k_F \sin\frac{\theta}{2} \tag{A.4}$$

Now let us consider two types of disorder potential to see how helicity helps transport scattering times.

A.1.1. Small-Angle Scattering

For small angle scattering, we can take an approximation:

$$\frac{1}{\tau_{tr}^h} \approx \frac{2n_i k_F}{h} \int_0^\pi d\theta \frac{\frac{1}{2}\theta^2}{\sin^2 \frac{\theta}{2}} \left\langle (V(q))^2 \right\rangle \tag{A.5}$$

$$\frac{1}{\tau_{tr}^n} = \frac{2n_i k_F}{h} \int_0^\pi d\theta \frac{\frac{1}{2}\theta^2}{\sin^2 \frac{\theta}{2}} \left\langle (V(q))^2 \right\rangle \tag{A.6}$$

and we see that, to first order, the results are exactly the same. This is intuitive because helicity only prevents back-scattering, so if one is already in the small-angle scattering limit then helicity provides no protection.

A.1.2. Point-Like Scatterers

For point-like scatterers, the scattering matrix element is constant in momentum space $V(q) = v_0$[1], so the scattering time becomes:

$$\frac{1}{\tau_{tr}^h} = \frac{2n_i k_F v_0^2}{h} \int_0^\pi d\theta \frac{1}{2} \sin^2 \theta \tag{A.7}$$

Without helicity, we have

$$\frac{1}{\tau_{tr}^n} = \frac{2n_i k_F v_0^2}{h} \int_0^\pi d\theta \, (1 - \cos\theta) \tag{A.8}$$

giving us the ratio:

$$\frac{\tau_{tr}^h}{\tau_{tr}^n} = 2 \frac{\int_0^\pi d\theta \, (1 - \cos\theta)}{\int_0^\pi d\theta \sin^2 \theta} \tag{A.9}$$

$$= 4. \tag{A.10}$$

As we see, the beneficial effects of helicity are at best[2] a factor of 4. This can be wholly overwhelmed by differences in the density of impurities n_i, which can be different by orders of magnitude from system to system.

A.2. Graphene vs TI surface State

Electrons in graphene and TI surface states both have a helical Dirac spectrum, and yet only the former has achieved particularly high mobilities. As we see above for point-like disorder,

[1] For graphene, we may assume that it is constant on the scale of k_F, but zero at the inter-valley momentum scale. So the disorder potential must be sharp, but not atomically sharp.

[2] In principal, one could improve on this number by engineering a scattering potential that is maximal at $q \sim 2k_F$ and minimal at small q, but this would require a special system and is somewhat artificial.

the strength of the disorder potential is dominant in determining the scattering rate, not the helicity.

We can make an additional comparison for the case of Coulombic impurities. For this, we first inspect the effective fine-structure constant for a Dirac-like 2D electron system:

$$\alpha = \frac{e^2}{2hv_F\kappa_s} \tag{A.11}$$

where v_F is Fermi velocity and κ_s is the effective permittivity at the surface. Known results for scattering off of 2D-disributed [342] and 3D-distributed [2] charged impurities naturally depend on α:

$$\text{2D distributed impurities: } \tau \sim n_i \frac{k_F}{v_F\alpha^2} \tag{A.12}$$

$$\text{3D distributed impurities: } \tau \sim n_i \frac{k_F^2}{\kappa_s\alpha \ln\frac{1}{\alpha}},\ \alpha < 1 \tag{A.13}$$

where n_i is again the impurity density. In graphene on typical substrates $\alpha \sim 0.8$. A typical TI surface state has about half the Fermi velocity, an order of magnitude larger effective dielectric constant, and a quarter of the degeneracies, giving $\alpha \sim 0.1$. This suggests something remarkable – for equivalent disorder potentials, the scattering time could be substantially longer on the TI surface state as compared with graphene (particularly in the first formula above). As such, in the early days it seemed reasonable to believe that TI surface states could become of comparable quality to graphene. As it turned out, this has not yet occurred – the materials are simply more disordered or more easily damaged. In other words, there is no magic bullet, and n_i is always important. Hence, the notion of "topological protection" was never a magic shield against material quality, and it was no mystery that a disordered material would exhibit poor mobilities. However, it does protect the boundary modes from localization and thereby allows for their persistence in some form even when conventional bands would have been destroyed.

B. Additional Details for Experiment on Electrostatic Coupling between Surface States of a 3D Topological Insulator

B.1. ARPES Measurement Methods and Analysis

Single crystals of BSTS were cleaved under ultra-high vacuum ($< 1 \times 10^{-10}$ Torr) at room temperature. Angle resolved photoemission spectroscopy (ARPES) measurements are taken using 6.3 eV femtosecond laser pulses, generated by quadrupling the output of a Ti:sapphire amplifier. Time-resolved spectra (TrARPES) are obtained by using 1.5eV, 100fs pulses as the "pump" beam and the 6.3eV beam as the "probe". The time delay t between the pump and the probe is controlled by a linear delay stage. A time-of-flight electron energy analyzer is

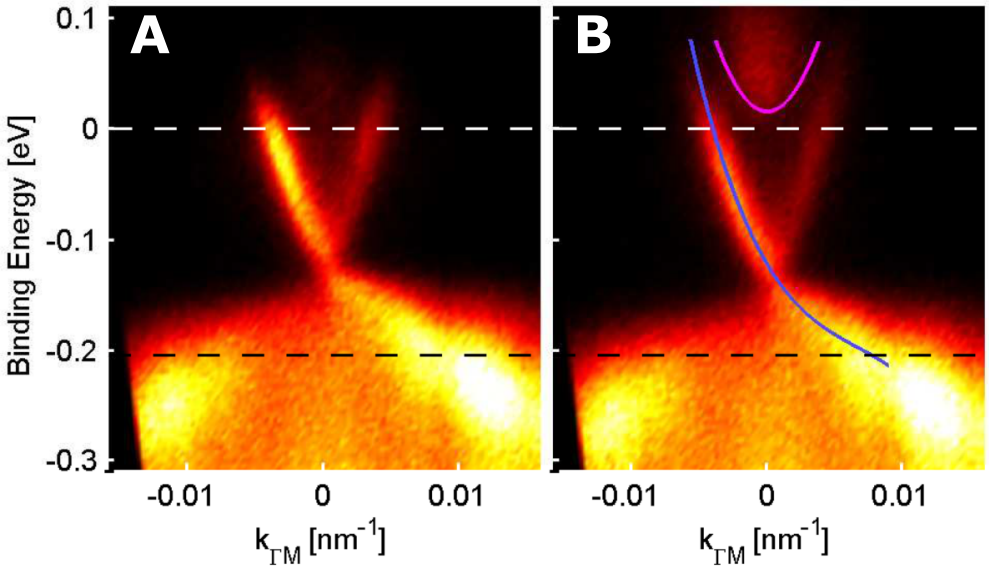

Figure B.1.: **A,** Static ARPES and **B,** TrARPES data ($t = 1500$ fs after pumping the system). The chemical potential is indicated by a white dashed line, and the energy of the valence band maximum is indicated by a dark dashed line. In **B**, the cubic fit to the surface state dispersion is superimposed on the data by a blue line. The magenta quadratic curve is the estimation for the conduction band energy and effective mass.

used to simultaneously measure the energy and the 2D momentum of the photo-emitted electrons. Thus, the time-resolved energy-momentum spectra $I(t, k_x, k_y, E)$ is obtained without sample or detector rotation. The TrARPES spectrum shown in the main text and here in Fig. B.1b was taken $t = 1500$ fs after pumping the system, which gives good visibility of states at energies higher than the chemical potential.

In the static ARPES spectrum (Fig.B.1a), the first immediate observation is that the chemical potential is located inside the gap, which remains true even after the surface has been exposed in vacuum for several days. The Dirac point and the valence band maximum are also observed. Information about the band gap and the conduction band can only be obtained with TrARPES (Fig.B.1b), which allows access to unoccupied states. The band gap (indirect) is 240 meV at room temperature, which is expected to increase by roughly 30 meV at low temperatures[343].

Band structure parameters can be extracted from these data. The surface state dispersion was obtained by extracting local maxima in intensity as a function of energy and momentum. The dispersion is well-fit by a phenomenological cubic dispersion (see Fig. B.1b, blue line):

$$E_{SS} = \hbar v_F k + \frac{\hbar^2}{2m_{ss}} k^2 + \lambda k^3. \tag{B.1}$$

The coefficients are found to be $v_F \approx 3.2 \times 10^5$ m/s, $m_{ss} \approx 0.2 m_e$, and $\lambda \approx 0.078$ eV nm^3. Light hexagonal warping is observed and was taken into account to obtain an appropriate average density of states. Additionally, the Dirac point energy is about $E_D - E_{VBM} \approx 100$ meV above the valence band maximum. Finally, assuming the conduction band is quadratic at low energies, a conduction band effective mass of $m_{CB} \sim 0.07 \pm 0.02\ m_e$ is consistent with the data.

B.2. Third Device

We also measured a third device with the same thickness as the thin device discussed in the main text (device A). Both devices behave qualitatively similarly, showing a similarly shaped $V_{peak}(V_B)$ (Fig B.2a). Fig B.2b shows the fit of the data to the spectrum derived from ARPES, showing a good fit. This device has a smaller interlayer capacitance of $C_{TI} \sim 500 \pm 10$ nF cm^{-2}. This may be due to flake-to-flake variability of the relative permittivity – bulk measurements of similar quaternary topological insulators show unclean phonon features due to disorder [344], and it is known that quaternary compounds are inhomogeneous [89]. It is possible that the bulk permittivity may vary throughout a macroscopic piece, which would mean that exfoliated nano-flakes from the same bulk piece can have distinctly different bulk permittivities.

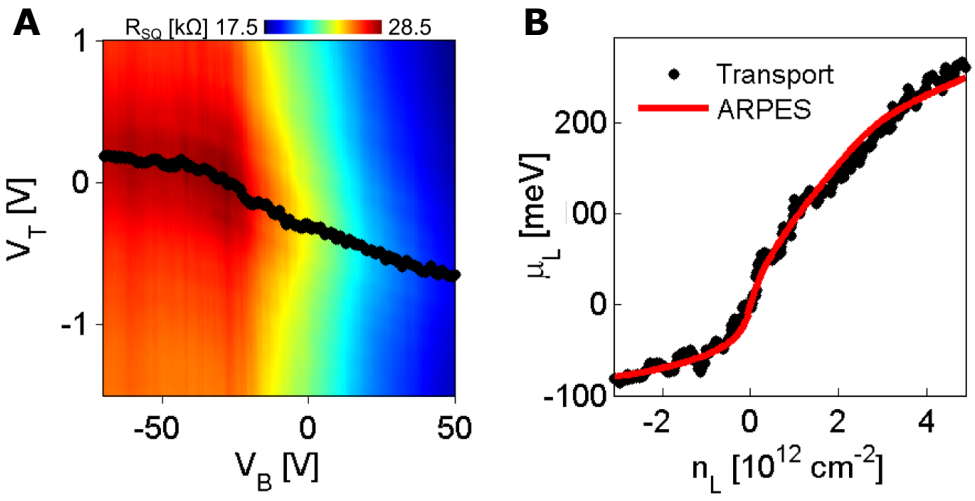

Figure B.2.: Data from a second thin device, 42nm thick, showing similar behavior to the thin device in the main text. **A,** Color plot of resistivity as a function of both gate voltages, with the upper surface resistance peak marked by black circles. **B,** Fit of the transport data (black dots) to ARPES data (red line).

B.3. Temperature Dependence

In the main text it was shown that device A (thin) has an inter-layer capacitive coupling, whereas device B (thick) does not. This is likely due to the presence of bulk states that screen electric fields inside the crystal. This is corroborated by the temperature dependence of the devices, shown in Fig. B.3. Device B has an insulating-like temperature dependence similar to that of large single crystals (Fig. B.3b), suggesting that conducting bulk states are still prominent. These states would exist at the interior of the crystal and screen electric fields, as seen in the gating behavior. In contrast, device A has a metallic-like temperature dependence (Fig. B.3a), indicating the surface states dominate. This correlation with thickness is consistent with previous reports [80, 81].

B.4. Hall Effect

Hall effect data from device A are shown in Fig. B.4. Fig. B.4a presents the transverse resistance R_{xy} as a function of magnetic field for three representative V_B, showing that R_{xy} is linear in magnetic field, consistent with a low mobility, i.e. $\mu^H B \ll 1$. The slope of this line is the Hall coefficient $R_H = \frac{dR_{xy}}{dB}$. R_H has a peaked structure as a function of the back-gate, reaching a maximum at roughly $V_B \approx -20$ V (Fig. B.4b). Note the lower surface R_{peak} is close to this value of V_B.

This gating behavior can be quantitatively and qualitatively understood by using the fact that the presence of two surface states results in a two-carrier Hall coefficient, which has the

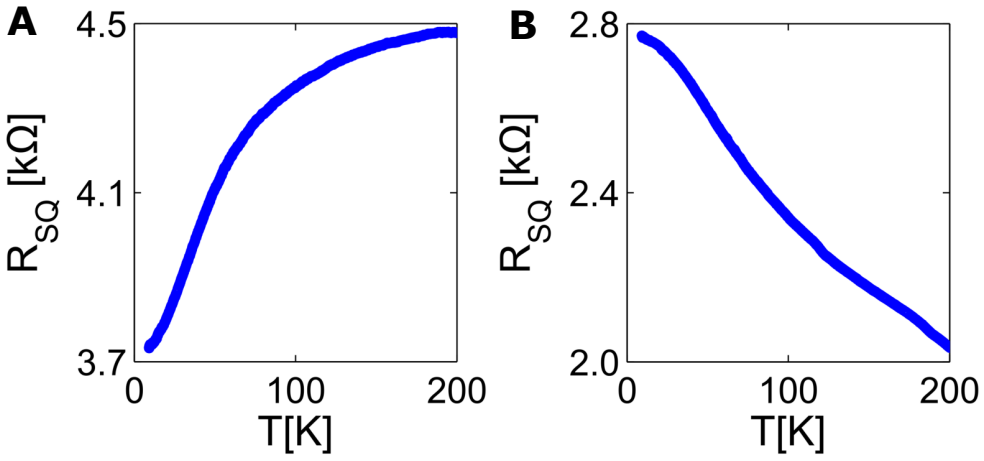

Figure B.3.: Temperature dependence without any applied gate voltages for **A,** device A and **B,** device B, which display qualitatively different behavior.

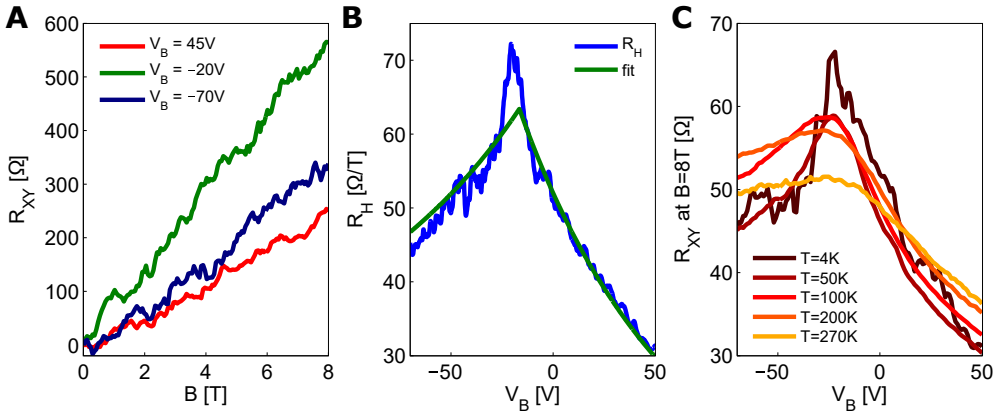

Figure B.4.: Hall effect data in device A. **A,** $R_{xy}(B)$ at three different back gate voltages. **B,** R_H, obtained from the slope of $R_{xy}(B)$, as a function of V_B. **C,** R_{xy} at 8T as a function of back-gate voltage at different temperatures.

following form:

$$R_H = \frac{1}{e}\frac{n_U\beta^2 + n_L}{\left(|n_U|\beta + |n_L|\right)^2}, \quad \beta = \frac{\mu_U^H}{\mu_L^H}, \tag{B.2}$$

where $\mu_{U,L}^H$ is the Hall mobility of the upper and lower surface states. If we approximate $n_L \approx C_B\left(V_B - V_B^0\right)$ and $n_U \approx n_U^0$ then we get the following form of the equation:

$$R_H \approx \frac{1}{e}\frac{n_U^0\beta^2 + C_B\left(V_B - V_B^0\right)}{\left(|n_U^0|\beta + C_B\left|V_B - V_B^0\right|\right)^2}. \tag{B.3}$$

This form allows for a least-squares fit of the data, which is also shown in Fig. B.4b. The model fits the data well and gives values of $n_U^0 \approx 9 \cdot 10^{12}\ cm^{-2}$, $\beta \approx 1.6$, and $V_B^0 \approx -17$ V. Note that $V_B = V_B^0$ is equivalent to the condition that $n_L = 0$, i.e. charge neutrality for the

lower surface.

Fig. B.4c shows the gate dependence of the Hall resistance R_{xy} at 8T for temperatures from 4K up to 270K. The sharp peak at $V_B \approx -20$ V broadens, but the overall values of R_{xy} remain largely unchanged. This result demonstrates that bulk states, which may be activated at high temperatures, appear to have neither enough density nor mobility to significantly affect the Hall effect. This underscores the dominance of the surface states.

B.5. Evidence for top-gate to lower-surface coupling

Effects of finite C_{TI} can also been seen in smaller features in the gating map. By taking derivatives of the resistivity with respect to either gate voltage, small conductance fluctuations can be more prominently observed. For example, in Fig. B.5a, we see that features in $\frac{dR}{dV_T}$, i.e. fluctuations associated with the upper surface state in the thin device, disperse in exactly the same way as R_{peak} itself, shown as black dots. Features in $\frac{dR}{dV_B}$, i.e. conductance fluctuations associated with the lower surface, behave in two ways (Fig. B.5b). Some features appear to be completely vertical, i.e. unaffected by the top gate electrode. Other features disperse with respect to both gate voltages, indicating coupling to both gate electrodes. The superposition of both types of features can be explained by the geometry of the device – the bottom gate electrode couples to the entire device area, whereas the top gate couples only to a portion. This means that lower surface conductance features may come from either singly- or dually-gated areas, resulting in both types of features in the data. The overall R_{peak} also disperses with both gates, but it is difficult to extract an R_{peak} associated only with the dually-gated area.

The same analysis on device B is shown in Fig. B.5c-d. All features are completely non-dispersive, i.e. either completely vertical or horizontal in gate-gate space. This corroborates the behavior of the resistance maxima, further indicating that the surfaces are completely screened from each other in thick devices.

B.6. Model Details

B.6.1. Charging Model Equations

Four coupled equations govern the charging of the system. As noted in the main text, these are a result of charge neutrality and Faraday's law, which restricts the sum of voltage drops around a loop to equal zero. In this system three types of voltage drops must be considered: voltages applied to the gate electrodes $V_{T,B}$, voltage drops from electric fields inside the dielectrics (e.g. en_T/C_T, from Gauss's Law), and the voltage drop at the edge of the gated region to due the change in chemical potential $\Delta\mu_{U,L}$. We use the three voltage loops defined

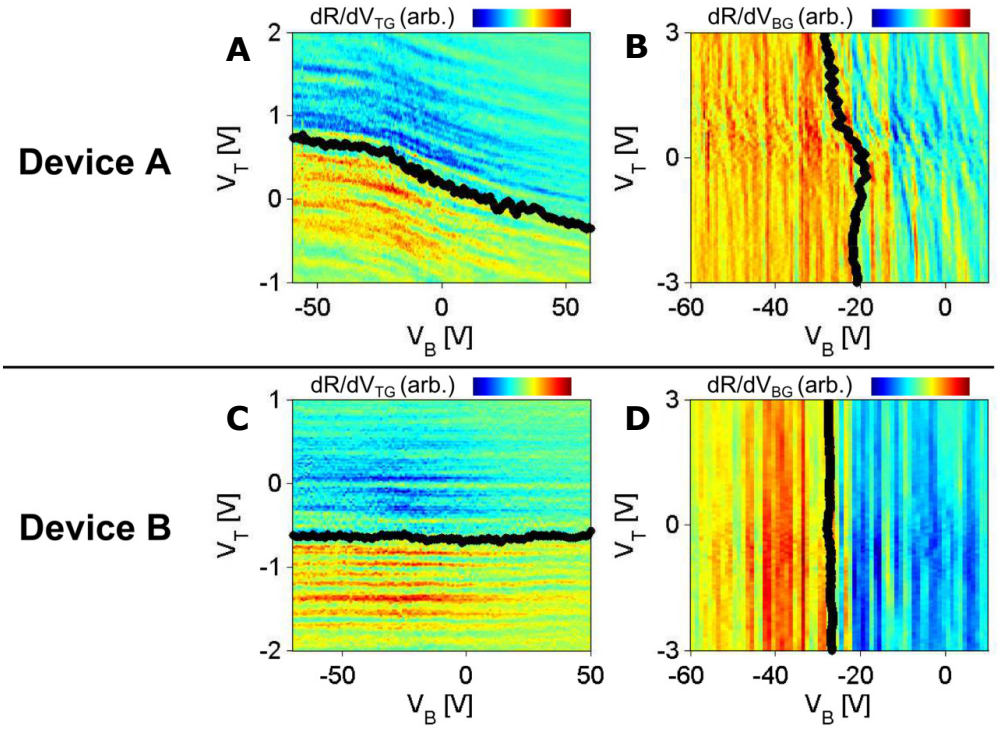

Figure B.5.: Derivative of resistance as a function of either gate voltage. **A-B,** Device A, $\frac{dR}{dV_B}$ and $\frac{dR}{dV_T}$ as a function of both gate voltages, respectively. **C-D,** Device B, $\frac{dR}{dV_B}$ and $\frac{dR}{dV_T}$ as a function of both gate voltages, respectively. The black dots are the position of the resistance peak for upper surface (panels **A** and **C**) and lower surface (**B** and **D**).

in Fig. B.6. As such, the following four equations can be written down:

$$n_T + n_B + \Delta n_U + \Delta n_L = 0 \tag{B.4}$$

$$V_T + \frac{e n_T}{C_T} - \frac{\Delta \mu_U}{e} = 0 \tag{B.5}$$

$$\frac{\Delta \mu_U - \Delta \mu_L}{e} + e\frac{\Delta n_U + n_T}{2C_{TI}} - e\frac{\Delta n_L + n_B}{2C_{TI}} = 0 \tag{B.6}$$

$$V_B + \frac{e n_B}{C_B} - \frac{\Delta \mu_L}{e} = 0. \tag{B.7}$$

Here, $\Delta n_{U,L} = n_{U,L} - n^0_{U,L}$ and $\Delta \mu_{U,L} = \mu_{U,L} - \mu^0_{U,L}$, reflecting the fact that both surfaces may initially have a finite density of carriers (or equivalently a Fermi energy away from the Dirac point). These four equations can be condensed into an equivalent set of two equations that reflect the mirror symmetry of the system:

$$e\Delta n_U = C_T\left[V_T - \frac{\Delta \mu_U}{e}\right] - C_M\left[\frac{\Delta \mu_U}{e} - \frac{\Delta \mu_L}{e}\right] \tag{B.8}$$

$$e\Delta n_L = C_B\left[V_B - \frac{\Delta \mu_L}{e}\right] - C_M\left[\frac{\Delta \mu_L}{e} - \frac{\Delta \mu_U}{e}\right] \tag{B.9}$$

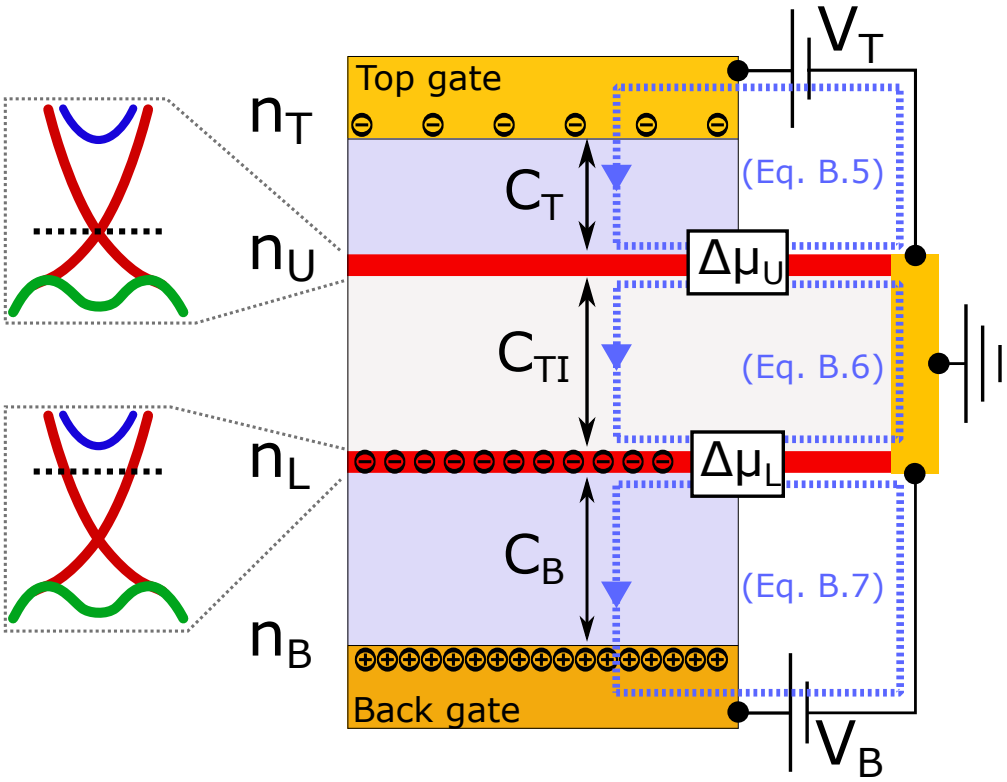

Figure B.6.: Schematic of the charging model from the main text. The equation labels refer to the equation associated with the surrounding voltage loop.

Written this way, equations B.8 and B.9 describe the net charge acquired by the upper and lower surface states, respectively. In both equations, the first bracket represents classical capacitive charging with a quantum capacitance correction. The second bracket represents an additional correction due to the inter-surface potential difference.

B.6.2. Fitting Procedure

Equations 5 and 6 in the main text serve as a transformation of the trajectory in gate-gate space into μ and n, with three unknowns: the inter-surface capacitance C_{TI} and the initial densities of the two surface states $n^0_{U,L}$. The latter two quantities can be equivalently written down as an initial chemical potential relative to the Dirac point $\mu^0_{U,L}$ or as offset voltages necessary to reach charge neutrality $V^0_{T,B}$ for both surfaces simultaneously. The ARPES-derived model for $\mu(n)$ serves as a fixed relationship against which to compare. This can be done in two ways (see table B.1): (1) transform the ARPES measurement into gate-gate space and fit to the transport data, or (2) transform the gate-gate trajectory to μ and n and fit to the ARPES data. These two methods are equivalent, and a least-squares fit is easily performed either way to obtain the same results. In Table B.1, the offset voltages $V^0_{T,B}$ are given as functions of the initial densities $n^0_{U,L}$ and initial chemical potentials $\mu^0_{U,L}$ of the two surfaces. Note that the ARPES model provides a 1:1 relationship between μ and n, thereby reducing $\mu^0_{U,L}$ and $n^0_{U,L}$ to a single variable for each surface.

	Fit transport to ARPES	Fit ARPES to transport
Transformation	$\mu_L = -\frac{C_T}{C_{TI}} e V_T'$ $\frac{en_L}{C_B} = V_B' + \left(\frac{1}{C_B} + \frac{1}{C_{TI}}\right) C_T V_T'$	$V_T' = -\frac{C_{TI}}{C_T}\frac{\mu_L}{e}$ $V_B' = \frac{en_L}{C_B} + \left(\frac{C_{TI}}{C_B} + 1\right)\frac{\mu_L}{e}$
Offset values	$eV_T^0 = -\left(1 + \frac{C_{TI}}{C_T}\right)\mu_U^0 - \frac{e^2 n_U^0}{C_T} + \frac{C_{TI}}{C_T}\mu_L^0$ $eV_B^0 = -\left(1 + \frac{C_{TI}}{C_B}\right)\mu_L^0 - \frac{e^2 n_L^0}{C_T} + \frac{C_{TI}}{C_B}\mu_U^0$	V_T^0 (same) V_B^0 (same)

Table B.1.: The equivalent pair of equations for fitting transport to ARPES (left) or ARPES to transport (right), including the values for the a priori unknown offset voltages.

B.6.3. Surface-State Model

To constrain $\mu(n)$, the analysis of the ARPES data presented earlier is used for the surface bands by substituting $k = \sqrt{4\pi n}$ into equation B.1. Additionally, in BSTS crystals of the same composition as in this study, scanning tunneling microscopy measurements on bulk pieces have found a disorder-induced distribution of Dirac point energies that can vary by up to 40 meV [123, 109]. To account for this effect, the surface state density of states is convolved with a Gaussian that has a standard deviation of 20 meV. Variation of this number has minimal effect on the analysis.

To complete $\mu(n)$, the bulk bands must be addressed. Along the considered trajectory in gate-gate space (see main text), the chemical potential of the upper surface state is at the Dirac point. As the lower surface charges, a large potential gradient forms in the bulk, equivalent to the chemical potential difference between the surfaces $edV/dz \sim \mu_L/(42\text{ nm})$. This potential gradient forms a strong, asymmetric confining potential for the bulk bands. The lowest bulk sub-bands become significantly separated in energy while also being pushed to higher energies overall, as shown in Fig. B.7. As a result, more charge is necessary to reach the bulk bands than naively expected from looking at the static bulk band structure in ARPES. This is taken into account for the effective relationship for $\mu_L(n_L)$ – the bulk conduction band is approximated as a massive two-dimensional electron gas at the upper surface and at an energy 50 meV above the ARPES value for the conduction band minimum. The final relationship between μ and n is best written as

$$n(\mu) = n_{SS}(\mu) + n_{CB}(\mu) \tag{B.10}$$

$$n_{CB}(\mu) = \frac{m_{CB}}{2\pi\hbar^2}\theta\left[\mu - E_{CBM}\right], \tag{B.11}$$

where n_{SS} is the inverted form of Eq. B.1 and $\theta[x]$ is the Heaviside step function. This contribution of bulk states to the model is relevant for less than 10% of the data. Note that this approximation for the conduction band ignores the fact that the center of charge of the sub-band exists at a finite distance from the surface (≈ 5 nm) and that the potential well continues to change shape as the sub-band is filled. A complete treatment of this effect is beyond the scope of this study and would require fully self-consistent Poisson-Schrodinger calculations.

Finally, to determine the top gate geometric capacitances, all devices are measured by Atomic

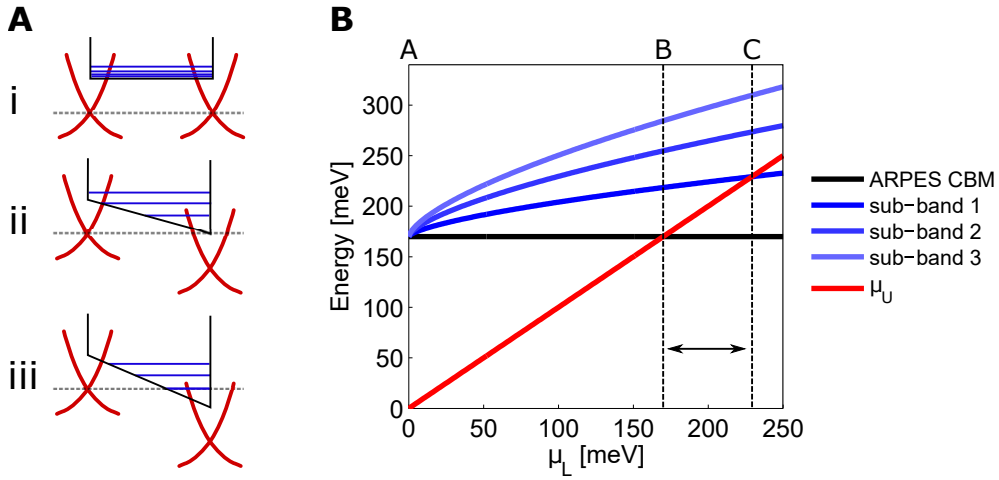

Figure B.7.: Evolution of quantum well states of the conduction band when the upper surface is at the Dirac point while the lower surface is charged by a gate. **A,** Schematic of the band structure at three different doping configurations. (i) is when both surface states are at the Dirac point; (ii) is when μ_L state is at the nominal ARPES value for the conduction band minimum; (iii) is the condition when a bulk sub-band actually begins to be filled. **B,** Energy levels of states in the system as a function of μ_L while keeping μ_U at the Dirac point. The red line is μ_L itself, and the solid black line is the nominal energy of the conduction band minimum given by ARPES. The three blue lines are the first three sub-bands if a half-triangular confining potential is assumed. In reality the confinement is stronger due to the finite thickness of the sample, as shown schematically in **A**. Finally, the configurations i, ii, and iii are labeled at the top of **B**, including vertical dashed lines for ii and iii to emphasize the energy difference.

Force Microscopy to obtain the thickness of the hexagonal boron nitride (h-BN) layer. For all devices, the h-BN (top-gate dielectric) is 13nm thick, and a dielectric constant of 3 is assumed. Additionally, the SiO_2 (bottom gate dielectric) is 285 nm thick with a dielectric constant of 3.9. These numbers give $C_B = 12.1$ nF cm^{-2} and $C_T = 204.3$ nF cm^{-2}.

B.7. Temperature-Dependence of Charging Behavior

A finite inter-surface capacitance C_{TI} persists up to high temperatures, as observed by the $V_{peak}(V_B)$ shown in Fig. B.8a at 100 K. The characteristic non-linear shape of the gate-gate trajectory remains, indicating the continued prominence of screening by the lower surface density of states, allowing the model to be applied as before. At 100 K, C_{TI} is reduced by approximately 35% relative to low temperatures, and this relative reduction is independent of magnetic field (Fig. B.8b). Thermal expansion of the crystal lattice may cause less than a 1% change in C_{TI} [345], and the permittivities of related materials are not known to have significant temperature dependence. Temperature is also unlikely to significantly change the surface state band-structure (this would require an increase in the surface density of states by over 30%). Therefore, weak screening from activated bulk states is a likely cause, and we interpret the temperature dependence as an effect on C_{TI} and not a change to the surface state band structure.

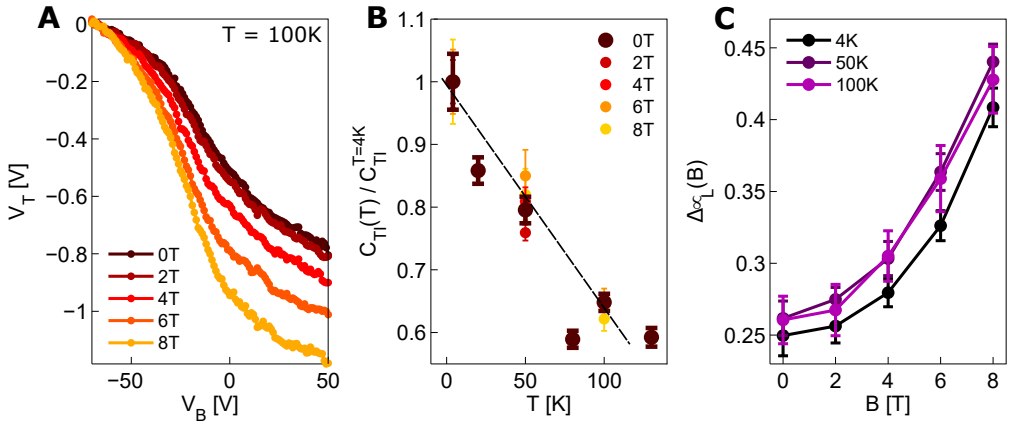

Figure B.8.: Temperature dependence of the device A's charging behavior. **A,** $V_{peak}(V_B)$ at $T = 100$ K and at different magnetic fields. The behavior is qualitatively similar to the low-temperature data. Curves have been offset to align at $V_B = -70$ V to increase clarity of the field dependence. **B,** Temperature dependence of the inter-surface capacitance for different magnetic fields normalized to the low-temperature value: $C_{TI}(T)/C_{TI}^{T=4\mathrm{K}}$. The dashed line is a guide to the eye. Error bars represent 90% confidence intervals from the fit. **C,** The total chemical potential change as a function of magnetic field assuming C_{TI} only depends on temperature and not magnetic field. For all three temperatures, the total chemical potential change remains approximately the same magnitude. Error bars represent a standard-deviation of possible values.

Despite the large reduction, C_{TI} remains significant even at 100 K. The fact that magnetic field has no measurable effect on the temperature dependence of C_{TI} is a possible indication that magnetic field and temperature affect distinctly different parts of the system. For each temperature, C_{TI} is extracted at $B = 0$. We then assume that C_{TI} depends only on temperature and not magnetic field: for each temperature, the zero-field C_{TI} is used to transform the gate-gate trajectories at higher magnetic fields. In this way the field-dependence of the total chemical potential change is obtained (see also the main text), as shown in Fig. B.8c. For all temperatures, the total chemical potential change has the same magnetic field dependence. If a large band-gap is indeed opening in the surface state, a temperature scale of ~ 8 meV will do little to modify the overall density of states. This analysis supports the hypothesis that temperature and magnetic field separately affect, C_{TI} and $\mu(n)$, respectively.

C. Additional Details for Charge Puddle Model

C.1. Reminder On Dielectric Image Charges

Screening from dielectric interfaces is modeled by "imperfect dielectric image charges", which are the same as the image charges that appear at metal-dielectric interfaces except with a smaller value to the image charge's magnitude. In the case of two semi-infinite regions of different dielectric constants, only a single pair of image charges must be considered, one for each region. Taking the original charge q_{charge} at position z inside the material with permittivity κ_1, then

$$Q' = q_{charge}\frac{\kappa_1 - \kappa_2}{\kappa_1 + \kappa_2} \tag{C.1}$$

This image charge is located at the usual position, $-z$. Note that this is consistent with the case of one of the "dielectrics" being a metal by setting $\kappa_2 \to \infty$ which gives $Q' = -q_{charge}$. The sanity checks are:

$$\lim_{\kappa_2 \to \kappa_1} Q' = 0 \tag{C.2}$$

$$\lim_{\kappa_2 \to \infty} Q' = -q \tag{C.3}$$

Note that the above image charge only corrects the field in the dielectric with κ_1. For the field in the dielectric with κ_2 (where the original charge is not), then we simply replace the original charge with a charge of different magnitude and use only that new charge to determine the potential:

$$Q'' = q_{charge}\frac{2\kappa_2}{\kappa_1 + \kappa_2} \tag{C.4}$$

as sanity checks:

$$\lim_{\kappa_2 \to 0} Q'' = 0 \tag{C.5}$$

$$\lim_{\kappa_2 \to \kappa_1} Q'' = q_{charge} \tag{C.6}$$

We see that

$$Q' + Q'' = q_{charge}, \tag{C.7}$$

which is related to one of the electrostatic boundary conditions of the problem.

For determining the potential at the interface of the two semi-infinite slabs, we can use

$$\begin{aligned}
\phi &= \phi_q + \phi_{Q'} && \text{(C.8)}\\
&= \frac{1}{\kappa_1}\frac{q}{\sqrt{0+r^2}}\left(1+\frac{\kappa_1-\kappa_2}{\kappa_1+\kappa_2}\right) && \text{(C.9)}\\
&= \frac{1}{\kappa_1}\frac{q}{r}\left(\frac{2\kappa_1}{\kappa_1+\kappa_2}\right) && \text{(C.10)}\\
&= \frac{2}{\kappa_1+\kappa_2}\frac{q}{r} && \text{(C.11)}
\end{aligned}$$

which is a way to derive that the effective dielectric constant κ_s for a 2D system is the arithmetic mean of the dielectrics above and below.

C.2. Image Charge Approximation for Imperfect 2DEG

Here, we check the approximation stated in section 2.3.2.2, that the screened potential of a charged impurity a distance z from a metallic surface state with a finite screening length r_s is well-approximated by introducing a single image charge located at $z + r_s$ [2]:

$$\phi_1 = \frac{e}{\kappa_s}\left(\frac{1}{\sqrt{r'^2+(z'-z)^2}} - \frac{1}{\sqrt{r'^2+(z'+r_s+z_0)^2}}\right). \tag{C.12}$$

Because the surface state also exists at a dielectric discontinuity, we can (in linear response) model the response with several image charges. First is the image charge of the dielectric itself, which is placed at $-z$ and has a reduced charge

$$Q' = \frac{\kappa_1-\kappa_2}{\kappa_1+\kappa_2}q \tag{C.13}$$

where $\kappa_{1,2}$ are the dielectric constants of the TI and outside dielectric, respectively. To model the screened potential due to the surface state, we can write down that the surface state screens both of the charge and the dielectric image charge. So we have four terms for the potential inside the TI:

$$\frac{\kappa_1}{e}\phi_1 = \frac{1}{\sqrt{r'^2+(z'-z)^2}} - \frac{1}{\sqrt{r'^2+(z'+r_s+z)^2}} + \frac{\kappa_1-\kappa_2}{\kappa_1+\kappa_2}\frac{1}{\sqrt{r'^2+(z'+z)^2}} - \frac{\kappa_1-\kappa_2}{\kappa_1+\kappa_2}\frac{1}{\sqrt{r'^2+(z'+r_s+z)^2}} \tag{C.14}$$

At the surface, $z = 0$:

$$\frac{\kappa_1}{e}\phi_1 = \frac{1}{\sqrt{r'^2+z'^2}} - \frac{1}{\sqrt{r'^2+(r_s+z')^2}} + \frac{\kappa_1-\kappa_2}{\kappa_1+\kappa_2}\left(\frac{1}{\sqrt{r'^2+z'^2}} - \frac{1}{\sqrt{r'^2+(r_s+z')^2}}\right) \tag{C.15}$$

$$= \frac{2\kappa_1}{\kappa_1+\kappa_2}\frac{1}{\sqrt{r'^2+z'^2}} - \frac{2\kappa_1}{\kappa_1+\kappa_2}\frac{1}{\sqrt{r'^2+(r_s+z')^2}} \tag{C.16}$$

$$\phi_1 = \frac{e}{\kappa_s}\left(\frac{1}{\sqrt{r'^2+z'^2}} - \frac{1}{\sqrt{r'^2+(r_s+z')^2}}\right) \tag{C.17}$$

Where we see that the problem reduces to two image charges with the effective surface permittivity κ_s as we had hoped. For completeness, let us take the limit of large z'/r_s:

$$\phi_1 = \frac{e}{\kappa_s}\left(\frac{1}{\sqrt{r'^2+z'^2}} - \frac{1}{\sqrt{r'^2+z'^2(1+\frac{r_s}{z'})^2}}\right) \tag{C.18}$$

$$\approx \frac{e}{\kappa_s}\frac{1}{\sqrt{r'^2+z'^2}}\left(1 - \frac{1}{\sqrt{1+\frac{2zr_s}{r'^2+z'^2}}}\right) \tag{C.19}$$

$$\approx \frac{e}{\kappa_s}\frac{z'r_s}{(r'^2+z'^2)^{\frac{3}{2}}} \tag{C.20}$$

which reproduces equation 13 in [2].

For the $z' > 0$ case, equation C.14 can be partially reduced:

$$\frac{\kappa_1}{e}\phi_1 = \frac{1}{\sqrt{r'^2+(z'-z)^2}} + \frac{\kappa_1-\kappa_2}{\kappa_1+\kappa_2}\frac{1}{\sqrt{r'^2+(-z'-z)^2}} - \frac{2\kappa_1}{\kappa_1+\kappa_2}\frac{1}{\sqrt{r'^2+(-z'-r_s-z)^2}} \tag{C.21}$$

and for $z' \gg r_s$ we can approximate:

$$\frac{\kappa_1}{e}\phi_1 \approx \frac{1}{\sqrt{r'^2+(z'-z)^2}} - \frac{1}{\sqrt{r'^2+(z'+z)^2}} + \frac{2\kappa_1 r_s}{\kappa_1+\kappa_2}\frac{(z'+z)+\frac{1}{2}r_s}{(r'^2+(z'+z)^2)^{3/2}} \tag{C.22}$$

This formula deserves a comment. The first two terms represent the approximation of a perfectly screening surface, e.g. the original charge and a simple image charge. The last

term is the correction, which represents an anti-screening dipole moment located directly on top of the image charge. This dipole has a moment of $p = \frac{2e\kappa_1}{\kappa_1+\kappa_2} r_s$. As a sanity check, we see that $p \to 0$ if either $r_s \to 0$ or $\frac{\kappa_2}{\kappa_1} \to \infty$, both of which represent the creation of a perfect metal at or beyond the interface.

C.3. Slab Geometry Results

C.3.1. Potential at a test charge

The iteration method in Section C.2 can be used to solve for the potential of a test charge between two grounded metallic plates, which is often done to derive the "corrected" barrier height for a tunnel junction between two metallic plates. A closed-form analytical solution exists at $z = d/2$. Simmons gives a well-known approximation, albeit inexact[346].

$$V_{approx}(z) = -\frac{1.15e^2 \ln(2)}{8\pi\varepsilon} \frac{d}{z(d-z)} \tag{C.23}$$

However, there is a simple numerical solution. Separating out the first image charge that doesn't involve any factors of d, the remainder of the sum of images has a useful reduction, as shown by the sequence of equations below

$$\begin{aligned} \frac{4\pi\varepsilon}{e^2} V &= -\frac{1}{2z} + \frac{1}{2d} \sum_{n=1}^{\infty} \left[\frac{2}{n} - \frac{1}{n+\frac{z}{d}} - \frac{1}{n-\frac{z}{d}} \right] && \text{(C.24)} \\ &= -\frac{1}{2z} + \frac{1}{2d} \left[\psi^{(0)}\left(1-\frac{z}{d}\right) + \psi^{(0)}\left(1+\frac{z}{d}\right) + 2\gamma \right] && \text{(C.25)} \\ &\approx -\frac{1}{2z} + \frac{1}{2d} \left[\psi^{(0)}\left(1-\frac{z}{d}\right) + \psi^{(0)}\left(1+\frac{z}{d}\right) + 1.15443 \right] && \text{(C.26)} \end{aligned}$$

where $\psi^{(0)}(z)$ is the 0th derivative of the digamma function, and γ is the Euler-Mascheroni constant. As shown in Figure C.1, this function lands exactly in the middle of any sequential iterations of the sum (which converge slowly and have an even-odd effect). Equation (C.26) moreover has the correct analytic value at the center of the system. So we have found our function!

C.3.2. Potential with Perfectly Screening Surfaces

Now we need also to consider the potential due to the original charge. For this appendix section we stay in the axis of the test charge, e.g. $r = 0$. The potential in summation form

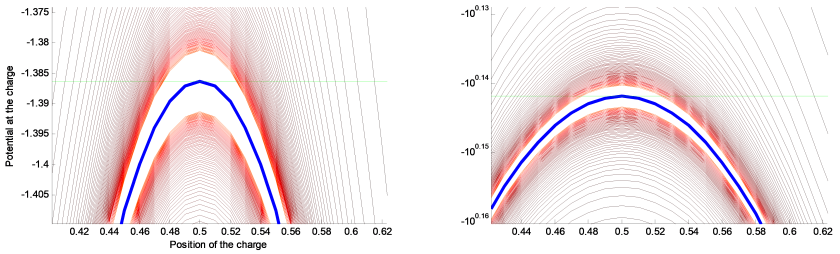

Figure C.1.: Potential at the position of the test charge as a result of its images. From black to red are lines indicating progressively more terms being included in the sum the convergence eventually is very slow and alternates about the ultimate mean curve. The blue line is Eq. (C.26), which is clearly the converged case, and the green line represents the analytical value at the position exactly between the surfaces ($z = 0.5$).

is then

$$\begin{aligned}\frac{4\pi\kappa_1}{e^2}\phi_1\left(z;z_0\right) =& \frac{1}{|z_0 - z|} - \frac{1}{|-z_0 - z|} \\ &+ \frac{1}{2d}\sum_{n=1}^{\infty}\left[\frac{1}{\left|n + \frac{z_0 - z}{2d}\right|} + \frac{1}{\left|-n + \frac{z_0 - z}{2d}\right|} - \frac{1}{\left|n - \frac{z_0 + z}{2d}\right|} - \frac{1}{\left|-n - \frac{z_0 + z}{2d}\right|}\right]\end{aligned} \tag{C.27}$$

which also happens to have a useful reduction:

$$\begin{aligned}\frac{4\pi\kappa_1}{e^2}\phi_1\left(z;z_0\right) =& \frac{1}{|z_0 - z|} - \frac{1}{|-z_0 - z|} \\ &+ \frac{1}{2d}\left[\psi^{(0)}\left(1 + \frac{z_0 + z}{2d}\right) + \psi^{(0)}\left(1 - \frac{z_0 + z}{2d}\right)\right] \\ &- \frac{1}{2d}\left[\psi^{(0)}\left(1 + \frac{z_0 - z}{2d}\right) + \psi^{(0)}\left(1 - \frac{z_0 - z}{2d}\right)\right]\end{aligned} \tag{C.28}$$

where again $\psi^{(0)}(x)$ is the 0th derivative of the digamma function. With this function in hand, we can show that the potential does indeed go to zero at the surfaces, as shown for a few test cases in Figure C.2.

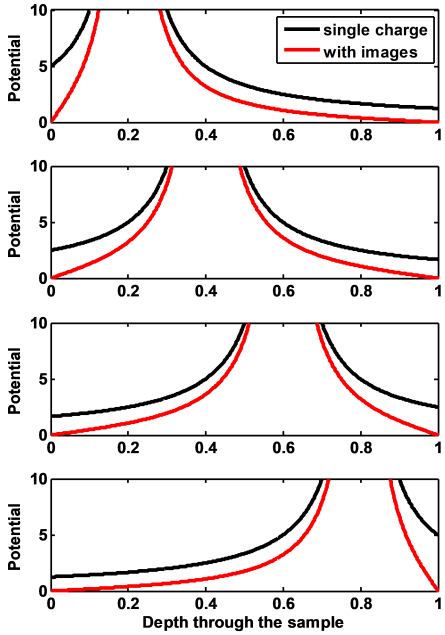

Figure C.2.: Electrostatic potential due to a test charge at different positions in a slab geometry. Black line is the bare test charge potential, while the red line includes the image charges.

D. Additional Details for Experiment on Semimetallic Phase in Trilayer WTe_2

D.1. Semiclassical Model

D.1.1. Two-Carrier Model

The model equations for magnetoresistance for a two carrier system are given in the main chapter as equations (4.38) and (4.39), and reproduced below. The R_{xx} and R_{xy} data are fitted simultaneously by these equations. Three different methods for accomplishing the fit are shown in the following subsections. Note that while the data does not display enough complexity to add additional carriers to the model without over-specifying the problem, the simplest-case two-carrier model is sufficient to qualitatively describe the system.

$$e\rho_{xx} = \frac{n\mu_n + p\mu_p + (n\mu_p + p\mu_n)\,\mu_n\mu_p B^2}{(n\mu_n + p\mu_p)^2 + (p-n)^2\,\mu_n^2\mu_p^2 B^2} \tag{D.1}$$

$$e\rho_{xy} = \frac{\left(p\mu_p^2 - n\mu_n^2\right) B + (p-n)\,\mu_n^2\mu_p^2 B^3}{(n\mu_n + p\mu_p)^2 + (p-n)^2\,\mu_n^2\mu_p^2 B^2}, \tag{D.2}$$

D.1.1.1. Unconstrained Fit

An unconstrained fit produces acceptable results with small confidence intervals for the fit parameters, as shown in Figure D.1. However, the total carrier density does not evolve monotonically with the gate voltage. In order to address this problem, we use a constrained fit (see next subsection).

D.1.1.2. Constrained Fit

Here, we constrain the electron density to be within 10% of the total value measured from the Shubnikov-de Haas (SdH) oscillation analysis (see main text). To convert the SdH frequency to density, we assume a degeneracy factor of two, which is justified by finding that the electron density from the unconstrained fit (previous subsection) has roughly double the total electron charge density from the SdH analysis. A valley degeneracy factor of two is indeed expected for all thicknesses for the conduction band (see various band structure calculations, e.g. [171]), and the two pockets seen in the SdH analysis (labeledα and β in

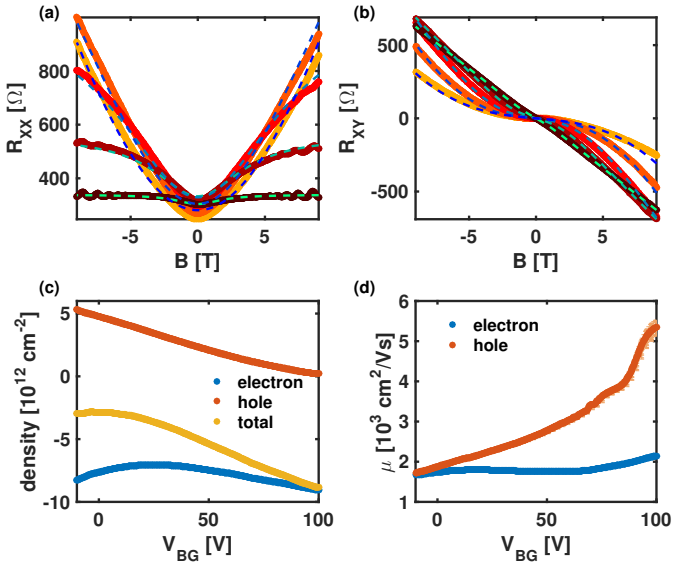

Figure D.1.: Unconstrained Fit. (a) $R_{xx}(B)$ and (b) $R_{xy}(B)$ for a representative set of gate voltages. Solid lines are the raw data, and dashed lines are the fits. (c) The electron, hole, and total charge densities (including charge sign) as a function of gate voltage. (d) Mobility of the electrons and holes as a function of gate voltage. 95% confidence intervals are included in (c-d) but may be smaller than the marker size.

the main text) likely come from a lifting of the spin degeneracy by spin-orbit coupling. With this constraint, the fit parameters have the same qualitative behavior as the unconstrained fit, with an overall monotonic gate-dependence of the total carrier density (see Fig. D.2(c)).

D.1.1.3. Fitting without Magnetoresistance

Another possible concern is that a non-quadratic magnetoresistance (see Figure (4.5)(e-f)) is being fit by a model that expects quadratic behavior. To avoid this, we can fit just the Hall effect constrained by the zero-field longitudinal resistance and the quantum oscillation information (as in the previous subsection). These fit are shown in Figure D.3. Again, the fit parameters display similar qualitative behavior, although the confidence intervals are not as good for low gate voltages, and the model does underestimate the magnitude of the magnetoresistance.

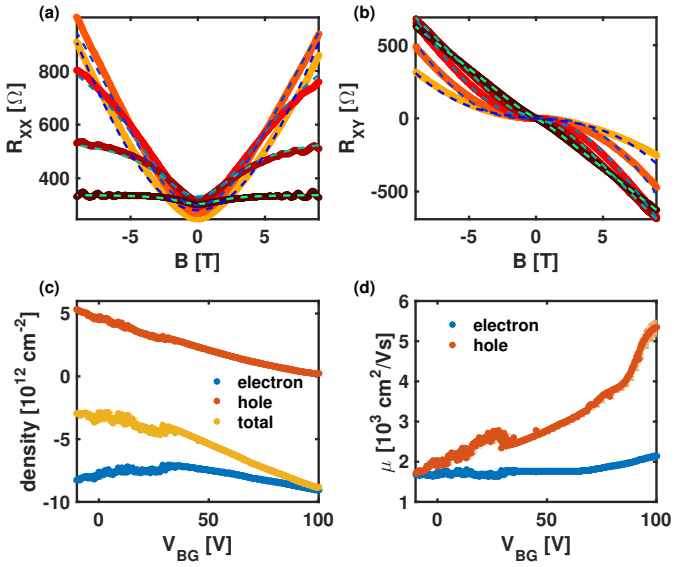

Figure D.2.: Constrained Fit. (a) $R_{xx}(B)$ and (b) $R_{xy}(B)$ for a representative set of gate voltages. Solid lines are the raw data and dashed lines are the constrained fits described in the text. (c) The electron, hole, and total charge densities (including charge sign) as a function of gate voltage. (d) Mobility of the electrons and holes as a function of gate voltage. 95% confidence intervals are included in (c-d) but may be smaller than the marker size.

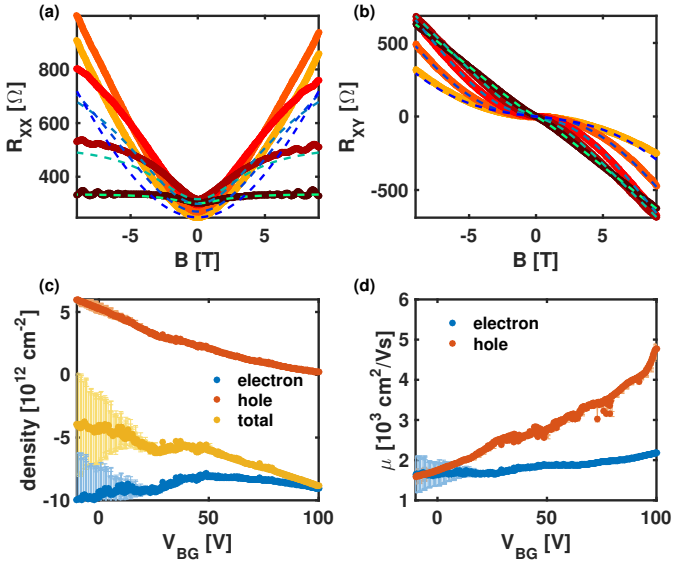

Figure D.3.: Fitting without magnetoresistance. (a) $R_{xx}(B)$ and (b) $R_{xy}(B)$ at a representative set of gate voltages. Solid lines are the raw data and dashed lines are the fits described in the main text. (c) The electron, hole, and total charge densities (including charge sign) as a function of gate voltage. (d) Mobility of the electrons and holes as a function of gate voltage. 95% confidence intervals are included in (c-d) but may be smaller than the marker size.

D.2. Characterization of Few-Layer Graphene Contacts

Few-layer graphene (FLG) is a component of our contacts, which may have non-trivial magnetic-field and/or gate dependence. We show the behavior of all utilized FLG contacts in Figure D.4 by measuring in two-probe format. The FLG and its contact resistance to the WTe_2constitutes the greatest resistance in the sample and therefore dominates the signal in two-probe measurements. We observe ambipolar gating behavior in the resistance at zero magnetic field as well as SdH oscillations that are indicative of FLG at different doping. By simultaneously measuring the source-drain current and local voltage drops in a four-probe configuration, these features in the contact resistance do not appear in the data.

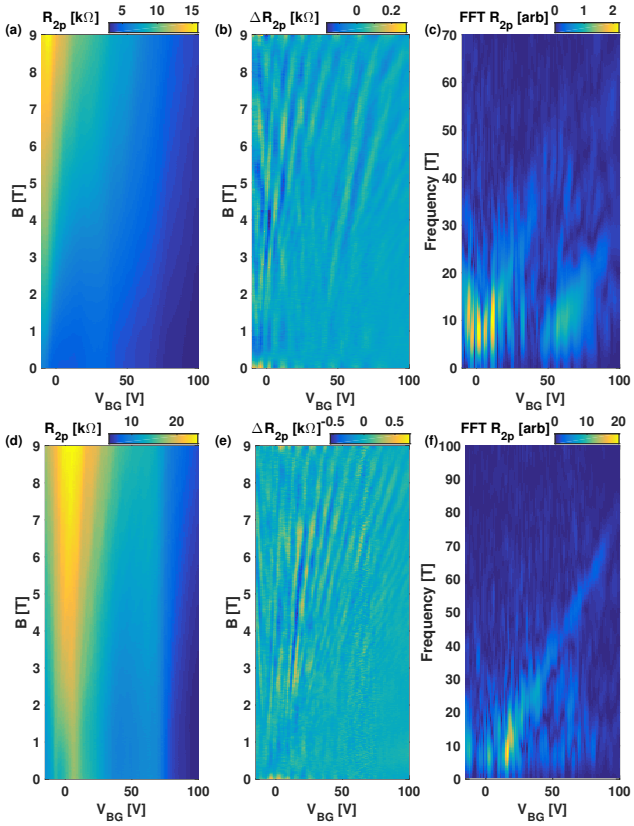

Figure D.4.: First row: source and drain electrodes. Second row: side contacts. (a,d) Raw two-probe resistance as a function of gate voltage and magnetic field. (b,e) Two-probe resistance after subtracting a smooth polynomial as a function of magnetic field for each gate voltage, ΔR_{2p}. (c,f) The amplitude of the Fourier transform of $\Delta R_{2p}(\frac{1}{B})$ (from b and e, respectively) at each gate voltage.

D.3. Quantum Oscillation Analysis

D.3.1. Additional Plots of the SdH Data

Additional figures of the SdH oscillations are shown in Figure D.5. Figure D.5(a) shows the raw data of the gate and magnetic field dependence of the longitudinal resistance. Figure D.5(b) shows the same data with a smooth background subtracted at each gate voltage, similar to Figure (4.6)(c), except that here we additionally normalize each magnetic field sweep to its maximal value so that the weaker oscillations at low gate voltage are easier to discern. In Figure D.5(c) we show the fast Fourier transform (FFT) of the subtracted data vs $1/B$, which gives peaks at frequencies in units of Tesla. For clarity of presentation, here we separately normalized the data above and below $90T$, as the very strong $\sim 60T$ oscillation around $V_{BG} \sim 100V$ produces a tall peak that tends to wash out the other data. We obtain the the peak position values shown in Figure (4.6)(d) in the main text from this map.

We note that the the strength of the α pocket for gate voltages $V_{BG} < 50V$ is substantially weaker than for $V_{BG} > 50$. There is still spectral weight there from which we extract an approximate peak value. However, the α peak is much more easily seen in the R_{xy} data in cooldown 1, shown in Figure D.6(d) (highlighted by the red arrow). The data from longitudinal resistance data is consistent across both cooldowns, as seen in Figures D.5(c) and D.6(c).

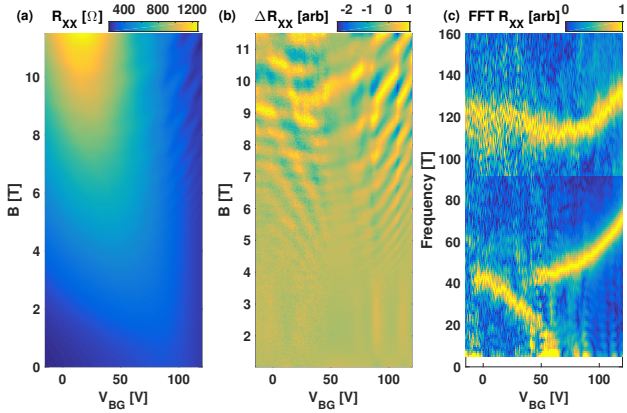

Figure D.5.: Data same as in Figure (4.6) in the main text, which is from cooldown 2 at 30 mK. (a) Color map of the longitudinal resistance as a function of magnetic field and gate voltage. (b) Colormap of the longitudinal resistance with a smooth magnetoresistance background subtracted at each gate voltage. The colorscale is normalized at each gate voltage to highlight the gate voltage dependence independent of oscillation amplitude. (c) FFT of the quantum oscillations at each gate voltage. The FFT is normalized in separate sections above and below $90T$ to highlight the different FFT peak positions.

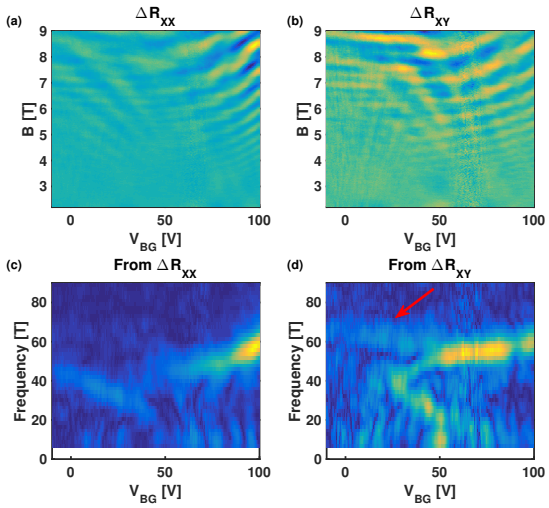

Figure D.6.: Data from cooldown 1 at 300mK. Colormaps of the (a) longitudinal resistance and (b) transverse resistance with a smooth background subtracted at each gate voltage. Here the colorscale is NOT normalized at each gate voltage. (c,d) FFT of the quantum oscillations in R_{xx} and R_{xy} at each gate voltage, again with no normalization. In (d) we highlight the gate-dependence of the α pocket with an arrow.

D.3.2. Temperature Dependence

The temperature dependence of SdH oscillation resistance peaks follows the form of the Lifshitz-Kosevich formula

$$\Delta\rho_{xx}^{peak} = \rho_0 \frac{2\pi^2 k_B T}{\hbar\omega_c} \frac{1}{\sinh\left(\frac{2\pi^2 k_B T}{\hbar\omega_c}\right)} \tag{D.3}$$

$$= \rho_0 \frac{2\pi^2 k_B m^* T}{\hbar e B^{peak}} \frac{1}{\sinh\left(\frac{2\pi^2 k_B m^* T}{\hbar e B^{peak}}\right)} \tag{D.4}$$

where $\Delta\rho_{xx}^{peak}$ is the maximum of a resistivity oscillation relative to the background resistance. Fitting the temperature dependence of a particular resistance maximum to Equation (D.4) is a means of extracting the effective mass of the associated band. In the case of an anisotropic Fermi surface (which is expected for WTe_2), the geometric mean of the effective masses in the plane perpendicular to the magnetic field is extracted.

In a sample with multiple Fermi surfaces (e.g. multiple oscillations in the data), care must be taken to extract information only from an individual oscillation. Here, we use the procedure followed in[347] to extract the temperature dependence of oscillations from individual Fermi surfaces, which involves the following steps: take an FFT of the subtracted resistance data, use a window filter function to isolate the peak in frequency space of the target oscillation, then inverse-FFT the filtered FFT back to resistance space to see the contribution of the individual oscillation. Figures D.7(a-c) show representative Lifshitz-Kosevich fits for the

extracted peak values for each oscillation. We note that the effective masses shown in the main text are determined by doing this fit to multiple resistance peaks at multiple gate voltages and taking the average of the extracted effective mass for each frequency. We only do this analysis for gate voltages at which the peaks are maximally prominent: the α and β frequencies for $V_{BG} > 80V$, and the δ frequency for $V_{BG} < 40V$.

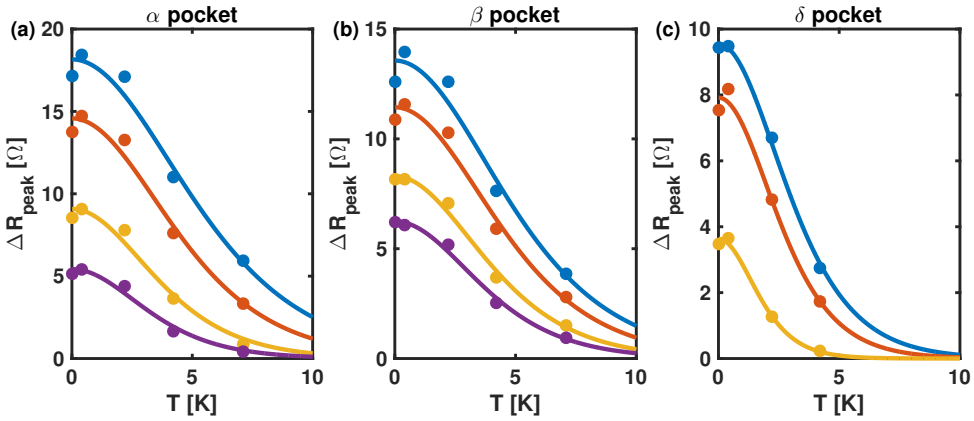

Figure D.7.: Temperature dependence of different SdH oscillation maxima at a fixed gate voltage for each of the three pockets . (a) The α pocket at $V_{BG} = 120V$. (b) The β pocket at $V_{BG} = 120V$. (c) The δ pocket at $V_{BG} = 0V$.

D.4. Additional Data

Here we present additional data on two further devices (devices B and C), corroborating the data presented in the main text. These devices were fabricated by picking up 3-layer thick WTe_2 with an approximately 30nm-thick piece of hBN and placing it onto pre-deposited 70nm-thick PdAu contacts. This results in a suspended device for which the hBN serves as a stiff backbone to support the WTe_2. Optical microscopy images of both devices are shown in Figure D.8.

These devices had residual resistivity ratios of 4.7 and 3.3, affirming the metallic nature of the samples. Plots of the temperature dependence are not shown because the cryostat used to measure devices B and C was not equipped for temperature measurements above 10K.

These devices were also found to have a magnetoresistance with a power law $\sim B^{1.6}$, as shown in Figures D.9 and D.10. The power law exponent remains within 10% of this value for all gate voltages investigated for both devices, as shown in Figure D.9(c-d) and Figure D.10(c-d). We note that for Device B, when applying a high gate voltage, the device mobility abruptly changed (likely due to a change in the configuration of the suspended structure), resulting in an offset in the curves between Figure D.9(b) and Figure D.9(c). However, the general behavior does not otherwise change. Additionally, we also find quantum oscillations in device C, which can be seen in Figure D.10(b).

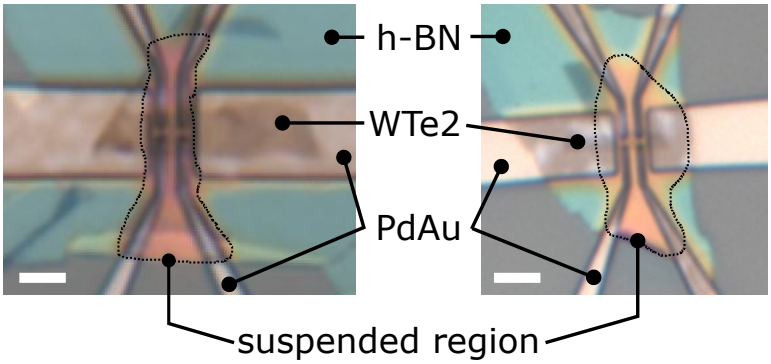

Figure D.8.: Optical microscopy images of devices B (left) and C (right), with different aspects labeled. Scale bar is $3\mu m$.

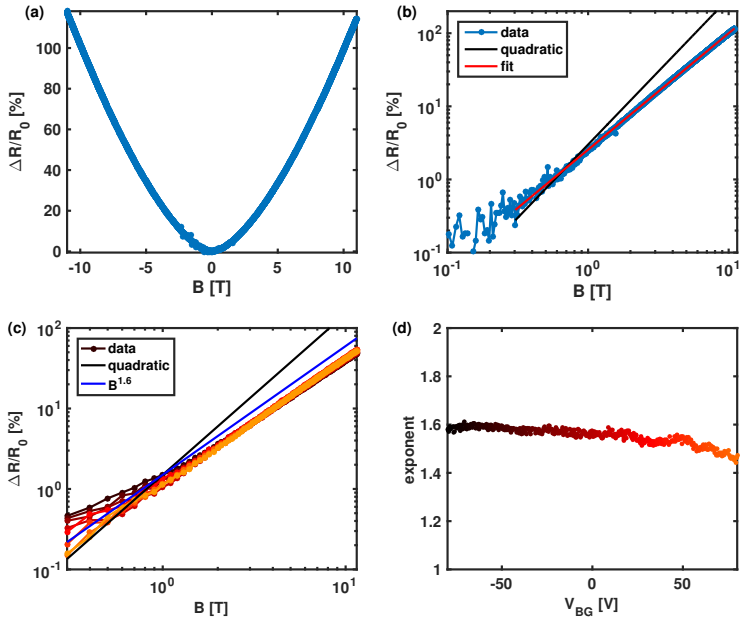

Figure D.9.: (a-b) Magnetoresistance of device B before applying a gate voltage. In (b) the black and red lines are quadratic field dependence and power law fit (fit between 0.3 and 11.5 T), giving an exponent of 1.6. (c) Data (connected dots) at several different gate voltages (color indexed by color in (d)) between -80V and +80V, with solid lines showing B^2 (black) and $B^{1.6}$ (blue) behaviors for comparison. Note that this is after a change of the device mobility, resulting in a lower total MR but the same power law. (d) Fitted exponent (for the field range between 1 and 11.5 T) as a function of gate voltage.

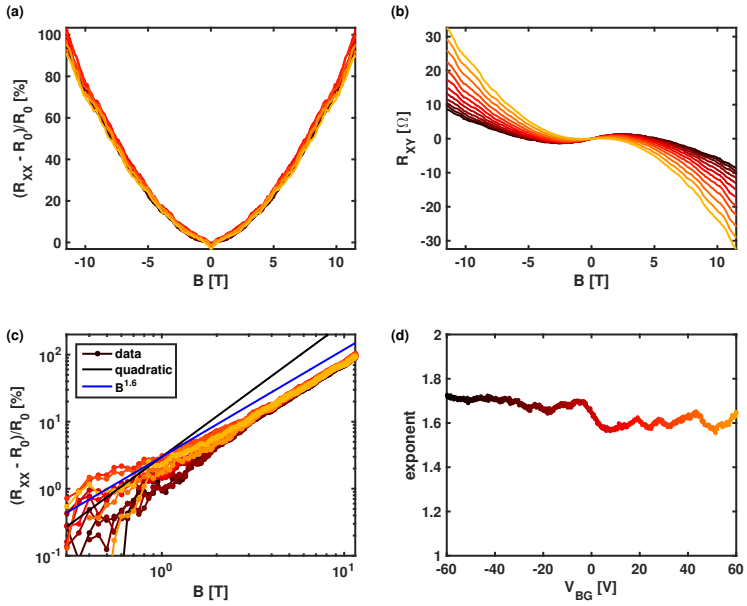

Figure D.10.: Measurements for device C. For this device, only the source, drain, and a pair of Hall probes were functioning. The Hall measurements were found to have a large mixing of the longitudinal signal. The data presented as R_{xx} and R_{xy} is the symmetric and antisymmetric portion of this signal, respectively. (a-b) Magnetoresistance ratio and Hall effect at different gate voltages. Weak quantum oscillations can also be seen in (b). (c) Data (connected dots) at several different gate voltages between -60V and +60V indexed by color consistent with (d). Solid lines show B^2 (black) and $B^{1.6}$ (blue) behaviors for comparison. (d) Fitted exponent (for the field range between 3 and 11.5 T) as a function of gate voltage.

E. Additional Details for Topological Insulator Study

E.1. Materials and Methods

E.1.1. General Fabrication Scheme

The WTe_2 bulk crystals were grown as described in[138]. The gates and electrodes of our devices are fabricated prior to the exfoliation of WTe_2. The detailed fabrication process is described below and illustrated in Fig. E.1.

1. Creation of Gate Electrodes (Fig. E.1(a-c))
    a) Dice Si++/SiO_2 wafer into appropriately sized pieces, followed by spin-coating and baking a bilayer PMMA-based resist:
        i. 495A5, spun at 2000 rpm for 60 seconds, baked at 180C for 7 minutes
        ii. 950A5, spun at 3000 rpm for 60 seconds, baked at 180C for 3 minutes
    b) Electron beam lithography in an Elionix F125 system (acceleration voltage 125keV) to define gate electrodes with widths ranging from 50nm to 900nm.
    c) Develop resist in a cold water:IPA (1:3 by weight) mixture.
    d) Deposit Cr(3nm)/PdAu(30nm) in a thermal evaporator.
    e) Liftoff with successive baths of acetone and dichloromethane (DCM), followed by sonication in Remover PG, and final rinse in acetone and IPA.
    f) Heat clean at 300C for 3+ hours in forming gas (H2 + Ar).
2. Transfer of bottom hBN (Fig. E.1(d-f))
    a) Exfoliate hBN onto cleaned Si/SiO_2 wafer.
    b) Heat clean at 400C for 3+ hours in forming gas.
    c) AFM to ensure cleanliness of the flake.
    d) Pick up and transfer the flake onto the gates via standard dry transfer techniques using a polycarbonate/PDMS stamp.
    e) Remove the transfer polymer with chloroform.
    f) Heat clean at 300C for 3+ hours in forming gas.

3. Creation of Contact Electrodes (Fig. E.1(g-i))

   a) Spin and bake of a PMMA-based bilayer resist recipe.

   b) Electron beam lithography to define contacts.

   c) Develop resist in a cold water:IPA (1:3 by weight) mixture.

   d) Deposit Ti(3nm)/PdAu(30nm) in a thermal evaporator. The height of the electrodes matches the local gates, to minimize the stressed (not fully encapsulated) region at the vicinity of the inner-most contacts.

   e) Liftoff with successive baths of acetone, DCM, and IPA.

   f) Tip clean surface of hBN with contact mode AFM.

   g) Mount chip into chip carrier and wire bond.

4. Transfer of WTe_2 and top gate electrode (Fig. E.1(j,k))

   a) Prepare appropriate hBN and graphite pieces as per steps 2(a-c).

   b) WTe_2 flakes are exfoliated and identified in an argon glove box system with < 0.1 ppm of both O2 and H2O.

   c) Also in the glove box, pick up a global top hBN, then graphite top-gate electrode, then hBN to serve as top gate dielectric, and finally the target WTe_2 flake.

   d) Transfer entire stack onto pre-fabricated and pre-bonded gates and contacts.

   e) Remove transfer polymer with chloroform.

   f) Extract from glove box and immediately pump down in a cryostat.

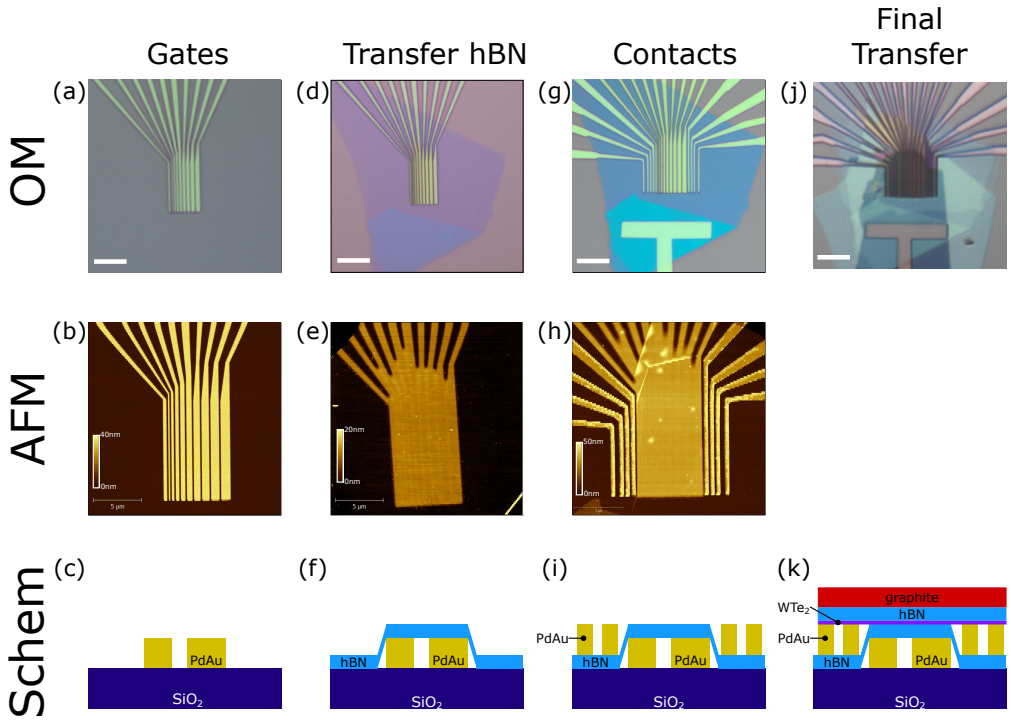

Figure E.1.: Images of fabrication steps. Optical microscopy (OM) images (upper row) and atomic force microscopy (AFM) images (middle row) taken at each key stage of the fabrication process. The images in the lower row are cross-sectional schematics to illustrate the structure.

E.1.2. Individual Device Details

Five devices are investigated in this study. Device 1 is discussed in depth in the main text, and images from its fabrication are shown in Fig. E.1. Table E.1 displays important parameters for each device.

Dev. #	Bottom hBN Thickness	Top hBN Thickness	Length btwn Contacts	WTe_2 Width
1	13 nm	9 nm	7.2 μm	1 μm
2	16 nm	9 nm	4.0 μm	3 μm
3	10 nm	11 nm	4.0 μm	4 μm
4	19 nm	10 nm	7.2 μm	7 μm
5	15 nm	9 nm	2.7 μm	4 μm

Table E.1.: Table of Device Parameters

E.1.3. Raman Analysis

We show a typical Raman spectrum taken from our exfoliated monolayer in Fig. E.2. The spectrum is consistent with the literature[175, 172, 348], verifying the 1T' phase. The monolayer nature is also characterized by its transport behavior, as shown in Fig. 5.2B.

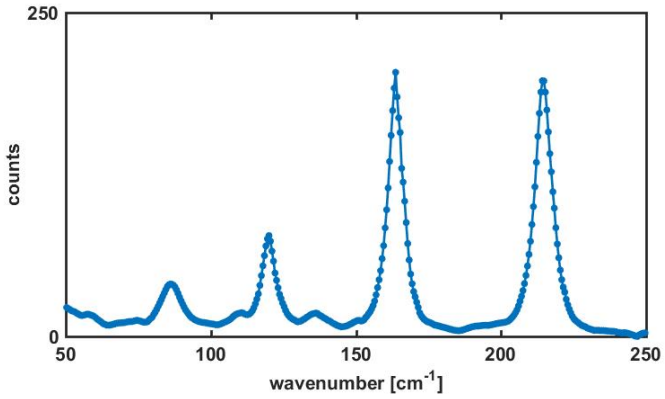

Figure E.2.: Raman spectrum of an exfoliated monolayer of WTe_2 taken at room temperature with a 532nm excitation laser, consistent with the 1T' phase of monolayer WTe_2.

E.1.4. Measurement Details

Electronic transport measurements are conducted in a cryostat equipped with a superconducting magnet and a variable temperature 3He insert. The resistance is typically measured by applying a ~50μV low-frequency AC voltage source (~17Hz) using lock-in techniques. All the resistance data is measured under zero DC bias. DC bias almost has no effect on the resistance, as summarized in Fig. E.3, indicating Ohmic contacts.

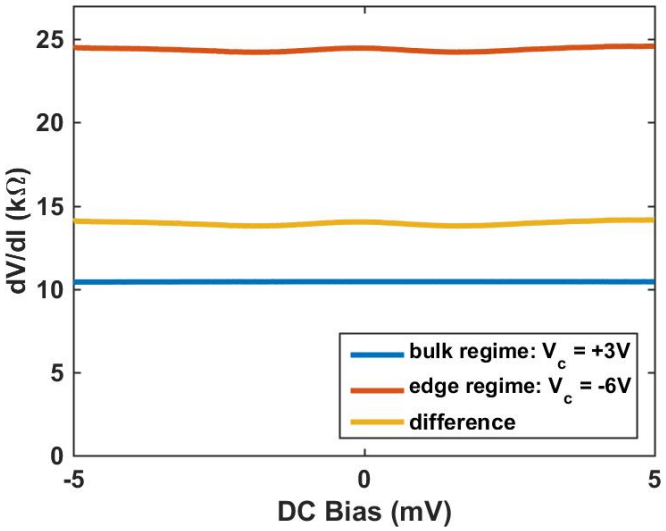

Figure E.3.: dV/dI as a function of DC bias for $V_{tg} = 3.5$V on device 1 measured in four-terminal configuration at 4K. Blue and orange correspond to the bulk regime (V_c = 3V) and edge regime (V_c = -6V), respectively. The difference is in yellow. The flat dV/dI indicates linear ohmic contacts.

E.2. Additional Data

E.2.1. Extracting the Plateau Values

As mentioned in Fig. 5.2 of the main text, we performed a careful analysis to extract the value of the resistance plateaus. Generically, when we sweep the local gate voltage V_c to negative values, we observe a resistance step in transition to the QSH plateau. This resistance step is measured as a function of the global top-gate voltage V_{tg}, as illustrated in Fig. E.4. The onset of the step in V_c changes with top gate voltage because the doping level local region is determined coordinately by both gates. In general, as the bulk becomes more highly doped by the top gate, the resistance step decreases and then converges, indicating the improvement of the contact between the doped bulk regions and the edge modes. We consider the converged value at the highest gate voltage as the extracted edge resistance ΔR_s, with an error given by the standard deviation of the step height at that top-gate voltage. We present figures displaying representative analysis of several cases (Fig. E.4-E.7).

We also notice a particular case shown in Fig. E.7 (the 500 nm-wide gate in Device 1), in which the resistance trace displays a second step appearing at even more negative V_c. This second step is a feature that appears for some of the longer channels (some hints of it are also visible in Fig. E.4). A natural explanation is that the local gate dopes the channel into the valence band, transitioning from a n-edge-n device configuration of the first plateau to an n-edge-p-edge-n junction, as shown in the inset schematics. In this case, the second step would reflect the resistance change between the new n-edge-p-edge-n junction and n-edge-n junction. For example, the p-region may break the single edge mode into two edge modes in series, and may also scatter the carriers from one edge to the opposite. Therefore, a p region can reduce their transmission and result in an increase in resistance, as we observe. In our main analysis, we focus on the first step, which captures the resistance of just the edge mode with a length defined by the local gate.

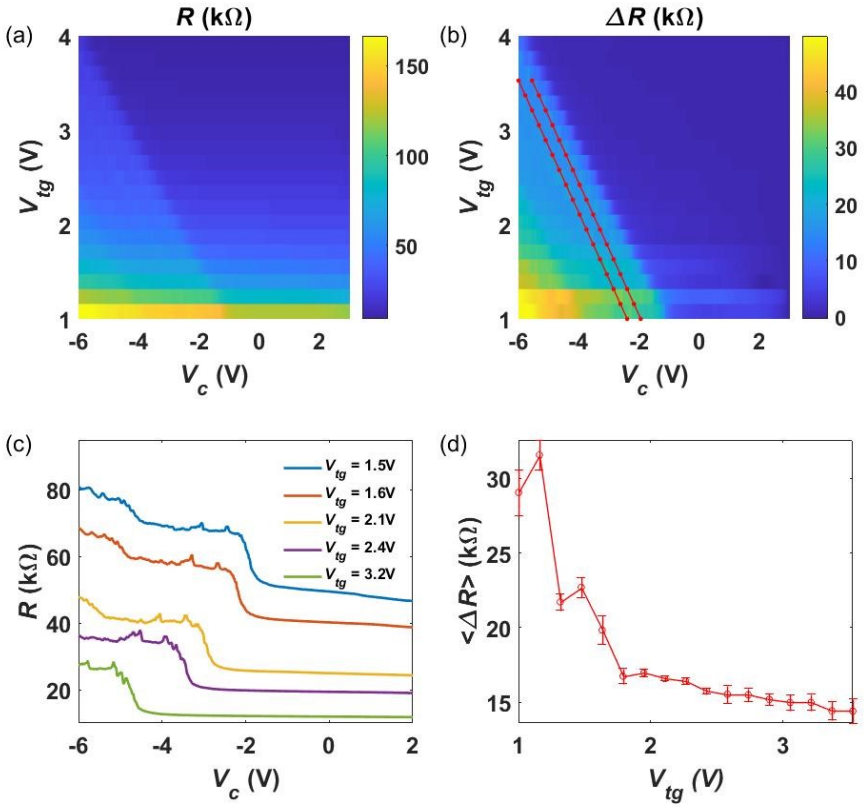

Figure E.4.: Analysis to extract the edge resistance – Device 1, 100nm gate, 4 K. (a) Total resistance as a function of top gate and local gate voltage (V_{tg} and V_c, respectively), for device 1 with the 100nm-wide local gate. (b) The same data as (a) with the resistance at $V_c = 3$V subtracted away, which we designate ΔR. The space between the red dotted lines indicates the range of ΔR on the step that is averaged to extract the step height. (c) Specific traces of total resistance vs V_c showing how the traces change progressively with increasing top-gate voltage. (see the Appendix text and Fig. E.7 for explanation on signatures of second step). (d) A plot of the step resistance as a function of V_{tg}, showing the saturation at large V_{tg}. The error bars indicate a full standard deviation from the mean ΔR in the range given by the red dots in (b).

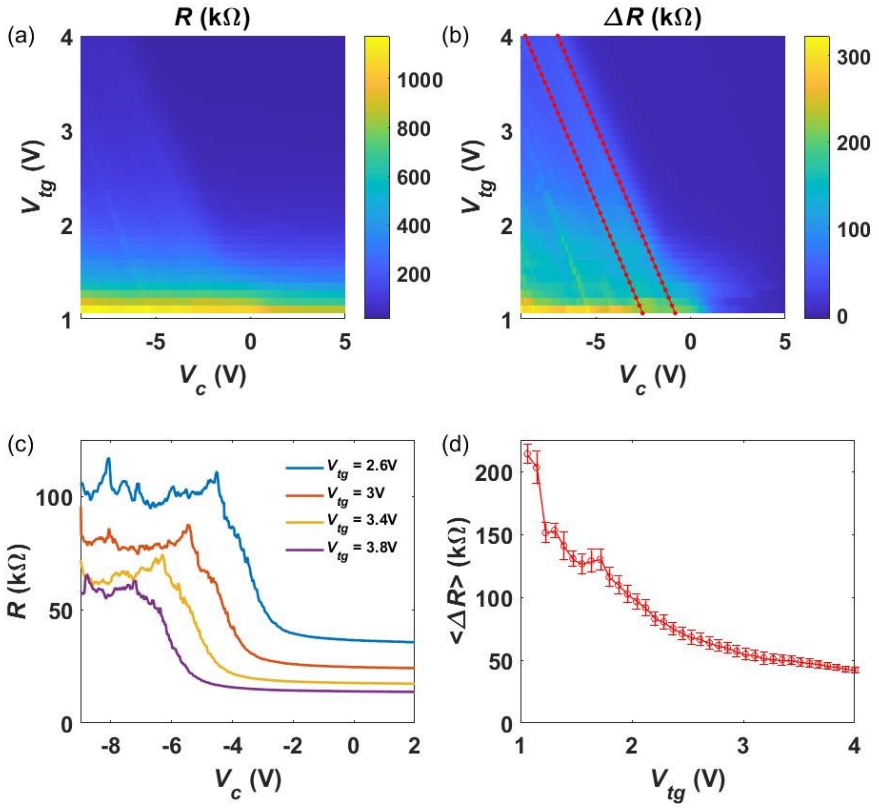

Figure E.5.: Analysis to extract the edge resistance – Device 4, 400nm gate, 4 K. Same as Fig.E.4, but for the 400nm-wide gate in Device 4. The resistance of this long channel saturates to a resistance well above what is measured in the short-channel limit. In general, we have observed increased resistance with increasing length in long channel devices (Fig. 5.3). This increase of resistance can be understood by considering dephasing scatterers at the edges. The helical edge mode is equilibrated at the dephasing sites, which effectively break the long edge mode into multiple in series, resulting in a trend of increasing total resistance. Device-to-device variation for the same channel length can thus be attributed to differing disorder realizations for the different devices.

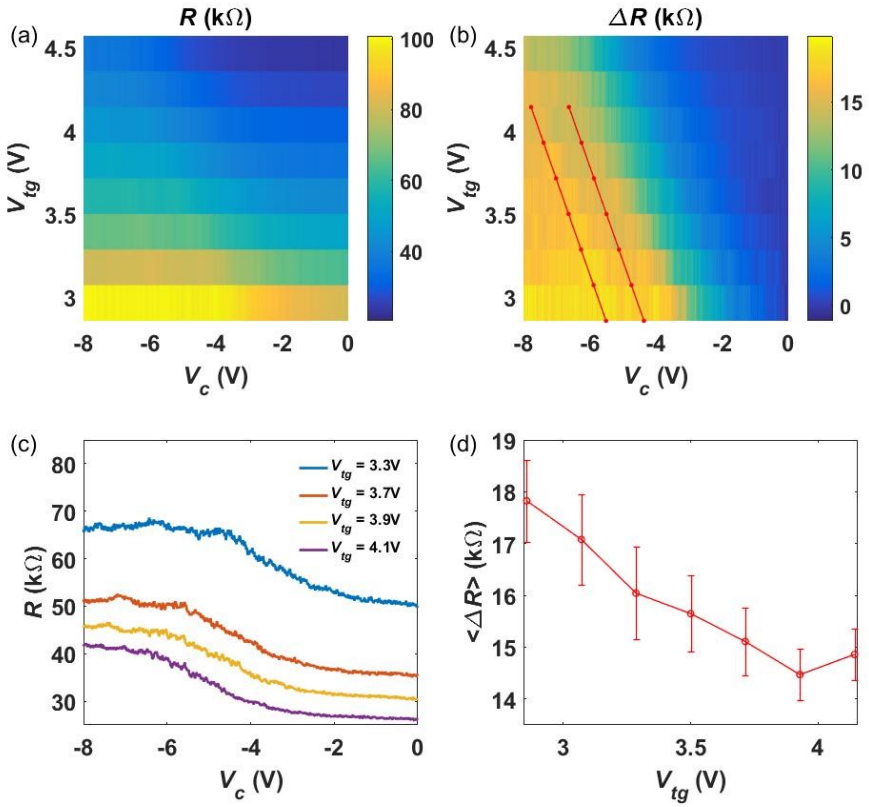

Figure E.6.: Analysis to extract the edge resistance – Device 2, 100 nm gate, 4 K. Same as Fig. E.4, but for the 100nm-wide gate in Device 2, which shows a similar converged resistance step value as in Device 1.

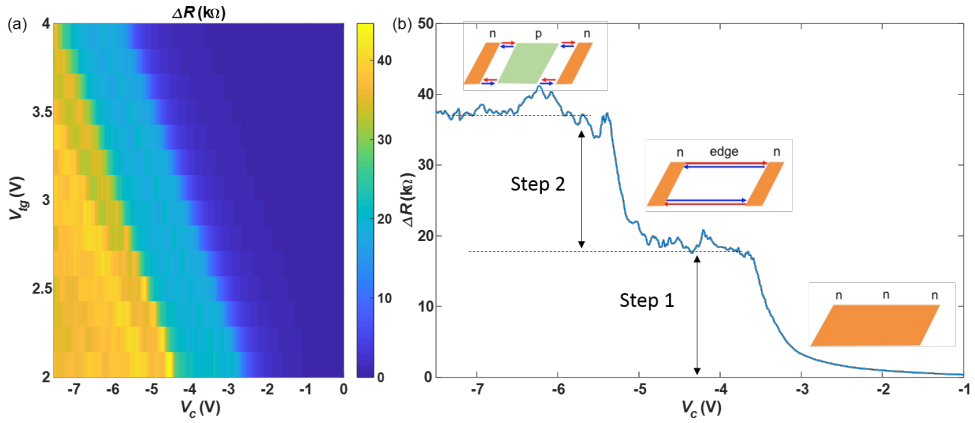

Figure E.7.: Channel resistance with a second step. (a) ΔR as a function of both gate voltages and (b) a representative line-cut of ΔR vs. V_c at V_{tg} = 2.6 V for the 500nm-wide local gate in Device 1 at 4 K. The second step exhibited here appears especially for a few of our longer channels. It could be related to the creation of an n-edge-p-edge-n junction as indicated by the schematics in panel (b). See supplementary text for details. The height of the first step is extracted as the channel resistance of the edge mode with length defined by the local gate.

E.2.2. Bulk State Magnetic Field Dependence

The magnetoresistance in the highly doped bulk regime is small and approximately linear with field, as shown in Fig. E.8. This magnetoresistance is largely temperature independent, and its weakness (< 5% change up to 8T) shows that the strong magnetic field dependence displayed in the edge regime does not originate from bulk states

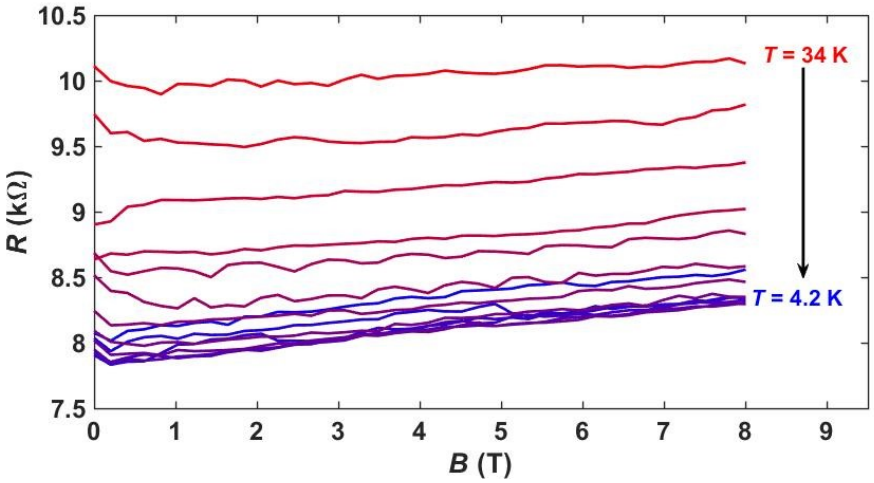

Figure E.8.: Magnetic field dependence of the resistance in the bulk-doped regime (V_{tg} = +3.5 V) at different temperatures. The weak magnetoresistance here shows that the strong magnetoresistance observed in the edge regime is unrelated to bulk states.

E.2.3. Saturation Conductance in High Magnetic Field

In the main text, it was noted that the edge conductance saturates to a finite value at high magnetic field for most gate voltages in the QSH regime. In Fig. E.9(a), we show the gate dependence of the edge conductance for magnetic fields between 5 and 8 Tesla. The device has little change of behavior in this field range for most gate voltages away from Dirac point, again demonstrating the saturation. Fig. E.9(b) shows characteristic magnetic-field dependences at the same gate voltages as in the main text (Fig. 5.5B), but on a linear scale. A histogram of all conductance extrema along gate voltage traces (determined algorithmically in MATLAB) at magnetic fields between 5 and 8 T produces the plot shown in Fig. E.9(c). Theoretical predictions suggest that a single ballistic helical edge mode with a single charge puddle is expected to exhibit a 50% reduction of transmission at high magnetic fields(24), or similarly a dephasing charge puddle can effectively "break" a single QSH mode into two in series(30). Extending this to two edges and multiple puddles leads to a high-field conductance of $\left(\frac{1}{m+1}+\frac{1}{n+1}\right)e^2/h$ where m and n are integers that count the number of charge puddles coupled to each edge. The expected saturated values (0.5, 0.66, 0.83, and 1) e^2/h for several cases of m and n are indicated in the plots. Our data is suggestive of the prediction, with the number of charge puddles varying with the local gate voltage but usually very few (< 3 per edge). Further investigation in both experiment and theory are necessary to fully understand the mechanism.

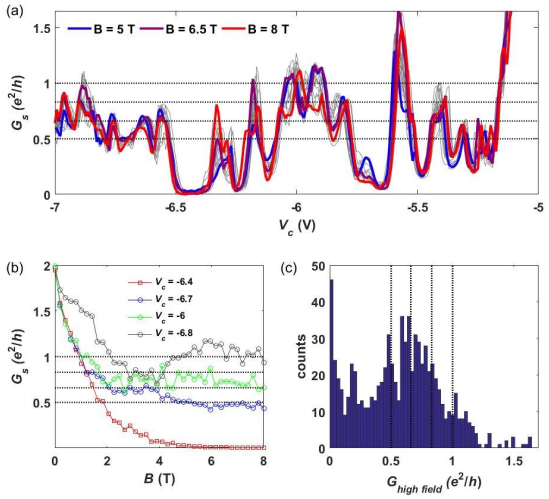

Figure E.9.: Saturation conductance of the edge modes at high magnetic fields. (a) Magnetic field dependence of the edge conductance from $B = 5$T to 8T, with three specific traces highlighted and all others in gray. The dotted lines indicate values (0.5, 0.66, 0.83, 1) expected from scenarios based on charge puddles (see supplemental text for details). (b) A few specific traces of the edge conductance as a function of magnetic field. In red is the exponential behavior near the Dirac point, and the other three traces show typical saturation behavior. Dotted lines are the same as in (a). (c) A histogram of all local conductance extrema along gate voltage traces ($G_{high\ field}$) from 5T to 8T, with dotted lines again highlighting the same values (see supplementary text for details).

E.2.4. In-Plane Magnetic Field

We also find that in-plane magnetic fields degrade the edge conductance. In Fig. E.10, we show the edge conductance as a function of local gate voltage for a 100nm-wide gate in Device 2. In this case, we don't see a clear Dirac point but rather a more uniform degradation of the edge conductance for all gate voltages. The absence of the Dirac point in this case requires future work to understand. Generally, the observation of a gap opening at the Dirac point requires a magnetic field non-parallel to the spin polarization axis of the edge modes as well as nearly identical conditions for both edges, which may include offset density, disorder strength, crystallographic orientation, and edge termination. Moreover, crystallographic orientation and edge termination may influence whether a Dirac point in the edge state exists inside the bulk gap. We currently do not have the fine control over these parameters to engage in a targeted study of this physics. Nonetheless, our observations encourage further studies of the Dirac point in monolayer TIs, both experimentally and theoretically.

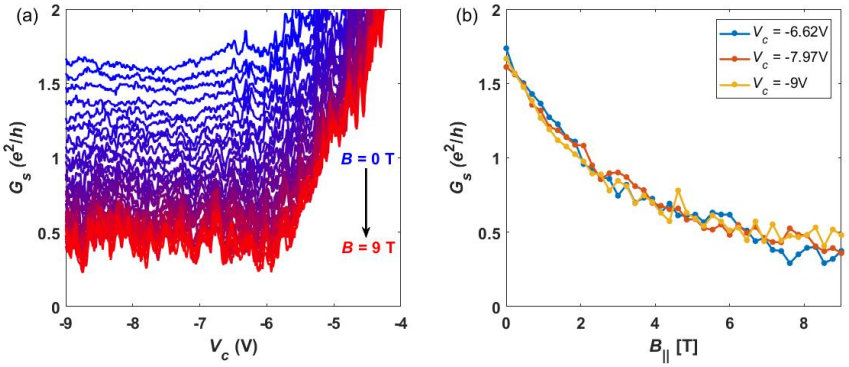

Figure E.10.: In-plane magnetoresistance. (a) Edge conductance as a function of local gate voltage V_c for different in-plane, roughly perpendicular-to-edge, magnetic field strengths at 4 K for the 100nm-wide gate of Device 2. (b) Line traces of resistance as a function of magnetic field for selected V_c. The conductance is clearly suppressed under in-plane magnetic fields. This device does not have a distinct Dirac point, but instead sees a uniform decrease in conductance, possibly due to a different edge configuration or non-uniform disorder strength at the edges compared to Device 1.

E.2.5. Temperature Dependence of the Edge Resistance in High Magnetic Field

As shown in Fig. 5.4(c) of the main text, the edge resistance has temperature and magnetic field dependences that suggest a Zeeman-like gap in a narrow gate voltage range. All of the high-resistance features that exist at low temperature are strongly suppressed with increasing temperature. In Fig. E.11 we show the gate voltage dependence as a function of magnetic field for four representative temperatures, observing that sharp and tall features become broad and shallow as temperature is raised.

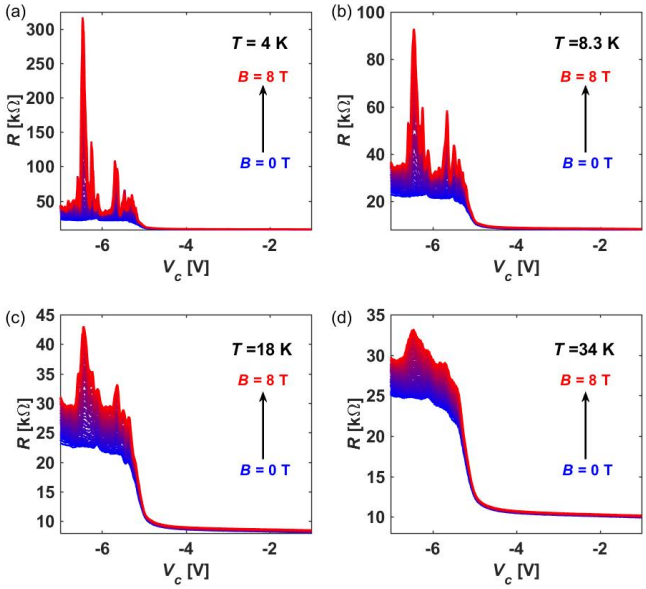

Figure E.11.: Magnetic field effect at different temperatures. Raw data for the temperature dependent magnetoresistance measurements for Device 1, 100 nm local channel. Resistance vs. local gate voltage V_c subjected to different magnetic fields for a representative set of temperatures: (a) 4 K, (b) 8.3 K, (c) 18K, and (d) 34 K.

F. Additional Details for Experiment on Superconductivity in Monolayer WTe_2

F.1. Transition to Insulating State in Device 1

The evolution of the $R(T)$ characteristic for device 1 in shown in Figure F.1. The transition to the insulating phase occurs at roughly $V_{tg} \approx 1.1V$. The top hBN has a thickness of 9 nm, giving a critical density of $n \sim 3 \times 10^{12} cm^{-2}$.

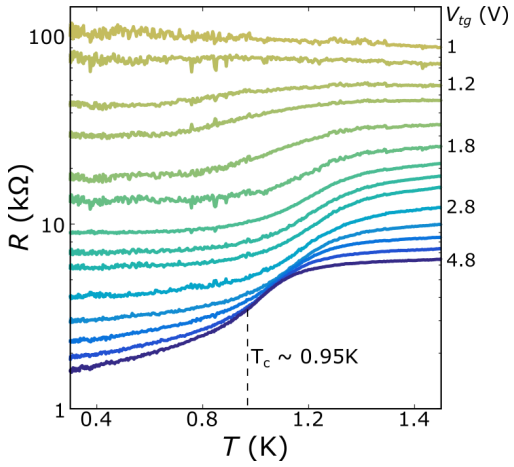

Figure F.1.: Gate voltage dependence of of the $R(T)$ curves for device 1.

F.2. Extrapolation of T_C

Figure F.2 shows the relation between T_c and ρ_n for device 2, which is much less non-linear than the relationship between T_c and V_{bg}. Also shown are fits to a phenomenological cubic relationship between T_c and ρ_n (red) and a linear relationship for low T_c (blue). Because we can measure R_n for a range of gate voltages extending beyond the range at which T_c is measurable, we can extrapolate T_c based on these fits, as shown. While the extended cubic fit is used in Fig. 2B of the main text, we note that the linear (blue) and cubic (red) fittings yield similar critical gate voltages, as indicated in the figure. Note that the extrapolated critical resistances are larger than the pair quantum resistance expected for a bosonic phase transition, but not by much.

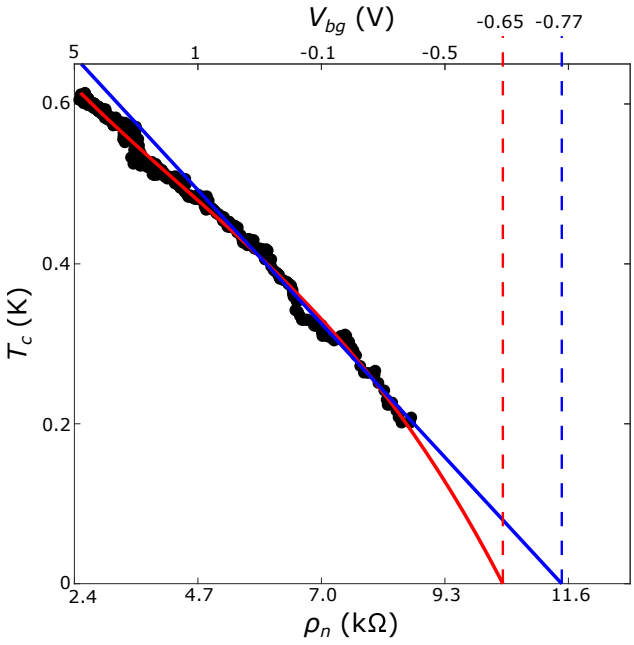

Figure F.2.: T_c as a function of ρ_n, which exhibits a less non-linear relationship than T_c as a function of V_{bg}. The red and blue curves are cubic and linear fits with extrapolation to $T_c = 0$.

F.3. Model Device to Infer Resistivity

The COMSOL simulation for the geometry of device 1 is shown in Figure F.3. Colored lines indicate isopotentials. Red is high voltage and blue is low voltage. Current is sourced from the right-middle contact and drained from the upper-left contact (as may be inferred from the isopotentials). We compare the defined resistivity of the triangular region with the simulated voltage drop between the two contacts on the upper right, which gives us a geometry factor of ~ 0.43.

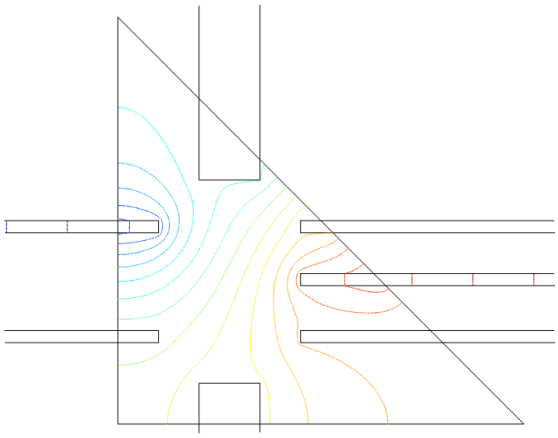

Figure F.3.: Image of the simulated device in COMSOL, with colored lines representing constant voltage lines.

Bibliography

[1] H. O. H. Churchill, V. Fatemi, K. Grove-Rasmussen, M. T. Deng, P. Caroff, H. Q. Xu, and C. M. Marcus. Superconductor-nanowire devices from tunneling to the multichannel regime: Zero-bias oscillations and magnetoconductance crossover. *Physical Review B*, 87(24):241401, June 2013.

[2] B. Skinner, T. Chen, and B. I. Shklovskii. Effects of bulk charged impurities on the bulk and surface transport in three-dimensional topological insulators. *Journal of Experimental and Theoretical Physics*, 117(3):579–592, October 2013.

[3] Baojie Feng, Yang-Hao Chan, Ya Feng, Ro-Ya Liu, Mei-Yin Chou, Kenta Kuroda, Koichiro Yaji, Ayumi Harasawa, Paolo Moras, Alexei Barinov, Walid G. Malaeb, Cedric Bareille, Takeshi Kondo, Shik Shin, Fumio Komori, Tai-Chang Chiang, Youguo Shi, and Iwao Matsuda. Spin Texture in Type-II Weyl Semimetal WTe2. *arXiv:1606.00085 [cond-mat]*, May 2016. arXiv: 1606.00085.

[4] Domenico Di Sante, Pranab Kumar Das, C. Bigi, Z. Ergönenc, N. Gürtler, J. A. Krieger, T. Schmitt, M. N. Ali, G. Rossi, R. Thomale, C. Franchini, S. Picozzi, J. Fujii, V. N. Strocov, G. Sangiovanni, I. Vobornik, R. J. Cava, and G. Panaccione. Three-Dimensional Electronic Structure of the Type-II Weyl Semimetal ${\mathrm{WTe}}_{2}$. *Physical Review Letters*, 119(2):026403, July 2017.

[5] Yun Wu, Daixiang Mou, Na Hyun Jo, Kewei Sun, Lunan Huang, S. L. Bud'ko, P. C. Canfield, and Adam Kaminski. Observation of Fermi arcs in the type-II Weyl semimetal candidate ${\mathrm{WTe}}_{2}$. *Physical Review B*, 94(12):121113, September 2016.

[6] F. Y. Bruno, A. Tamai, Q. S. Wu, I. Cucchi, C. Barreteau, A. de la Torre, S. McKeown Walker, S. Riccò, Z. Wang, T. K. Kim, M. Hoesch, M. Shi, N. C. Plumb, E. Giannini, A. A. Soluyanov, and F. Baumberger. Observation of large topologically trivial Fermi arcs in the candidate type-II Weyl semimetal $\mathrm{WT}{\mathrm{e}}_{2}$. *Physical Review B*, 94(12):121112, September 2016.

[7] Ilya Belopolski, Su-Yang Xu, Yukiaki Ishida, Xingchen Pan, Peng Yu, Daniel S. Sanchez, Hao Zheng, Madhab Neupane, Nasser Alidoust, Guoqing Chang, Tay-Rong Chang, Yun Wu, Guang Bian, Shin-Ming Huang, Chi-Cheng Lee, Daixiang Mou, Lunan Huang, You Song, Baigeng Wang, Guanghou Wang, Yao-Wen Yeh, Nan Yao, Julien E. Rault, Patrick Le Fèvre, François Bertran, Horng-Tay Jeng, Takeshi Kondo, Adam Kaminski, Hsin Lin, Zheng Liu, Fengqi Song, Shik Shin, and M. Zahid Hasan. Fermi arc electronic structure and Chern numbers in the type-II

Weyl semimetal candidate ${\mathrm{Mo}}_{x}{\mathrm{W}}_{1\ensuremath{-}x}{\mathrm{Te}}_{2}$. *Physical Review B*, 94(8):085127, August 2016.

[8] Shujie Tang, Chaofan Zhang, Dillon Wong, Zahra Pedramrazi, Hsin-Zon Tsai, Chunjing Jia, Brian Moritz, Martin Claassen, Hyejin Ryu, Salman Kahn, Juan Jiang, Hao Yan, Makoto Hashimoto, Donghui Lu, Robert G. Moore, Chan-Cuk Hwang, Choongyu Hwang, Zahid Hussain, Yulin Chen, Miguel M. Ugeda, Zhi Liu, Xiaoming Xie, Thomas P. Devereaux, Michael F. Crommie, Sung-Kwan Mo, and Zhi-Xun Shen. Quantum spin Hall state in monolayer 1t'-WTe2. *Nature Physics*, 13(7):683–687, July 2017.

[9] Mazhar N. Ali, Jun Xiong, Steven Flynn, Jing Tao, Quinn D. Gibson, Leslie M. Schoop, Tian Liang, Neel Haldolaarachchige, Max Hirschberger, N. P. Ong, and R. J. Cava. Large, non-saturating magnetoresistance in WTe2. *Nature*, 514(7521):205–208, October 2014.

[10] J. D. van der Waals. J. D. van der Waals - Nobel Lecture: The Equation of State for Gases and Liquids.

[11] H. P. Boehm, R. Setton, and E. Stumpp. Nomenclature and terminology of graphite intercalation compounds. Report by a subgroup of the international committee for characterization and terminology of carbon and graphite on suggestions for rules for the nomenclature and terminology of graphite intercalation compounds. *Synthetic Metals*, 11(6):363–371, October 1985.

[12] K. S. Novoselov, A. K. Geim, S. V. Morozov, D. Jiang, M. I. Katsnelson, I. V. Grigorieva, S. V. Dubonos, and A. A. Firsov. Two-dimensional gas of massless Dirac fermions in graphene. *Nature*, 438(7065):197–200, November 2005.

[13] Yuanbo Zhang, Yan-Wen Tan, Horst L. Stormer, and Philip Kim. Experimental observation of the quantum Hall effect and Berry's phase in graphene. *Nature*, 438(7065):201–204, November 2005.

[14] K. S. Novoselov, A. K. Geim, S. V. Morozov, D. Jiang, Y. Zhang, S. V. Dubonos, I. V. Grigorieva, and A. A. Firsov. Electric Field Effect in Atomically Thin Carbon Films. *Science*, 306(5696):666–669, October 2004.

[15] H. P. Boehm, A. Clauss, G. Fischer, and U. Hofmann. SURFACE PROPERTIES OF EXTREMELY THIN GRAPHITE LAMELLAE. In *Proceedings of the Fifth Conference on Carbon*, pages 73–80. Pergamon, 1962. DOI: 10.1016/B978-0-08-009707-7.50013-3.

[16] R. F. Frindt. Superconductivity in Ultrathin Nb${\mathrm{Se}}_{2}$ Layers. *Physical Review Letters*, 28(5):299–301, January 1972.

[17] S. Helveg, J. V. Lauritsen, E. Lægsgaard, I. Stensgaard, J. K. Nørskov, B. S. Clausen, H. Topsøe, and F. Besenbacher. Atomic-Scale Structure of Single-Layer ${\mathrm{MoS}}_{2}$ Nanoclusters. *Physical Review Letters*, 84(5):951–954, January 2000.

[18] V. Podzorov, M. E. Gershenson, Ch. Kloc, R. Zeis, and E. Bucher. High-mobility field-effect transistors based on transition metal dichalcogenides. *Applied Physics Letters*, 84(17):3301–3303, April 2004.

[19] A. K. Geim and I. V. Grigorieva. Van der Waals heterostructures. *Nature*, 499(7459):419–425, July 2013.

[20] Javier Daniel Sancehz-Yamagishi. *Superlattices and Quantum Spin Hall States in Graphene and Hexagonal Boron Nitride Heterostructures*. PhD thesis, MIT, 2015.

[21] B. Hunt, J. D. Sanchez-Yamagishi, A. F. Young, M. Yankowitz, B. J. LeRoy, K. Watanabe, T. Taniguchi, P. Moon, M. Koshino, P. Jarillo-Herrero, and R. C. Ashoori. Massive Dirac Fermions and Hofstadter Butterfly in a van der Waals Heterostructure. *Science*, 340(6139):1427–1430, June 2013.

[22] C. R. Dean, L. Wang, P. Maher, C. Forsythe, F. Ghahari, Y. Gao, J. Katoch, M. Ishigami, P. Moon, M. Koshino, T. Taniguchi, K. Watanabe, K. L. Shepard, J. Hone, and P. Kim. Hofstadter's butterfly and the fractal quantum Hall effect in moiré superlattices. *Nature*, 497(7451):598, May 2013.

[23] L. A. Ponomarenko, R. V. Gorbachev, G. L. Yu, D. C. Elias, R. Jalil, A. A. Patel, A. Mishchenko, A. S. Mayorov, C. R. Woods, J. R. Wallbank, M. Mucha-Kruczynski, B. A. Piot, M. Potemski, I. V. Grigorieva, K. S. Novoselov, F. Guinea, V. I. Fal'ko, and A. K. Geim. Cloning of Dirac fermions in graphene superlattices. *Nature*, 497(7451):594, May 2013.

[24] Y. Cao, J. Y. Luo, V. Fatemi, S. Fang, J. D. Sanchez-Yamagishi, K. Watanabe, T. Taniguchi, E. Kaxiras, and P. Jarillo-Herrero. Superlattice-Induced Insulating States and Valley-Protected Orbits in Twisted Bilayer Graphene. *Physical Review Letters*, 117(11):116804, September 2016.

[25] R. O. Jones. Model calculation of surface states in silicon. *Journal of Physics C: Solid State Physics*, 5(13):1615, 1972.

[26] C. L. Kane and E. J. Mele. Z2 Topological Order and the Quantum Spin Hall Effect. *Physical Review Letters*, 95(14):146802, September 2005.

[27] M. Z. Hasan and C. L. Kane. Colloquium: Topological insulators. *Reviews of Modern Physics*, 82(4):3045–3067, November 2010.

[28] Xiao-Liang Qi and Shou-Cheng Zhang. Topological insulators and superconductors. *Reviews of Modern Physics*, 83(4):1057–1110, October 2011.

[29] J. E. Moore and L. Balents. Topological invariants of time-reversal-invariant band structures. *Physical Review B*, 75(12):121306, March 2007.

[30] Xiao-Gang Wen. Zoo of quantum-topological phases of matter. *arXiv:1610.03911 [cond-mat]*, October 2016. arXiv: 1610.03911.

[31] D. J. Thouless, M. Kohmoto, M. P. Nightingale, and M. den Nijs. Quantized Hall Conductance in a Two-Dimensional Periodic Potential. *Physical Review Letters*, 49(6):405–408, August 1982.

[32] K. v. Klitzing, G. Dorda, and M. Pepper. New Method for High-Accuracy Determination of the Fine-Structure Constant Based on Quantized Hall Resistance. *Physical Review Letters*, 45(6):494–497, August 1980.

[33] R. Jackiw and C. Rebbi. Solitons with fermion number 1/2. *Physical Review D*, 13(12):3398–3409, June 1976.

[34] B. I. Halperin. Quantized Hall conductance, current-carrying edge states, and the existence of extended states in a two-dimensional disordered potential. *Physical Review B*, 25(4):2185–2190, February 1982.

[35] P. Elbau and G. M. Graf. Equality of Bulk and Edge Hall Conductance Revisited. *Communications in Mathematical Physics*, 229(3):415–432, September 2002.

[36] A. Elgart, G. M. Graf, and J. H. Schenker. Equality of the Bulk and Edge Hall Conductances in a Mobility Gap. *Communications in Mathematical Physics*, 259(1):185–221, October 2005.

[37] Xiao-Liang Qi, Taylor L. Hughes, S. Raghu, and Shou-Cheng Zhang. Time-Reversal-Invariant Topological Superconductors and Superfluids in Two and Three Dimensions. *Physical Review Letters*, 102(18):187001, May 2009.

[38] Yi Zhang, Ke He, Cui-Zu Chang, Can-Li Song, Li-Li Wang, Xi Chen, Jin-Feng Jia, Zhong Fang, Xi Dai, Wen-Yu Shan, Shun-Qing Shen, Qian Niu, Xiao-Liang Qi, Shou-Cheng Zhang, Xu-Cun Ma, and Qi-Kun Xue. Crossover of the three-dimensional topological insulator Bi2se3 to the two-dimensional limit. *Nature Physics*, 6(8):584–588, August 2010.

[39] Andrew M. Essin and Victor Gurarie. Bulk-boundary correspondence of topological insulators from their respective Green's functions. *Physical Review B*, 84(12):125132, September 2011.

[40] Markus König, Steffen Wiedmann, Christoph Brüne, Andreas Roth, Hartmut Buhmann, Laurens W. Molenkamp, Xiao-Liang Qi, and Shou-Cheng Zhang. Quantum Spin Hall Insulator State in HgTe Quantum Wells. *Science*, 318(5851):766–770, November 2007.

[41] Liang Fu, C. L. Kane, and E. J. Mele. Topological Insulators in Three Dimensions. *Physical Review Letters*, 98(10):106803, March 2007.

[42] Rahul Roy. Topological phases and the quantum spin Hall effect in three dimensions. *Physical Review B*, 79(19):195322, May 2009.

[43] Shinsei Ryu, Andreas P. Schnyder, Akira Furusaki, and Andreas W. W. Ludwig. Topological insulators and superconductors: tenfold way and dimensional hierarchy. *New Journal of Physics*, 12(6):065010, 2010.

[44] A. Yu Kitaev. Unpaired Majorana fermions in quantum wires. *Physics-Uspekhi*, 44(10S):131, 2001.

[45] A. Yu. Kitaev. Fault-tolerant quantum computation by anyons. *Annals of Physics*, 303(1):2–30, January 2003.

[46] Michael Freedman, Alexei Kitaev, Michael Larsen, and Zhenghan Wang. Topological quantum computation. *Bulletin of the American Mathematical Society*, 40(1):31–38, 2003.

[47] Chetan Nayak, Steven H. Simon, Ady Stern, Michael Freedman, and Sankar Das Sarma. Non-Abelian anyons and topological quantum computation. *Reviews of Modern Physics*, 80(3):1083–1159, September 2008.

[48] C.w.j. Beenakker. Search for Majorana Fermions in Superconductors. *Annual Review of Condensed Matter Physics*, 4(1):113–136, March 2013.

[49] Sankar Das Sarma, Michael Freedman, and Chetan Nayak. Majorana zero modes and topological quantum computation. *npj Quantum Information*, 1:npjqi20151, October 2015.

[50] Yafis Barlas, Kun Yang, and A. H. MacDonald. Quantum Hall effects in graphene-based two-dimensional electron systems. *Nanotechnology*, 23(5):052001, 2012.

[51] M. O. Goerbig. Electronic properties of graphene in a strong magnetic field. *Reviews of Modern Physics*, 83(4):1193–1243, November 2011.

[52] Armin Khamoshi, Fan Zhang, Gen Long, Gui-Bin Liu, Huanhuan Lu, Jiangxiazi Lin, Ning Wang, Shuigang Xu, Tianyi Han, Yingying Wu, Yuan Cai, Yugui Yao, Yuheng He, and Zefei Wu. Even–odd layer-dependent magnetotransport of high-mobility Q-valley electrons in transition metal disulfides. *Nature Communications*, 7:12955, September 2016.

[53] Shuigang Xu, Junying Shen, Gen Long, Zefei Wu, Zhi-qiang Bao, Cheng-Cheng Liu, Xiao Xiao, Tianyi Han, Jiangxiazi Lin, Yingying Wu, Huanhuan Lu, Jianqiang Hou, Liheng An, Yuanwei Wang, Yuan Cai, K. M. Ho, Yuheng He, Rolf Lortz, Fan Zhang, and Ning Wang. Odd-Integer Quantum Hall States and Giant Spin Susceptibility in p-Type Few-Layer ${\mathrm{WSe}}_{2}$. *Physical Review Letters*, 118(6):067702, February 2017.

[54] Hema C. P. Movva, Babak Fallahazad, Kyounghwan Kim, Stefano Larentis, Takashi Taniguchi, Kenji Watanabe, Sanjay K. Banerjee, and Emanuel Tutuc. Density-Dependent Quantum Hall States and Zeeman Splitting in Monolayer and Bilayer ${\mathrm{WSe}}_{2}$. *Physical Review Letters*, 118(24):247701, June 2017.

[55] Chang Liu, Chih-Kang Shih, Hyoungdo Nam, Ireneusz Miotkowski, Jifa Tian, Jiuning Hu, M. Zahid Hasan, Nasser Alidoust, Yang Xu, and Yong P. Chen. Observation of topological surface state quantum Hall effect in an intrinsic three-dimensional topological insulator. *Nature Physics*, 10(12):956, December 2014.

[56] Ireneusz Miotkowski, Yang Xu, and Yong P. Chen. Quantum transport of two-species Dirac fermions in dual-gated three-dimensional topological insulators. *Nature Communications*, 7:11434, May 2016.

[57] A. F. Young, J. D. Sanchez-Yamagishi, B. Hunt, S. H. Choi, K. Watanabe, T. Taniguchi, R. C. Ashoori, and P. Jarillo-Herrero. Tunable symmetry breaking and helical edge transport in a graphene quantum spin Hall state. *Nature*, 505(7484):528–532, January 2014.

[58] J. D. Sanchez-Yamagishi, J. Y. Luo, A. F. Young, B. Hunt, K. Watanabe, T. Taniguchi, R. C. Ashoori, and P. Jarillo-Herrero. Observation of Helical Edge States and Fractional Quantum Hall Effect in a Graphene Electron-hole Bilayer. *arXiv:1602.06815 [cond-mat]*, February 2016. arXiv: 1602.06815.

[59] Javier D. Sanchez-Yamagishi, Jason Y. Luo, Andrea F. Young, Benjamin M. Hunt, Kenji Watanabe, Takashi Taniguchi, Raymond C. Ashoori, and Pablo Jarillo-Herrero. Helical edge states and fractional quantum Hall effect in a graphene electron–hole bilayer. *Nature Nanotechnology*, 12(2):118–122, February 2017.

[60] D. Hsieh, D. Qian, L. Wray, Y. Xia, Y. S. Hor, R. J. Cava, and M. Z. Hasan. A topological Dirac insulator in a quantum spin Hall phase. *Nature*, 452(7190):970–974, April 2008.

[61] D. Hsieh, Y. Xia, L. Wray, D. Qian, A. Pal, J. H. Dil, J. Osterwalder, F. Meier, G. Bihlmayer, C. L. Kane, Y. S. Hor, R. J. Cava, and M. Z. Hasan. Observation of Unconventional Quantum Spin Textures in Topological Insulators. *Science*, 323(5916):919–922, February 2009.

[62] Y. Xia, D. Qian, D. Hsieh, L. Wray, A. Pal, H. Lin, A. Bansil, D. Grauer, Y. S. Hor, R. J. Cava, and M. Z. Hasan. Observation of a large-gap topological-insulator class with a single Dirac cone on the surface. *Nature Physics*, 5(6):398–402, June 2009.

[63] Tong Zhang, Peng Cheng, Xi Chen, Jin-Feng Jia, Xucun Ma, Ke He, Lili Wang, Haijun Zhang, Xi Dai, Zhong Fang, Xincheng Xie, and Qi-Kun Xue. Experimental Demonstration of Topological Surface States Protected by Time-Reversal Symmetry. *Physical Review Letters*, 103(26), December 2009.

[64] Zhanybek Alpichshev, J. G. Analytis, J.-H. Chu, I. R. Fisher, Y. L. Chen, Z. X. Shen, A. Fang, and A. Kapitulnik. STM Imaging of Electronic Waves on the Surface of Bi2te3: Topologically Protected Surface States and Hexagonal Warping Effects. *Physical Review Letters*, 104(1):016401, January 2010.

[65] James G. Analytis, Jiun-Haw Chu, Yulin Chen, Felipe Corredor, Ross D. McDonald, Z. X. Shen, and Ian R. Fisher. Bulk Fermi surface coexistence with Dirac surface state in ${\text{Bi}}_{2}{\text{Se}}_{3}$: A comparison of photoemission and Shubnikov\char21{}de Haas measurements. *Physical Review B*, 81(20):205407, May 2010.

[66] Y. S. Hor, A. Richardella, P. Roushan, Y. Xia, J. G. Checkelsky, A. Yazdani, M. Z. Hasan, N. P. Ong, and R. J. Cava. p-type Bi2se3 for topological insulator and low-temperature thermoelectric applications. *Physical Review B*, 79(19):195208, May 2009.

[67] Dong-Xia Qu, Y. S. Hor, Jun Xiong, R. J. Cava, and N. P. Ong. Quantum Oscillations and Hall Anomaly of Surface States in the Topological Insulator Bi2te3. *Science*, 329(5993):821–824, August 2010.

[68] James G. Analytis, Ross D. McDonald, Scott C. Riggs, Jiun-Haw Chu, G. S. Boebinger, and Ian R. Fisher. Two-dimensional surface state in the quantum limit of a topological insulator. *Nature Physics*, 6(12):960–964, November 2010.

[69] Hadar Steinberg, Dillon R. Gardner, Young S. Lee, and Pablo Jarillo-Herrero. Surface State Transport and Ambipolar Electric Field Effect in Bi2se3 Nanodevices. *Nano Letters*, 10(12):5032–5036, December 2010.

[70] J. G. Checkelsky, Y. S. Hor, R. J. Cava, and N. P. Ong. Bulk Band Gap and Surface State Conduction Observed in Voltage-Tuned Crystals of the Topological Insulator Bi2se3. *Physical Review Letters*, 106(19):196801, May 2011.

[71] Benjamin Sacépé, Jeroen B. Oostinga, Jian Li, Alberto Ubaldini, Nuno J. G. Couto, Enrico Giannini, and Alberto F. Morpurgo. Gate-tuned normal and superconducting transport at the surface of a topological insulator. *Nature Communications*, 2:575, December 2011.

[72] Desheng Kong, Judy J. Cha, Keji Lai, Hailin Peng, James G. Analytis, Stefan Meister, Yulin Chen, Hai-Jun Zhang, Ian R. Fisher, Zhi-Xun Shen, and Yi Cui. Rapid Surface Oxidation as a Source of Surface Degradation Factor for Bi2se3. *ACS Nano*, 5(6):4698–4703, June 2011.

[73] J. Chen, H. J. Qin, F. Yang, J. Liu, T. Guan, F. M. Qu, G. H. Zhang, J. R. Shi, X. C. Xie, C. L. Yang, K. H. Wu, Y. Q. Li, and L. Lu. Gate-Voltage Control of Chemical Potential and Weak Antilocalization in ${\mathrm{Bi}}_{2}{\mathrm{Se}}_{3}$. *Physical Review Letters*, 105(17):176602, October 2010.

[74] Sungjae Cho, Nicholas P. Butch, Johnpierre Paglione, and Michael S. Fuhrer. Insulating Behavior in Ultrathin Bismuth Selenide Field Effect Transistors. *Nano Letters*, 11(5):1925–1927, May 2011.

[75] J. Chen, X. Y. He, K. H. Wu, Z. Q. Ji, L. Lu, J. R. Shi, J. H. Smet, and Y. Q. Li. Tunable surface conductivity in Bi${}_{2}$Se${}_{3}$ revealed in diffusive electron transport. *Physical Review B*, 83(24):241304, June 2011.

[76] H. Steinberg, J.-B. Laloë, V. Fatemi, J. S. Moodera, and P. Jarillo-Herrero. Electrically tunable surface-to-bulk coherent coupling in topological insulator thin films. *Physical Review B*, 84(23):233101, December 2011.

[77] Dohun Kim, Sungjae Cho, Nicholas P. Butch, Paul Syers, Kevin Kirshenbaum, Shaffique Adam, Johnpierre Paglione, and Michael S. Fuhrer. Surface conduction of topological Dirac electrons in bulk insulating Bi2se3. *Nature Physics*, 8(6):459–463, June 2012.

[78] Namrata Bansal, Yong Seung Kim, Matthew Brahlek, Eliav Edrey, and Seongshik Oh. Thickness-Independent Transport Channels in Topological Insulator Bi_{2}Se_{3} Thin Films. *Physical Review Letters*, 109(11):116804, September 2012.

[79] Dohun Kim, Qiuzi Li, Paul Syers, Nicholas P. Butch, Johnpierre Paglione, S. Das Sarma, and Michael S. Fuhrer. Intrinsic Electron-Phonon Resistivity of Bi_{2}Se_{3} in the Topological Regime. *Physical Review Letters*, 109(16):166801, October 2012.

[80] Janghee Lee, Joonbum Park, Jae-Hyeong Lee, Jun Sung Kim, and Hu-Jong Lee. Gate-tuned differentiation of surface-conducting states in Bi_{1.5}Sb_{0.5}Te_{1.7}Se_{1.3} topological-insulator thin crystals. *Physical Review B*, 86(24), December 2012.

[81] Bin Xia, Peng Ren, Azat Sulaev, Peng Liu, Shun-Qing Shen, and Lan Wang. Indications of surface-dominated transport in single crystalline nanoflake devices of topological insulator Bi_{1.5}Sb_{0.5}Te_{1.8}Se_{1.2}. *Physical Review B*, 87(8):085442, February 2013.

[82] Jaesung Son, Karan Banerjee, Matthew Brahlek, Nikesh Koirala, Seoung-Ki Lee, Jong-Hyun Ahn, Seongshik Oh, and Hyunsoo Yang. Conductance modulation in topological insulator Bi2se3 thin films with ionic liquid gating. *Applied Physics Letters*, 103(21):213114, November 2013.

[83] Jinsong Zhang, Cui-Zu Chang, Zuocheng Zhang, Jing Wen, Xiao Feng, Kang Li, Minhao Liu, Ke He, Lili Wang, Xi Chen, Qi-Kun Xue, Xucun Ma, and Yayu Wang. Band structure engineering in (Bi1-xSbx)2te3 ternary topological insulators. *Nature Communications*, 2:574, December 2011.

[84] Desheng Kong, Yulin Chen, Judy J. Cha, Qianfan Zhang, James G. Analytis, Keji Lai, Zhongkai Liu, Seung Sae Hong, Kristie J. Koski, Sung-Kwan Mo, Zahid Hussain, Ian R. Fisher, Zhi-Xun Shen, and Yi Cui. Ambipolar field effect in the ternary topological insulator (BixSb1-x)2te3 by composition tuning. *Nature Nanotechnology*, 6(11):705–709, November 2011.

[85] Zhi Ren, A. A. Taskin, Satoshi Sasaki, Kouji Segawa, and Yoichi Ando. Fermi level tuning and a large activation gap achieved in the topological insulator Bi2te2se by Sn doping. *Physical Review B*, 85(15):155301, April 2012.

[86] Jun Xiong, A. C. Petersen, Dongxia Qu, Y. S. Hor, R. J. Cava, and N. P. Ong. Quantum oscillations in a topological insulator Bi2te2se with large bulk resistivity (). *Physica E: Low-dimensional Systems and Nanostructures*, 44(5):917–920, February 2012.

[87] Zhi Ren, A. A. Taskin, Satoshi Sasaki, Kouji Segawa, and Yoichi Ando. Large bulk resistivity and surface quantum oscillations in the topological insulator Bi_{2}Te_{2}Se. *Physical Review B*, 82(24), December 2010.

[88] A. A. Taskin, Zhi Ren, Satoshi Sasaki, Kouji Segawa, and Yoichi Ando. Observation of Dirac Holes and Electrons in a Topological Insulator. *Physical Review Letters*, 107(1), June 2011.

[89] Zhi Ren, A. A. Taskin, Satoshi Sasaki, Kouji Segawa, and Yoichi Ando. Optimizing Bi_{2-x}Sb_{x}Te_{3-y}Se_{y} solid solutions to approach the intrinsic topological insulator regime. *Physical Review B*, 84(16):165311, October 2011.

[90] T. Arakane, T. Sato, S. Souma, K. Kosaka, K. Nakayama, M. Komatsu, T. Takahashi, Zhi Ren, Kouji Segawa, and Yoichi Ando. Tunable Dirac cone in the topological insulator Bi2-xSbxTe3-ySey. *Nature Communications*, 3:636, January 2012.

[91] Rui Jiang, Lin-Lin Wang, Mianliang Huang, R. S. Dhaka, Duane D. Johnson, Thomas A. Lograsso, and Adam Kaminski. Reversible tuning of the surface state in a pseudobinary Bi_{2}(Te-Se)_{3} topological insulator. *Physical Review B*, 86(8), August 2012.

[92] Kouji Segawa, Zhi Ren, Satoshi Sasaki, Tetsuya Tsuda, Susumu Kuwabata, and Yoichi Ando. Ambipolar transport in bulk crystals of a topological insulator by gating with ionic liquid. *Physical Review B*, 86(7):075306, August 2012.

[93] Su-Yang Xu, L. A. Wray, Y. Xia, R. Shankar, A. Petersen, A. Fedorov, H. Lin, A. Bansil, Y. S. Hor, D. Grauer, R. J. Cava, and M. Z. Hasan. Discovery of several large families of Topological Insulator classes with backscattering-suppressed spin-polarized single-Dirac-cone on the surface. *arXiv:1007.5111 [cond-mat, physics:physics, physics:quant-ph]*, July 2010. arXiv: 1007.5111.

[94] Valla Fatemi, Benjamin Hunt, Hadar Steinberg, Stephen L. Eltinge, Fahad Mahmood, Nicholas P. Butch, Kenji Watanabe, Takashi Taniguchi, Nuh Gedik, Raymond C. Ashoori, and Pablo Jarillo-Herrero. Electrostatic Coupling between Two Surfaces of a Topological Insulator Nanodevice. *Physical Review Letters*, 113(20):206801, November 2014.

[95] Brian Skinner, T. Chen, and B. I. Shklovskii. Why Is the Bulk Resistivity of Topological Insulators So Small? *Physical Review Letters*, 109(17), 2012.

[96] Brian Skinner and B. I. Shklovskii. Theory of the random potential and conductivity at the surface of a topological insulator. *Physical Review B*, 87(7), February 2013.

[97] Pascal Gehring, Bo F. Gao, Marko Burghard, and Klaus Kern. Growth of High-Mobility Bi2te2se Nanoplatelets on hBN Sheets by van der Waals Epitaxy. *Nano Letters*, 12(10):5137–5142, October 2012.

[98] Hongtao Yuan, Hongwen Liu, Hidekazu Shimotani, Hua Guo, Mingwei Chen, Qikun Xue, and Yoshihiro Iwasa. Liquid-Gated Ambipolar Transport in Ultrathin Films of a Topological Insulator Bi2te3. *Nano Letters*, 11(7):2601–2605, July 2011.

[99] Dagim Tilahun, Byounghak Lee, E. M. Hankiewicz, and A. H. MacDonald. Quantum Hall Superfluids in Topological Insulator Thin Films. *Physical Review Letters*, 107(24):246401, December 2011.

[100] Oskar Vafek. Quantum Hall effect in a singly and doubly connected three-dimensional topological insulator. *Physical Review B*, 84(24):245417, December 2011.

[101] J. R. Williams, A. J. Bestwick, P. Gallagher, Seung Sae Hong, Y. Cui, Andrew S. Bleich, J. G. Analytis, I. R. Fisher, and D. Goldhaber-Gordon. Unconventional Josephson Effect in Hybrid Superconductor-Topological Insulator Devices. *Physical Review Letters*, 109(5):056803, July 2012.

[102] M. Veldhorst, M. Snelder, M. Hoek, T. Gang, V. K. Guduru, X. L. Wang, U. Zeitler, W. G. van der Wiel, A. A. Golubov, H. Hilgenkamp, and A. Brinkman. Josephson supercurrent through a topological insulator surface state. *Nature Materials*, 11(5):417–421, May 2012.

[103] Leonid P. Rokhinson, Xinyu Liu, and Jacek K. Furdyna. The fractional a.c. Josephson effect in a semiconductor-superconductor nanowire as a signature of Majorana particles. *Nature Physics*, 8(11):795–799, November 2012.

[104] B. Seradjeh, J. E. Moore, and M. Franz. Exciton Condensation and Charge Fractionalization in a Topological Insulator Film. *Physical Review Letters*, 103(6):066402, August 2009.

[105] Rui Yu, Wei Zhang, Hai-Jun Zhang, Shou-Cheng Zhang, Xi Dai, and Zhong Fang. Quantized Anomalous Hall Effect in Magnetic Topological Insulators. *Science*, 329(5987):61–64, July 2010.

[106] Cui-Zu Chang, Jinsong Zhang, Xiao Feng, Jie Shen, Zuocheng Zhang, Minghua Guo, Kang Li, Yunbo Ou, Pang Wei, Li-Li Wang, Zhong-Qing Ji, Yang Feng, Shuaihua Ji, Xi Chen, Jinfeng Jia, Xi Dai, Zhong Fang, Shou-Cheng Zhang, Ke He, Yayu Wang, Li Lu, Xu-Cun Ma, and Qi-Kun Xue. Experimental Observation of the Quantum Anomalous Hall Effect in a Magnetic Topological Insulator. *Science*, 340(6129):167–170, April 2013.

[107] J. A. Sobota, S. Yang, J. G. Analytis, Y. L. Chen, I. R. Fisher, P. S. Kirchmann, and Z.-X. Shen. Ultrafast Optical Excitation of a Persistent Surface-State Population in the Topological Insulator Bi2se3. *Physical Review Letters*, 108(11):117403, March 2012.

[108] Y. H. Wang, D. Hsieh, E. J. Sie, H. Steinberg, D. R. Gardner, Y. S. Lee, P. Jarillo-Herrero, and N. Gedik. Measurement of Intrinsic Dirac Fermion Cooling on the Surface of the Topological Insulator Bi2se3 Using Time-Resolved and Angle-Resolved Photoemission Spectroscopy. *Physical Review Letters*, 109(12):127401, September 2012.

[109] Sunghun Kim, Shunsuke Yoshizawa, Yukiaki Ishida, Kazuma Eto, Kouji Segawa, Yoichi Ando, Shik Shin, and Fumio Komori. Robust Protection from Backscattering in the Topological Insulator Bi1.5sb0.5te1.7se1.3. *Physical Review Letters*, 112(13):136802, April 2014.

[110] C. R. Dean, A. F. Young, I. Meric, C. Lee, L. Wang, S. Sorgenfrei, K. Watanabe, T. Taniguchi, P. Kim, K. L. Shepard, and J. Hone. Boron nitride substrates for high-quality graphene electronics. *Nature Nanotechnology*, 5(10):722–726, October 2010.

[111] S. Adam, E. H. Hwang, and S. Das Sarma. Two-dimensional transport and screening in topological insulator surface states. *Physical Review B*, 85(23):235413, June 2012.

[112] Jiamin Xue, Javier Sanchez-Yamagishi, Danny Bulmash, Philippe Jacquod, Aparna Deshpande, K. Watanabe, T. Taniguchi, Pablo Jarillo-Herrero, and Brian J. LeRoy. Scanning tunnelling microscopy and spectroscopy of ultra-flat graphene on hexagonal boron nitride. *Nature Materials*, 10(4):282–285, April 2011.

[113] Joseph G. Checkelsky, Jianting Ye, Yoshinori Onose, Yoshihiro Iwasa, and Yoshinori Tokura. Dirac-fermion-mediated ferromagnetism in a topological insulator. *Nature Physics*, 8(10):729–733, August 2012.

[114] Seyoung Kim, Insun Jo, D. C. Dillen, D. A. Ferrer, B. Fallahazad, Z. Yao, S. K. Banerjee, and E. Tutuc. Direct Measurement of the Fermi Energy in Graphene Using a Double-Layer Heterostructure. *Physical Review Letters*, 108(11):116404, March 2012.

[115] Collaboration: Authors and editors of the volumes III/17E-17F-41C. Antimony telluride (Sb2te3) dielectric constants. In O. Madelung, U. Rössler, and M. Schulz, editors,

Non-Tetrahedrally Bonded Elements and Binary Compounds I, volume 41C, pages 1–4. Springer-Verlag, Berlin/Heidelberg.

[116] J. Petzelt and J. Grigas. Far infrared dielectric dispersion in Sb2s3, Bi2s3 and Sb2se3 single crystals. *Ferroelectrics*, 5(1):59–68, 1973.

[117] W. Richter and C. R. Becker. A Raman and far-infrared investigation of phonons in the rhombohedral V2–VI3 compounds Bi2te3, Bi2se3, Sb2te3 and Bi2(Te1-xSex)3 (0 < x < 1), (Bi1-ySby)2te3 (0 < y < 1). *physica status solidi (b)*, 84(2):619–628, 1977.

[118] A. A. Taskin and Yoichi Ando. Berry phase of nonideal Dirac fermions in topological insulators. *Physical Review B*, 84(3):035301, July 2011.

[119] Jeroen B. Oostinga, Hubert B. Heersche, Xinglan Liu, Alberto F. Morpurgo, and Lieven M. K. Vandersypen. Gate-induced insulating state in bilayer graphene devices. *Nature Materials*, 7(2):151–157, February 2008.

[120] A. B. Sushkov, G. S. Jenkins, D. C. Schmadel, N. P. Butch, J. Paglione, and H. D. Drew. Far-infrared cyclotron resonance and Faraday effect in Bi2se3. *Physical Review B*, 82(12):125110, September 2010.

[121] A. D. LaForge, A. Frenzel, B. C. Pursley, Tao Lin, Xinfei Liu, Jing Shi, and D. N. Basov. Optical characterization of Bi2se3 in a magnetic field: Infrared evidence for magnetoelectric coupling in a topological insulator material. *Physical Review B*, 81(12):125120, March 2010.

[122] Haim Beidenkopf, Pedram Roushan, Jungpil Seo, Lindsay Gorman, Ilya Drozdov, Yew San Hor, R. J. Cava, and Ali Yazdani. Spatial fluctuations of helical Dirac fermions on the surface of topological insulators. *Nature Physics*, 7(12):939–943, December 2011.

[123] Wonhee Ko, Insu Jeon, Hyo Won Kim, Hyeokshin Kwon, Se-Jong Kahng, Joonbum Park, Jun Sung Kim, Sung Woo Hwang, and Hwansoo Suh. Atomic and electronic structure of an alloyed topological insulator, Bi1.5sb0.5te1.7se1.3. *Scientific Reports*, 3, September 2013.

[124] T. Knispel, W. Jolie, N. Borgwardt, J. Lux, Zhiwei Wang, Yoichi Ando, A. Rosch, T. Michely, and M. Grüninger. Charge puddles in the bulk and on the surface of the topological insulator ${\mathrm{BiSbTeSe}}_{2}$ studied by scanning tunneling microscopy and optical spectroscopy. *Physical Review B*, 96(19):195135, November 2017.

[125] N. Borgwardt, J. Lux, I. Vergara, Zhiwei Wang, A. A. Taskin, Kouji Segawa, P. H. M. van Loosdrecht, Yoichi Ando, A. Rosch, and M. Grüninger. Self-organized charge puddles in a three-dimensional topological material. *Physical Review B*, 93(24):245149, June 2016.

[126] C. W. Rischau, A. Ubaldini, E. Giannini, and C. J. van der Beek. Charge puddles in a completely compensated topological insulator. *New Journal of Physics*, 18(7):073024, 2016.

[127] T. Knispel, W. Jolie, N. Borgwardt, J. Lux, Zhiwei Wang, Yoichi Ando, A. Rosch, T. Michely, and M. Grüninger. Charge puddles in the bulk and on the surface of the

topological insulator BiSbTeSe$_2$ studied by scanning tunneling microscopy and optical spectroscopy. *arXiv:1708.09166 [cond-mat]*, August 2017. arXiv: 1708.09166.

[128] Thomas Bömerich, Jonathan Lux, Qingyufei Terenz Feng, and Achim Rosch. Length scale of puddle formation in compensation-doped semiconductors and topological insulators. *Physical Review B*, 96(7):075204, August 2017.

[129] B. A. Aronzon and I. M. Tsidilkovskii. Magnetic-Field-Induced Localization of Electrons in Fluctuation Potential Wells of Impurities. *physica status solidi (b)*, 157(1):17–59, January 1990.

[130] Anand Bhattacharya, Brian Skinner, Guru Khalsa, and Alexey V. Suslov. Spatially inhomogeneous electron state deep in the extreme quantum limit of strontium titanate. *Nature Communications*, 7:12974, September 2016.

[131] A. Tsukazaki, J. Falson, J. G. Checkelsky, K. S. Takahashi, M. Kawasaki, R. Yoshimi, Y. Kozuka, and Y. Tokura. Trajectory of the anomalous Hall effect towards the quantized state in a ferromagnetic topological insulator. *Nature Physics*, 10(10):731, October 2014.

[132] Cui-Zu Chang, Weiwei Zhao, Duk Y. Kim, Haijun Zhang, Badih A. Assaf, Don Heiman, Shou-Cheng Zhang, Chaoxing Liu, Moses H. W. Chan, and Jagadeesh S. Moodera. High-precision realization of robust quantum anomalous Hall state in a hard ferromagnetic topological insulator. *Nature Materials*, advance online publication, March 2015.

[133] Cui-Zu Chang, Weiwei Zhao, Duk Y. Kim, Peng Wei, J. K. Jain, Chaoxing Liu, Moses H. W. Chan, and Jagadeesh S. Moodera. Zero-Field Dissipationless Chiral Edge Transport and the Nature of Dissipation in the Quantum Anomalous Hall State. *Physical Review Letters*, 115(5):057206, July 2015.

[134] Yang Feng, Xiao Feng, Yunbo Ou, Jing Wang, Chang Liu, Liguo Zhang, Dongyang Zhao, Gaoyuan Jiang, Shou-Cheng Zhang, Ke He, Xucun Ma, Qi-Kun Xue, and Yayu Wang. Observation of the Zero Hall Plateau in a Quantum Anomalous Hall Insulator. *Physical Review Letters*, 115(12):126801, September 2015.

[135] V. A. Obolonchik, L. S. Vainer, and A. A. Yanaki. Chemical stability of tellurides of subgroup VIa transition metals in various corrosive media. *Soviet Powder Metallurgy and Metal Ceramics*, 11(9):727–729, September 1972.

[136] L. H. Brixner. Preparation and properties of the single crystalline AB2-type selenides and tellurides of niobium, tantalum, molybdenum and tungsten. *Journal of Inorganic and Nuclear Chemistry*, 24(3):257–263, March 1962.

[137] B. E. Brown. The crystal structures of WTe2 and high-temperature MoTe2. *Acta Crystallographica*, 20(2):268–274, February 1966.

[138] Mazhar N. Ali, Leslie Schoop, Jun Xiong, Steven Flynn, Quinn Gibson, Max Hirschberger, N. P. Ong, and R. J. Cava. Correlation of crystal quality and extreme magnetoresistance of WTe 2. *EPL (Europhysics Letters)*, 110(6):67002, 2015.

[139] I. Pletikosić, Mazhar N. Ali, A. V. Fedorov, R. J. Cava, and T. Valla. Electronic Structure Basis for the Extraordinary Magnetoresistance in WTe2. *Physical Review Letters*, 113(21):216601, November 2014.

[140] D. Rhodes, S. Das, Q. R. Zhang, B. Zeng, N. R. Pradhan, N. Kikugawa, E. Manousakis, and L. Balicas. Role of spin-orbit coupling and evolution of the electronic structure of ${\mathrm{WTe}}_{2}$ under an external magnetic field. *Physical Review B*, 92(12):125152, September 2015.

[141] J. Jiang, F. Tang, X. C. Pan, H. M. Liu, X. H. Niu, Y. X. Wang, D. F. Xu, H. F. Yang, B. P. Xie, F. Q. Song, P. Dudin, T. K. Kim, M. Hoesch, P. Kumar Das, I. Vobornik, X. G. Wan, and D. L. Feng. Signature of Strong Spin-Orbital Coupling in the Large Nonsaturating Magnetoresistance Material WTe2. *Physical Review Letters*, 115(16):166601, October 2015.

[142] L. R. Thoutam, Y. L. Wang, Z. L. Xiao, S. Das, A. Luican-Mayer, R. Divan, G. W. Crabtree, and W. K. Kwok. Temperature-Dependent Three-Dimensional Anisotropy of the Magnetoresistance in WTe2. *Physical Review Letters*, 115(4):046602, July 2015.

[143] Zengwei Zhu, Xiao Lin, Juan Liu, Benoît Fauqué, Qian Tao, Chongli Yang, Youguo Shi, and Kamran Behnia. Quantum Oscillations, Thermoelectric Coefficients, and the Fermi Surface of Semimetallic ${\mathrm{WTe}}_{2}$. *Physical Review Letters*, 114(17):176601, April 2015.

[144] Zhujun Yuan, Hong Lu, Yongjie Liu, Junfeng Wang, and Shuang Jia. Large magnetoresistance in compensated semimetals ${\mathrm{TaAs}}_{2}$ and ${\mathrm{NbAs}}_{2}$. *Physical Review B*, 93(18):184405, May 2016.

[145] Kefeng Wang, D. Graf, Lijun Li, Limin Wang, and C. Petrovic. Anisotropic giant magnetoresistance in $NbSb_2$. *Scientific Reports*, 4:srep07328, December 2014.

[146] Tian Liang, Quinn Gibson, Mazhar N. Ali, Minhao Liu, R. J. Cava, and N. P. Ong. Ultrahigh mobility and giant magnetoresistance in the Dirac semimetal Cd_3As_2. *Nature Materials*, 14(3):nmat4143, November 2014.

[147] Yongkang Luo, N. J. Ghimire, M. Wartenbe, Hongchul Choi, M. Neupane, R. D. McDonald, E. D. Bauer, Jianxin Zhu, J. D. Thompson, and F. Ronning. Electron-hole compensation effect between topologically trivial electrons and nontrivial holes in NbAs. *Physical Review B*, 92(20):205134, November 2015.

[148] Chandra Shekhar, Ajaya K. Nayak, Yan Sun, Marcus Schmidt, Michael Nicklas, Inge Leermakers, Uli Zeitler, Yurii Skourski, Jochen Wosnitza, Zhongkai Liu, Yulin Chen, Walter Schnelle, Horst Borrmann, Yuri Grin, Claudia Felser, and Binghai Yan. Extremely large magnetoresistance and ultrahigh mobility in the topological Weyl semimetal candidate NbP. *Nature Physics*, 11(8):nphys3372, June 2015.

[149] F. F. Tafti, Q. D. Gibson, S. K. Kushwaha, N. Haldolaarachchige, and R. J. Cava. Resistivity plateau and extreme magnetoresistance in LaSb. *Nature Physics*, 12(3):nphys3581, December 2015.

[150] Shanshan Sun, Qi Wang, Peng-Jie Guo, Kai Liu, and Hechang Lei. Large magnetoresistance in LaBi: origin of field-induced resistivity upturn and plateau in compensated semimetals. *New Journal of Physics*, 18(8):082002, 2016.

[151] Yi-Yan Wang, Qiao-He Yu, Peng-Jie Guo, Kai Liu, and Tian-Long Xia. Resistivity plateau and extremely large magnetoresistance in ${\mathrm{NbAs}}_{2}$ and ${\mathrm{TaAs}}_{2}$. *Physical Review B*, 94(4):041103, July 2016.

[152] Desheng Wu, Jian Liao, Wei Yi, Xia Wang, Peigang Li, Hongming Weng, Youguo Shi, Yongqing Li, Jianlin Luo, Xi Dai, and Zhong Fang. Giant semiclassical magnetoresistance in high mobility TaAs2 semimetal. *Applied Physics Letters*, 108(4):042105, January 2016.

[153] Alexey A. Soluyanov, Dominik Gresch, Zhijun Wang, QuanSheng Wu, Matthias Troyer, Xi Dai, and B. Andrei Bernevig. Type-II Weyl semimetals. *Nature*, 527(7579):495–498, November 2015.

[154] Valla Fatemi, Quinn D. Gibson, Kenji Watanabe, Takashi Taniguchi, Robert J. Cava, and Pablo Jarillo-Herrero. Magnetoresistance and quantum oscillations of an electrostatically tuned semimetal-to-metal transition in ultrathin WTe2. *Physical Review B*, 95(4):041410, January 2017.

[155] Manoj K. Jana, Anjali Singh, Dattatray J. Late, Catherine R. Rajamathi, Kanishka Biswas, Claudia Felser, Umesh V. Waghmare, and C. N. R. Rao. A combined experimental and theoretical study of the structural, electronic and vibrational properties of bulk and few-layer Td-WTe 2. *Journal of Physics: Condensed Matter*, 27(28):285401, 2015.

[156] Y. C. Jiang, J. Gao, and L. Wang. Raman fingerprint for semi-metal WTe2 evolving from bulk to monolayer. *Scientific Reports*, 6:19624, January 2016.

[157] Zhen-Yu Jia, Ye-Heng Song, Xiang-Bing Li, Kejing Ran, Pengchao Lu, Hui-Jun Zheng, Xin-Yang Zhu, Zhi-Qiang Shi, Jian Sun, Jinsheng Wen, Dingyu Xing, and Shao-Chun Li. Direct visualization of a two-dimensional topological insulator in the single-layer 1t'-WTe2. *Physical Review B*, 96(4):041108, July 2017.

[158] Xiaofeng Qian, Junwei Liu, Liang Fu, and Ju Li. Quantum spin Hall effect in two-dimensional transition metal dichalcogenides. *Science*, 346(6215):1344–1347, December 2014.

[159] Hai He, Pengfei Lu, Liyuan Wu, Chunfang Zhang, Yuxin Song, Pengfei Guan, and Shumin Wang. Structural Properties and Phase Transition of Na Adsorption on Monolayer MoS2. *Nanoscale Research Letters*, 11:330, July 2016.

[160] Duk-Hyun Choe, Ha-Jun Sung, and K. J. Chang. Understanding topological phase transition in monolayer transition metal dichalcogenides. *Physical Review B*, 93(12):125109, March 2016.

[161] Liang Fu and C. Kane. Topological insulators with inversion symmetry. *Physical Review B*, 76(4), July 2007.

[162] Feipeng Zheng, Chaoyi Cai, Shaofeng Ge, Xuefeng Zhang, Xin Liu, Hong Lu, Yudao Zhang, Jun Qiu, Takashi Taniguchi, Kenji Watanabe, Shuang Jia, Jingshan Qi, Jian-Hao Chen, Dong Sun, and Ji Feng. On the Quantum Spin Hall Gap of Monolayer 1t'-WTe2. *Advanced Materials*, 28(24):4845–4851, June 2016.

[163] M. B. Vellinga, R. de Jonge, and C. Haas. Semiconductor to metal transition in MoTe2. *Journal of Solid State Chemistry*, 2(2):299–302, August 1970.

[164] IND Sardar Patel univ., dep. physics, AGARWAL M. K, PATEL P. D, and JOSHI R. M. Growth conditions and structural characterization of MoSe?x?Te?2-d?x(0<=x<=2) single crystals
. *Journal of materials science letters*, 5(1):66–68, 1986.

[165] E. (Universite de Paris-Sud Canadell and Myung-Hwan (North Carolina State Univ Whangbo. Semimetallic Versus Semiconducting Properties of Mx Sub 2 Layer Compounds Containing D Sup 2 Metal Ions. *Inorganic Chemistry; (USA)*, 29:7, April 1990.

[166] M. Albert, R. Kershaw, K. Dwight, and A. Wold. Preparation and characterization of semiconducting α-MoTe2 single crystals. *Solid State Communications*, 81(8):649–651, February 1992.

[167] Thorsten Zandt, Helmut Dwelk, Christoph Janowitz, and Recardo Manzke. Quadratic temperature dependence up to 50 K of the resistivity of metallic MoTe2. *Journal of Alloys and Compounds*, 442(1):216–218, September 2007.

[168] Ke Deng, Guoliang Wan, Peng Deng, Kenan Zhang, Shijie Ding, Eryin Wang, Mingzhe Yan, Huaqing Huang, Hongyun Zhang, Zhilin Xu, Jonathan Denlinger, Alexei Fedorov, Haitao Yang, Wenhui Duan, Hong Yao, Yang Wu, Shoushan Fan, Haijun Zhang, Xi Chen, and Shuyun Zhou. Experimental observation of topological Fermi arcs in type-II Weyl semimetal $MoTe_2$. *Nature Physics*, 12(12):nphys3871, September 2016.

[169] Yanpeng Qi, Pavel G. Naumov, Mazhar N. Ali, Catherine R. Rajamathi, Walter Schnelle, Oleg Barkalov, Michael Hanfland, Shu-Chun Wu, Chandra Shekhar, Yan Sun, Vicky Süß, Marcus Schmidt, Ulrich Schwarz, Eckhard Pippel, Peter Werner, Reinald Hillebrand, Tobias Förster, Erik Kampert, Stuart Parkin, R. J. Cava, Claudia Felser, Binghai Yan, and Sergey A. Medvedev. Superconductivity in Weyl semimetal candidate $MoTe_2$. *Nature Communications*, 7:ncomms11038, March 2016.

[170] Kenan Zhang, Changhua Bao, Qiangqiang Gu, Xiao Ren, Haoxiong Zhang, Ke Deng, Yang Wu, Yuan Li, Ji Feng, and Shuyun Zhou. Raman signatures of inversion symmetry breaking and structural phase transition in type-II Weyl semimetal $MoTe_2$. *Nature Communications*, 7:ncomms13552, December 2016.

[171] H. Y. Lv, W. J. Lu, D. F. Shao, Y. Liu, S. G. Tan, and Y. P. Sun. Perfect charge compensation in WTe2 for the extraordinary magnetoresistance: From bulk to monolayer. *EPL (Europhysics Letters)*, 110(3):37004, May 2015.

[172] Lin Wang, Ignacio Gutiérrez-Lezama, Céline Barreteau, Nicolas Ubrig, Enrico Giannini, and Alberto F. Morpurgo. Tuning magnetotransport in a compensated semimetal at the atomic scale. *Nature Communications*, 6:8892, November 2015.

[173] John M. Woods, Jie Shen, Piranavan Kumaravadivel, Yuan Pang, Yujun Xie, Grace A. Pan, Min Li, Eric I. Altman, Li Lu, and Judy J. Cha. Suppression of Magnetoresistance in Thin WTe2 Flakes by Surface Oxidation. *ACS Applied Materials & Interfaces*, 9(27):23175–23180, July 2017.

[174] Fan Ye, Jaesung Lee, Jin Hu, Zhiqiang Mao, Jiang Wei, and Philip X.-L. Feng. Environmental Instability and Degradation of Single- and Few-Layer WTe2 Nanosheets in Ambient Conditions. *Small*, 12(42):5802–5808, November 2016.

[175] Zaiyao Fei, Tauno Palomaki, Sanfeng Wu, Wenjin Zhao, Xinghan Cai, Bosong Sun, Paul Nguyen, Joseph Finney, Xiaodong Xu, and David H. Cobden. Edge conduction in monolayer WTe2. *Nature Physics*, advance online publication, April 2017.

[176] Antonius Brugmans, Elie (Leiden) Luzac, and Jan Hendrik van (Leiden) Damme. *Antonii Brugmans Magnetismus, seu De affinitatibus magneticis observationes academicæ.* apud Luzac & Van Damme, Lugduni Batavorum„ 1778. OCLC: 64832588.

[177] Seebeck T. J. Ueber die magnetische Polarisation der Metalle und Erze durch Temperatur-Differenz. *Annalen der Physik*, 82(2):133–160, March 2006.

[178] v. Ettingshausen A. and Nernst W. Ueber das Auftreten electromotorischer Kräfte in Metallplatten, welche von einem Wärmestrome durchflossen werden und sich im magnetischen Felde befinden. *Annalen der Physik*, 265(10):343–347, March 2006.

[179] L. Schubnikow and Wander Johannes de Haas. Magnetische Widerstandsvergrösserung in Einkristallen von Wismut bei tiefen Temperaturen. *Proceedings of the Netherlands Royal Academy of Science*, 33(2):130–133, 1930.

[180] Om Prakash, Anil Kumar, A. Thamizhavel, and S. Ramakrishnan. Evidence for bulk superconductivity in pure bismuth single crystals at ambient pressure. *Science*, page aaf8227, December 2016.

[181] P. B. Alers and R. T. Webber. The Magnetoresistance of Bismuth Crystals at Low Temperatures. *Physical Review*, 91(5):1060–1065, September 1953.

[182] Benoît Fauqué, Baptiste Vignolle, Cyril Proust, Jean-Paul Issi, and Kamran Behnia. Electronic instability in bismuth far beyond the quantum limit. *New Journal of Physics*, 11(11):113012, 2009.

[183] Aurélie Collaudin, Benoît Fauqué, Yuki Fuseya, Woun Kang, and Kamran Behnia. Angle Dependence of the Orbital Magnetoresistance in Bismuth. *Physical Review X*, 5(2):021022, June 2015.

[184] I. L. Spain and R. O. Dillon. Kohler's rule and other scaling relationships for the magnetoresistance of graphite. *Carbon*, 14(1):23–26, January 1976.

[185] Y. Kopelevich, J. H. S. Torres, R. R. da Silva, F. Mrowka, H. Kempa, and P. Esquinazi. Reentrant Metallic Behavior of Graphite in the Quantum Limit. *Physical Review Letters*, 90(15):156402, April 2003.

[186] S. M. Young, S. Zaheer, J. C. Y. Teo, C. L. Kane, E. J. Mele, and A. M. Rappe. Dirac Semimetal in Three Dimensions. *Physical Review Letters*, 108(14):140405, April 2012.

[187] Z. K. Liu, B. Zhou, Y. Zhang, Z. J. Wang, H. M. Weng, D. Prabhakaran, S.-K. Mo, Z. X. Shen, Z. Fang, X. Dai, Z. Hussain, and Y. L. Chen. Discovery of a Three-Dimensional Topological Dirac Semimetal, Na3bi. *Science*, 343(6173):864–867, February 2014.

[188] Sergey Borisenko, Quinn Gibson, Danil Evtushinsky, Volodymyr Zabolotnyy, Bernd Büchner, and Robert J. Cava. Experimental Realization of a Three-Dimensional Dirac Semimetal. *Physical Review Letters*, 113(2):027603, July 2014.

[189] Hermann Weyl. Elektron und Gravitation. I. *Zeitschrift für Physik*, 56(5-6):330–352, May 1929.

[190] Conyers Herring. Accidental Degeneracy in the Energy Bands of Crystals. *Physical Review*, 52(4):365–373, 1937.

[191] Shuichi Murakami. Phase transition between the quantum spin Hall and insulator phases in 3d: emergence of a topological gapless phase. *New Journal of Physics*, 9(9):356, 2007.

[192] Guoqing Chang, Su-Yang Xu, Shin-Ming Huang, Daniel S. Sanchez, Chuang-Han Hsu, Guang Bian, Zhi-Ming Yu, Ilya Belopolski, Nasser Alidoust, Hao Zheng, Tay-Rong Chang, Horng-Tay Jeng, Shengyuan A. Yang, Titus Neupert, Hsin Lin, and M. Zahid Hasan. Nexus fermions in topological symmorphic crystalline metals. *Scientific Reports*, 7(1):1688, May 2017.

[193] Lukas Muechler, A. Alexandradinata, Titus Neupert, and Roberto Car. Topological Nonsymmorphic Metals from Band Inversion. *Physical Review X*, 6(4):041069, December 2016.

[194] Benoît Fauqué, Baptiste Vignolle, Cyril Proust, Jean-Paul Issi, and Kamran Behnia. Electronic instability in bismuth far beyond the quantum limit. *New Journal of Physics*, 11(11):113012, 2009.

[195] Y. Kaburagi. Magnetoresistance of highly oriented graphite at 77k and 4.2k. *Journal of Physics C: Solid State Physics*, 15(26):5425, 1982.

[196] S. A. Solin, Tineke Thio, D. R. Hines, and J. J. Heremans. Enhanced Room-Temperature Geometric Magnetoresistance in Inhomogeneous Narrow-Gap Semiconductors. *Science*, 289(5484):1530–1532, September 2000.

[197] Lisa M. Pugsley, L. R. Ram-Mohan, and S. A. Solin. Extraordinary magnetoresistance in two and three dimensions: Geometrical optimization. *Journal of Applied Physics*, 113(6):064505, February 2013.

[198] Geometrical enhancement of low-field magnetoresistance in silicon.

[199] A. B. Pippard. *Magnetoresistance in Metals*. Cambridge University Press, January 1989. Google-Books-ID: D5XHMARd2ocC.

[200] D. T. Son and B. Z. Spivak. Chiral anomaly and classical negative magnetoresistance of Weyl metals. *Physical Review B*, 88(10):104412, September 2013.

[201] A. A. Burkov. Chiral anomaly and transport in Weyl metals. *Journal of Physics: Condensed Matter*, 27(11):113201, 2015.

[202] Xiaochun Huang, Lingxiao Zhao, Yujia Long, Peipei Wang, Dong Chen, Zhanhai Yang, Hui Liang, Mianqi Xue, Hongming Weng, Zhong Fang, Xi Dai, and Genfu Chen. Observation of the Chiral-Anomaly-Induced Negative Magnetoresistance in 3d Weyl Semimetal TaAs. *Physical Review X*, 5(3):031023, August 2015.

[203] Jun Xiong, Satya K. Kushwaha, Tian Liang, Jason W. Krizan, Max Hirschberger, Wudi Wang, R. J. Cava, and N. P. Ong. Evidence for the chiral anomaly in the Dirac semimetal Na3bi. *Science*, 350(6259):413–416, October 2015.

[204] Cai-Zhen Li, Li-Xian Wang, Haiwen Liu, Jian Wang, Zhi-Min Liao, and Da-Peng Yu. Giant negative magnetoresistance induced by the chiral anomaly in individual Cd3as2 nanowires. *Nature Communications*, 6:10137, December 2015.

[205] Cheng-Long Zhang, Su-Yang Xu, Ilya Belopolski, Zhujun Yuan, Ziquan Lin, Bingbing Tong, Guang Bian, Nasser Alidoust, Chi-Cheng Lee, Shin-Ming Huang, Tay-Rong Chang, Guoqing Chang, Chuang-Han Hsu, Horng-Tay Jeng, Madhab Neupane, Daniel S. Sanchez, Hao Zheng, Junfeng Wang, Hsin Lin, Chi Zhang, Hai-Zhou Lu, Shun-Qing Shen, Titus Neupert, M. Zahid Hasan, and Shuang Jia. Signatures of the Adler-Bell-Jackiw chiral anomaly in a Weyl fermion semimetal. *Nature Communications*, 7:10735, February 2016.

[206] Albert Fert. Nobel Lecture: Origin, development, and future of spintronics. *Reviews of Modern Physics*, 80(4):1517–1530, December 2008.

[207] Peter A. Grünberg. Nobel Lecture: From spin waves to giant magnetoresistance and beyond. *Reviews of Modern Physics*, 80(4):1531–1540, December 2008.

[208] Di Xiao, Ming-Che Chang, and Qian Niu. Berry phase effects on electronic properties. *Reviews of Modern Physics*, 82(3):1959–2007, July 2010.

[209] S. Das Sarma, E. H. Hwang, and Hongki Min. Carrier screening, transport, and relaxation in three-dimensional Dirac semimetals. *Physical Review B*, 91(3):035201, January 2015.

[210] Jaesung Lee, Fan Ye, Zenghui Wang, Rui Yang, Jin Hu, Zhiqiang Mao, Jiang Wei, and Philip Feng. Single- and Few-Layer WTe2 and Their Suspended Nanostructures: Raman Signatures and Nanomechanical Resonances. *Nanoscale*, March 2016.

[211] Yun Wu, Na Hyun Jo, Masayuki Ochi, Lunan Huang, Daixiang Mou, Sergey L. Bud'ko, P. C. Canfield, Nandini Trivedi, Ryotaro Arita, and Adam Kaminski. Temperature-Induced Lifshitz Transition in WTe2. *Physical Review Letters*, 115(16):166602, October 2015.

[212] Tian Liang, Quinn Gibson, Jun Xiong, Max Hirschberger, Sunanda P. Koduvayur, R. J. Cava, and N. P. Ong. Evidence for massive bulk Dirac fermions in $Pb_{1-x}Sn_xSe$ from Nernst and thermopower experiments. *Nature Communications*, 4:ncomms3696, November 2013.

[213] G.I. Babkin and V. Ya. Kravchenko. Influence of Surface Scattering on the Magnetoresistance and Hall Effect in Plates. *JETP*, 33(2):378, August 1971.

[214] P. S. Alekseev, A. P. Dmitriev, I. V. Gornyi, V. Yu. Kachorovskii, B. N. Narozhny, M. Schütt, and M. Titov. Magnetoresistance in Two-Component Systems. *Physical Review Letters*, 114(15):156601, April 2015.

[215] Pranab Kumar Das, D. Di Sante, I. Vobornik, J. Fujii, T. Okuda, E. Bruyer, A. Gyenis, B. E. Feldman, J. Tao, R. Ciancio, G. Rossi, M. N. Ali, S. Picozzi, A. Yadzani, G. Panaccione, and R. J. Cava. Layer-dependent quantum cooperation of electron and hole states in the anomalous semimetal WTe2. *Nature Communications*, 7:10847, February 2016.

[216] Yilin Wang, Kefeng Wang, Janice Reutt-Robey, Johnpierre Paglione, and Michael S. Fuhrer. Breakdown of compensation and persistence of nonsaturating magnetoresistance in gated $\mathrm{WT}{\mathrm{e}}_{2}$ thin flakes. *Physical Review B*, 93(12):121108, March 2016.

[217] Lin Wang, Ignacio Gutiérrez-Lezama, Céline Barreteau, Dong-Keun Ki, Enrico Giannini, and Alberto F. Morpurgo. Direct Observation of a Long-Range Field Effect from Gate Tuning of Nonlocal Conductivity. *Physical Review Letters*, 117(17):176601, October 2016.

[218] Chia-Hui Lee, Eduardo Cruz Silva, Lazaro Calderin, Minh An T. Nguyen, Matthew J. Hollander, Brian Bersch, Thomas E. Mallouk, and Joshua A. Robinson. Tungsten Ditelluride: a layered semimetal. *Scientific Reports*, 5:10013, June 2015.

[219] Adam W. Tsen, Robert Hovden, Dennis Wang, Young Duck Kim, Junichi Okamoto, Katherine A. Spoth, Yu Liu, Wenjian Lu, Yuping Sun, James C. Hone, Lena F. Kourkoutis, Philip Kim, and Abhay N. Pasupathy. Structure and control of charge density waves in two-dimensional 1t-TaS2. *Proceedings of the National Academy of Sciences*, 112(49):15054–15059, December 2015.

[220] L. Wang, I. Meric, P. Y. Huang, Q. Gao, Y. Gao, H. Tran, T. Taniguchi, K. Watanabe, L. M. Campos, D. A. Muller, J. Guo, P. Kim, J. Hone, K. L. Shepard, and C. R. Dean. One-Dimensional Electrical Contact to a Two-Dimensional Material. *Science*, 342(6158):614–617, November 2013.

[221] Xu Cui, Gwan-Hyoung Lee, Young Duck Kim, Ghidewon Arefe, Pinshane Y. Huang, Chul-Ho Lee, Daniel A. Chenet, Xian Zhang, Lei Wang, Fan Ye, Filippo Pizzocchero, Bjarke S. Jessen, Kenji Watanabe, Takashi Taniguchi, David A. Muller, Tony Low, Philip Kim, and James Hone. Multi-terminal transport measurements of MoS2 using a van der Waals heterostructure device platform. *Nature Nanotechnology*, 10(6):534–540, June 2015.

[222] Xu Du, Shan-Wen Tsai, Dmitrii L. Maslov, and Arthur F. Hebard. Metal-Insulator-Like Behavior in Semimetallic Bismuth and Graphite. *Physical Review Letters*, 94(16):166601, April 2005.

[223] P. L. Cai, J. Hu, L. P. He, J. Pan, X. C. Hong, Z. Zhang, J. Zhang, J. Wei, Z. Q. Mao, and S. Y. Li. Drastic Pressure Effect on the Extremely Large Magnetoresistance in ${\mathrm{WTe}}_{2}$: Quantum Oscillation Study. *Physical Review Letters*, 115(5):057202, July 2015.

[224] B. N. Narozhny and A. Levchenko. Coulomb drag. *Reviews of Modern Physics*, 88(2):025003, May 2016.

[225] Thiti Taychatanapat and Pablo Jarillo-Herrero. Electronic Transport in Dual-Gated Bilayer Graphene at Large Displacement Fields. *Physical Review Letters*, 105(16):166601, October 2010.

[226] Zaiyao Fei, Tauno Palomaki, Sanfeng Wu, Wenjin Zhao, Xinghan Cai, Bosong Sun, Paul Nguyen, Joseph Finney, Xiaodong Xu, and David H. Cobden. Edge conduction in monolayer WTe2. *Nature Physics*, 13(7):nphys4091, April 2017.

[227] Sanfeng Wu, Valla Fatemi, Quinn D. Gibson, Kenji Watanabe, Takashi Taniguchi, Robert J. Cava, and Pablo Jarillo-Herrero. Observation of the Quantum Spin Hall Effect up to 100 Kelvin in a Monolayer Crystal. *ArXiv (online)*, 2017.

[228] C. L. Kane and E. J. Mele. Quantum Spin Hall Effect in Graphene. *Physical Review Letters*, 95(22):226801, November 2005.

[229] B. Andrei Bernevig and Shou-Cheng Zhang. Quantum Spin Hall Effect. *Physical Review Letters*, 96(10):106802, March 2006.

[230] Ivan Knez, Rui-Rui Du, and Gerard Sullivan. Evidence for Helical Edge Modes in Inverted InAs/GaSb Quantum Wells. *Physical Review Letters*, 107(13):136603, September 2011.

[231] Shuichi Murakami. Quantum Spin Hall Effect and Enhanced Magnetic Response by Spin-Orbit Coupling. *Physical Review Letters*, 97(23):236805, December 2006.

[232] Yong Xu, Binghai Yan, Hai-Jun Zhang, Jing Wang, Gang Xu, Peizhe Tang, Wenhui Duan, and Shou-Cheng Zhang. Large-Gap Quantum Spin Hall Insulators in Tin Films. *Physical Review Letters*, 111(13):136804, September 2013.

[233] Jin-Jian Zhou, Wanxiang Feng, Cheng-Cheng Liu, Shan Guan, and Yugui Yao. Large-Gap Quantum Spin Hall Insulator in Single Layer Bismuth Monobromide Bi4br4. *Nano Letters*, 14(8):4767–4771, August 2014.

[234] Sheng-shi Li, Wei-xiao Ji, Chang-wen Zhang, Shu-jun Hu, Ping Li, Pei-ji Wang, Bao-min Zhang, and Chong-long Cao. Robust Room-Temperature Quantum Spin Hall Effect in Methyl-functionalized InBi honeycomb film. *Scientific Reports*, 6:23242, March 2016.

[235] Y. Cao, A. Mishchenko, G. L. Yu, E. Khestanova, A. P. Rooney, E. Prestat, A. V. Kretinin, P. Blake, M. B. Shalom, C. Woods, J. Chapman, G. Balakrishnan, I. V. Grigorieva, K. S. Novoselov, B. A. Piot, M. Potemski, K. Watanabe, T. Taniguchi, S. J. Haigh, A. K. Geim, and R. V. Gorbachev. Quality Heterostructures from Two-Dimensional Crystals Unstable in Air by Their Assembly in Inert Atmosphere. *Nano Letters*, 15(8):4914–4921, August 2015.

[236] C. Sabater, D. Gosálbez-Martínez, J. Fernández-Rossier, J. G. Rodrigo, C. Untiedt, and J. J. Palacios. Topologically Protected Quantum Transport in Locally Exfoliated Bismuth at Room Temperature. *Physical Review Letters*, 110(17):176802, April 2013.

[237] Ilya K. Drozdov, A. Alexandradinata, Sangjun Jeon, Stevan Nadj-Perge, Huiwen Ji, R. J. Cava, B. Andrei Bernevig, and Ali Yazdani. One-dimensional topological edge states of bismuth bilayers. *Nature Physics*, 10(9):664–669, September 2014.

[238] Fabrizio Nichele, Henri J. Suominen, Morten Kjaergaard, Charles M. Marcus, Ebrahim Sajadi, Joshua A. Folk, Fanming Qu, Arjan J. A. Beukman, Folkert K. de Vries, Jasper van Veen, Stevan Nadj-Perge, Leo P. Kouwenhoven, Binh-Minh Nguyen, Andrey A. Kiselev, Wei Yi, Marko Sokolich, Michael J. Manfra, Eric M. Spanton, and Kathryn A. Moler. Edge transport in the trivial phase of InAs/GaSb. *New Journal of Physics*, 18(8):083005, 2016.

[239] Eric Yue Ma, M. Reyes Calvo, Jing Wang, Biao Lian, Mathias Mühlbauer, Christoph Brüne, Yong-Tao Cui, Keji Lai, Worasom Kundhikanjana, Yongliang Yang, Matthias Baenninger, Markus König, Christopher Ames, Hartmut Buhmann, Philipp Leubner, Laurens W. Molenkamp, Shou-Cheng Zhang, David Goldhaber-Gordon, Michael A. Kelly, and Zhi-Xun Shen. Unexpected edge conduction in mercury telluride quantum wells under broken time-reversal symmetry. *Nature Communications*, 6:7252, May 2015.

[240] Sven Essert and Klaus Richter. Magnetotransport in disordered two-dimensional topological insulators: signatures of charge puddles. *2D Materials*, 2(2):024005, 2015.

[241] Lingjie Du, Ivan Knez, Gerard Sullivan, and Rui-Rui Du. Robust Helical Edge Transport in Gated InAs/GaSb Bilayers. *Physical Review Letters*, 114(9):096802, March 2015.

[242] Jukka I. Väyrynen, Moshe Goldstein, Yuval Gefen, and Leonid I. Glazman. Resistance of helical edges formed in a semiconductor heterostructure. *Physical Review B*, 90(11):115309, September 2014.

[243] Joseph Maciejko, Chaoxing Liu, Yuval Oreg, Xiao-Liang Qi, Congjun Wu, and Shou-Cheng Zhang. Kondo Effect in the Helical Edge Liquid of the Quantum Spin Hall State. *Physical Review Letters*, 102(25):256803, June 2009.

[244] Tingxin Li, Pengjie Wang, Hailong Fu, Lingjie Du, Kate A. Schreiber, Xiaoyang Mu, Xiaoxue Liu, Gerard Sullivan, Gábor A. Csáthy, Xi Lin, and Rui-Rui Du. Observation of a Helical Luttinger Liquid in InAs/GaSb Quantum Spin Hall Edges. *Physical Review Letters*, 115(13):136804, September 2015.

[245] Markus Konig, Hartmut Buhmann, Laurens W. Molenkamp, Taylor Hughes, Chao-Xing Liu, Xiao-Liang Qi, and Shou-Cheng Zhang. The Quantum Spin Hall Effect: Theory and Experiment. *Journal of the Physical Society of Japan*, 77(3):031007, March 2008.

[246] Joseph Maciejko, Xiao-Liang Qi, and Shou-Cheng Zhang. Magnetoconductance of the quantum spin Hall state. *Physical Review B*, 82(15):155310, October 2010.

[247] Andreas Roth, Christoph Brüne, Hartmut Buhmann, Laurens W. Molenkamp, Joseph Maciejko, Xiao-Liang Qi, and Shou-Cheng Zhang. Nonlocal Transport in the Quantum Spin Hall State. *Science*, 325(5938):294–297, July 2009.

[248] D. C. Tsui, H. L. Stormer, and A. C. Gossard. Two-Dimensional Magnetotransport in the Extreme Quantum Limit. *Physical Review Letters*, 48(22):1559–1562, May 1982.

[249] Tian Shen, Wei Wu, Qingkai Yu, Curt A. Richter, Randolph Elmquist, David Newell, and Yong P. Chen. Quantum Hall effect on centimeter scale chemical vapor deposited graphene films. *Applied Physics Letters*, 99(23):232110, December 2011.

[250] Hartmut Buhmann. The quantum spin Hall effect. *Journal of Applied Physics*, 109(10):102409, May 2011.

[251] G. M. Gusev, Z. D. Kvon, E. B. Olshanetsky, A. D. Levin, Y. Krupko, J. C. Portal, N. N. Mikhailov, and S. A. Dvoretsky. Temperature dependence of the resistance of a two-dimensional topological insulator in a HgTe quantum well. *Physical Review B*, 89(12):125305, March 2014.

[252] Kyoichi Suzuki, Yuichi Harada, Koji Onomitsu, and Koji Muraki. Edge channel transport in the InAs/GaSb topological insulating phase. *Physical Review B*, 87(23):235311, June 2013.

[253] Ivan Knez, Charles T. Rettner, See-Hun Yang, Stuart S. P. Parkin, Lingjie Du, Rui-Rui Du, and Gerard Sullivan. Observation of Edge Transport in the Disordered Regime of Topologically Insulating InAs/GaSb Quantum Wells. *Physical Review Letters*, 112(2):026602, January 2014.

[254] Christoph Brüne, Andreas Roth, Hartmut Buhmann, Ewelina M. Hankiewicz, Laurens W. Molenkamp, Joseph Maciejko, Xiao-Liang Qi, and Shou-Cheng Zhang. Spin polarization of the quantum spin Hall edge states. *Nature Physics*, 8(6):485–490, June 2012.

[255] H. Kamerlingh Onnes. Further experiments with liquid helium. C. On the change of electric resistance of pure metals at very low temperatures etc. IV. The resistance of pure mercury at helium temperatures. In *Through Measurement to Knowledge*, Boston Studies in the Philosophy of Science, pages 261–263. Springer, Dordrecht, 1991. DOI: 10.1007/978-94-009-2079-8_15.

[256] John M. Blatt and Colin J. Thompson. Shape Resonances in Superconducting Thin Films. *Physical Review Letters*, 10(8):332–334, April 1963.

[257] Yen-Hsiang Lin, J. Nelson, and A. M. Goldman. Superconductivity of very thin films: The superconductor–insulator transition. *Physica C: Superconductivity and its Applications*, 514:130–141, July 2015.

[258] Yu Saito, Tsutomu Nojima, and Yoshihiro Iwasa. Highly crystalline 2d superconductors. *Nature Reviews Materials*, 2:16094, December 2016.

[259] R. E. Glover and M. D. Sherrill. Changes in Superconducting Critical Temperature Produced by Electrostatic Charging. *Physical Review Letters*, 5(6):248–250, September 1960.

[260] H. L. Stadler. Changing Properties of Metals by Ferroelectric Polarization Charging. *Physical Review Letters*, 14(24):979–981, June 1965.

[261] A. Hebard, A. Fiory, and R. Eick. Experimental considerations in the quest for a thin-film superconducting field-effect transistor. *IEEE Transactions on Magnetics*, 23(2):1279–1282, March 1987.

[262] X. X. Xi, C. Doughty, A. Walkenhorst, C. Kwon, Q. Li, and T. Venkatesan. Effects of field-induced hole-density modulation on normal-state and superconducting transport in ${\mathrm{YBa}}_{2}$${\mathrm{Cu}}_{3}$${\mathrm{O}}_{7\mathrm{\ensuremath{-}}\mathit{x}}$. *Physical Review Letters*, 68(8):1240–1243, February 1992.

[263] A. Walkenhorst, C. Doughty, X. X. Xi, Qi Li, C. J. Lobb, S. N. Mao, and T. Venkatesan. Electric field effects on vortex dynamics in ultrathin ${\mathrm{YBa}}_{2}$${\mathrm{Cu}}_{3}$${\mathrm{O}}_{7\mathrm{\ensuremath{-}}\mathrm{\ensuremath{\delta}}}$ films. *Physical Review Letters*, 69(18):2709–2712, November 1992.

[264] J. Mannhart. High-Tc Transistors. *Superconductor Science and Technology*, 9(2):49, 1996.

[265] Kevin A. Parendo, K. H. Sarwa B. Tan, A. Bhattacharya, M. Eblen-Zayas, N. E. Staley, and A. M. Goldman. Electrostatic Tuning of the Superconductor-Insulator Transition in Two Dimensions. *Physical Review Letters*, 94(19):197004, May 2005.

[266] Kevin A. Parendo, K. H. Sarwa B. Tan, and A. M. Goldman. Electrostatic and parallel-magnetic-field tuned two-dimensional superconductor-insulator transitions. *Physical Review B*, 73(17):174527, May 2006.

[267] K. Ueno, S. Nakamura, H. Shimotani, A. Ohtomo, N. Kimura, T. Nojima, H. Aoki, Y. Iwasa, and M. Kawasaki. Electric-field-induced superconductivity in an insulator. *Nature Materials*, 7(11):855–858, November 2008.

[268] A. D. Caviglia, S. Gariglio, N. Reyren, D. Jaccard, T. Schneider, M. Gabay, S. Thiel, G. Hammerl, J. Mannhart, and J.-M. Triscone. Electric field control of the LaAlO3/SrTiO3 interface ground state. *Nature*, 456(7222):624–627, December 2008.

[269] J. Bardeen, L. N. Cooper, and J. R. Schrieffer. Microscopic Theory of Superconductivity. *Physical Review*, 106(1):162–164, April 1957.

[270] J. Bardeen, L. N. Cooper, and J. R. Schrieffer. Theory of Superconductivity. *Physical Review*, 108(5):1175–1204, December 1957.

[271] V. L. Gurevich, A. I. Larkin, and Yu. A. Firsov. On the possibility of superconductivity in semiconductors. *Soviet Physics – Solid State*, 4(1):185–190, July 1962.

[272] Marvin L. Cohen. Superconductivity in Many-Valley Semiconductors and in Semimetals. *Physical Review*, 134(2A):A511–A521, April 1964.

[273] C. S. Koonce and Marvin L. Cohen. Theory of Superconducting Semiconductors and Semimetals. *Physical Review*, 177(2):707–719, January 1969.

[274] Jonathan Ruhman and Patrick A. Lee. Superconductivity at very low density: The case of strontium titanate. *Physical Review B*, 94(22):224515, December 2016.

[275] Lev P. Gor'kov. Superconducting transition temperature: Interacting Fermi gas and phonon mechanisms in the nonadiabatic regime. *Physical Review B*, 93(5):054517, February 2016.

[276] Jonathan Ruhman and Patrick A. Lee. Pairing from dynamically screened Coulomb repulsion in bismuth. *arXiv:1706.00008 [cond-mat]*, May 2017. arXiv: 1706.00008.

[277] J. T. Ye, S. Inoue, K. Kobayashi, Y. Kasahara, H. T. Yuan, H. Shimotani, and Y. Iwasa. Liquid-gated interface superconductivity on an atomically flat film. *Nature Materials*, 9(2):125–128, February 2010.

[278] J. Biscaras, N. Bergeal, S. Hurand, C. Grossetête, A. Rastogi, R. C. Budhani, D. LeBoeuf, C. Proust, and J. Lesueur. Two-Dimensional Superconducting Phase in ${\mathrm{LaTiO}}_{3}/{\mathrm{SrTiO}}_{3}$ Heterostructures Induced by High-Mobility Carrier Doping. *Physical Review Letters*, 108(24):247004, June 2012.

[279] Julie A. Bert, Katja C. Nowack, Beena Kalisky, Hilary Noad, John R. Kirtley, Chris Bell, Hiroki K. Sato, Masayuki Hosoda, Yasayuki Hikita, Harold Y. Hwang, and Kathryn A. Moler. Gate-tuned superfluid density at the superconducting LaAlO${}_{3}$/SrTiO${}_{3}$ interface. *Physical Review B*, 86(6):060503, August 2012.

[280] J. T. Ye, Y. J. Zhang, R. Akashi, M. S. Bahramy, R. Arita, and Y. Iwasa. Superconducting Dome in a Gate-Tuned Band Insulator. *Science*, 338(6111):1193–1196, November 2012.

[281] Yu Saito, Tsutomu Nojima, and Yoshihiro Iwasa. Gate-induced superconductivity in two-dimensional atomic crystals. *Superconductor Science and Technology*, 29(9):093001, 2016.

[282] V. Mourik, K. Zuo, S. M. Frolov, S. R. Plissard, E. P. a. M. Bakkers, and L. P. Kouwenhoven. Signatures of Majorana Fermions in Hybrid Superconductor-Semiconductor Nanowire Devices. *Science*, 336(6084):1003–1007, May 2012.

[283] W. Chang, S. M. Albrecht, T. S. Jespersen, F. Kuemmeth, P. Krogstrup, J. Nygård, and C. M. Marcus. Hard gap in epitaxial semiconductor–superconductor nanowires. *Nature Nanotechnology*, 10(3):232–236, March 2015.

[284] Stevan Nadj-Perge, Ilya K. Drozdov, Jian Li, Hua Chen, Sangjun Jeon, Jungpil Seo, Allan H. MacDonald, B. Andrei Bernevig, and Ali Yazdani. Observation of Majorana fermions in ferromagnetic atomic chains on a superconductor. *Science*, 346(6209):602–607, October 2014.

[285] Sean Hart, Hechen Ren, Timo Wagner, Philipp Leubner, Mathias Mühlbauer, Christoph Brüne, Hartmut Buhmann, Laurens W. Molenkamp, and Amir Yacoby. Induced superconductivity in the quantum spin Hall edge. *Nature Physics*, 10(9):638–643, September 2014.

[286] J. Wiedenmann, E. Bocquillon, R. S. Deacon, S. Hartinger, O. Herrmann, T. M. Klapwijk, L. Maier, C. Ames, C. Brüne, C. Gould, A. Oiwa, K. Ishibashi, S. Tarucha,

H. Buhmann, and L. W. Molenkamp. 4π-periodic Josephson supercurrent in HgTe-based topological Josephson junctions. *Nature Communications*, 7:10303, January 2016.

[287] Erwann Bocquillon, Russell S. Deacon, Jonas Wiedenmann, Philipp Leubner, Teunis M. Klapwijk, Christoph Brüne, Koji Ishibashi, Hartmut Buhmann, and Laurens W. Molenkamp. Gapless Andreev bound states in the quantum spin Hall insulator HgTe. *Nature Nanotechnology*, 12(2):nnano.2016.159, August 2016.

[288] R. S. Deacon, J. Wiedenmann, E. Bocquillon, F. Domínguez, T. M. Klapwijk, P. Leubner, C. Brüne, E. M. Hankiewicz, S. Tarucha, K. Ishibashi, H. Buhmann, and L. W. Molenkamp. Josephson Radiation from Gapless Andreev Bound States in HgTe-Based Topological Junctions. *Physical Review X*, 7(2):021011, April 2017.

[289] Vlad S. Pribiag, Arjan J. A. Beukman, Fanming Qu, Maja C. Cassidy, Christophe Charpentier, Werner Wegscheider, and Leo P. Kouwenhoven. Edge-mode superconductivity in a two-dimensional topological insulator. *Nature Nanotechnology*, 10(7):593–597, July 2015.

[290] L. G. Aslamasov and A. I. Larkin. The influence of fluctuation pairing of electrons on the conductivity of normal metal. *Physics Letters A*, 26(6):238–239, February 1968.

[291] Kazumi Maki. The Critical Fluctuation of the Order Parameter in Type-II Superconductors. *Progress of Theoretical Physics*, 39(4):897–906, April 1968.

[292] Richard S. Thompson. Microwave, Flux Flow, and Fluctuation Resistance of Dirty Type-II Superconductors. *Physical Review B*, 1(1):327–333, January 1970.

[293] A. Larkin and A.A. Varlamov. *Theory of Fluctuations of Superconductors*.

[294] V. L. Berezinksii. Destruction of Long-range Order in One-dimensional and Two-dimensional Systems having a Continuous Symmetry Group I. Classical Systems. *Journal of Experimental and Theoretical Physics*, 32(3):493, March 1971.

[295] V. L. Berezinksii. Destruction of Long-range Order in One-dimensional and Two-dimensional Systems having a Continuous Symmetry Group II. Quantum Systems. *Journal of Experimental and Theoretical Physics*, 34(3):610, March 1972.

[296] J. M. Kosterlitz and D. J. Thouless. Ordering, metastability and phase transitions in two-dimensional systems. *Journal of Physics C: Solid State Physics*, 6(7):1181, 1973.

[297] M. R. Beasley, J. E. Mooij, and T. P. Orlando. Possibility of Vortex-Antivortex Pair Dissociation in Two-Dimensional Superconductors. *Physical Review Letters*, 42(17):1165–1168, April 1979.

[298] J. W. P. Hsu and A. Kapitulnik. Superconducting transition, fluctuation, and vortex motion in a two-dimensional single-crystal Nb film. *Physical Review B*, 45(9):4819–4835, March 1992.

[299] Matthew P. A. Fisher. Quantum phase transitions in disordered two-dimensional superconductors. *Physical Review Letters*, 65(7):923–926, August 1990.

[300] Ali Yazdani, W. R. White, M. R. Hahn, M. Gabay, M. R. Beasley, and A. Kapitulnik. Observation of Kosterlitz-Thouless-type melting of the disordered vortex lattice in thin films of a-MoGe. *Physical Review Letters*, 70(4):505–508, January 1993.

[301] Stephen W. Pierson, Mark Friesen, S. M. Ammirata, Jeffrey C. Hunnicutt, and LeRoy A. Gorham. Dynamic scaling for two-dimensional superconductors, Josephson-junction arrays, and superfluids. *Physical Review B*, 60(2):1309–1325, July 1999.

[302] D. Ephron, A. Yazdani, A. Kapitulnik, and M. R. Beasley. Observation of Quantum Dissipation in the Vortex State of a Highly Disordered Superconducting Thin Film. *Physical Review Letters*, 76(9):1529–1532, February 1996.

[303] Efrat Shimshoni, Assa Auerbach, and Aharon Kapitulnik. Transport through Quantum Melts. *Physical Review Letters*, 80(15):3352–3355, April 1998.

[304] D. Das and S. Doniach. Existence of a Bose metal at $T=0$. *Physical Review B*, 60(2):1261–1275, July 1999.

[305] B. Spivak, A. Zyuzin, and M. Hruska. Quantum superconductor-metal transition. *Physical Review B*, 64(13):132502, August 2001.

[306] Denis Dalidovich and Philip Phillips. Phase Glass is a Bose Metal: A New Conducting State in Two Dimensions. *Physical Review Letters*, 89(2):027001, June 2002.

[307] Philip Phillips and Denis Dalidovich. The Elusive Bose Metal. *Science*, 302(5643):243–247, October 2003.

[308] B. Spivak, P. Oreto, and S. A. Kivelson. Theory of quantum metal to superconductor transitions in highly conducting systems. *Physical Review B*, 77(21):214523, June 2008.

[309] Serena Eley, Sarang Gopalakrishnan, Paul M. Goldbart, and Nadya Mason. Approaching zero-temperature metallic states in mesoscopic superconductor-normal-superconductor arrays. *Nature Physics*, 8(1):59–62, January 2012.

[310] D. Bucheli, S. Caprara, C. Castellani, and M. Grilli. Metal–superconductor transition in low-dimensional superconducting clusters embedded in two-dimensional electron systems. *New Journal of Physics*, 15(2):023014, 2013.

[311] Zheng Han, Adrien Allain, Hadi Arjmandi-Tash, Konstantin Tikhonov, Mikhail Feigel'man, Benjamin Sacépé, and Vincent Bouchiat. Collapse of superconductivity in a hybrid tin-graphene Josephson junction array. *Nature Physics*, 10(5):380–386, May 2014.

[312] Yu Saito, Yuichi Kasahara, Jianting Ye, Yoshihiro Iwasa, and Tsutomu Nojima. Metallic ground state in an ion-gated two-dimensional superconductor. *Science*, 350(6259):409–413, October 2015.

[313] Chandra M. Varma. Quantum-critical fluctuations in 2d metals: strange metals and superconductivity in antiferromagnets and in cuprates. *Reports on Progress in Physics*, 79(8):082501, 2016.

[314] A. W. Tsen, B. Hunt, Y. D. Kim, Z. J. Yuan, S. Jia, R. J. Cava, J. Hone, P. Kim, C. R. Dean, and A. N. Pasupathy. Nature of the quantum metal in a two-dimensional crystalline superconductor. *Nature Physics*, 12(3):208–212, March 2016.

[315] I. Tamir, A. Benyamini, E. J. Telford, F. Gorniaczyk, A. Doron, T. Levinson, D. Wang, F. Gay, B. Sacépé, J. Hone, K. Watanabe, T. Taniguchi, C. R. Dean, A. N. Pasupathy,

and D. Shahar. Extreme Sensitivity of the Superconducting State in Thin Films. April 2018.

[316] Adrien Allain, Zheng Han, and Vincent Bouchiat. Electrical control of the superconducting-to-insulating transition in graphene–metal hybrids. *Nature Materials*, 11(7):nmat3335, May 2012.

[317] A. Kapitulnik and G. Kotliar. Anderson Localization and the Theory of Dirty Superconductors. *Physical Review Letters*, 54(5):473–476, February 1985.

[318] A. F. Hebard and M. A. Paalanen. Diverging Characteristic Lengths at Critical Disorder in Thin-Film Superconductors. *Physical Review Letters*, 54(19):2155–2158, May 1985.

[319] A. M. Finkel'stein. Suppression of superconductivity in homogeneously disordered systems. *Physica B: Condensed Matter*, 197(1):636–648, March 1994.

[320] M. Tinkham. *Introduction to Superconductivity*. Dover, New York, 2004.

[321] J. M. Lu, O. Zheliuk, I. Leermakers, N. F. Q. Yuan, U. Zeitler, K. T. Law, and J. T. Ye. Evidence for two-dimensional Ising superconductivity in gated MoS2. *Science*, 350(6266):1353–1357, December 2015.

[322] Xiaoxiang Xi, Zefang Wang, Weiwei Zhao, Ju-Hyun Park, Kam Tuen Law, Helmuth Berger, László Forró, Jie Shan, and Kin Fai Mak. Ising pairing in superconducting NbSe2 atomic layers. *Nature Physics*, 12(2):139–143, February 2016.

[323] Takashi Uchihashi. Two-dimensional superconductors with atomic-scale thickness. *Superconductor Science and Technology*, 30(1):013002, 2017.

[324] Sergio C. de la Barrera, Michael R. Sinko, Devashish P. Gopalan, Nikhil Sivadas, Kyle L. Seyler, Kenji Watanabe, Takashi Taniguchi, Adam W. Tsen, Xiaodong Xu, Di Xiao, and Benjamin M. Hunt. Tuning Ising superconductivity with layer and spin-orbit coupling in two-dimensional transition-metal dichalcogenides. *arXiv:1711.00468 [cond-mat]*, November 2017. arXiv: 1711.00468.

[325] Defen Kang, Yazhou Zhou, Wei Yi, Chongli Yang, Jing Guo, Youguo Shi, Shan Zhang, Zhe Wang, Chao Zhang, Sheng Jiang, Aiguo Li, Ke Yang, Qi Wu, Guangming Zhang, Liling Sun, and Zhongxian Zhao. Superconductivity emerging from a suppressed large magnetoresistant state in tungsten ditelluride. *Nature Communications*, 6:ncomms8804, July 2015.

[326] Xing-Chen Pan, Xuliang Chen, Huimei Liu, Yanqing Feng, Zhongxia Wei, Yonghui Zhou, Zhenhua Chi, Li Pi, Fei Yen, Fengqi Song, Xiangang Wan, Zhaorong Yang, Baigeng Wang, Guanghou Wang, and Yuheng Zhang. Pressure-driven dome-shaped superconductivity and electronic structural evolution in tungsten ditelluride. *Nature Communications*, 6:ncomms8805, July 2015.

[327] Pengchao Lu, Joon-Seok Kim, Jing Yang, Hao Gao, Juefei Wu, Dexi Shao, Bin Li, Dawei Zhou, Jian Sun, Deji Akinwande, Dingyu Xing, and Jung-Fu Lin. Origin of superconductivity in the Weyl semimetal $\mathrm{WT}{\mathrm{e}}_{2}$ under pressure. *Physical Review B*, 94(22):224512, December 2016.

[328] Jun-Ho Lee and Young-Woo Son. Reentrant Quantum Spin Hall States in Charge Density Wave Phase of Doped Single-Layer Transition Metal Dichalcogenides. *arXiv:1711.08073 [cond-mat]*, November 2017. arXiv: 1711.08073.

[329] Ernst Bauer and Manfred Sigrist, editors. *Non-Centrosymmetric Superconductors*, volume 847 of *Lecture Notes in Physics*. Springer Berlin Heidelberg, Berlin, Heidelberg, 2012. DOI: 10.1007/978-3-642-24624-1.

[330] B. Sacépé, C. Chapelier, T. I. Baturina, V. M. Vinokur, M. R. Baklanov, and M. Sanquer. Disorder-Induced Inhomogeneities of the Superconducting State Close to the Superconductor-Insulator Transition. *Physical Review Letters*, 101(15):157006, October 2008.

[331] Benjamin Sacépé, Thomas Dubouchet, Claude Chapelier, Marc Sanquer, Maoz Ovadia, Dan Shahar, Mikhail Feigel'man, and Lev Ioffe. Localization of preformed Cooper pairs in disordered superconductors. *Nature Physics*, 7(3):nphys1892, January 2011.

[332] T. Dvir, F. Massee, L. Attias, M. Khodas, M. Aprili, C. H. L. Quay, and H. Steinberg. Spectroscopy of bulk and few-layer superconducting NbSe 2 with van der Waals tunnel junctions. *Nature Communications*, 9(1):598, February 2018.

[333] P. W. Anderson. Theory of dirty superconductors. *Journal of Physics and Chemistry of Solids*, 11(1):26–30, September 1959.

[334] Toshihiko Tsuneto. On Dirty Superconductors. *Progress of Theoretical Physics*, 28(5):857–869, November 1962.

[335] Erwann Bocquillon, Russell S. Deacon, Jonas Wiedenmann, Philipp Leubner, Teunis M. Klapwijk, Christoph Brüne, Koji Ishibashi, Hartmut Buhmann, and Laurens W. Molenkamp. Gapless Andreev bound states in the quantum spin Hall insulator HgTe. *Nature Nanotechnology*, 12(2):137–143, February 2017.

[336] Cheng Gong, Lin Li, Zhenglu Li, Huiwen Ji, Alex Stern, Yang Xia, Ting Cao, Wei Bao, Chenzhe Wang, Yuan Wang, Z. Q. Qiu, R. J. Cava, Steven G. Louie, Jing Xia, and Xiang Zhang. Discovery of intrinsic ferromagnetism in two-dimensional van der Waals crystals. *Nature*, 546(7657):nature22060, April 2017.

[337] Bevin Huang, Genevieve Clark, Efrén Navarro-Moratalla, Dahlia R. Klein, Ran Cheng, Kyle L. Seyler, Ding Zhong, Emma Schmidgall, Michael A. McGuire, David H. Cobden, Wang Yao, Di Xiao, Pablo Jarillo-Herrero, and Xiaodong Xu. Layer-dependent ferromagnetism in a van der Waals crystal down to the monolayer limit. *Nature*, 546(7657):270–273, June 2017.

[338] Johan Nilsson, A. R. Akhmerov, and C. W. J. Beenakker. Splitting of a Cooper Pair by a Pair of Majorana Bound States. *Physical Review Letters*, 101(12):120403, September 2008.

[339] Liang Fu and C. L. Kane. Josephson current and noise at a superconductor/quantum-spin-Hall-insulator/superconductor junction. *Physical Review B*, 79(16):161408, April 2009.

[340] Liang Fu. Electron Teleportation via Majorana Bound States in a Mesoscopic Superconductor. *Physical Review Letters*, 104(5):056402, February 2010.

[341] E. H. Hwang and S. Das Sarma. Single-particle relaxation time versus transport scattering time in a two-dimensional graphene layer. *Physical Review B*, 77(19):195412, May 2008.

[342] S. Das Sarma, Shaffique Adam, E. H. Hwang, and Enrico Rossi. Electronic transport in two-dimensional graphene. *Reviews of Modern Physics*, 83(2):407–470, May 2011.

[343] J. Black, E. M. Conwell, L. Seigle, and C. W. Spencer. Electrical and optical properties of some M2v-bN3vi-b semiconductors. *Journal of Physics and Chemistry of Solids*, 2(3):240–251, 1957.

[344] Anjan A. Reijnders, Y. Tian, L. J. Sandilands, G. Pohl, I. D. Kivlichan, S. Y. Frank Zhao, S. Jia, M. E. Charles, R. J. Cava, Nasser Alidoust, Suyang Xu, Madhab Neupane, M. Zahid Hasan, X. Wang, S. W. Cheong, and K. S. Burch. Optical evidence of surface state suppression in Bi-based topological insulators. *Physical Review B*, 89(7):075138, February 2014.

[345] X. Chen, H. D. Zhou, A. Kiswandhi, I. Miotkowski, Y. P. Chen, P. A. Sharma, A. L. Lima Sharma, M. A. Hekmaty, D. Smirnov, and Z. Jiang. Thermal expansion coefficients of Bi2se3 and Sb2te3 crystals from 10 K to 270 K. *Applied Physics Letters*, 99(26):261912, December 2011.

[346] John G. Simmons. Generalized Formula for the Electric Tunnel Effect between Similar Electrodes Separated by a Thin Insulating Film. *Journal of Applied Physics*, 34(6):1793–1803, June 1963.

[347] Babak Fallahazad, Hema C. P. Movva, Kyounghwan Kim, Stefano Larentis, Takashi Taniguchi, Kenji Watanabe, Sanjay K. Banerjee, and Emanuel Tutuc. Shubnikov-de Haas Oscillations of High-Mobility Holes in Monolayer and ilayer WSe2: Landau Level Degeneracy, Effective Mass, and Negative Compressibility. *Physical Review Letters*, 116(8):086601, February 2016.

[348] Minjung Kim, Songhee Han, Jung Hwa Kim, Jae-Ung Lee, Zonghoon Lee, and Hyeonsik Cheong. Determination of the thickness and orientation of few-layer tungsten ditelluride using polarized Raman spectroscopy. *2D Materials*, 3(3):034004, 2016.